VNIVERSITAT ID VALÈNCIA

ulp
UNIVERSITÉ LOUIS PASTEUR STRASBOURG
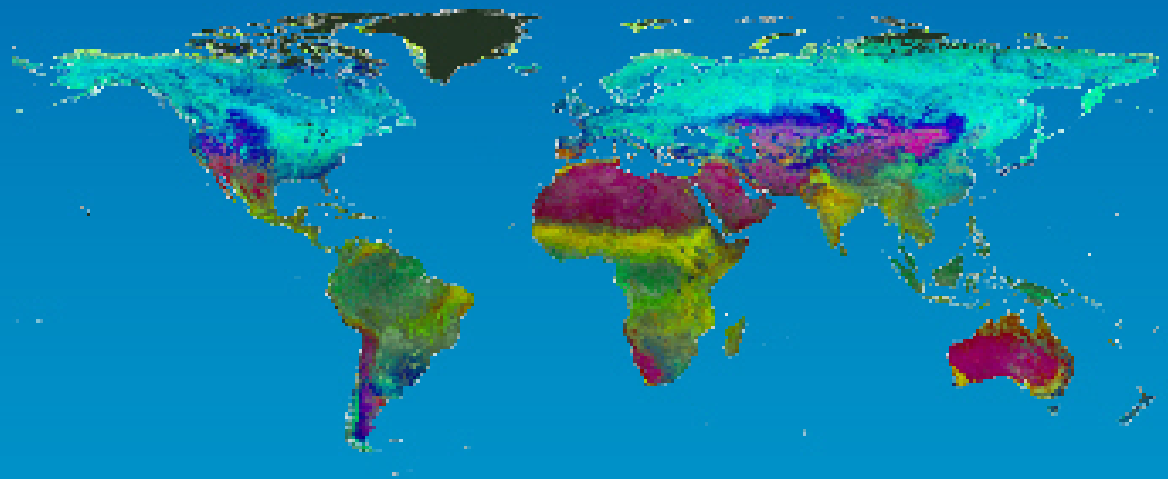
Vegetation monitoring through retrieval of NDVI and LST time series from historical databases

PhD Dissertation
Yves JULIEN
2008

UNIVERSITAT
DE VALÈNCIA

UNIVERSITÉ LOUIS PASTEUR
DE STRASBOURG

Facultat de Física
Departamento de Física de la Tierra y
Termodinámica

École Doctorale Mathématiques,
Sciences de l'Information et de
l'Ingénieur

Vegetation monitoring through retrieval of NDVI and LST time series from historical databases

Tribunal:

José A. Sobrino
Françoise Nerry
Zhao Liang Li
José F. Moreno
Alain Royer
Jihad Zallat

PhD DISSERTATION

Yves JULIEN

January 2008

José Antonio Sobrino Rodríguez, Profesor Titular de Física de la Tierra de la Universitat de València, y Director de la Unidad de Cambio Global,

y

Françoise Nerry, Investigadora del Laboratoire des Sciences de l'Image, de l'Informatique et de la Télédétection, y Directora del grupo de Télédétection, Radiométrie et Imagerie Optique en Estrasburgo (Francia),

CERTIFICAN:

Que la presente Memoria "**Vegetation monitoring through retrieval of NDVI and LST time series from historical databases**", ha sido realizado bajo nuestra direccion en el Departamento de Física de la Tierra y Termodinámica de la Facultat de Física por D. Yves Julien, y constituye su Tesis Doctoral para optar al grado de Doctor en Física.

Y para que así conste, en cumplimiento de la legislación vigente, firmo el presente certificado en Burjassot (Valencia), a 7 de Enero de 2008.

Fdo.: **J. A. Sobrino Rodríguez**   Fdo.: **F. Nerry**

ACKNOWLEDGEMENT

In the following paragraph, I would like to thank all the persons who have helped to realize this work, whether by their advice or their support.

To my director, Dr. **José Antonio Sobrino**, for offering me the opportunity to work on this subject, and for the advice, help and support brought during the past four years. Thank you for all of this. And thank you for letting me carry out my research freely, and for advising me when I was going astray.

To my other director, **Françoise Nerry**, for accepting to co-direct my PhD, and for all the advice, help and support provided. Thank you.

To Dr. **Joaquín Meliá Miralles**, previous Head of the Department of Thermodynamics, and to Dr. **Soledad Gandía**, actual Head of the Department of Earth Physics and Thermodynamics.

To the **secretaries** of the Department of Earth Physics and Thermodynamics, for their help and guidance through the whole administrative process.

To **Luis "Lucho" Morales**, for his invitation to and tour of his austral homeland, his friendship and those unending talks I enjoyed so much. I must also thank you Lucho for your scientific knowledge: you'll soon be a Monolith.

To **Molly E. Brown**, for getting through the tedious work of getting together and providing me with the GIMMS additional data described in chapter 2.

To **Wout Verhoef**, for his help with the HANTS software (see chapter 3).

To **Norden E. Huang**, for his help with the EMD decomposition (see chapter 3).

To all my past, present and future colleagues at the Global Change Unit, for their help, their support, and their tolerance towards my accent, my music and my wicked sense of humour. Thank you **Juan-Carlos** for all your help with theoretical aspects of my work. Thank you **Guillem** for all your help with the computers. Thank you **Mireia** for your tour of the Valencian rock scene. Thank you **Malena**, for introducing me to Valencia. Thank you **Juan** for your unfathomable knowledge. Thank you **Mariam** for all those little cakes. Thank you **Ana** for your lentils. Thank you **Cristián**, for introducing me to Santiago de Chile, and for your friendship now you're here. Thank you **Belén** for never getting angry when I need you to scan something for me. Thank you **Victoria** for your accent I'll understand one day. And thank you **Jauad**, for introducing me to all these people. I do know that thanking all of you for just one little thing does not make you justice, so be sure I'll bring some more of these pancakes to make it up to you all.

And finally, to my family and friends. To my family and friends in France, for being there in my absence. I may live far from you, but you're still important to me. To the friends I made here in Spain, if I'm planning to stay longer it's also because of you. To the Camboata Team and the Shaolin Warriors, for bringing me the physical strength to carry on, and to ATTAC-PV and Pobreza Cero, for bringing me the mental strength to carry on.

Acknowledgement

INDEX

x

LIST OF FIGURES

Chapter 3 – DATA PROCESSING

Chapter 4 – TIME SERIES ANALYSIS

black indicates statistically significant negative correlation, while grey indicates statistically insignificant correlation.

Figure 4.9.- Spring dates (in days of year) for a) year 1990 (beginning on January, 1st) and b) year 1990-1991 (beginning on July, 1st) retrieved from GIMMS (Global Inventory Modeling and Mapping Studies) data.

Figure 4.10.- Correlation values in threshold determination for degree-day calculations.

Figure 4.11.- Retrieved thresholds for spring dates estimation from degree-days: a) T_0 - daily threshold (in ºC) and b) DG - total degree-day amount (cf. Eq. 4.7).

Figure 4.12.- Spring dates (in day of years) for a) year 1990 (beginning on January, 1st) and b) year 1990-1991 (beginning on July, 1st) estimated from degree-day amounts.

Figure 4.13.- Trends for spring dates (in days per year) estimated from degree-day amounts for the 1948-2006 period (a) and for the 1981-2006 period (b). Only statistically meaningful trends (Mann-Kendall trend tests) are shown.

Figure 4.14.- Geographic distribution of potential climatic constraints to plant growth (adapted from Nemani et al., 2003).

Figure 4.15.- Results of empirical orthogonal analysis on correlation matrices for time series of NDVI metrics. 1st components are displayed for a) wNDVI (1st component explains 67% of total variance); b) mNDVI (94%); and c) mS (19%).

Figure 4.15.- (continued) Results of empirical orthogonal analysis on correlation matrices for time series of NDVI metrics. 1st components are displayed for d) mA (1st component explains 39% of total variance); and e) iNDVI (66%). Finally, the influence of each year in those first components is displayed (3f).

Figure 4.16.- Trends in a) wNDVI; b) mNDVI time series for pixels exhibiting trends at 90% confidence level.

Figure 4.16.- (continued) Trends in c) mS; d) mA; and e) integrated NDVI (iNDVI) time series for pixels exhibiting trends at 90% confidence level.

Figure 4.17.- Location of UNEP (2005) control points for validation.

Chapter 5 – NDVI/LST FEATURE SPACE

Figure 5.7.- Color code to identify phase values in IHS difference images.

Figure 5.8.- HANTS image of LST for 1982 and IHS difference images between LST for 1983 to 2000 and LST for 1982. The following thresholds have been applied to LST difference images: -20 K < Δaverage < 7 K ; -3 K < Δamplitude < 3 K ; -10º < Δphase < 10º.

Figure 5.9.- Differences in NDVI between periods 1982/1986 and 1995/1999.

Figure 5.10.- Differences in LST between periods 1982/1986 and 1995/1999.

Figure 5.11.- Difference images for NDVI and LST between periods 1982/1986 and 1995/1999 for a) mean value, b) 1st harmonic amplitude and c) 1st harmonic phase.

Figure 5.12.- IHS image of PAL NDVI-LST feature space parameter at global scale.

Figure 5.13.-Trends over the whole PAL database for a) θ, b) d, and c) R2 parameters following the traditional rainbow color code.

Figure 5.14.- Significance levels obtained with Kendall rank correlation test used to assess the independence between estimated satellite overpass times and a) θ, b) d, and c) R2 parameters.

Figure 5.15.- Normalized histograms for a) extreme downward trends and b) extreme upward trends in θ (blue), d (pink), and R2 (green) parameters in function of θ mean values, in degrees.

LIST OF TABLES

Chapter 2 – DATA DESCRIPTION

Chapter 3 – DATA PROCESSING

are given in 10-3 NDVI units per year; iVI in NDVI units year per year; and mS and mA in days-1 per year. X indicates no significant trend (at 90% confidence level).

Table 4.9.- Changes for all parameters for class 4 (land to water conversion) control points. S, A and G-S parameters are given in days per year; wVI and mVI are given in 10-3 NDVI units per year; iVI in NDVI units year per year; and mS and mA in days-1 per year. X indicates no significant trend (at 90% confidence level).

Table 4.10.- Changes for all parameters for class 5 (volcanic eruption) control points. S, A and G-S parameters are given in days per year; wVI and mVI are given in 10-3 NDVI units per year; iVI in NDVI units year per year; and mS and mA in days-1 per year. X indicates no significant trend (at 90% confidence level).

Table 4.11.- Changes for all parameters for class 6 (mine expansion) control points. S, A and G-S parameters are given in days per year; wVI and mVI are given in 10-3 NDVI units per year; iVI in NDVI units year per year; and mS and mA in days-1 per year. X indicates no significant trend (at 90% confidence level).

Table 4.12.- Changes for all parameters for class 7 (urbanization) control points. S, A and G-S parameters are given in days per year; wVI and mVI are given in 10-3 NDVI units per year; iVI in NDVI units year per year; and mS and mA in days-1 per year. X indicates no significant trend (at 90% confidence level).

Table 4.13.- Changes for all parameters for class 8 (glacier retreat) control points. S, A and G-S parameters are given in days per year; wVI and mVI are given in 10-3 NDVI units per year; iVI in NDVI units year per year; and mS and mA in days-1 per year. X indicates no significant trend (at 90% confidence level).

Table 4.14.- Changes for all parameters for class 9 (pollution) control points. S, A and G-S parameters are given in days per year; wVI and mVI are given in 10-3 NDVI units per year; iVI in NDVI units year per year; and mS and mA in days-1 per year. X indicates no significant trend (at 90% confidence level).

Table 4.15.- Changes for all parameters for class 10 (desertification) control points. S, A and G-S parameters are given in days per year; wVI and mVI are given in 10-3 NDVI units per year; iVI in NDVI units year per year; and mS and mA in days-1 per year. X indicates no significant trend (at 90% confidence level).

Table 4.16.- Changes for all parameters for class 11 (mangrove to shrimp farm conversion) control points. S, A and G-S parameters are given in days per year; wVI and mVI are given in 10-3 NDVI units per year; iVI in NDVI units year per year; and mS and mA in days-1 per year. X indicates no significant trend (at 90% confidence level).

Table 4.17.- Changes for all parameters for class 12 (land cover degradation) control points. S, A and G-S parameters are given in days per year; wVI and mVI are given in 10-3 NDVI units per year; iVI in NDVI units year per year; and mS and mA in days-1 per year. X indicates no significant trend (at 90% confidence level).

Table 4.18.- Changes for all parameters for class 13 (land use change) control points. S, A and G-S parameters are given in days per year; wVI and mVI are given in 10-3 NDVI units per year; iVI in NDVI units year per year; and mS and mA in days-1 per year. X indicates no significant trend (at 90% confidence level).

Table 4.19.- Average (mean) and standard deviation (dev) over land for retrieved parameters with the harmonic analysis and the double logistic fitting procedure, expressed in days for spring (S) and autumn (A), and in NDVI units for winter NDVI (wNDVI) and maximum NDVI (mNDVI) values.

"So, so you think you can tell Heaven from Hell,
Blue skies from pain.
Can you tell a green field from a cold steel rail? A smile from a veil?
Do you think you can tell?

And did they get you trade your heroes for ghosts?
Hot ashes for trees? Hot air for a cool breeze?
Cold comfort for change? And did you exchange
A walk on part in the war for a lead role in a cage?

How I wish, how I wish you were here.
We're just two lost souls swimming in a fish bowl,
Year after year,
Running over the same old ground. What have we found?
The same old fears,
Wish you were here."

Pink Floyd (*Wish You Were Here*)

SPANISH SUMMARY

En el marco del convenio de cotutela firmado por la Universitat de València (UVEG - España) y la Université Louis Pasteur de Estrasburgo (Francia), se acordó que la memoria del doctorado realizado por Yves JULIEN incluiría un resumen en francés y un resumen en castellano. A continuación se presenta el resumen en castellano de este trabajo de doctorado.

Introducción

A pesar de que la observación a distancia de la superficie terrestre comenzó con la aparición de la fotografía durante el siglo XIX, no es hasta los años 70, con el advenimiento de la era espacial, cuando alcanza proporciones antes inimaginables. El trabajo de tesis doctoral aquí presentado se desarrolla en el marco de la

observación de la Tierra, más específicamente de la vegetación terrestre, incluyendo en el termino de vegetación los diferentes estados de la superficie emergida de nuestro planeta (bosques, cultivos, sabanas, tundra, desiertos, campos de nieve o hielo, etc.). Este trabajo, llevado a cabo principalmente en el seno de la Unidad de Cambio Global de la Universidad de Valencia (España), consiste en el uso extensivo de bases de datos históricas de imágenes de satélite para el monitoreo de la vegetación, a través de dos parámetros; la temperatura de superficie terrestre (LST por sus siglas en inglés) y el índice de vegetación NDVI (Rouse *et al.*, 1973). La inserción del parámetro de temperatura de superficie para el monitoreo de la vegetación constituye el principal aporte novedoso de esta tesis doctoral.

La presente memoria se divide en 5 capítulos, que combinan aspectos teóricos y prácticos. El capítulo 1 describe el estado actual de la cuestión, desde los puntos de vista teórico y bibliográfico, Los parámetros abordados en esta memoria se describen en el capítulo 2, así como las diferentes bases de datos de las cuales se han obtenido. El capítulo 3 detalla los algoritmos aplicados a estos datos con el fin de obtener los parámetros de NDVI y LST necesarios al estudio de la vegetación. Los métodos y resultados obtenidos para el estudio temporal del NDVI se presentan en el capítulo 4. Finalmente, el capítulo 5 describe los avances realizados en el estudio conjunto de la vegetación con ayuda del NDVI y de la LST. A continuación se detalla el contenido de estos 5 capítulos.

1.- Estado de la cuestión

El primer capítulo de la presente memoria introduce en una primera parte las nociones de NDVI y LST desde una perspectiva teórica, abordando los métodos para obtenerlos desde observaciones de satélite, así como sus principales limitaciones. Se incluye una breve introducción a la fisiología vegetal, que permite entender como los parámetros de NDVI y LST están vinculados con la vegetación, a través de su actividad fotosintética, evidenciada por los índices de vegetación, así como a través de su transpiración, la cual afecta a la temperatura de superficie observada.

A continuación se presenta un estudio bibliográfico. Así desde el punto de vista de los índices de vegetación se muestra como la mayoría de los trabajos publicados

2

se limitan al hemisferio norte, a través un promedio espacial de las observaciones con el fin de obtener un significado estadístico de los resultados. En términos de la temperatura de la superficie terrestre, el estudio de sus variaciones temporales es casi inexistente, consagrándose la mayor parte de la literatura al diseño de algoritmos y su comparación. En cuanto al estudio conjunto de la evolución temporal del NDVI y de la LST la mayoría de los trabajos publicados se limita a sus aspectos teóricos y a aplicaciones de clasificación, hecho debido principalmente a la poca coherencia temporal de las observaciones de temperatura de superficie. Finamente, en el campo de la detección de cambios, son varios los métodos publicados, si bien no se adaptan al problema aquí analizado de detección de cambios a través de un análisis multitemporal de datos de satélite de baja resolución. La importancia de la revisión bibliográfica reside en que nos permite poner el acento sobre las lagunas en el uso de las bases de datos históricas, que definen nuestros principales ejes de trabajo.

2.- Descripción de los datos

Este capítulo empieza con una descripción de los diferentes sensores utilizados en la memoria, así como una rápida presentación de las plataformas que los albergan. El principal instrumento útilizado en esta tesis doctoral esta a bordo de la serie de satélites de la NOAA (National Oceanic and Atmospheric Administration). Este instrumento es el AVHRR (Advanced Very High Resolution Radiometer), que adquiere datos en el espectro visible e infrarrojo cercano (permitiendo calcular el NDVI) así como en el infrarrojo térmico (permitiendo el cálculo de la LST). Algunas imágenes adquiridas por el sensor SEVIRI (Spinning Enhanced Visible and InfraRed Imager) a bordo del satélite METEOSAT también han sido utilizadas con fines de validación.

Los datos AVHRR se han compilado en varias bases de datos, caracterizadas cada una por un procesamiento diferente. Las bases de datos utilizadas en este trabajo son las bases de datos PAL (Pathfinder AVHRR Land), que proporcionan los datos necesarios para la estimación del NDVI y de la LST entre el mes de julio de 1981 y el mes de septiembre de 2001 a la frecuencia de una imagen cada 10 días, y la base de datos GIMMS (Global Inventory Modeling and Mapping Studies), que proporciona solamente imágenes de NDVI entre julio del 1981 y

diciembre del 2003, con una frecuencia de una imagen cada 15 días. La colaboración con el equipo GIMMS (Molly E. Brown), nos ha permitido conseguir datos adicionales, necesarios para la corrección de la deriva orbital de los satélites NOAA entre noviembre 2000 y diciembre de 2006.

Finalmente, se presenta una descripción rápida de la base de datos Reanalysis. Esta base de datos proporciona datos de temperatura del aire a 2 metros de altura entre los años 1948 y 2006, datos necesarios para la validación así como la generalización de algunos resultados. Datos de precipitación de esta misma base también han sido utilizados de manera puntual.

3.- Procesado de los datos

El presente capítulo describe las operaciones aplicadas a los datos presentados en el capítulo anterior, con el fin de prepararlos para su análisis temporal. Estas operaciones empiezan con el cálculo de los parámetros de índice de vegetación y de temperatura de superficie. La estimación del NDVI es directa, mientras que la estimación de la temperatura de superficie necesita la determinación previa de la emisividad, del NDVI y del contenido total de la atmósfera en vapor de agua. Se incluye también un método para el cálculo del albedo de la superficie.

Una vez obtenidos el NDVI y la LST, es necesario proceder a un filtrado de estos datos, para considerar solo los datos relativos a la vegetación. Con este fin, se aplican varios tests para identificar los datos contaminados por la presencia de nubes o de nieve. Estos tests pueden ser implementados desde un punto de vista instantáneo o a partir de un análisis temporal de la evolución de los datos.

Los datos AVHRR utilizados en este trabajo están contaminados por la deriva orbital de los satélites NOAA, por ello una parte importante de esta tesis doctoral ha consistido en la determinación de un método par corregir este efecto. Después de intentar aplicar las pocas técnicas existentes, hemos elegido proponer una técnica propia aplicable a la detección de cambios, es decir sin suposición explicita previa del tipo de vegetación considerado. Este método ha sido validado por comparación directa con datos obtenidos por satélites geoestacionarios (que no sufren de esta deriva orbital).

4

4.- Análisis de series temporales

En una primera parte se presentan los diferentes métodos utilizados para el análisis temporal de los datos. Estos métodos consisten en la detección de tendencias, el análisis harmónico, y el ajuste de las series temporales a curvas de evolución anual, utilizado para ello el NDVI.

En una segunda parte, se presentan varios resultados en lo que se refiere al análisis temporal del NDVI. Comenzamos con un análisis fenológico, a partir del cual se obtienen tendencias acerca de las fechas en las que aparece la primavera y el otoño para la mayor parte del globo. Estas tendencias han sido validadas por comparación con numerosos estudios previos. El estudio de las fechas de primavera se extiende posteriormente al periodo 1948-2006 con la ayuda de datos de temperatura del aire, permitiendo establecer un vínculo entre las fechas observadas por satélite y los datos climáticos. Los resultados de este estudio concuerdan también con estudios anteriores. Aunque usemos solo imágenes de baja resolución, la observación de las tendencias a largo plazo de los diferentes indicadores de NDVI (valores máximas y mínimas, fenología, taza de crecimiento, etc.) también permiten la detección de cambios en la vegetación terrestre. La comparación de las tendencias observadas en diferentes lugares del globo con datos in situ ha permitido confirmar esta hipótesis. Finalmente, se comparan dos métodos de análisis temporal del NDVI, mostrándose sus límites y complementariedad.

5.- Análisis conjunto del NDVI y de la LST

En este capítulo se presenta en una primera fase una representación rápida del análisis conjunto del NDVI y de la LST, a través de un resumen de resultados ya publicados, seguido por observaciones efectuadas a partir de los datos corregidos de la deriva orbital. Estas observaciones han permitido la elaboración de indicadores de la evolución anual del NDVI y de la LST, posibilitando la caracterización de la vegetación a escala mundial.

Finalmente, se presenta un análisis harmónico del NDVI y de la LST a escala de Europa. Los resultados obtenidos con este análisis permiten la descripción de los procesos en desarrollo (desertificación, cambios fenológicos, etc.) así como elaborar hipótesis de explicación de los mismos.

5

Conclusión

Por último se presentan las conclusiones más relevantes del trabajo realizado. Los resultados incluyen el desarrollo de un método propio de corrección de la deriva orbital de los satélites NOAA, la implementación de un método de ajuste de los datos anuales de índice de vegetación a escala mundial, la obtención de tendencias fenológicas validadas por comparación con otros estudios, así como la validación de las tendencias observadas por zonas censadas de cambio en la vegetación, el desarrollo de un método para el estudio conjunto de la evolución temporal del NDVI y de la LST. Adicionalmente, este trabajo ha permitido la caracterización de los cambios que suceden en Europa y en el mundo en lo que a la vegetación se refiere, y ha proporcionado una prueba de la potencia de la teledetección de baja resolución espacial. En un futuro próximo, pensamos desarrollar y aplicar los métodos presentados en esta memoria a otros sensores, lo que sin duda nos posibilitará mejorar el análisis espacio-tiempo de la evolución de la vegetación de la escala local a la escala global.

6

FRENCH SUMMARY

Dans le cadre de la convention de co-tutelle de thèse signée entre les universités de Valence (Espagne) et Luis Pasteur de Strasbourg (France), il a été accordé que le mémoire de thèse réalisé par Yves JULIEN comporterait un résumé en français et un résumé en espagnol. C'est le résumé en français de ce travail de thèse qui est présenté ici.

Introduction

L'observation de la Terre a commencé avec l'apparition de la photographie au XIXe siècle, même si son développement a dû attendre jusqu'aux années 70 les débuts de l'ère spatiale pour atteindre les proportions qu'elle a aujourd'hui. Le travail de thèse présenté ici s'inscrit dans le cadre de l'observation de la Terre, plus

spécialement de la végétation, incluant dans le terme végétation les différents états de surface des terres émergées de notre planète (forêts, cultures, savanes, toundra, mais aussi déserts, étendues glacées, etc.). Ce travail, réalisé principalement au sein de l'Unité de Changement Global de l'Université de Valence (Espagne), consiste en l'exploitation extensive de bases de données historiques d'images satellite pour l'observation de la végétation, à travers deux paramètres, que sont la température de surface (LST : Land Surface Temperature) et un indice de végétation (NDVI : Normalized Difference Vegetation Index). Jusqu'ici, l'observation de la végétation s'est limitée à l'utilisation des indices de végétation, et l'insertion du paramètre de température de surface représente le principal aspect novateur de ce travail de doctorat.

Ce mémoire est constitué de 5 chapitres, compilant les aspects théoriques et pratiques du travail réalisé. Le chapitre 1 s'attache à réaliser un état de l'art, d'un point de vue théorique et bibliographique, des thèmes abordés par ce doctorat. Les différents paramètres utilisés dans ce mémoire sont décrits dans le chapitre 2, ainsi que les différentes bases de données par lesquelles ces données ont été obtenues. Le chapitre 3 décrit en détail les algorithmes appliqués à ces données, afin d'obtenir les paramètres de NDVI et LST nécessaires à l'étude de la végétation. Les méthodes et résultats obtenus par l'étude temporelle du NDVI sont présentés chapitre 4. Finalement, le chapitre 5 décrit les avancées réalisées dans l'étude conjointe de la végétation à l'aide du NDVI et de la LST.

1.- État de l'art

On introduit ici les notions de NDVI et LST d'un point de vue théorique, abordant les moyens de leur obtention à partir d'observations satellite, ainsi que leurs principales limitations. Vient ensuite une introduction à la physiologie végétale, qui permet de comprendre comment les paramètres NDVI et LST sont reliés aux végétaux, principalement à travers leur activité photosynthétique, mise en évidence à la fois par les indices de végétation et à travers leur transpiration, qui affecte la température de surface observée.

Une étude bibliographique en rapport avec les divers thèmes abordés est ensuite présentée. En ce qui concerne les études d'indices de végétation déjà publiées, celles-ci se focalisent principalement sur l'hémisphère nord, à travers une moyenne

spatiale des observations afin d'obtenir une signifiance statistique des résultats. En ce qui concerne la température de surface, l'étude de ses variations temporelles est quasi-inexistante, l'essentiel de la littérature étant consacré à l'obtention de ce paramètre ainsi qu'à la comparaison entre les différents algorithmes. L'étude conjointe des évolutions temporelles du NDVI et de la LST est limitée à ses aspects théoriques et à des applications de classification, dû principalement à la faible cohérence temporelle des mesures de température de surface. Finalement, différentes méthodes de détection de changement sont présentées, montrant que peu de méthodes sont applicables au cas envisagé ici de détection de changement à travers l'analyse multi-temporelle de données satellite de basse résolution. Cette revue bibliographique nous a permis ainsi de pointer les lacunes dans l'exploitation des bases de données historiques, qui vont définir nos grands axes de travail.

2.- Description des données

Une description des différents capteurs utilisés dans ce travail, ainsi qu'une rapide présentation des plateformes spatiales qui les accueillent sont présentés. L'instrument fournissant la plupart des données utiles à cette thèse est embarqué à bord de la série de satellites de la NOAA (National Oceanic and Atmospheric Administration). Cet instrument est le AVHRR (Advanced Very High Resolution Radiometer), et acquiert des données dans le spectre visible et proche infrarouge (permettant de calculer le NDVI) et l'infrarouge thermique (permettant de calculer la LST). Des données de l'instrument SEVIRI (Spinning Enhanced Visible and InfraRed Imager) à bord du satellite METEOSAT ont aussi utilisées dans ce mémoire dans un but de validation.

Les données AVHRR sont regroupées dans plusieurs bases de données, caractérisées chacune par un traitement des données différent. Les bases de données utilisées dans ce travail sont la base de données PAL (Pathfinder AVHRR Land), fournissant toutes les données nécessaires aux paramètres de NDVI et LST entre juillet 1981 et septembre 2001 à raison d'une image composite tous les 10 jours environ, et la base de données GIMMS (Global Inventory Modeling and Mapping Studies), qui fournit seulement des composites de NDVI entre juillet 1981 et décembre 2003 à raison d'une image tous les 15 jours environ. Nous avons

9

obtenu du groupe GIMMS des données supplémentaires nécessaires à la correction de la dérive orbitale des satellites NOAA entre novembre 2000 et décembre 2006.

Finalement, une description succincte de la base de données « Reanalysis » est présentée. Cette base de données a fourni des données de température de l'air à 2 mètres de hauteur entre 1948 et 2006, nécessaires à la validation ainsi qu'à l'extension de certains résultats. Des données de précipitation de cette même base de données ont aussi été utilisées ponctuellement.

3.- Traitement des données

Ce chapitre décrit les opérations appliquées aux données présentées au chapitre précédent, afin de préparer leur analyse temporelle. Ces opérations commencent par le calcul des paramètres d'indice de végétation et de température de surface. L'estimation du NDVI est directe, alors que l'estimation de la température de surface nécessite la détermination préalable de l'émissivité, du NDVI et du contenu total de l'atmosphère en vapeur d'eau. Une méthode pour le calcul de l'albédo de la surface est aussi présentée.

Une fois obtenus le NDVI et la LST, il est nécessaire de procéder à un filtrage des données, afin de ne considérer que les données relatives à la végétation. Pour ce faire, différents tests sont appliqués pour identifier les données contaminées par la présence de nuages ou de neige. Ces tests peuvent être implantés d'un point de vue instantané ou à partir d'une analyse temporelle de l'évolution des données.

Les données AVHRR utilisées dans ce travail étant contaminées par la dérive orbitale des satellites NOAA, une part importante de ce travail de doctorat a consisté en l'élaboration d'une technique de correction de cet effet. Après avoir tenté d'appliquer les quelques méthodes existantes, nous avons opté pour élaborer une technique propre, applicable à la détection de changements, c'est-à-dire sans supposition explicite préalable du type de végétation considéré. Cette technique a été validée par comparaison directe avec des données obtenus par des satellites géostationnaires (et donc ne présentant pas de cette dérive orbitale).

4.- Analyse de séries temporelles

Dans une première partie sont présentées les différentes méthodes utilisées pour l'analyse temporelle des données. Ces méthodes consistent en la détection de tendances, l'analyse harmonique, et l'ajustement des séries temporelles à des courbes d'évolution annuelle, utilisé pour le NDVI.

Dans une deuxième partie, différents résultats concernant l'analyse temporelle du paramètre NDVI sont présentés. Premièrement, une analyse phénologique est décrite, conduisant à l'obtention de tendances vis-à-vis des dates de printemps et d'automne pour la majorité du globe. Ces tendances sont validées par comparaison avec plusieurs études précédentes. L'étude des dates de printemps est ensuite élargie à la période 1948-2006 à l'aide de données de température de l'air, permettant d'établir un lien entre les dates du début de la croissance de la végétation observées par satellite et les données climatiques. Les résultats de cette étude sont eux aussi en accord avec de précédents travaux. L'observation des tendances à long terme des différents indicateurs de NDVI (valeurs maximales et minimales, phénologie, taux d'accroissement, etc.) permet aussi la détection de changements dans la végétation terrestre, même dans notre cas de basse résolution spatiale. La comparaison des tendances observées en certains points du globe avec des données terrain a permis de confirmer cette hypothèse. Finalement, deux méthodes d'analyse temporelle des données de NDVI sont comparées, montrant les limites de chacune des deux méthodes, et leur complémentarité.

5.- Analyse conjointe du NDVI et de la LST

Dans un premier temps, une rapide présentation de l'étude conjointe du NDVI et de la LST est développée, à travers un rappel des résultats précédents, suivi des observations effectuées à partir des données corrigées de la dérive orbitale. Ces observations ont permis la mise en place d'indicateurs de l'évolution annuelle du NDVI et de la LST, permettant la caractérisation de la végétation à échelle mondiale.

Enfin, dans un deuxième temps, une analyse harmonique du NDVI et de la LST à l'échelle de l'Europe est présentée. Les résultats obtenus par cette analyse

permettent la description des processus en cours (désertification, changement phénologiques, etc.) ainsi qu'un début d'explication.

Conclusion

En conclusion, les résultats obtenus sont rappelés brièvement. Ces résultats incluent le développement d'une méthode propre de correction de la dérive orbitale des satellites NOAA, l'implémentation d'une méthode d'ajustement des données annuelles d'indice de végétation à échelle mondiale, l'obtention de tendances phénologiques validées par comparaison avec d'autres études, la validation des tendances observées pour des zones recensées de changement de la végétation, ainsi que le développement d'une méthode pour l'étude conjointe de l'évolution temporelle du NDVI et de la LST. De plus, ce travail de doctorat a permis la caractérisation des changements en Europe et dans le monde en ce qui concerne la végétation. Dans un futur proche, nous pensons développer et appliquer les méthodes présentées ici à d'autres instruments, permettant une meilleure analyse spatio-temporelle de l'évolution de la végétation, de l'échelle locale à l'échelle globale.

ENGLISH SUMMARY

Introduction

Earth observation began with the apparition of photography during 19th century, even though its development really started during the 1970's with the coming of the Space Age, to reach the dimensions it has today. The PhD dissertation presented here falls into the Earth Observation field, specifically vegetation monitoring, and includes different states of the exposed surface of our planet (forests, cultures, savannahs, tundra, as well as deserts, ice, etc.). This work, carried out mainly within the Global Change Unit of the University of Valencia

(Spain), consists of the extensive exploitation of historical databases of satellite images for vegetation monitoring through two parameters, which are the land surface temperature (LST) and a vegetation index (NDVI, see Rouse *et al.*, 1973). Up to now, vegetation monitoring has been limited to the use of vegetation indices, so the addition of the land surface temperature parameter represents the main innovative character of this PhD study.

This dissertation is divided into 5 chapters, including the theoretical and experimental aspects of the work carried out. In chapter 1, an overview of the state of the various issues addressed in this study is realized from a theoretical and a bibliographical point of view. The different parameters used in this dissertation are described in chapter 2, along with a description of the databases through which these data were retrieved. The algorithms applied to the data to obtain the NDVI and LST parameters needed for vegetation monitoring are described in chapter 3. The methods and results obtained through NDVI temporal analysis are presented in chapter 4. Finally, chapter 5 describes the advances realized in the simultaneous study of the vegetation through NDVI and LST parameters. These different chapters are detailed below.

1.- Background

This first chapter begins by introducing the theoretical aspects of NDVI and LST parameters, addressing the means for retrieving them from remotely sensed observations, as well as their main limitations. Then, an introduction to vegetal physiology is developed, which allows for understanding how NDVI and LST parameters are linked to plants, mainly through their photosynthetic activity, evidenced by both vegetation indices and their transpiration, which affects the observed surface temperature.

A bibliographical study in relation to the various issues addressed is then presented. As regards already published studies on vegetation indices, these are principally focused on the northern hemisphere through a spatial averaging of the observations to obtain statistical significance for the results. Regarding land surface temperatures, studies of their temporal variations are quasi-inexistent, with most of the literature dedicated to retrieving this parameter and comparing algorithms. The simultaneous study of NDVI and LST temporal behavior has been limited to its

theoretical aspects and applied for classification purposes, due mainly to the weak temporal coherence of the surface temperature observations. Finally, several methods for change detection are presented and show that few methods were applicable to the case studied here, which corresponds to change detection through multitemporal analysis of low resolution satellite data. This bibliographic review thus allows us to point out the gaps in the exploitation of historical databases, which will define the main axes of our work.

2.- Data description

This chapter begins with a description of the various sensors used in this work, as well as a quick description of the satellites which host them. The instrument providing most of the data used in this PhD is embarked on the NOAA (National Oceanic and Atmospheric Administration) satellite series. This instrument is the AVHRR (Advanced Very High Resolution Radiometer), which acquires data in the visible and near-infrared (allowing for NDVI calculation) and the thermal infrared (allowing for LST calculation) wavelengths. Some data from the SEVIRI (Spinning Enhanced Visible and InfraRed Imager) sensor onboard METEOSAT satellite have also been used in this dissertation for validation purposes.

AVHRR data are compiled in various databases, each of them characterized by a different data process. The databases used in this work are the PAL (Pathfinder AVHRR Land) and GIMMS (Global Inventory Modeling and Mapping Studies) databases. The PAL database provides all the data needed for estimating NDVI and LST between July 1981 and September 2001 as 10-day composites. The GIMMS database only provides NDVI 15-day composites between July 1981 and September 2001. By contacting a member of the GIMMS group (Molly E. Brown), we managed to obtain additional data needed for orbital drift correction of NOAA satellites between November 2000 and December 2006.

Finally, a brief description of the Reanalysis database is presented. This database provided 2-meter high air temperature data between 1948 and 2006 needed for validation and for time extension of some results. Some precipitation data from this same database have also been used on specific occasions.

3.- Data processing

This chapter describes the operation applied to the data presented in the previous chapter, in order to prepare their temporal analysis. Those operations start with the calculations of vegetation index and land surface temperature parameters. NDVI estimation is direct, while for LST estimation, emissivity, NDVI and total amount of water vapor need to be determined beforehand. A method for albedo estimation is also presented.

The AVHRR data used in this work are contaminated by the orbital drift of NOAA satellites, so an important part of this doctorate consisted in developing a technique for correcting this effect. After trying to apply the existing methods, we chose to develop our own technique, which could be applied to change detection, which means that no previous knowledge of the considered vegetation had to be supposed. This technique has been validated by direct comparison with data retrieved by geostationary satellites, thus not suffering from this orbital drift.

4.- Time series analysis

In the first section, the different methods used for data temporal analysis are presented. Those methods consist of trend detection, harmonic analysis, and fitting the temporal series to annual evolution curves, used for NDVI parameter.

In the second section, various results regarding NDVI temporal analysis are presented. First, a phenological analysis is described, leading to the retrieval of trends in spring and autumn dates for most of the globe. These trends are validated by comparison with a large number of previous studies. The trend analysis for spring dates is then extended to the 1948-2006 period using air temperature data, making it possible to link the dates retrieved by remote sensing and climatic data. The results of this study also agree with previous works. The long-term observation of different NDVI indicators (maximum and minimum values, phenology, slopes, etc.) also allows for the detection of land vegetation changes, even in our case of coarse spatial resolution. The comparison of the retrieved trends in several locations on Earth with independent data enabled us to confirm this hypothesis. Finally, two methods for NDVI temporal analysis are compared, showing the limits of each of these two methods, as well as their complementarity.

5.- NDVI and LST feature analysis

In a first step, a quick presentation of simultaneous study of NDVI and LST is developed through a revision of previous results, followed by the observations carried out from the orbital drift corrected data. These observations allowed for the determination of indicators of NDVI and LST, thus enabling for the characterization of the vegetation at global scale.

Finally, in a second step, a harmonic analysis of NDVI and LST at European scale is presented. The results obtained by this analysis allow for the description of the ongoing processes (desertification, phenological changes, etc.) as well as for advancing an explication for these phenomena.

Conclusion

As a conclusion, the obtained results are summarized. These results include the development of an original method for correcting the orbital drift of NOAA platforms, the implementation of a fitting procedure for yearly NDVI data at global scale, the retrieval of phenological trends validated by comparison with previous studies, as well as the validation of the observed trends for referenced areas of vegetation changed, and the development of a method to analyze simultaneously the temporal evolution of NDVI and LST. Additionally, this PhD has allowed for the characterization of the ongoing changes in Europe and globally as regards vegetation, and has demonstrated that this work could be carried out in a small structure with limited resources. In the near future, we plan to develop and apply the methods presented here to other sensors, allowing for a better spatio-temporal analysis of vegetation changes, from local to global scale.

INTRODUCTION

A QUICK HISTORY OF EARTH OBSERVATION

Since the first images of the Earth from the air (XIXth century) and then from space, Earth observation disciplines have occupied an increasing place in scientific investigation. First photographs of the Earth were probably taken in Paris, France, by G. Tournachon (a.k.a. Nadar) from his balloon in 1858. With the rise of the aeronautics, photographs taken from airplanes became progressively more common. As usually occurs with scientific advances, the first applications were military, for surveillance and recognition purposes, especially during World War I. With the beginning of the Cold War, United Sates and Russia started concurrent space programs, which resulted in the so called Space Race. On the 4th of November 1957, Russia managed to launch the first man-made satellite, Sputnik I, which orbited the Earth during three months, and allowed the first retrievals of atmospheric temperature and pressure. It was followed rapidly by the launch of Vanguard I, the first satellite launched by the United States, which still orbits the Earth. However, those early satellites did not provide images of the Earth, since no other measurements than pressure and temperature had been scheduled. However,

by analyzing Vanguard I orbit, geodetic information was retrieved, which improved our knowledge of the Earth. As instrumentation techniques improved, sensors were progressively introduced in satellites, in a first step to observe the Moon to prepare inhabited missions, but the advantages of these sensors for Earth observation were quickly understood, leading to the acquisition of the first images of the Earth by the first TIROS (Television Infra-Red Observation Satellite) satellites. Those first steps in Earth observation were dedicated mainly to taking images of the atmosphere.

Earth Observation began seriously in 1972 with the launch of the Landsat program, earlier named ERTS (Earth Resources Technology Satellite), dedicated entirely to monitoring the Earth. The Landsat program is still active, Landsat-7 (launched in 1999) being still active, although with some technical problems. Next Landsat platform is scheduled to be launched in July 2011. Landsat satellites have provided medium resolution images of the Earth for the past 35 years.

A second source of invaluable information for Earth observation has been the followers of the TIROS satellite series, first the Nimbus series (Nimbus-1 was launched in 1964; Nimbus-7, launched in 1978, remained active until 1994), and then the NOAA (National Oceanic and Atmospheric Administration) series. NOAA first 5 satellites were launched during the 1970s, with the VHRR (Very High Resolution Radiometer) on-board, which provided images at coarse spatial resolution in one visible band and one thermal band. Since 1978, NOAA satellites have embarked the AVHRR (Advanced Very High Resolution Radiometer) on-board, with one visible band, one band in the near-infrared, one band in middle infrared and two bands in thermal infrared. Those sensors marked the birth of vegetation indices, essential for Earth observation.

RESEARCH OBJECTIVES

The Global Change Unit of the University of Valencia (Spain) has focused its research in the field of quantitative thermal remote sensing. This research has led to the development of surface temperature algorithms for all available sensors equipped with thermal infrared bands. However, applications of those retrieved surface temperatures for monitoring the Earth have been seldom. Large datasets of remotely sensed information are now freely available from space agencies, but

have been used mainly to monitor vegetation indices at local to continental scale. Since those dataset allow surface temperature estimation, why not include this parameter for vegetation monitoring?

There are several reasons for the under-exploitation of these global databases. First, there are historical reasons: when first released, those datasets were accompanied with preliminary studies, which provided first estimates of change in vegetation indices. This gave the feeling that global studies had already been carried out, while those results were merely applications of the whole process of building the database. Secondly, the nature of the data also played a role in hindering its scientific use. Since the data was made freely available at the same time that the first medium and high spatial resolution sensors appeared, scientists generally chose to focus on newly available high resolution data for change studies, since more detailed information on specific areas could be obtained. Additionally, coarse spatial resolution means that all details in the data are averaged, not only over space, but also over species, fact which hides individual spectral signatures in the averaged signal. However, this does not happen over large homogeneous areas. On another hand, changes happening at a finer spatial resolution than the data are still present in the data, although abrupt changes appear smoothed and progressive. This means that usual change analysis (image comparison at two different dates) can difficultly be applied to these data, while trend analysis seems the best way to retrieve change information. Third, the available datasets present some residual errors as regards data continuity, due mainly to sensor ageing, sensor artifacts (orbital drift) and temporal changes in observation conditions (volcanic eruptions). Those residual errors, especially in the case of surface temperature, prevent any long-term change analysis of the data, the conditions of image acquisition being substantially different from one year to the other. Finally, those databases have been studied mainly for their flaws, providing various techniques for their correction, whether locally or globally.

Thus, in spite of the fact that those databases have been available for some years now, there is still some scientific potential in them. In the context of global change, those databases are invaluable tools for change monitoring, and the NOAA-AVHRR archive can be stressed out as the most important one, since it covers almost 25 years of the period where changes have been most documented and most important (increases in air temperature, atmospheric carbon dioxide, deforestation,

etc.). Therefore, thorough change analyses from these databases have still to be carried out.

This work aims at analyzing changes in vegetation with the help of historical databases, focusing on the use of normalized difference vegetation index (NDVI) and land surface temperature (LST). This work represents the first attempt at global vegetation monitoring within the Global Change Unit, and, to our knowledge, the first attempt at land surface temperature multitemporal monitoring in the scientific community, as well as the first attempt at combined multitemporal analysis of NDVI and LST. This work is the continuation of the study sketched out in the investigation project also realized within the Global Change Unit and presented in November 2004, titled "Análisis multitemporal de imágenes PAL para el estudio de la dinámica de la cobertura terrestre en Europa y América del Sur" (Multitemporal analysis of PAL images for land cover dynamics monitoring in Europe and South America).

In order to achieve this purpose, the work has been carried out following two major axes: data correction and trend analysis. Since reliable time series of land surface temperatures had to be built to carry out trend analysis, our work started with land surface temperature correction, and, in parallel, trend analysis of vegetation index. When we managed to develop a good correction of LST time series, trend analysis was extended to both NDVI and LST parameters.

OUTLINE OF THE DISSERTATION

To describe the work carried out during the past four years, this work has been divided in 5 chapters, presenting the major axes of investigation.

In **Chapter 1**, we describe the state of the art in vegetation indices, land surface temperature retrieval and change analysis. To this end, a quick presentation of the theoretical aspects hidden behind vegetation indices, land surface temperature retrieval are presented, along with a brief description of plant physiology, which relates vegetation indices to land surface temperature. In addition, we provide a review of past studies dealing with NDVI and its application to vegetation

monitoring, LST retrieval and applications, combined use of LST and NDVI, as well as change detection techniques.

Chapter 2 describes the data used for this work, first through a presentation of the acquiring platform (NOAA) and sensor (AVHRR), and then a description of the available data. This chapter also includes a description of the three sets of data retrieved for this study, presenting the process carried out to obtain the data as available from the databases. A brief presentation of METEOSAT-SEVIRI has been included, since data from this sensor have been used for validation purposes.

Having presented the data used in this work, **Chapter 3** describes the processing carried out within the Global Change Unit. This process consists in retrieving NDVI and LST parameters for all available dates, completed by filtering of the eventual cloud-contaminated areas and dates, as well as eventual sensor failures. A description of methods previously applied for NOAA orbital drift correction is included, along with the method we developed to correct this orbital drift.

In **Chapter 4**, we present the techniques applied for time series analysis, which rely on harmonic analysis as well as yearly data fitting procedure. Those techniques are then applied to vegetation indices, and compared with previous results, in terms of trends in phenological phases as well as NDVI metrics. Results are then validated by comparison with documented changes around the world. The results obtained by both methods are then compared.

Chapter 5 describes the results obtained as regards combined use of LST and NDVI. First, a globally applicable method is presented, followed by results obtained over Europe with harmonic analysis. Finally, the application of the global method for vegetation monitoring using both NDVI and LST parameters is presented, along with early results regarding extreme land cover changes.

After this last chapter, the **Conclusion** section summarizes the results obtained, followed by an Appendix where are reproduced all published and sent papers to international journals in relation with this work.

Chapter 1

BACKGROUND

"It is a mistake to think you can solve any major problems just with potatoes."

Douglas Adams

This chapter presents the concepts that will be needed in the following chapters, explaining how remotely sensed parameters are retrieved and estimated, as well as the phenomenon they describe. This is followed by a state of the art of vegetation monitoring, describing the most relevant works in which those parameters have been developed and used for vegetation monitoring.

1.1.- Theoretical bases

The concepts presented below are remotely sensed parameters, such as normalized difference vegetation index (NDVI) and land surface temperature (LST).

1.1.1.- NDVI

The Normalized Difference Vegetation Index (NDVI) is a simple parameter used mainly in remote sensing for green vegetation identification and monitoring. This indicator was developed by Rouse *et al.* (1973), after the need of identification of vegetation from satellite data in various illumination and

observation conditions. This index has been used in numerous vegetation studies (see for example Tucker, 1979; Tucker, 1980; Sellers, 1985; Sellers *et al.*, 1994).

1.1.1.1.- Description

Solar radiation is absorbed by plants in the photosynthetically active radiation (PAR) spectral region, and is used as a source of energy in the process of photosynthesis. Leaves reflect and transmit solar radiation in the near-infrared, so that live green plants appear relatively dark in the PAR and relatively bright in the near-infrared (Gates, 1980). By contrast, mediums rich in water (clouds, snow, sea) tend to be rather dark in the near-infrared, and bright in the visible spectrum, and thus in the red. Figure 1.1 shows vegetation spectrum, as well as dry vegetation and soil spectrum.
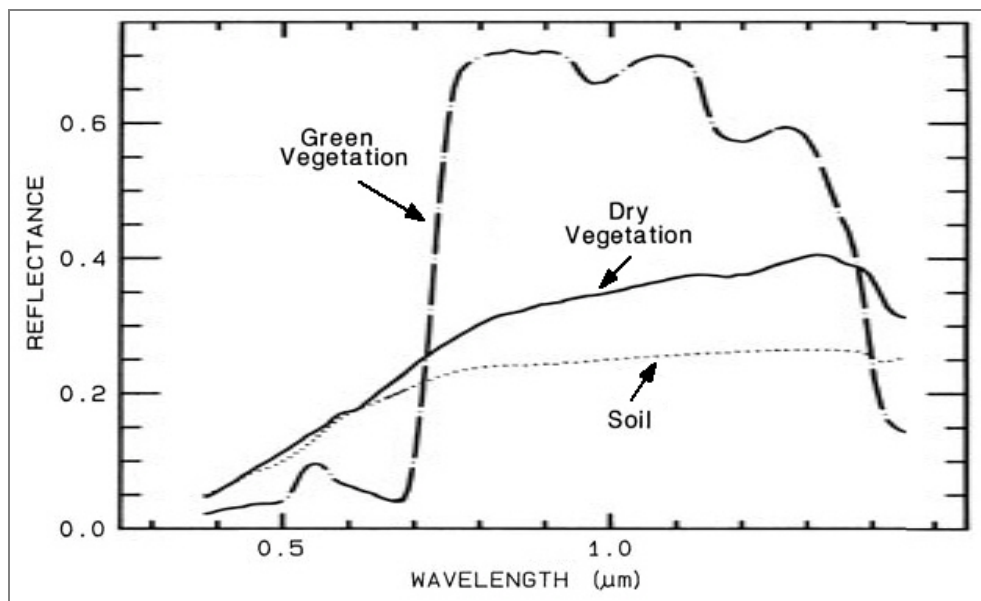
Figure 1.1.- Visible and near infrared spectrum for soil and vegetation (adapted from http://www.iac.ethz.ch/staff/stockli/ndvimeasurement/ndvimeasurement.html).

Early satellite platforms embarked sensors which happen to acquire data in red and near infrared wavelengths. NOAA platforms, for example, were designed for atmospheric and oceanic observation purposes, although the inclusion of red and near-infrared bands in their AVHRR sensor has expanded their use to Earth

28

observation. Thus, exploiting the strong differences in plant reflectance at red and near-infrared wavelengths, vegetation spatial distribution can be determined from remotely sensed measurements. Although there are other ways to obtain this index, we calculate NDVI values from reflectances, following Goward *et al.* (1991):

$$NDVI = \frac{(NIR - RED)}{(NIR + RED)}$$ (1.1)

where RED and NIR stand respectively for the spectral reflectance measurements acquired in the red and near-infrared regions. These spectral reflectances are ratios of the reflected radiation over the incoming radiation in each spectral band. Thus, RED and NIR reflectance values vary between 0.0 and 1.0, and, as a consequence, NDVI varies between -1.0 and +1.0. Various studies have related NDVI directly to the photosynthetic capacity and hence energy absorption of plant canopies (Sellers, 1985; Myneni *et al.*, 1995).

1.1.1.2.- Performance and limitations

From its mathematical definition, one can see that the NDVI value of an area containing a dense vegetation canopy will tend to positive values (0.3 – 0.8) while clouds and snow fields will be characterized by negative values of this index. Water areas (oceans, seas, lakes, rivers) will have very low positive or even slightly negative NDVI values, since their reflectance is rather low in both red and near-infrared wavelengths. Bare soils also tend to generate rather small positive NDVI values (0.1 – 0.2), since they generally exhibit a near-infrared spectral reflectance somewhat larger than the red, as shown in Figure 1.1. For a global view of NDVI spatial repartition, see Chapter 3.

However, NDVI values tend to be affected by factors such as atmospheric effects, clouds, soil effects, anisotropic effects and spectral effects. Atmospheric effects have a particularly strong influence when NDVI is estimated from raw measurements. This is the reason why we estimate NDVI from reflectances. Deep clouds are easily identified in NDVI images due to their negative values; however, thin clouds (such as cirrus) and clouds with dimensions lower than the sensor spatial resolution may lower NDVI values without reaching negative values, and thus contaminating the data. This effect is lowered by forming composite images from daily images (Holben, 1986), obtaining 7-, 10-, 15- or 30-day composite

images. In this work, we use only 10- and 15-day composite images, since vegetation changes happen typically at that time scale. As for soil effects, soils tend to darken when wet, so that their reflectance is a direct function of water content. This means that the NDVI of an area can change as a result of soil moisture changes only, due for example to precipitation, irrigation or evaporation. Anisotropic effects are due to the fact that all surfaces, whether natural or man-made, reflect light differently in different directions, and this property is generally spectrally dependent. This effect is present in all NDVI data, since observation and illumination geometries and time of acquisition differ for each platform overpass, due to nominal orbit characteristics, and NOAA orbital drift. However, image compositing also tends to minimize those effects. Finally, each sensor has its own spectral characteristics, which yield different NDVI results for different instruments. Additionally, NDVI has been showed to be responding primarily to the highly absorbing red reflective band, thus mimicking red reflectance and saturating over forested regions, while being sensitive to canopy background variation in arid and semi-arid areas (Huete *et al.*, 1997).

NDVI analyses have to be carried out with those effects in mind, especially for quantitative applications. Recent versions of NDVI dataset have attempted to account for these factors. Other vegetation indices have been developed to minimize those factors, including RVI (Ratio Vegetation Index – low sensibility to illumination conditions, but high sensibility to soil optical properties, Pearson & Miller, 1972), PVI (Perpendicular Vegetation Index – minimizes soil influence, Richardson & Wiegand, 1977), SAVI (Soil Adjusted Vegetation Index – minimizes soil reflectivity influence, Huete, 1988), MSAVI (Modified Soil Adjusted Vegetation Index – minimizes bare soil influence, Qui *et al.*, 1994), TSAVI (Transformed Soil Adjusted Vegetation Index – introduces soil parameters in the calculation to reach global validity, Baret & Guyot, 1991), GEMI (Global Environment Monitoring Index – minimizes atmospheric influence, Pinty & Verstraete, 1992), ARVI (Atmospherically Resistant Vegetation Index – decreases atmospheric aerosol influence, Kaufman & Tanré, 1992), SARVI (Soil and Atmosphere Resistant Vegetation Index – minimizes both atmosphere and soil influences, Huete *et al.*, 1994), OSAVI (Optimized Soil Adjusted Vegetation Index, Rondeaux *et al.*, 1996), GARVI (Green Atmospherically Resistant Vegetation Index, Gitelson *et al.*, 1996), GESAVI (Generalized Soil Adjusted

30

Vegetation Index, Gilabert *et al.*, 2002), VARI (Visible Atmospherically Resistant Index, Gitelson *et al.*, 2002), MNLI (Modified NonLinear vegetation Index, Gong *et al.*, 2003), LVI (Linearized Vegetation Index, Ünsalan & Boyer, 2004) and WDRVI (Wide Dynamic Range vegetation Index, Gitelson, 2004; Viña *et al.*, 2004). Ji & Peters (2007) have developed a statistical method to compare the performance some of those indices. Some of those indices have also been used for soil degradation analysis (Singh *et al.*, 2004).

The great mathematical simplicity and the easy interpretation of the NDVI in comparison to the other above mentioned indices make it the most widely used index.

1.1.2.- LST

Different methods and algorithms have been published in order to retrieve land surface temperature (LST) from thermal infrared remote sensing data. A full revision of methods can be found in Sobrino *et al.* (2002) and Dash *et al.* (2002), among others. In the literature, methods using three or more thermal channels or algorithms based on different techniques can be also found (see for example Becker & Li, 1990; Wan & Li, 1997; Sun & Pinker, 2003). Those algorithms are validated with field campaigns, such as the ones described in Sobrino et al. (2006b; 2007).

1.1.2.1.- The Radiative Transfer Equation

Different algorithms have been developed in the last years in order to retrieve LST from thermal infrared data. Most of them are based on the radiative transfer equation, from which the at-sensor radiance is given by

$$L_i^{at-sensor} \equiv B_i(T_i) = \left[\varepsilon_i B_i(T_s) + (1-\varepsilon_i)L_i^{atm\downarrow}\right]\tau_i + L_i^{atm\uparrow} \qquad (1.2)$$

where the subindex 'i' refers to one thermal channel, ε_i is the channel surface emissivity, B_i is the radiance emitted by a blackbody, T_s is the surface temperature or LST, T_i is the at-sensor brightness temperature, $L_i^{atm\downarrow}$ is the down-welling irradiance, τ_i is the total transmission of the atmosphere (transmissivity) and $L_i^{atm\uparrow}$ is the up-welling atmospheric radiance. These magnitudes also depend on the observation angle, except for T_s and $L_i^{atm\downarrow}$. When Equation (1.2) is applied only to

one thermal channel, single-channel algorithms are obtained, and when Equation (1.2) is applied to two thermal channels located in the spectral range from 10 to 12 µm, split-window algorithms are obtained. It is also possible to apply Equation (1.2) to one thermal channel with two different view angles, obtaining in this way the dual-angle algorithms.

1.1.2.2.- Single-Channel Methods

Based on the radiative transfer equation (Equation 1.2), it is possible to obtain different single-channel algorithms. The RTE (Radiative Transfer Equation) algorithm can be obtained directly from Equation (1.2) and considering a linear relationship between Planck's law and temperature. In this way, LST is given by (Sobrino & Raissouni, 2000):

$$
\begin{aligned}
T_s = T_i &+ \left(\frac{1-\varepsilon_i}{\varepsilon_i}\right)\left\{ L_i(T_i) - \left(1 - \tau_i^{53°}\right)\left[T_a + L_i(T_i) - T_i\right]\right\} \\
&+ \left(\frac{1-\tau_i}{\varepsilon_i\tau_i}\right)(T_i - T_a)
\end{aligned}
\tag{1.3}
$$

where T_a is the mean atmospheric temperature, $\tau_i^{53°}$ is the atmospheric transmissivity for an observation angle of 53º and L_i is a parameter given by

$$
L_i(T_i) = \frac{B_i(T_i)}{\left[\dfrac{\partial B_i(T)}{\partial T}\right]_{T_i}}
\tag{1.4}
$$

1.1.2.3.- Two-Channel (Split-Window) Method

A similar procedure as in the generalized single-channel method allows to obtain generalized two-channel (or split-window) algorithms for different wavelength combinations. The following mathematical structure of the algorithms can be considered (Sobrino & Raissouni, 2000):

$$
\begin{aligned}
T_s = T_i &+ a_1(T_i - T_j) + a_2(T_i - T_j)^2 + (a_3 + a_4 W)(1 - \varepsilon) \\
&+ (a_5 + a_6 W)\cdot\Delta\varepsilon + a_0
\end{aligned}
\tag{1.5}
$$

32

where i, j are the sensor channels, T_i and T_j are the at-sensor brightness temperatures (in K), W is the atmospheric water vapor content (in g·cm^{-2}), ε is the mean emissivity, $(\varepsilon_i + \varepsilon_j)/2$, and $\Delta\varepsilon$ is the emissivity difference, $\varepsilon_i - \varepsilon_j$. The split-window coefficients, from a_0 to a_6, are obtained by means of a simulation, using the MODTRAN code (Abreu & Anderson, 1996), various standard atmospheric profiles and emissivity spectra covering a variety of natural surfaces extracted from the ASTER (Advanced Spaceborne Thermal Emission and Reflection radiometer) spectral library (http://speclib.jpl.nasa.gov).

1.1.2.4.- Split-Window versus Single-Channel

In the previous sections generalized single-channel and two-channel algorithms have been discussed. Both of them assume that land surface emissivity is known and need the atmospheric water vapor content in order to retrieve the LST, so one may wonder what the difference between them is. If we simulate temperature from various atmospheric profiles and water vapor content, the split-window algorithm gives more or less a constant difference in all the cases, whereas the single-channel algorithm increases the difference when the atmospheric water vapor content increases. So for low atmospheric water vapor content, the single-channel method provides similar or better results than split-window algorithms, but for high water vapor the split-window always provides better results. This is the main advantage of the split-window algorithms compared with single-channel ones.

1.2.- Introduction to vegetation biology

In this paragraph, we describe briefly the general vegetation structure, to explain transpiration mechanisms, which allow plants to regulate their temperature.

1.2.1.- Vegetation physiology

Here, no difference is made between trees, cereals, or bushes, since their physiology is quite similar from a functioning point of view. As is generally well-known, plants can be divided in three parts: roots, trunk (or stem) and leaves. This division seems obvious from simple observation, but is based on functioning differences. The roots provide nutrients for the whole plant, while the trunk sustains and protects the ensemble, and the leaves transform the nutrients into sugars by photosynthesis.

33

The roots are covered of millions of tiny root hair cells which have a large surface area, so that the plant can absorb water from the soil, as well as minerals. Water and minerals are carried up through the xylem vessels to the leaves. These xylem vessels are strong, thick pipes, made of dead cells with no end walls, which contain lignin (a hard cellulose-like substance which gives rigidity to plant tissues) to form stiff tubes. They are impermeable, and are strengthened with fibers.

Water is carried to the leaves where it provides both hydrogen and oxygen, needed for photosynthesis. Carbon is also needed for photosynthesis, which is provided by air carbon dioxide. With the help of chlorophyll and sunlight, carbon dioxide and water are transformed by photosynthesis into glucose and oxygen, following the equation:

$$6 \cdot CO_2 + 6 \cdot H_2O \xrightarrow{sunlight+chlorophyll} C_6H_{12}O_6 + 6 \cdot O_2 \qquad (1.6)$$
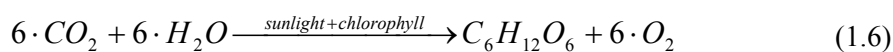
Oxygen is then released into the atmosphere, while glucose can be converted to sucrose and carried to other parts of the plant. Glucose can also be converted into starch and stored (in tubers or bulbs), to be later converted back to glucose. Glucose is carried through the plant within phloem vessels, which consist of living cells lined with cytoplasm, with walls made of cellulose and perforated end walls called sieve plates. They are permeable, and are surrounded by companion cells.

Figure 1.2 shows the arrangement of phloem and xylem vessels in roots and stems, the arrangement being similar for trees.

1.2.2.- Transpiration mechanism

Transpiration is vital to plant life, since it participates in most of the phenomena at stake, from temperature regulation to plant stiffness or organic fluxes within the plant.

Transpiration occurs when the stomata (located on the underside of the leaves) open and release water in the atmosphere. The opening of the stomata happens when the leaves' guard cells shrink, allowing the regulation of the amount of water released. Since water evaporation is a process that needs heat, this mechanism decreases the leaf temperature. This means that by regulating the amount of water being released in the atmosphere, plants regulate their temperature.
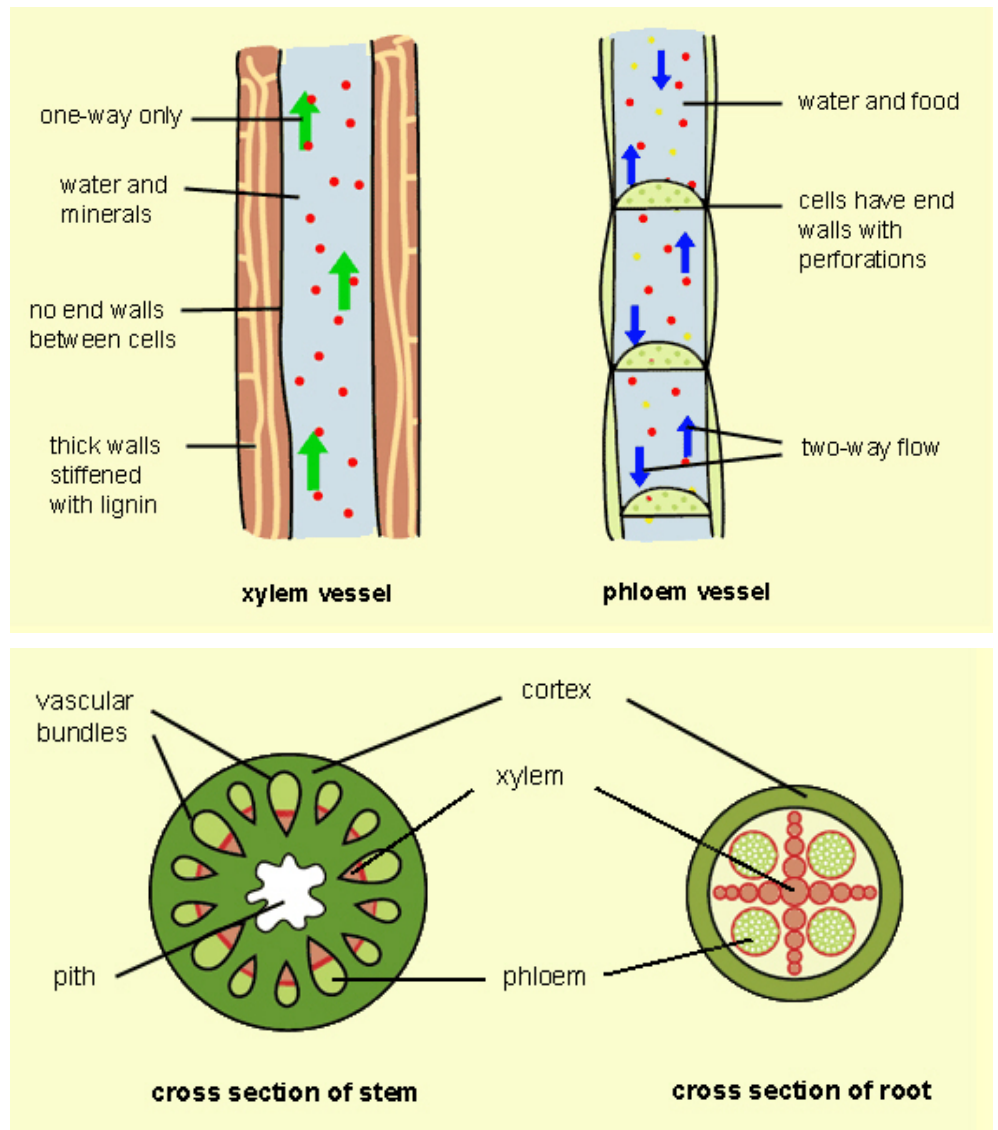
Figure 1.2.- Xylem and phloem vessels structure (adapted from http://www.bbc.co.uk/schools/gcsebitesize/biology/greenplantsasorganisms/1water transportrev3.shtml).

At the same time, the release of water induces more water to be pulled through the plant from the roots, by suction and capillarity in the xylem vessels. This way,

transpiration is the main motor of circulation in the plant, allowing the nutrients to be moved to the leaves, as well as the glucose and starch to reach their destination.

Since the stiffness (for non woody plants) is based on water presence in the plant cells, transpiration also participates to this mechanism. Basically, plant cells have a cellulose cell wall surrounding the cell membrane. The cell wall, although strong and rigid, is completely permeable to water and dissolved minerals. The cell membrane on the other hand is partially permeable, so water can enter the cell by osmosis. The water swells the vacuole, increasing the pressure inside the cell and pushing out against the cell wall, giving stiffness to the cell. The turgid cells in turn press against the packing tissue or cortex of the plant stem - giving stiffness to the stem and holding the plant upright. If the plant's environment is lacking in water, the concentration gradient is reversed and water starts to move the other way. As the cells lose water their internal pressure drops and they lose shape, becoming flaccid: the plant will droop and wilt.

In larger woody perennial plants or trees it is mostly the strong conducting tissues, or xylem vessels, which support the plant. These vessels are made of thickened cells lined or impregnated with a substance called lignin which makes them strong and impermeable. Each year the cells die and new xylem rings are added forming annual rings. The annual woody growth makes the tree trunks very stiff and they do not need turgor to hold them upright (http://www.bbc.co.uk/schools/gcsebitesize/biology/index.shtml).

In total, transpiration uses about 90 percent of the water that enters a plant's roots. The other 10 percent is used in chemical reactions and in plant tissues.

1.2.3.- Effect on land surface temperatures

Since remotely sensed measurements only give information on the upper level of the land cover, retrieved land surface temperature correspond to the upper part of the plant, namely tree canopy or plant stems, which happen to be the plant parts where transpiration occur. As explained above, transpiration allows plants to regulate their temperature. However, transpiration efficiency depends on factors such as surrounding temperature, humidity, and wind or air movement, as well as plant characteristics. Thus, climatic conditions (temperature, humidity, wind) influence retrieved land surface temperature, but also vegetation characteristics.

By measuring land surface temperature over a vegetated area (medium to high NDVI), one also estimates its ability to regulate its temperature, and can thus infer the type of the observed land cover. For example, trees can regulate perfectly their temperature (in conditions of non limited water availability), due to the amount of leaves available for transpiration. Cereals, for example can regulate their temperature to some extent, provided the temperatures do not reach a given threshold, dependent of the cereal species. This particularity is particularly useful since NDVI does not allow perfect differentiation between land cover types, since it measures only the vegetation greenness. Thus, combining remotely sensed land surface temperature with NDVI should allow a better monitoring of vegetation.

1.3.- Bibliographical review

This section presents the relevant studies published previously regarding vegetation monitoring, through multitemporal monitoring of remotely sensed parameters and change detection methods.

1.3.1.- NDVI

1.3.1.1.- NDVI methods

As stated above, NDVI parameter has first been presented by Rouse *et al.* (1973) for vegetation monitoring uses. However, many corrections have been developed for an adequate retrieval of this parameter, not to mention other indices developed to palliate NDVI flaws. Those other vegetation indices having been detailed above, only corrections for NDVI retrieval are presented here.

The maximum value compositing technique (MVC), generally applied to freely available datasets (see Chapter 2), has been used to decrease the influence of most NDVI flaws (Holben, 1986). This technique consists in the selection of maximum NDVI values over a given time interval (common intervals are 7, 10, 15 or 30 days) for each pixel, to build a composite NDVI image with better reliability. When the compositing is carried out over short periods of time (up to 15 days), changes in vegetation are low, and thus this compositing technique does not hinder vegetation monitoring. MVC technique is useful for problems in NDVI retrieval such as:

37

- changes in illumination angle: since NOAA platforms are polar orbiting satellites (see Chapter 2), their overpass hour changes from day to day, leading to changes in illumination angles.

- changes in viewing angle: due to orbit characteristics, NOAA satellites do not observe one location on Earth with the same viewing angle. Since NDVI values tend to decrease with viewing angle, the MVC method tends to lower this effect, by selecting close to nadir observations.

- changes in atmospheric conditions: increases in oxygen concentration in the atmosphere tends to decrease NDVI values. Water vapor and aerosols presence in the atmosphere also tend to decrease NDVI values. Clouds have a low NDVI value (close to zero or negative), also decreasing retrieved NDVI values. Those effects are thus diminished by using the MVC method. However, increases in ozone concentration tend to increase NDVI values, so a specific correction is needed for this component of the atmosphere.

- changes due to directional surface reflectance: these are changes in viewing and illumination geometry, and their effect on NDVI depends on seasonal variations in solar zenithal angle. However, those effects are unimportant relative to changes in atmospheric conditions. To correct this effect, Los *et al.* (2005) developed a method to convert AVHRR NDVI time series to a standard viewing and illumination geometry.

However, the MVC technique is unreliable in some cases. Those are:

- cloud presence during the whole compositing period: then, a cloud mask need to be built to screen out the contaminated pixels (see Chapter 3). Roerink *et al.* (2000) developed a method for reconstructing cloud-free time series using Fourier analysis.

- desert anomalies: changes in soil and atmospheric conditions due to meteorology have an influence on desert NDVI values, which have a rather high variability considering their overall low NDVI values. However, those NDVI values are low enough not to be misregistered as vegetation.

- terminator effects: at twilight terminator (area between day and night conditions), NDVI values tend to be abnormally high, in response to very long path lengths in the atmosphere, largely independent of surface reflectance. These effects can be eliminated by simple thresholds set on solar zenithal angles.

- pixel misregistration: inaccuracies in sensor acquisition times and satellite pitch (due to bad compensation of yaw and roll) can lead to pixel misregistration, leading to differences in observed areas coupled with differences in sun and sensor geometry, atmospheric conditions, etc. Therefore, NDVI images have to be correctly georeferenced before the application of the MVC technique.

Chen *et al.* (2003) showed that NDVI maximum value composites have to be screened out for cloud contamination before compositing in order to avoid irregular NDVI patterns.

Other NDVI flaws have to be corrected separately, such as temporal atmospheric effects, like those generated by Mount Pinatubo's eruption after June 1991 (Vermote *et al.*, 1997). Efforts have been made to correct available datasets for specific locations, for example Lovell & Graetz (2001) corrected PAL NDVI data (see Chapter 2) for Australia. Moreover, since NOAA platforms derive slowly from their nominal orbit (orbital drift effect), images have been acquired progressively later in the afternoon, inducing changes in observation and sun geometry. Although Kaufmann *et al.* (2000) have shown that its influence is not critical for analyzing interannual variability of global vegetation activity, they state that its influence is higher for vegetation with low leaf area. This led the GIMMS group to correct the NOAA archive from orbital drift influence, using the Empirical Mode Decomposition technique (Pinzon, 2002; Pinzon *et al.*, 2005). As for Bacour *et al.* (2006), they normalized the directional effects in reflectance measurements using POLDER database, before calculating NDVI time series.

Additionally to these NDVI drawbacks, trends have been detected in the NDVI archive, different for each satellite platform. Kogan & Zhou (2001) showed that those trends were higher in desert and tropical forests, while de Beurs & Henebry (2004b) showed that arid and semi-arid ecoregions in Central Asia showed significant differences between satellites.

1.3.1.2.- Monitoring vegetation with NDVI

Many studies have dealt with NDVI as regards vegetation monitoring. Excepting other vegetation indices, few studies have been carried out on vegetation from remotely sensed data without taking into account the NDVI parameter. This review focuses on detecting trends in vegetation by different methods, although NDVI has been used for retrieving biophysical parameters, such as leaf area index (Wang *et al.*, 2005), productivity (Field *et al.*, 1995; Prince & Goward, 1995; Nemani *et al.*, 2003; Maselli, 2004; Running *et al.*, 2004; Boisvenue & Running, 2006; Maselli & Chiesi, 2005; Maselli *et al.*, 2006), vegetation fraction (Jiang *et al.*, 2006), fraction of photosynthetically active radiation absorbed by green vegetation (Sellers, 1987), photosynthetic activity (Slayback *et al.*, 2003), water stress (Duchemin *et al.*, 1999), evapotranspiration (Suzuki *et al.*, 2007), classification purposes (Tucker *et al.*, 1985; Loveland *et al.*, 2000; Morales *et al.*, 2004; Wang & Tenhunen, 2004; Evans & Gerkeen, 2006; Sobrino *et al.*, 2006a), fire disturbance (Goetz *et al.*, 2006), or links with climate (Braswell *et al.*, 1997; Asner *et al.*, 2000; Los *et al.*, 2001; Chen & Pan, 2002; Kaufmann *et al.*, 2003; de Beurs & Henebry, 2004a; de Beurs & Henebry, 2005b; Chen *et al.*, 2005; Verhoef *et al.*, 2005; Neigh *et al.*, 2007).

Regarding land surface phenology, numerous studies have been carried out, using different methods to retrieve phenological phases. The first method (method 1) consists in the prescription of thresholds (Lloyd, 1990; Fischer, 1994; Myneni *et al.*, 1997; Zhou *et al.*, 2001; Shabanov *et al.*, 2002; Reed *et al.*, 2003; Zhou *et al.*, 2003; Chen *et al.*, 2005; Høgda *et al.*, 2005), corresponding to a given percentage of NDVI amplitude. This method, though easy to implement, suffers a major drawback, which is the noise present in temporal NDVI series, caused both by atmospheric and sensor variations. The second method (method 2) consists in the identification of phenological dates based on the mid-point in the annual range of NDVI values (White *et al.*, 1997; Delbart *et al.*, 2005). This method suffers from the same drawbacks than the first one. The third method (method 3) is based on the rate of change in NDVI values to estimate the transition dates, and is also influenced by atmospheric conditions (Moulin *et al.*, 1997; Tateishi & Ebata, 2004; Piao *et al.*, 2006). The fourth method (method 4) allows the estimation of transition dates via spectral or harmonic analysis (Moody & Johnson, 2001; Stöckli & Vidale, 2004), which diminishes the influence of cloud-contaminated NDVI values

on the transition dates. Another method (method 5) consists in fitting NDVI temporal series to a given function, which provides transition dates among other parameters (Badhwar, 1984; Tucker *et al.*, 2001; Jönsson & Ekhlund, 2002; Heumann *et al.*, 2007; Zhang *et al.*, 2004; Beck *et al.*, 2006; Bradley *et al.*, 2007). This method also allows screening cloud-contaminated values during the fitting procedure, though its application is highly computer time demanding, especially for global studies. The last method (method 6), consists in conducting a principal component analysis on NDVI time series (Hall-Beyer, 2003; Jarlan *et al.*, 2005). However, the retrieved components are difficult to interpret in terms of climate or biophysical changes.

Those five methods have been used for three purposes: studying temporal variations of phenological dates (see for example Zhang *et al.*, 2004; Sakamoto *et al.*, 2005; Beck *et al.*, 2006; Bradley *et al.*, 2007), real-time monitoring and short-term forecasting of land surface phenology (White & Nemani, 2006) and retrieving trends for phenological dates (see for example Myneni *et al.*, 1997; Tucker *et al.*, 2001; Zhou *et al.*, 2001). Since the work presented in this paper focuses on retrieved trends for phenology, only phenological studies dedicated to trend retrieval are reviewed here. Myneni *et al.* (1997) carried out a global land surface phenology study using method 1, finding a general advance in spring dates of 8 days between 1981 and 1991, and an increase in growing-season (defined as photosynthetic active period) around 12 days over the same period. Using method 5, Tucker *et al.* (2001) estimated, during the 1982-1991 period (respectively 1992-1999 period), an advance of 5.6 days (resp. 1.7 days) in spring phases for the latitudes between 45ºN and 75ºN. Growing season length increased by 4 days (resp. 0.4 days) over the same periods. Using method 1, Zhou *et al.* (2001) evidenced for the 1981-1999 period an advance in spring phases of 7 days over Eurasia (respectively 8 days over North America), a delay of 11 days (resp. 4 days) for autumn phases, resulting in an increase in growing season of 18 days (resp. 12 days). Using method 4, Stöckli & Vidale (2004) observed an advance in spring phases of 10.8 days over Europe between 1982 and 2000, and a lengthening of the growing season of 19.2 days over the same period. Using method 1, Chen *et al.* (2005) estimated an increase of growing season length of 17 days over China for the 1982-1993 period. Delbart *et al.* (2006) found an advance (respectively a delay) in spring phases of 8 days (resp. 3.6 days) over boreal areas for the 1982-1991

period (resp. 1993-2004 period) using method 2 on NDVI and NDWI (Normalized Difference Water Index, calculated similarly to NDVI from short-wave and near-infrared bands of SPOT-VEGETATION sensor) time series. Using method 3, Piao *et al.* (2006) evidenced over Northern China an advance of 0.79 days per year for spring phases and a delay of 0.37 days per year for autumn phases, resulting in a lengthening of growing season of 1.16 days per year between 1982 and 1999. Heumann *et al.* (2007) showed that no significant trend could be evidenced for the Sahel region between 1982 and 2005, while significant trends in length and end of growing-season were observed in Soudan and Guinea.

Other studies have dealt with the determination of land surface phenology over smaller areas (see for example Osborne *et al.*, 2000; Tao *et al.* 2006; Høgda *et al.*, 2005), generally pointing at an advance in spring phases and a delay in autumn phases, resulting in a lengthening of the growing season, similar to the global studies reviewed above. Høgda *et al.* (2002) showed that data acquired from low resolution satellites could perfectly be used for growing-season start monitoring, at least for homogeneous areas (birch forests), and provided similar results to ground phenological records. White *et al.* (1997) developed a model for prediction of onset and offset of greenness using past land surface phenology observations and available climate data. White & Nemani (2006) have used the first method for real-time monitoring and short-term forecasting of land surface phenology, considering phenoregions separately.

Additionnally, many other studies have been conducted from other satellite platform data, such as MODIS (Moderate Resolution Imaging Spectroradiometer) EVI (Enhanced Vegetation Index, previously known as SARVI – Soil and Atmosphere Resistant Vegetation Index, Huete *et al.*, 1994; Liu & Huete, 1995; Huete *et al.*, 1997). For example, Zhang *et al.* (2003) showed that MODIS data were suitable for monitoring vegetation phenology in Northeastern United States. Lupo *et al.* (2007) have retrieved five phenological indicators from MODIS EVI data, namely start of the growing season, EVI amplitude, growing season length, integrated area below the growing vegetation curve, and date of maximum EVI value. Those indicators were then used for classifying land cover change processes. Sakamoto *et al.* (2005) also used MODIS EVI for phenological purposes, this time in the case of rice crops, associated to wavelet transform. MODIS EVI data have also been used to detect green-up in Amazon rainforests in dry season (Huete *et al.*,

42

2006; Xiao *et al.*, 2006), and swings in Leaf Area Index in the same region (Myneni *et al.*, 2007). From SPOT VEGETATION data, Delbart *et al.* (2005; 2006) have used Normalized Difference Water Index (NDWI) to retrieve phenological dates at higher northern latitudes.

As can be observed, few studies (Myneni *et al.*, 1997) have been carried out at global scale, the other studies being centred on the Northern Hemisphere, at local to continental scale. Moreover, phenological results have been averaged over large areas before trend retrieval, local trends being dissolved into the main trend. Finally, the studies with the largest geographical extension have been conducted on datasets suffering from various flaws, such as orbital drift and volcanic aerosol contamination after Mount Pinatubo's eruption in 1991.

As for studies regarding NDVI metrics (maximum, minimum and average values, coefficient of variation), they are generally based on annual evolution observation (Myneni *et al.*, 1997; Tucker *et al.*, 2001; Zhou *et al.*, 2001; Paruelo *et al.*, 2004), and sometimes on model fitting (Jönsson & Eklundh, 2004). For example, Tucker *et al.* (1984) have used NDVI for vegetation monitoring in the Nile Delta, using additional thermal data for cloud screening. Myneni *et al.* (1997), observed a global NDVI increase between 1981 and 1991 for inland regions corresponding to areas with high NDVI. Paruelo *et al.* (2004) evidenced an increase in NDVI in humid temperate forests in South America between 1981 and 2000, and NDVI reduction in desert areas. Zhou *et al.* (2001) observed a persistent increase in NDVI for about 61% of the total vegetated area between 40ºN and 70ºN in Eurasia, while North America shows a more fragmented pattern of change. Those results were shown to be due mainly to changes in temperature (Zhou *et al.*, 2003). De Beurs & Henebry (2004a) evidenced that structural changes in Kazakhstan could be identified from satellite data through statistical analysis. Barbosa *et al.* (2006) showed that the Northeast region of Brazil has a high variability in NDVI levels, seasonal variations ranging from 14% to 32%, with an upward trend in vegetation between 1984 and 1990, which was reverted between 1991 and 1998. Tucker *et al.* (2001) observed an increase in average May to September NDVI from 45ºN to 75ºN of 9% between 1982 and 1991, followed by a decrease of 5% from 1991 to 1992 (corresponding to Mount Pinatubo's eruption influence), and by an increase of 8% from 1992 to 1999, linked with air temperature increases. Bogaert *et al.* (2002) showed that detected increasing trends

43

in NDVI data were persistent and spatially extensive and connected in Eurasia, but showed a more fragmented pattern in North America. Slayback *et al.* (2003) estimated trends in yearly averaged NDVI as varying between 0.0015 and 0.0045 NDVI units per year for global latitude bands from 35ºN to 75ºN, with trends generally higher in the 1990s than in the 1980s.

As can be observed, many studies of NDVI temporal variations have already been carried out, though their spatial extension has often been limited to local or continental scale, focused on the northern hemisphere. However, results are usually averaged over large areas to reach statistical confidence, drowning local characteristics in large trends. Thus, a pixel by pixel analysis still has to be conducted, especially with the availability of newer versions of AVHRR data (see Chapter 2).

1.3.2.- LST

Various methods have been developed for land surface temperature estimation. Those methods are based on the principles presented before, with coefficients adapted to the wavelength range of each sensor band. In this paragraph, we describe only algorithms developed for NOAA-AVHRR sensor (see Chapter 2), since these are the ones used in this work. The methods for retrieving LST from other sensors differ only in coefficients values, due to differences in acquiring wavelengths. An example of LST comparison between sensors can be found in Atitar et al. (2007).

Algorithms for LST retrieval can be classified in 4 groups, whether they take into account local emissivity, total atmospheric water vapor or observation angle effects to correct at sensor brightness temperatures. For example, May *et al.* (1992) algorithm only takes into account observation angle. Becker & Li (1990), Ulivieri *et al.* (1992) and Yang & Yang (2006) algorithms take into account only mean land surface emissivity over observation bands. Price (1984), Prata & Platt (1991), Sobrino *et al.* (1993) and Ulivieri *et al.* (1994) algorithms do take into account land surface emissivities in each observation band. As for Sobrino *et al.* (1991), Sobrino & Raissouni (2000), Qin *et al.* (2001) and Mito *et al.* (2002) algorithms, they take into account both spectral emissivities and total atmospheric water vapor content. Another algorithm worth mentioning, since it has also been used in this work, is the

one developed by Sobrino & Romaguera (2004) for MSG1 SEVIRI data (see Chapters 2 and 3), which is also a split-window algorithm taking into account spectral emissivities, total atmospheric water vapor content and observation angle.

Various studies have dealt with the accuracy of LST estimation from AVHRR data of those different algorithms, generally agreeing on the method presented in Sobrino & Raissouni (2000) as being the best when no additional data is known, such as water vapor or emissivity, and have to be inferred from the data (Qin *et al.*, 2004; Gusso *et al.*, 2007). Han *et al.* (2004) have compared five of the algorithms presented before over a boreal forest in Québec, Canada, and concluded that Ulivieri *et al.* (1994) LST algorithm was better fitted for this study area. However, Sobrino & Raissouni (2000) algorithm was not included in their comparison.

Retrieved LSTs have been used for various purposes. Muzylev *et al.* (2001) used LST estimates for modelling the hydrological cycle of river basins in central Russia, demonstrating that the use of satellite data leads to improved output results. Manzo-Delgado *et al.* (2004) related LST time series in Central Mexico to El Niño and La Niña events, El Niño events being characterized by a higher number of forest fires. They concluded that LST estimation was useful for modelling the probability of forest fire occurrence. Liu *et al.* (2005) have monitored desertification in arid and semi-arid areas of China from AVHRR and MODIS LST, showing that the speed of desertification is faster than that of land rehabilitation.

One can observe that little use has been made of LST time series, mainly due to satellite orbital drift (Price, 1991 – see Chapters 2 and 3), while research has been focused mainly on LST retrieval. This dissertation is thus dedicated partly to LST time series analysis for vegetation monitoring, retrieved using the algorithm developed by Sobrino & Raissouni (2000).

1.3.3.- LST/NDVI

To this date, the relations between NDVI and LST have been studied in two different ways. The first one is related to their spatial variation, when the purpose is the determination of land surface parameters such as surface moisture or evapotranspiration; the second one is related to their temporal variation, to characterize vegetation changes. However, many of the studies carried out used

LST retrieved only from at sensor brightness temperatures (BT). In those cases, LST is replaced by BT in the following paragraphs.

Nemani & Running (1989) studied temporal variations of NDVI and BT in Montana, showing that this relation evolved in time. The slope between BT and NDVI was sensitive to changes in canopy resistance, identifying this slope as a useful parameter for evapotranspiration estimation. Ehrlich & Lambin (1996) built a land cover classification of Africa through PCA of TB/NDVI slopes over a year of monthly data. This classification compared well with a previous classification. Shultz & Halpert (1995) studied the correlations between NDVI, BT and precipitation over the globe, evidencing a generally positive correlation, especially in the high and middle latitudes, with some subtropical areas presenting a negative correlation. They also found low correlations between NDVI and BT anomaly. Lambin & Ehrlich (1996) reviewed extensively the drivers between NDVI and BT, describing a general spatial pattern of relationships between NDVI and BT, related to land cover. They conclude than BT/NDVI slope can be used to classify land cover, and monitor land cover changes over time, when associated to seasonality information, retrieved from NDVI annual variations alone. Nemani & Running (1997) used BT and NDVI annual variations to build a classification of United States (later extended to the whole globe) that they validated from a previous classification. Lambin & Ehrlich (1997) used the results of Lambin & Ehrlich (1996) to build a change index based on NDVI and BT to retrieve change patterns in sub-Saharan Africa, which they found to be highly erratic due to interannual climatic variability. Sobrino & Raissouni (2000) presented two methods for land cover change detection in Morocco based on NDVI and LST annual variations. Borak *et al.* (2000) confirmed that coarse resolution estimates of change were best related to fine resolution estimates when BT and NDVI evolutions were considered. Bayarjargal *et al.* (2006) compared over Mongolia arid regions various drought indices retrieved from satellite data, among which BT and NDVI ratio, concluding that no index could be pointed out as most reliable, and that those indices were difficult to relate to ground observations.

As for spatial variations, Nemani *et al.* (1993) used remotely sensed NDVI and BT to estimate surface moisture status in western Montana (USA), observing a strong negative relationship between NDVI and LST over all present biomes (grass, crops and forests). Gillies *et al.* (1997) validated the estimation of surface

soil water content and energy fluxes from NDVI and BT with ground measurements, leading to an accuracy around 20% in those parameters. Clarke (1997) used the combined values of NDVI and BT to detect water stress in irrigated fields. Goward *et al.* (2002) used Simplified Simple Biosphere model to examine LST/NDVI relationships with biophysical parameters. Near-surface soil moisture, incident radiation, plant stomatal function and to a lesser degree, wind speed were found to be the most critical parameters. Soil moisture estimates from satellite data obtained using a model derived equation showed good concordance with ground measurements. Sandholt *et al.* (2002) designed a Temperature-Vegetation Dryness Index, related to surface moisture status from relationships between BT and NDVI, which they validate from comparison with a hydrological model over Senegal. Hope *et al.* (2005) evidenced a negative linear relationship between LST and NDVI in Arctic tundra ecosystems. Wang *et al.* (2006) designed a method for retrieving evaporative fraction from a combination of day and night LST and NDVI with an increased accuracy. Yue *et al.* (2007) studied Landsat retrieved NDVI and BT over various urban classes, and showed that each class showed a different pattern of relationship, validating those parameters for urban land occupation classification. Finally, Goetz (1997) showed that the use of data with different spatial resolution led to similar results regarding spatial and temporal behaviour of BT/NDVI relationship.

As a conclusion few studies have used LST coupled with NDVI for vegetation monitoring, BT parameter being generally preferred over LST because of the simplicity of its estimation. Moreover, temporal analyses of the relation between LST and NDVI have been limited to theory and classification purposes, while spatial analyses have been carried out only locally, generally to estimate biophysical parameters linked to photosynthesis.

1.3.4.- Change detection

Coppin *et al.* (2004) have listed different methods for vegetation monitoring. This section summarizes those methods, completed with other references. Detection of changes in remotely sensed images presupposes having access to similar data, whether regarding acquisition (cloud free images, atmospheric effects, illumination and observation geometry, similar wavelengths and spatial resolutions), time scale (comparable phenological state of the vegetation), data

47

processing (similar methods, accurate georeferenciation). Change detection algorithms are mainly based on bi-temporal analysis, i.e. comparison of two sets of data, preferably from before and after the change.

First, one can compare two classifications obtained using the same methodology on similar data, identifying the pixels attributed to different classes in the "before" and "after" images. This method has a generally low accuracy, due to each classification own accuracies. This method has been applied for example to a couple or more of Landsat images (Hall *et al.*, 1991; Etter *et al.*, 2006). Xu & Young (1990) showed that manual segmentation of the images helped avoid obvious errors in classification. Giri *et al.* (2003) used this method on low resolution data for change "hot spot" identification, and high resolution data for change analysis. Stehman *et al.* (2005) used ecosystem based statistical sampling on two classifications of United States land cover to retrieve changes between 1973 and 2000. Tømmervik *et al.* (2003) also used this method on Landsat data to monitor vegetation changes in given locations of Norway and Russia in relation with air pollution. Another method consists in classifying both "before" and "after" images with the same classification procedure, including changes as supplementary classes. This results in a very complex classification procedure, which needs good knowledge of the study area. This technique has been used for example by Colwell *et al.* (1980), Hall *et al.* (1984) and Sader (1988). A third technique for change detection is univariate image differencing, which consists in the simple subtraction of two images previously co-georeferenced, such as NDVI (Banner & Lynham, 1981; Lyon *et al.*, 1998; Nelson, 1983). This method has the advantage of low cost in processing time. A fourth technique consists in image ratioing on a pixel by pixel basis, resulting in an image where change pixels have a value different to unity. This technique has been applied by Howarth & Wickware (1981), unfortunately without being able to make a quantitative assessment of the changes. A fifth method is to carry out a bi-linear data transformation on the data, such as principal component analysis (PCA). Standardized PCA, in opposition to normal PCA, seems to be more focused on change features (Singh & Harrison, 1985; Fung & LeDrew, 1987). Another method for change detection is the use of change vector analysis (CVA), which combines spectral and temporal dimensions, resulting in change magnitude and direction maps. CVA has been applied mainly to Landsat images (Yokota & Matsumoto, 1988; Lambin & Strahler, 1994; Johnson &

Kasischke, 1998; Nackaerts *et al.*, 2005). An eighth technique is image regression, which consists in assuming that the "after" image is linearly related to the "before" image for all bands, implying that the spectral properties of most pixels have not changed between images. Changes are then identified by setting thresholds to the residuals. This technique has not been proven to reach high accuracies (Burns & Joyce, 1981; Singh, 1989; Ridd & Liu, 1998). A ninth method is multi-temporal spectral mixture analysis, which supposes that the images (preferably with high spatial resolution) include pixels with pure spectral signatures or end-members, present in all pixels with different proportions. Then, change results in variation in end-member percentiles. This method was implemented successfully using Landsat images of Brazilian Amazon by Adams *et al.* (1995) and Roberts *et al.* (1998). Finally, a tenth technique is multidimensional temporal feature space analysis, which consists in overlaying selected bands of the "before" and "after" images in a composite image as red, green and blue bands, in which changes appear in unique colors. This technique does not provide any insight on the drivers of the changes, and is usually applied for mask building before change detection. For example, Alwashe & Bokhari (1993) and Wilson & Sader (2002) have applied this technique to Landsat bands or derived indices. Finally, combinations of those different techniques have also been used (Desclée *et al.*, 2006).

Most of the methods presented above have been designed for high resolution images, such as those retrieved by SPOT or Landsat sensors, for which temporal resolution is quite low. However, in our case, time resolution is higher (from ten to fifteen days) and spatial resolution is lower (see Chapter 2), resulting in an averaging over species and events. Thus, different techniques have to be applied, which can be summarized as temporal trajectory analyses. These techniques include statistical analysis (departure from averages, optima, etc. – Lambin & Strahler, 1994), simple anomalies (instantaneous departure from average corresponding period over the whole time series – Myneni *et al.*, 1997; Plisnier *et al.*, 2000), Fourier analysis (Andres *et al.*, 1994), PCA (Eastman & Fulk, 1993; Young & Wang, 2001) and CVA (Lambin & Strahler, 1994; Lambin & Ehrlich, 1997). Additionally, de Beurs & Hennebry (2005a) designed a statistical framework for land cover change analysis. Those last methods are thus being used in this dissertation for change detection in the context of global vegetation monitoring.

Chapter 2

DATA DESCRIPTION

"I never guess. It is a capital mistake to theorize before one has data. Insensibly one begins to twist facts to suit theories, instead of theories to suit facts."

Sir Arthur Conan Doyle.

This chapter describes the data used for this work, as well as how they were retrieved and compiled. First, remotely sensed data (NOAA, MSG) are presented, followed by a description of the historical databases (PAL, GIMMS) from which they were downloaded. Finally, Reanalysis database is presented briefly.

2.1.- SENSORS

Data used in this work were mainly retrieved by AVHRR instrument onboard NOAA satellite series. These data are presented thoroughly, and a brief introduction to MSG SEVIRI data follows, these latter having been used for orbital drift correction validation purposes (see Chapter 3).

2.1.1.- NOAA AVHRR

The AVHRR (Advanced Very High Resolution Radiometer) instrument has been onboard NOAA (National Oceanic and Atmospheric Administration) satellites since 1978. It acquires data in 5 spectral bands; one visible, one near infrared and three thermal bands, all with 1024 quantizing levels. The AVHRR produces images at 1.1 and 4 km spatial resolution. The 4-km product, also called global area coverage (GAC) product is derived from the 1-km product by onboard sampling (Townshend, 1994). The 4-km product is available globally from July 1981 until the present. The 1-km record is not continuous. Its availability depends upon prior arrangements made by NOAA, or on the proximity of a local receiving station that can capture the data directly from the satellite. See NOAA–KLM user

guide for specifications of the newest NOAA AVHRR instruments (http://www2.ncdc.noaa.gov/docs/klm/).

2.1.1.1.- Platform

NOAA AVHRR satellite series -7, -9, -11, -14, -16 (see Figure 2.1) and -17, used for both PAL and GIMMS NDVI records, flow in sun-synchronous polar orbits with a nominal 1:30 or 2:30 PM local daytime overpass time at launch. However, the overpass times drifted by 1-2 minutes per month to as much as 4 1/2 hours later in the day creating variable illumination and view angles over the period of record (Price, 1991). This orbital drift can be observed clearly figure 2.2.

The 55-degree sensor swath width permits a daily view of each pixel on Earth although at different illumination and view angles during the 9-day repeat cycle. Maximum value NDVI data compositing (MVC, see Holben, 1986) tends to select pixels acquired in a near-nadir mode with minimum atmospheric effects. Even so, view, illumination and atmospheric effects remain.

2.1.1.2.- Mission objectives

The AVHRR radiometer was initially designed for weather observation (determination of cloud coverage and surface temperature). Later the data were found to be useful for numerous applications in the field of Earth Observation and AVHRR sensor became one of the most popular sources of remote sensing data. Some of its applications are:

- land surface temperature (LST) and sea surface temperature (SST).

- marine contamination due to oil spills.

- cloud coverage and precipitation.

- volcanic eruptions.

- ice and snow cover.

- normalized difference vegetation index (NDVI – see Chapter 1).

AVHRR data archives extend back to July 1981.

Figure 2.1.- NOAA-16 artistic view.
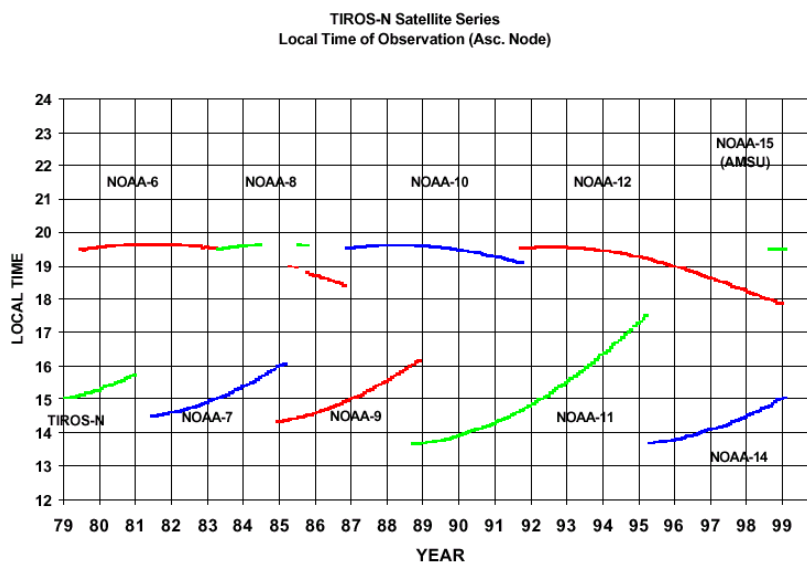
Figure 2.2.- NOAA satellites orbital drift.

2.1.1.3.- Instrument spectral characteristics

Three different models of this instrument can be distinguished: AVHRR/1, AVHRR/2 and AVHRR/3. The latter is the one on board the KLM series satellites (NOAA-15, -16, -17, …). The AVHRR instrument provides data from different

portions of the visible (0.6 μm), near infrared (0.9 μm) and thermal infrared (3.7, 11 and 12 μm) spectrum. Observation from channels corresponding to the visible and near infrared allows the study of vegetation, clouds, lakes, coasts, snow and ice. The three remaining channels operating in the thermal infrared are used to obtain products for land, water, sea surface and cloud temperature. The additional 3A channel (1.6 μm) present in AVHRR/3 improves the capability for distinguishing among snow, ice and clouds. See respectively table 2.1 and 2.2 for more precision on AVHRR sensors and spectral bands.

Table 2.1.- AVHRR sensor.

Sensor	Spectral resolution	Spatial resolution	Radiometric resolution
AVHRR/2 (NOAA-14)	5 bands	1100 m	10 bits
AVHRR/3 (NOAA-15)	6 bands	1100 m	10 bits
AVHRR/3 (NOAA-16)	6 bands	1100 m	10 bits

Table 2.2.- AVHRR spectral characteristics.

BAND	WAVE LENGTH NOAA – 6, 8, 10 (μm)	WAVE LENGTH NOAA – 7, 9, 11, 12, 14 (μm)	WAVE LENGTH NOAA – 15, 16, 17 (μm)	IFOV (mrad)	Detector material	Scan angle	NE ΔT (°K)
1	0.58 - 0.68	0.58 - 0.68	0.58 - 0.68	1.39	Si	± 55º	
2	0.725 - 1.10	0.725 - 1.10	0.725 - 1.10	1.41	Si	± 55º	
3A			1.58 - 1.64	1.30	InGaAs	± 55º	
3B	3.55 - 3.93	3.55 - 3.93	3.55 - 3.93	1.51	InSb	± 55º	0.12
4	10.50 - 11.50	10.30 - 11.30	10.30 - 11.30	1.41	HgCd Te	± 55º	0.12
5	10.50 - 11.50	11.50 - 12.50	11.50 - 12.50	1.30	HgCd Te	± 55º	0.12

2.1.1.4.- Principles of operation

The NOAA satellite series, NOAA-7, -9, -11, -14, -16 and -17 follow polar, sun synchronous orbits with nadir afternoon overpass times. NOAA-7 data span the years 1981-1985, NOAA-9 the years 1986-1989, NOAA-11 the years 1989-1995, NOAA-14 the years 1995-2000, NOAA-16 the years 2000-2004, and NOAA-17 from 2004 to present. In September 1994, NOAA-11 started to malfunction and its replacement, NOAA-13, failed shortly after launch, and was not replaced until January 1995. Each AVHRR sensor has different and variable calibration and overpass time.

2.1.1.5.- Instrument measurement geometry

The AVHRR is a scanning, imaging radiometer, scanning ± 55 degrees, providing a 2800 km swath width. This swath width is greater than the 25.3 degrees separation between successive orbital tracks and provides overlapping coverage (side-lap). The orbital configuration permits daily coverage at a maximum spatial resolution (in nadir direction) of 1 km of each point on Earth, although at different viewing and illumination geometries on subsequent days. The orbital period of about 102 minutes produces 14.1 orbits per day. Because the daily number of orbits is not an integer, the suborbital tracks do not repeat daily, although the local solar time of the satellite's passage is essentially unchanged for any latitude. The orbit repeats its ground track each 9 days.

2.1.1.6.- Data transmission

AVHRR transmits data in three different ways: High Resolution Picture Transmission (HRPT), Local Area Coverage (LAC) and Global Area Coverage (GAC). HRPT data is transmitted to a ground station as they are collected. The average instantaneous field-of-view of 1.4 milliradians yields to a ground resolution of approximately 1.1 km around nadir at a nominal orbit altitude of 833 km. LAC data are high resolution data that are recorded on an onboard tape for subsequent transmission during a station overpass. GAC data are derived from a sample averaging of the full resolution AVHRR data. Four out of every five samples along the scan line are used to compute one average value and the data from only every third scan line is processed, yielding to a 1.1 km by 4 km resolution at the sub-point.

2.1.2.- MSG SEVIRI

At the end of November 1977, ESA's (European Space Agency) first geostationary meteorological satellite, named Meteosat, was put in orbit. This satellite inaugurated a series which have been providing images and information almost continuously to this day.

2.1.2.1.- METEOSAT 8 satellite

Meteosat 8 platform reached its orbit in August 2002, and is fully operating since the beginning of year 2004. This is the first-born of a series of four Meteosat

Second Generation satellites, designed to serve the needs of Nowcasting applications, short- and very short-term weather forecast, and also to develop climatic applications in Africa and Europe. This satellite has an estimated lifetime of 7 years. The technical characteristics of the rest of the MSG (Meteosat Second Generation) series are the same than the ones developed for Meteosat 8.

Meteosat 8 has been placed on a geostationary orbit, located at an altitude of 36 000 km and centered at 0º latitude on the Equator. Figure 2.3 shows its spatial coverage compared with the other geostationary satellites.

Meteosat 8 has a cylindrical body, with a diameter of 3.2 m and a height of 2.4 m, rotating along its longitudinal axis, which is aligned with the Earth's rotation axis, at 100 rpm speed. This stabilizes the satellite as well as allows a progressive scanning of the Earth. The resulting zenithal viewing angle is shown in Figure 2.4.

Longitude (º)
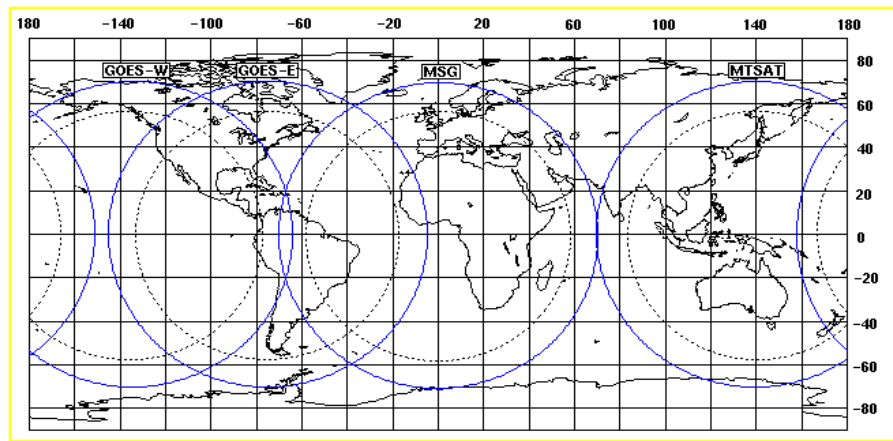
Latitude (º)

——— 80º zenithal observation angle ------ 65º zenithal observation angle

Figure 2.3.- Spatial coverage of Meteosat 8 satellite compared with Geostationary Operations Environmental Satellites (GOES) and Multi-functional Transport Satellite (MTSAT).

This satellite is divided in three principal units (see Figure 2.5): the sensors are located in the central part, the Mission Communication Payload (MCP) which includes antennas and transmitters in its superior part, and finally the platform

support subsystems in the inferior part, dedicated to propulsion, orbit control and solar panels (Veith, 2000).

Meteosat 8 carries two sensors, the Geostationary Earth Radiation Budget (GERB) and the Spinning Enhanced Visible and InfraRed Imager (SEVIRI).
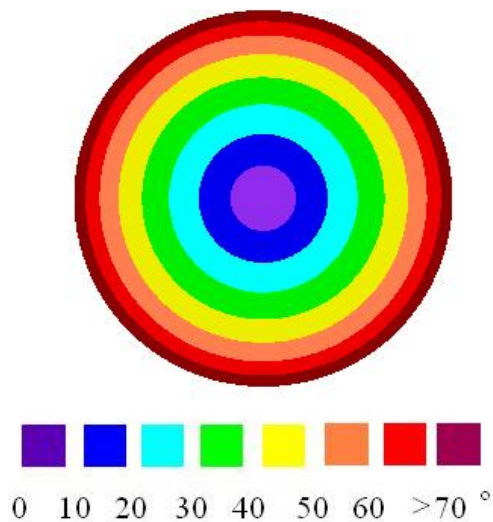
Figura 2.4.- Zenithal observation angle of Meteosat 8 satellite.

Figure 2.5.- Meteosat 8 satellite.

GERB sensor is a radiometer with two broad observation bands, the first one embracing the solar spectrum (0.32 to 4 μm), and the second one the whole

58

electromagnetic spectrum (0.32 to 30 μm), with a 40 × 45 km2 spatial resolution. This sensor retrieves reflected solar radiation and emitted thermal radiation fluxes.

2.1.2.2.- SEVIRI sensor

SEVIRI radiometer provides images in 12 observation channels, with a 15-minute frequency, at a spatial resolution of 3 km for the High-Resolution Visible channel (HRV) and 3 km for the rest of the channels. SEVIRI has a 50 cm diameter aperture on the side of Meteosat 8. The radiation that arrives at the target is focused by means of a telescope on detectors sensible to 12 different bands of the electromagnetic spectrum, to be then processed electronically. The acquisition is realized from East to West due to the rotation of the satellite, combined with a northward movement generated by a mirror (see Figure 2.6). SEVIRI has 3 channels dedicated to visible and near-infrared, centered at 0.6, 0.8 and 1.6 μm, 8 channels for the infrared, centered at 3.9, 6.2, 7.3, 8.7, 9.7, 10.8, 12.0 and 13.4 μm, and finally a broad band (0.5 to 0.9 μm) in the visible, called High-Resolution Visible (HRV) channel. These channels are respectively named VIS0.6, VIS0.8, IR1.6, IR3.9, WV6.2, WV7.3, IR8.7, IR9.7, IR10.8, IR12.0 and HRV. Figure 2.7 shows the atmospheric transmission and the position of the mentioned thermal channels.
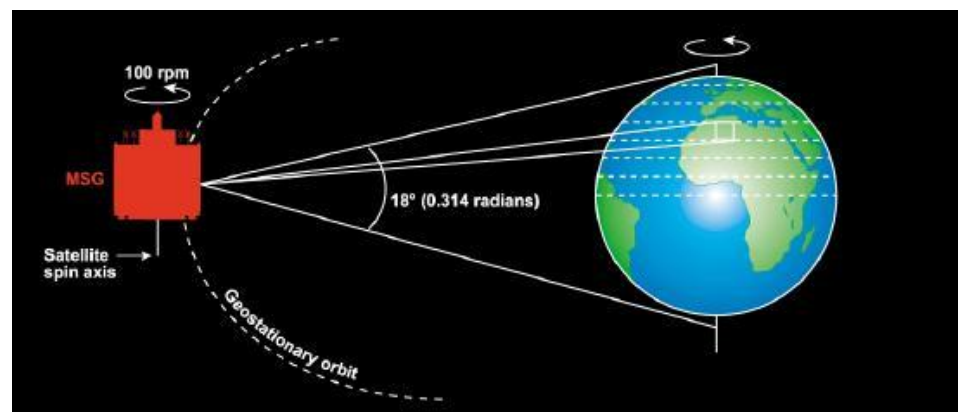
Figure 2.6.- Scanning mechanical Principle of SEVIRI sensor..
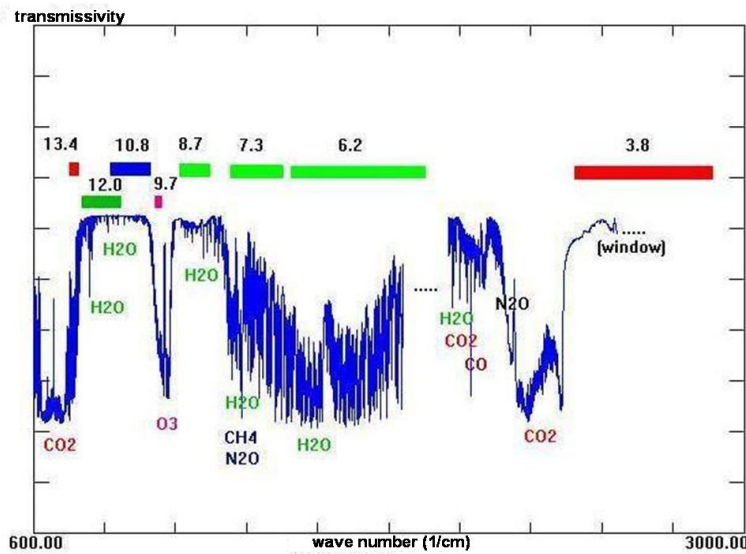
Figure 2.7.- Atmospheric transmissivity and SEVIRI channels (adapted from technical information provided by EUMETSAT).

The two visible channels, VIS0.6 and VIS0.8, provide land surface and cloud images during the day. Those wavelengths help to discriminate vegetated surfaces from cloud for different periods of the year, to determine vegetation indices and atmospheric aerosol amounts. IR1.6 channel is used to discriminate clouds from ice, and water vapor clouds from ice clouds. Combined with the two visible channels, it improves the observation of aerosols, soil moisture and vegetation indices. HRV channel serves nowcasting purposes, observations and applications regarding very short-term forecasting. WV6.2 and WV7.3 are used for the determination of water vapor distribution at two different atmospheric levels. Combined with higher wavelength channels, they also help to determine thin cloud temperature and wind speed in cloud free areas. IR3.8, IR8.7, IR10.8 and IR12.0 channels provide continuous cloud observation, along with cloud, land and sea surface temperature. IR3.8 band is used especially at night-time to detect fog and very low clouds. IR9.7 and IR13.4 are used to analyze air masses, and to help generating multispectral images, cloud movement vectors and surface parameters behavior. IR9.7 is also included in ozone absorption band, and is used for monitoring mainly tropopause characteristics and stratospheric winds in the high levels of the atmosphere. It also helps monitoring total ozone amount. Finally,

60

IR13.4 is situated in carbon dioxide absorption band, and its use is for cirrus discrimination, pressure estimation at cloud top, cloud monitoring and wind vertical component determination.

Errors in temperature retrieval for the five higher wavelength channels are defined at beginning and end of life conditions (Aminou *et al.*, 2003), and values of noise equivalent delta temperature (NEΔT) at a given source radiometric temperature for those SEVIRI channels are given in Table 2.3. Finally, the most technical aspects, relative to the format, georeferenciation, calibration in the different spectral regions, observation and solar angles of the SEVIRI images used in this work were realized using the MSG Shell software (Gieske, 2007).

Table 2.3.- SEVIRI Thermal channels associated errors at beginning and end of life conditions.

Channel	Band width	NEΔT (beginning of life conditions)	NEΔT (end of life conditions)
IR8.7	8.30-7.15	0.07K at 300K	0.28K at 300K
IR9.7	9.38-9.94	0.11K at 255K	1.50K at 255K
IR10.8	9.80-11.80	0.074K at 300K	0.25K at 300K
IR12.0	11.00-13.00	0.11K at 300K	0.37K at 300K
IR13.4	12.40-14.40	0.295K at 270K	1.80K at 270K

2.2.- AVHRR DATABASES

The following information has been extracted from the documentation available for the considered databases, which can be easily downloaded from the webpages of those databases.

2.2.1.- PAL

To obtain the Pathfinder AVHRR Land (PAL) archive, the scientific community had to reach a consensus on the algorithms which would be used: NASA (National Aeronautics and Space Administration) and NOAA united a team of investigators from universities and federal agencies to lead work groups on which products had to be processed, and which algorithms should be used to retrieve geophysical parameters. NOAA was in charge of providing AVHRR raw

data, while NASA did the processing, quality control, archiving and distribution of the produced dataset. The following procedures represent the recommendations of the Pathfinder AVHRR Land Science Working Group (LSWG).

This global dataset is of great utility for the monitoring of the vegetation, which allows the observation of the global change occurring at the surface level. The LSWG labeled as high priority the generation of global NDVI data. Some other surface parameters, like photosynthetic activity and surface temperature are also of great importance, but at that time some more investigation in these fields were needed to obtain reliable information at global scale for lengthy temporal series.

Pathfinder data aims at generating at a moderate resolution a regular process, widely recognized and validated algorithms, and the availability of a global product. Many scientific advances used in the production of Pathfinder data include atmospheric correction application, improvements in navigation and inter-satellite calibration.

2.2.1.1.- Product description

Basically, there are three PAL datasets:

• daily, with global coverage, containing land surface NDVI along with the distinct channels at a resolution of 8 km,

• NDVI 10-day composites, with global coverage at 8 km,

• NDVI 10-day composites, only for climate studies, with 0.1º, 0.5º or 1º spatial resolution.

8-km data are produced and archived globally and are transformed to an equal-area projection. A list of data levels included in daily and 10-day composite images is shown in Table 2.4. Along with these data, an auxiliary dataset is provided, which contains latitude, longitude, elevation and land/sea mask values for pixel centers (Table 2.5).

2.2.1.2.- General view of the process

Before starting with the processing of AVHRR data, level 1B NOAA GAC data have been acquired and transferred to be stored at the DAAC (Distributed Active Archive Center) within U.S. Geological Survey (USGS) Center for Earth Resources Observation and Science (EROS). The general view of the Pathfinder

processing chain is shown in Figure 2.8, the different steps taken following the recommendations agreed within the LSWG. In the next paragraph we describe briefly some selected aspects of Pathfinder process.

Table 2.4.- Data available in the Pathfinder AVHRR Land dataset.

Band	Description	Units	Valid range	Quantif.
1	NDVI	ndvi	-1 a 1	8 bit
2	Flag CLAVR*[+]	n/a		8 bit
3	Flag QC*[+]	n/a		8 bit
4	Scan Angle[+]	radians	-1.0472 +1.0472	16 bit
5	Zenithal Solar A.[+]	radians	0-1.3962 (0-90º)	16 bit
6	Relative Azimuth A.[+]	radians	0-6.2832 (0-360º)	16 bit
7	Ch1 Reflectivity	% reflectivity	0-100 %	16 bit
8	Ch2 Reflectivity	% reflectivity	0-100 %	16 bit
9	Ch3 Brightness Temp.[+]	degrees ºK	160-340 ºK	16 bit
10	Ch4 Brightness Temp.	degrees ºK	160-340 ºK	16 bit
11	Ch5 Brightness Temp.	degrees ºK	160-340 ºK	16 bit
12	Day of year[+]	DDD.HH	001.00-366.23	16 bit

* Numeric values which labels each pixel in function of cloud screening algorithms and quality control.

+ Data not available for global or continental images.

Table 2.5.- Auxiliary data provided with Pathfinder product.

Description	Units	Range	Quantif.
Latitude	degrees	-90 – 90	16 bit
Longitude	degrees	-180 – 180	16 bit
Elevation	meters	-15000 – 10000	16 bit
Sea/Land	--	0 – 2*	8 bit

(*) Land = 0, Sea = 1, Goode interrupted space = 2.
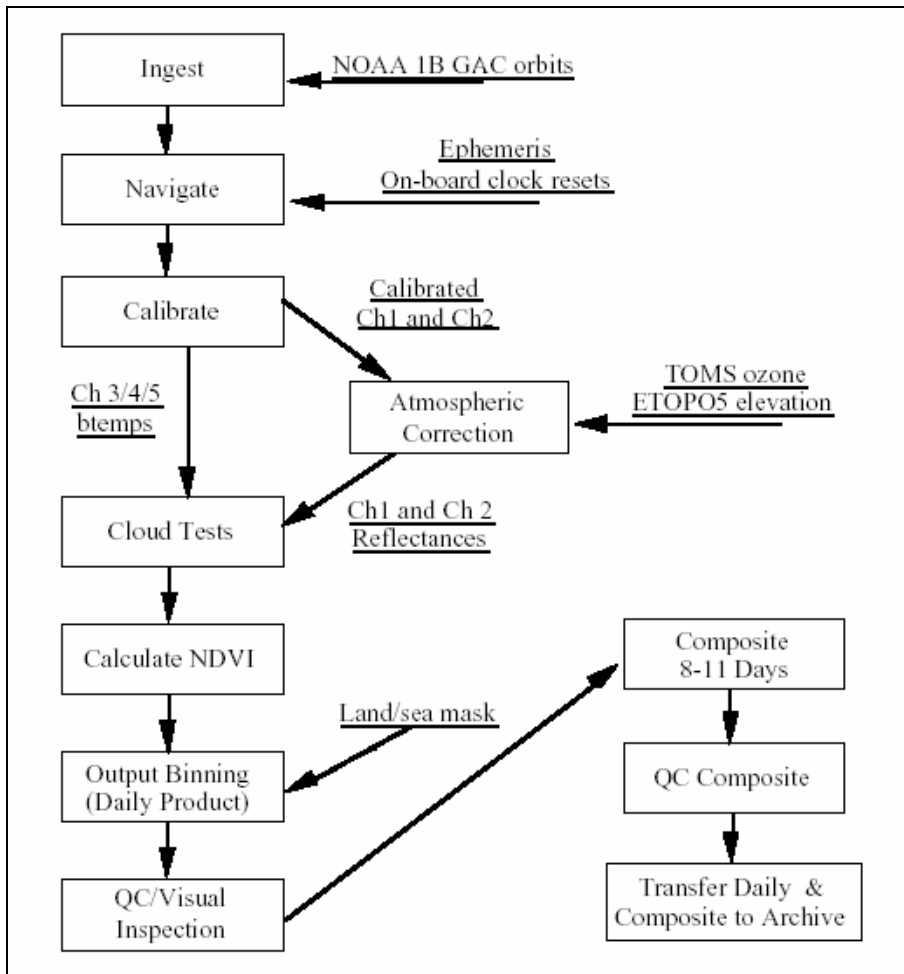
Figure 2.8.- Overview of Pathfinder Processing

Reading the archived data

GAC orbits are read and the information included in each header is carefully checked, the reading going on for the first 120 scan lines. The scan lines corresponding to descending orbits are omitted in the processing. Channel data and auxiliary GAC data (such as gain and offset) are uncompressed and archived in memory for processing. These auxiliary data, like surface elevation, ozone or land/sea mask are appended to processed data.

Navigation

Due to the volume for the more than 20 years of Pathfinder data, interactive navigation was considered as unsuitable, so autocorrelation advanced methods were implemented, increasing considerably the time of global data process. For various GAC pixels observed on NOAA provided land localization points, frequent errors were found in the GAC 1B dataset, so it was decided to consider data using an orbit model and actualized ephemerid. A precise navigation system, available from Colorado University, provides accurateness for the navigation of GAC pixels (Baldwin & Emery, 1993), and was adapted for Pathfinder process. An archive of temporal offsets (calculated by the on-board clock) was used to actualize the times for each scan line, and then solar and scan geometry were calculated for each pixel, and some localizations on land were revised. As a consequence, within Pathfinder processing scheme, the navigation system of Colorado University is used to propagate the ephemerid data, and the geo-localization algorithm developed at the NASA Goddard Space Flight Center (GSFC) is used for geo-localizing the scanned data (Patt & Gregg, 1994).

The Pathfinder processing team checks routinely the differences between the control points provided by NOAA and the calculated localizations, and found that the difference generally lies between 6 and 8 km in latitude and 0 to 4 km in longitude, the biggest differences being located in the outer part of the image.

Calibration

Channels 1 and 2 are calibrated using a time-dependent correction, which takes into account sensor degradation and satellite inter-calibration. Channels 4 and 5 are calibrated using a non-lineal function based on the internal calibration targets (ICT), on the variations of black body temperature (baseplate), instrument dependent response curves, and NOAA-provided gains and offsets. Channel 3 is calibrated using gains and offsets of GAC data record.

- calibration of visible and near-infrared

The key issue in Pathfinder process resides in the calibration between satellites. For visible and near-infrared channels, there is no on-board calibration and there are notable differences in sensor stability and precision of the three first satellites (NOAA 7, 9 and 11). To allow inter-calibration between visible and near infrared

for various satellites, several methods have been used, including calibration techniques which monitor time-invariant bright calibration targets (such as deserts, sun glint, high clouds) and through low flight plane missions.

For Channels 1 and 2, the calibration follows equation 2.1:

$$R = A \cdot \exp(B \cdot d) \cdot (C(10) - C(0)) \tag{2.1}$$

where R is the radiance (in $W \cdot m^{-2} \cdot \mu m^{-1} \cdot sr^{-1}$), d is the number of days since launch, $C(10)$ is the measured counts on the 10-bit scale, and A, B, $C(0)$ are parameters supplied by the NOAA/NASA Pathfinder Calibration Working Group (Rao, 1993b).

The offsets ($C(0)$) recommended by NOAA-NASA workgroup were retrieved from data obtained by low flight plane U2 in 1986 and 1988, and the gain values, related to A and B, are based on calibration slope determined using the Libyan south-east desert as a time-invariant target.

- calibration of thermal infrared

Channel 3 is converted to brightness temperature following procedures described in Kidwell (1991). Since channel 3 is not available at global scale from NOAA website, its calibration will not be discussed here.

Channels 4 and 5 are calibrated using coefficients and methods described in Rao (1993a). To this end, before calculating brightness temperatures, raw counts have to be converted to radiances, which have to be corrected from sensor non-linearity. First, the raw counts (C) are converted to radiances (N_{lin}) using a linear function (Eq. 2.2):

$$N_{lin} = G \cdot C + I \tag{2.2}$$

where the gain G corresponds to the slope value, and I is the intersection value that represents the ordinate at the origin.

The gain G is given by:

66

$$G = G_{1B}^{'} \cdot \left(\frac{N_{ICT} - N_S}{N_{ICT} - N_S^{'}}\right) \qquad (2.3)$$

where N_{ICT} is the internal calibration target radiance, N_S and $N_{S'}$ are the correction terms proposed to minimize the effect of temperature variations of the ICT, following Rao (1993a), and G'_{1B} is the specific gain for level 1B data.

The intersection value is given for each channel by an equation of the following form:

$$I = N_S - (G/G') \cdot N_S^{'} + (G/G') \cdot I' \qquad (2.4)$$

where I' is the intersection value specific to the level 1B data.

Once obtained the "linear" correspondence between radiance and digital counts, the true radiance is calculated taking into account the non-linear behavior of the sensor through a quadratic expression:

$$N_{true} = A \cdot (N_{lin}) + B \cdot (N_{lin})^2 + C \qquad (2.5)$$

where A, B and C coefficients can be obtained from Rao (1993a). The conversion to brightness temperature from radiance is done inverting the Planck radiation equation:

$$T(N_{true}) = \frac{C_2 \cdot \nu}{\ln(\frac{C_1 \cdot \nu}{N_{true}})} \qquad (2.6)$$

where T is the temperature (in K) corresponding to the radiance value Ntrue, ν is the channel central wavelength (cm^{-1}) and C1 and C2 are constants (C1 = 1.19104282 10^{-5}mW/($m^2 \cdot sr \cdot cm^{-4}$) and C2 = 1.4387752 cm·K).

For thermal channels (namely 3, 4 and 5), the onboard presence of a calibration target provides a continuous calibration; nevertheless, many post-launch studies have been carried out to reanalyze pre-flight calibration data, and to model a non-linear response of the detectors (Weinreb *et al.*, 1990).

Radiances in channels 3, 4 and 5 are calculated in units of mW·m^{-2}·sr^{-1}·cm.

Parameter retrieval

Reflectance for Channels 1 and 2 is derived as follows:

$$\text{Reflectance} = \frac{\textit{calibrated surface leaving radiance}}{\textit{calibrated incoming radiance}} \qquad (2.7)$$

Brightness temperatures for Channels 4 and 5 are derived as follows: the calibrated radiances are converted to brightness temperatures using Planck function. NOAA provides look-up tables for each satellite (Kidwell, 1991; Brown *et al.*, 1985; Weinreb *et al.*, 1990).

Atmospheric correction

Among all the atmospheric factors, four main ones affect AVHRR channels 1 and 2: water vapor, ozone, molecular dispersion (Rayleigh) and aerosols.

A Rayleigh correction is applied to the data, using a standard radiative transfer equation and methodology, which follows the work of Gordon *et al.* (1988), which takes into account ozone absorption (using ozone level measurements retrieved by Nimbus 7 Total Ozone Mapping Spectrometer – TOMS; see McPeters *et al.*, 1993) and land surface elevation (from ETOPO-5 dataset; see NGDC, 1993). Corrections including earth eccentricity and solar illumination are also applied.

On the other hand, H2O and aerosol effects are not corrected, due to the difficulty of finding auxiliary H2O and aerosol datasets corresponding to satellite overpass time, and to the lack of experience in applying these corrections globally. The LSWG recommended correcting Pathfinder dataset only from Rayleigh scattering and ozone absorption in channels 1 and 2. Anyway, the compositing technique (MVC, see Holben, 1986) lowers the influence of atmospheric effects, because of the selection of higher NDVI values (see Chapter 1), corresponding to better atmospheric conditions.

Binning/Mapping

Binning is the process by which the information of one pixel is assigned to another one, generally of different size and orientation. The pixel which will be filled with the information of one or more pixels of the original image is called the receiving bin or receiving pixel.

There are many complex issues involving definition of the output grid and methods for selecting pixels to populate the bin in the output grid. The methods used in the Pathfinder process for mapping, binning, and navigation were selected based on LWSG recommendations and processing throughput limitations. The Pathfinder daily and composite data are mapped to a Goode Interrupted Homolosine Projection at a resolution of 8 km (Steinwand, 1994), the global composite data being also available in equi-angular projection (lat/lon). The output resolution of the Pathfinder data was chosen to maintain highest possible resolution using data up to 42 degrees off nadir. The map projection chosen was based on analyses performed by the USGS, in support of the IGBP (International Geosphere-Biosphere Programme) Land Cover project, in which the Goode Interrupted Homolosine Projection was determined to provide the best global, equal area representation of the data while still allowing easy display and subsetting. Compatibility with the IGBP product map projection was also seen as a benefit to researchers.

Because the AVHRR scan data and the output 8 km grid are not affine surfaces and there are significant changes in scale, resolution, and orientation between the two data planes, the identification of output bins for each observed pixel must be based on the Earth location of the satellite pixel and the output bin. The method of determining into which output bin a satellite pixel is mapped is based on the "nearest neighbor, forward binning" approach. In this approach, the center latitude and longitude of each satellite pixel is used to determine into which output 8 km bin the satellite pixel maps. At nadir there may be as many as six pixels mapping to one output bin; however, the general case is four pixels per bin. In some cases around the equator no satellite pixel will be mapped to an output bin. This resultant Moiré pattern of null values has to be taken into consideration in image display and quantitative analysis.

In the case of the Pathfinder processing, forward binning was chosen primarily because of processing throughput considerations, due to the fact that no data gaps (holes) are present in data within 42 degrees off nadir, and, as Justice *et al.* (1989) processing algorithm description shows, the degradation of the data introduced by the onboard GAC sampling are as significant as the effects of forward or inverse binning. The Pathfinder processing simply copies the pixel to the east of a data gap to fill small data gaps (i.e., gaps of two or fewer pixels) in the daily data, and a

quality control flag is set for all of those values that were copied to fill data gaps. To maintain physical values derived from the satellite, no data smoothing or interpolation is performed. As a result, in areas of orbital overlap a checkered pattern is often formed due to cloud fronts moving in the 101 minutes between orbits or extreme bidirectional effects.

The remaining consideration in forward mapping is how to select which pixel values are retained in the output bin for the daily data. This occurs most frequently at high latitudes where there is daily orbital overlap, and at all latitudes near nadir where the input pixels are significantly smaller than the output bins. Following the reasoning that maximum NDVI pixels generally represent the pixels with the clearest atmosphere, the selection of the maximum NDVI pixel is being used in the Pathfinder processing.

Cloud mask

The cloud mask algorithm uses the five AVHRR channels (top of atmosphere reflectivity) and thresholds derived from data samples collected on a wide range of surfaces, including deserts and ice fields. All tests are realized on arrays of 2x2 pixels, and if all pixels of the array pass all the tests, they are labeled as cloud-free. The arrays are labeled as mix if one to three pixels do not pass the cloud tests, and cloud-contaminated if none of the four pixels pass the tests. Some of the tests are used to restore those pixels wrongly identified as clouds, since the CLAVR (Clouds from AVHRR – Stowe *et al.*, 1995) algorithm is very conservative in cloud-free pixel identification. One of the drawbacks of the CLAVR algorithm is that inhomogeneous areas, severe elevation changing areas and some riverbeds can be wrongly labeled as cloudy.

Quality control

During the whole automated process, validity checks are conducted to localize out of range or lost values. When serious errors occur, the corresponding pixels are excluded from the product, while less serious errors have to be flagged for each affected pixel. Finally, the images are visually checked by an operator, to detect obvious errors and correct them before compositing. Table 2.6 shows the different error flags.

Compositing

Pathfinder data are composed on a base of quasi 10-day periods. Within each month, the first 10 days correspond to the first composite, the following 10 days correspond to the second composite, and the remaining days (8 to 11 days) to the third and last composite. This compositing is done by selecting, for each pixel, the day corresponding to maximum NDVI value within the compositing period. This method, named Maximum Value Compositing (MVC), tends to minimize atmospheric effects of clouds and aerosols (Holben, 1986 – see Chapter 1). For the composition, only pixels with scanning angles lower than 42º are used, to avoid the influence of bidirectional effects.

Table 2.6.- Quality control flags.

Value	Description	Example
0	Normal	
1	No standard processing in Ch 1/2	Ozone values not available, so climate data were used
2	No standard processing in Ch 3/4/5	Calibration coefficients not available
4	Interpolated data	Fill value, result of forward transformation used for the binning
8	Error in range check	Calculated value out of range
16	NOAA QC flag set	Many of the conditions (reference) are not necessarily fatal, these pixels are indeed used in the process, but are labeled for reference

2.2.2.- GIMMS

The Global Inventory Modeling and Mapping Studies (GIMMS) dataset is a global measure of normalized difference vegetation index (NDVI - see Chapter 1) covering a 23-year period, from July 1981 through December 2003. The GIMMS dataset was originally generated to characterize biophysical change as defined in the International Satellite Land Surface Climatology Project (ISLSCP) Initiative II collection. NDVI is used in climate models and biogeochemical models to calculate photosynthesis, the exchange of CO_2 between atmosphere and land surface, land-surface evapo-transpiration and absorption and release of energy by land surface. The GIMMS dataset provides improved results based on corrections for calibration, view geometry, volcanic aerosols, and other effects not related to actual vegetation change.

At the moment of redaction of this dissertation, the only available data from GIMMS database is the normalized difference vegetation index over land areas, at global scale, except inland Greenland and Antarctica. As in Pathfinder dataset, NDVI values are composited (see Holben, 1986), this time with reference compositing periods of one month and 15 days: the first (named 15a) composite is the maximum value composite from the first 15 days of the month, and the second (named 15b) is from days 16 through the end of the month. For our applications, 15-day composites were used.

Here we present a general view of the procedure followed to construct the GIMMS database.

2.2.2.1.- Data acquisition

Input data for GIMMS Land data processing is NOAA AVHRR GAC 1B data. GAC 1B data were obtained from NOAA and from NCAR (National Center for Atmospheric Research) sources at the time of acquisition from 1985 to the present. This dataset was augmented with GAC 1B data available from NOAA's Satellite Active Archive. The GIMMS NDVI datasets were corrected using solar zenith angle (SZA) values from the AVHRR sensor for the period of 1981-2003 (Pinzon, 2002; Pinzon *et al.*, 2005; Tucker *et al.*, 2005).

Satellite data in NOAA level-1b format (Kidwell, 1998) were ingested from magnetic media, were forward mapped to the output bin closest to the center location of each 8 km equal area grid cell, respective calibration values were applied to each channel (Vermote & Kaufman, 1995), and the other values associated with maximum NDVI were retained for each compositing period. Data from seven AVHRR instruments on different satellite platforms were used in this dataset (Table 2.7).

Table 2.7.- Instrument change times for the GIMMS dataset.

AVHRR instrument	Start date	End date
NOAA-7	July 1, 1981	February 8, 1985
NOAA-9	February 11, 1985	November 7, 1988
NOAA-11	November 11, 1988	September 19, 1994
NOAA-9 (descending)	September 20, 1994	January 18, 1995
NOAA-14	January 19, 1995	October 31, 2000
NOAA-16	November 1, 2000	December 31, 2003
NOAA-17	January 1, 2004	continuing

2.2.2.2.- Navigation

A similar navigation procedure to El Saleous *et al.* (2000) was used, which in turn is based upon the work of Baldwin & Emery (1995). The orbital model predicts the position of the satellite at any time, using the satellite on-board clock and orbital elements to determine the predicted position. From this perspective, the sun-target-sensor geometry is determined. The NOAA satellites' velocity with respect to the earth's surface is roughly 7 km•s-1 and the output bin size employed is 8 km. This translates into a timing error of roughly one second to achieve navigation accuracy better than one pixel. The majority of navigation errors were due to errors of the on-board spacecraft clock.

Every composite image was manually checked for navigation accuracy by comparing the mapped data to a reference coastline for the continent in question. Images with more than one pixel navigation error were investigated and the day(s) of the navigation error identified. These days were reprocessed separately and manually registered to the reference data, to bring the badly navigated day(s) into agreement with the reference coastline, and the composite image was reconstructed by maximum value NDVI compositing (Holben, 1986). In a few cases it was necessary to discard data from specific days, as the navigation errors were impossible to adjust.

With the failure of NOAA-13 to achieve orbit in 1992, NOAA-11 continued to provide global afternoon/early morning AVHRR data. By 1994, the afternoon equatorial overpass time for NOAA-11 was around 17:00 hours. So the choice to use NOAA-9 descending node AVHRR data was made, in order to obtain global NDVI data set in September 1994, and these data were used until NOAA-14 became operational in late January 1995. This allows the filling of the gap in AVHRR data that exists in other databases (such as PAL).

2.2.2.3.- Radiometric calibration

Satellite determination of long-term surface trends requires precision within and among various space-borne instruments. It is also crucial to document the within- and among-sensor calibration uncertainty to determine the accuracy with which surface trends over time can be ascertained. The NDVI data were processed in two ways:

• NOAA-7 through NOAA-14 channel 1 and 2 data were processed using the Vermote and Kaufman (1995) channel 1 and channel 2 calibrations. The resulting NDVI fields were further adjusted using the desert calibration technique from Los (1998), then decomposed and reconstructed using empirical mode decomposition to correct for solar zenith angle effects (Pinzon, 2002)

• Data from NOAA-16 were processed using the pre-flight channel 1 and channel 2 calibration values and formed into maximum values composites. An empirical mode decomposition (EMD, see Chapter 3) and reconstruction was performed to insure a slope with respect to time of 0.00 in desert areas and was also used to correct solar zenith angle artifacts. This NOAA-16 NDVI time series was adjusted by a constant offset to match up with a coincident-in-time and spatially-aggregated 8-km SPOT (Satellite Pour l'Observation de la Terre) Vegetation NDVI time series, which had previously been adjusted to match up with the corresponding coincident-in-time NOAA-14 NDVI time series. Thus overlapping SPOT Vegetation NDVI time series were used as the means to inter-calibrate or tie together the NOAA-14 and NOAA-16 NDVI time series (Pinzon *et al.*, 2004). This was necessary because the bi-linear gain for channel 1 and channel 2 of NOAA-16's AVHRR instrument complicates ex post facto calibration. Thermal calibration coefficients after Weinreb *et al.* (1990) were used for the calibration of all thermal channels.

2.2.2.4.- Atmospheric correction and cloud screening

The choice was made to produce a maximum value NDVI composite data set, and associated layers, without any atmospheric correction, except during the El Chichon and Mt. Pinatubo volcanic stratospheric aerosol periods. A stratospheric aerosol correction was applied as proposed by Vermote *et al.* (1997) from April 1982 through December 1984 and from June 1991 through December 1994. A composite stratospheric aerosol optical depth fields was formed by combining the work of Sato *et al.* (1993), and Vermote *et al.* (1997). Rosen *et al.* (1994), Russell *et al.* (1993) and Dutton (1994) were used to compare specific optical depth measurements to the blended global fields.

Cloud screening was provided by a channel 5 thermal mask of 0º C for all continents except Africa, where a cloud mask of 10º C was used. In addition, the bimonthly composites significantly reduced cloud contamination.

2.2.2.5.- Satellite drift correction

The GIMMS group uses Empirical Mode Decomposition (EMD) to identify and remove parts of the NDVI signal that are most related to the satellite drift (Pinzon, 2002; Pinzon *et al.*, 2004). The EMD technique was introduced by Norden E. Huang in 1998 as an alternative to standard decomposition techniques for representation of nonlinear and non-stationary data that show clear physical scales or frequency content. Unlike Fourier decomposition (Wilks, 1995; Trefethen & Bau, 1997), the EMD creates a basis for the signal from the data itself. The EMD is empirical, intuitive, direct, a posteriori, and adaptive, with the decomposition functions based on and derived from the data (Huang *et al.*, 1998; Huang *et al.*, 1999). Pinzon *et al.* (2001) showed that EMD was applicable to NDVI time series from the AVHRR sensor to isolate orbital drift effects from the NDVI signal. Orbital drift results in later equatorial crossing times for the NOAA satellites and results in changes of illumination that affect the NDVI. An increasing trend is observed in each satellite due to its delay in the equatorial crossing time. This trend, superimposed on each plot, is more pronounced at lower latitude, whereas seasonal variations dominate at higher latitudes. Note that equatorial latitudes have an extra oscillation due to solar nadir moving past the target latitude, causing an increase in SZA at six month intervals rather than at yearly intervals (Privette *et al.*, 1995). The EMD is used to extract NDVI trends that may be caused by the satellite orbital drift, reducing the interference of other components in the NDVI signal. The EMD is used to isolate the components of the NDVI signal that are related to SZA trends and remove them from the corrected NDVI. The technique removes NDVI trends that are more than 80% correlated to the SZA trends. Areas with trends that have a lower correlation are not corrected. The areas where the correction is the strongest are the tropics (due to the SZA trend magnitudes), while the high northern latitude and regions with low vegetation biomes are less contaminated since the SZA component represents a small part of the NDVI signal. The correction is performed pixel-by-pixel. After the satellite drift correction, a krigging interpolation removes noise and attenuates the effects of cloudy and missing pixels.

2.2.2.6.- Inter-calibration of NDVI from all instruments using narrow-band instruments such as MODIS and SPOT-Vegetation

In order to include data from NOAA-16, an inter-calibration of the single-gain satellites NOAA-7 to -14 (historical data) and the dual-gain NOAA-16 was conducted, using overlapping data from SPOT-Vegetation global data at 1 km (Achard *et al.*, 1994). SPOT data were averaged from 1 km to 8 km globally and then decomposed using the EMD method. The inter-annual trend from three years of data, 20 months overlapping with NOAA-14 and the rest with NOAA-16, was extracted. This trend was determined to be invariant through time over the considered period. A similar trend was extracted from the same period of NOAA-14. A non-linear regression was performed to establish coefficients that transform the historical data into the same range as that of the current and upcoming suite of visible and NIR (Near Infra-Red) sensors, such as MODIS (MODerate resolution Imaging Spectroradiometer), SPOT-Vegetation, etc. A similar regression was performed for NOAA-16 data. Once trends from the historical and NOAA-16 data were transformed into the common range, data was reconstructed and a consistent time series was established.

2.2.2.7.- Errors

Some sources of error in the NDVI dataset are not accounted for with the GIMMS corrections. These errors are caused by soil background reflectance; this affects low NDVI values, but does not affect high NDVI values. Thus, similar low NDVI values may indicate different amounts of vegetation. However, the EMD noise removal diminishes it.

Earlier versions of the GIMMS-NDVI data have been used in various models and seem to capture well general patterns of vegetation. Tests on sites showed reasonable agreement of inter-annual variation in GIMMS NDVI and other measures of vegetation (Davenport & Nicholson, 1993; Malmstrom *et al.*, 1997; D'Arrigo *et al.*, 2000). These tests show that the variation in GIMMS NDVI is realistic on specific sites. Comparisons between climate signals and GIMMS NDVI show realistic patterns in many semi-arid regions and temperate regions. Recent independent research has verified the quality of the NDVI data. For example, Lotsch *et al.* (2003a), using the GIMMS NDVI and global standardized precipitation index (SPI) data, revealed geographically extensive patterns of joint

NDVI-SPI variability. Jia *et al.* (2003) analyzed the GIMMS NDVI data for three bio-climate sub-zones in northern Alaska and confirmed a long-term trend of increase in vegetation greenness for the Alaskan tundra that has been detected globally for the northern latitudes. There was a 16.9% (±5.6%) increase in peak vegetation greenness across the region that corresponded to simultaneous increases in temperatures. In the Amazon basin, a publication by Poveda & Salazar (2004) showed that at inter-annual timescales, the NDVI shows a reaction to both phases of ENSO. Dryness was seen due to El Niño, whereas NDVI spatial variability is enhanced during La Niña. Lotsch *et al.* (2003b) demonstrated that regarding seasonal GIMMS-NDVI anomalies for Africa, spatial independent component analysis (ICA) reveals coherent regions that capture high inter-annual variability in arid and semiarid areas of eastern and southern Africa that were associated with fluctuations in sea surface temperature anomalies (SSTA). When using other AVHRR datasets (in that case, PAL dataset) known to be contaminated with volcanic aerosols and sensor transition discontinuities, Lotsch *et al.* (2003b) needed to apply ICA correction to account for these artefacts. When using those other datasets, results must be treated with caution. Nemani *et al.* (2002) found a 6% increase in NPP (Net Primary Production) using the GIMMS NDVI in their primary production model corresponding with known changes in CO_2 concentrations. 42% of the increase was from tropical forests due to decreases in cloud cover. Their satellite-based estimates of NPP show significant growth stimulation in both the tropics and the northern high-latitude ecosystems. Assuming that carbon emissions, including those from biomass burning and land use changes, are properly accounted for in the atmospheric inversions, this spatial discrepancy means that respiration as well as NPP is a major driver of terrestrial carbon-sink dynamics.

As NDVI data are increasingly being used to assess inter-annual variations in the biosphere, one should distinguish between the following types of temporal analysis (see also Gutman *et al.*, 1995): seasonal analysis, for which NDVI data should have more than sufficient accuracy to assess seasonality of vegetation with great confidence – the one exception may be the small seasonal cycles observed in the Sahara, this seasonality is most likely caused by variations in atmospheric water vapor, not by variations in vegetation; inter-annual analysis, for which NDVI data have been used to look at year-to-year variations in desert margins (Tucker *et*

al., 1991) and at variations associated with climate oscillations (Myneni *et al.*, 1995) – the inter-annual signal in semi-arid regions and temperate regions is in general larger than the residual errors in the data; trend analysis which is generally the smallest inter-annual signal in the data, errors in the NDVI data are often as large or larger than the magnitude of trends, at this stage the magnitude of trends in NDVI data is uncertain within an order of magnitude.

2.2.2.8.- GIMMS additional data

As stated before, the GIMMS dataset available for download is limited to NDVI data. In order to develop an algorithm for orbital drift correction, additional data were needed (see Chapter 3). Molly E. Brown, from the GIMMS group, provided these additional data. These data have been corrected geometrically and composited bimonthly based on the final NDVI values (after the steps described in part 2.2.2.3 to 2.2.2.6) following the MVC method (Holben, 1986), although these additional data were not corrected for those effects, since these corrections are applied to NDVI values only. Thus, these additional data are raw parameters. The parameters provided are the following:

• DAY: composite day of year corresponding to the day of acquisition of the corresponding pixel for each composite image (from 0 to 364).

• RHO1: composite reflectance acquired by AVHRR channel 1 (visible – from 0 to 1).

• RHO2: composite reflectance acquired by AVHRR channel 2 (near infrared – from 0 to 1).

• T4: composite radiometric temperature acquired by AVHRR channel 4 (thermal infrared – from 160 to 340 K).

• T5: composite radiometric temperature acquired by AVHRR channel 5 (thermal infrared – from 160 to 340 K).

• TS: composite solar zenithal angle at the time of the acquisition (in degrees).

• TV: composite viewing angle at the time of the acquisition (from 0 to 42º).

These data cover the period November 2000 to December 2006, for all continents (Africa, North America, South America, Australia, and Eurasia).

2.3.- REANALYSIS DATABASE

The REANALYSIS project of the National Center for Environmental Prediction (NCEP) and the National Center for Atmospheric Prediction (NCAR) has provided the scientific community with a large amount of atmospheric data. Those two agencies collaborated initially to compile 41 years (1958-1998) of various global land and atmosphere climatic data, research oriented, using a global data assimilation system. This project was integrated in the numerous efforts to reanalyze historical data with a fixed assimilation system (see for example, Bengtsson & Shukla, 1988; Schubert *et al.*, 1993; Gibson *et al.*, 1997). The first aim of this project was to identify climatic anomalies (Higgins *et al.*, 1996). Estimated values linked to water cycle, such as precipitation, evaporation, water vapor flux convergence, etc, are particularly sensible to these changes.

NCEP/NCAR REANALYSIS system is based on the NCEP Medium Range Forecasting (MRF) spectral model (Kanamitsu, 1989) and on the NCEP Spectral Statistical Interpolation (SSI) model (Parrish & Derber, 1992). The global model used has a T-62 Gaussian grid (Kanamitsu *et al.*, 1991) with 192 longitudes by 94 latitudes (192 x 94 nodes), corresponding to an approximate horizontal resolution of 211 km along the Equator. The model also includes 28 atmosphere levels, of which 17 are actually available: 1000, 925, 850, 700, 600, 500, 400, 300, 250, 200, 100, 70, 50, 30, 20 and 10 hPa.

The databases are generated from a data assimilation system (Schubert *et al.*, 1993). This is the reason why these databases do not suffer from incoherencies introduced by changes in models or data assimilation procedures, unlike previous analyses of the ECMWF (European Centre for Medium-Range Weather Forecasts) and the National Meteorological Center (Sperber *et al.*, 1997). Physical and dynamical details of the model are described in the 1998 NOAA/NMC (National Meteorological Center) Development Division report (Kalnay & Jenne, 1991; Kanamitsu *et al.*, 1991).

There are 3 principle phases in REANALYSIS system:

• a first phase of data decoding and preprocessing, with a quality control process,

•   a second phase of data assimilation by the MRF model, with an automatic quality control system,

•   a last phase of reanalyzed product archiving in the WMO (World Meteorological Organization) Binary Universal Form for the Representation of meteorological data (BUFR).

Obtaining the retrieved data is one of the priorities of REANALYSIS project. On land, the first assimilated database in the model is the synoptic station red. Data from ocean surface are provided from COADS (Comprehensive Ocean-Atmosphere Data Set) files. Aeronautic, land and field campaign data are also available. Remotely sensed data allow completing the radiative parameters and altitude winds.

MRF model produces the first initial field by a forecast every 6 hour. For 0Z, 6Z, 12Z and 18Z hours, integrated data (in situ, plane, satellite,…) are compared with those of the initial field. The quality control (QC) system calculates the difference between entering data and first estimation values: if the differences are lower than given thresholds, the entering data are accepted, else, they are rejected. Thus, the assimilation system integrates the entering data to build the first estimation and produces an intermediary analysis for the GDAS (Global Data Assimilation and Forecast System) assimilation system (Kanamitsu, 1989).

From this first analysis, which builds by interpolation homogenized global fields close to reality, the model produces a forecast at six hour, and this forecast will serve as initial fields for the following six hours. The estimated field is created by a six hour forecast, and its quality depends indeed of the model accuracy and of the previous analysis quality (Mo *et al.*, 1995). When no data exist for a given site, as for example over austral oceans, the first initial field is used without any change. For example, let's consider a station "alpha", located in the South Atlantic Ocean, for which the sea level pressure is 990 hPa. If the quality control system considers that the value is too low and rejects the data, its value will be given by the forecast model at 6 hour. Thus, REANALYSIS atmospheric fields must be considered more as observation fields than as "outputs" of the climatologic model. Due to the integration of a great number of observations, REANALYSIS data are closer to the observed than the modeled climatology. The available parameters (around 60) are

placed on a regular 2.5º x 2.5º grid, for 17 pressure levels (from 1000 to 10 hPa) and every 6 hours.

The original dataset has been extended to the 1948-2007 period, and recent data are added every month. But all years do not have the same confidence level. Moreover, satellite observations were added in REANALYSIS for data posterior to 1978. Thus, one can separate three clear periods regarding the quality of the data, which have to be taken into account when using the data. REANALYSIS data span was initially from 1958 to 1998, to which data from 1948 to 1957 were added later, although those are less reliable, due to measurements less homogeneous during this decade. Moreover, stratospheric observations through radio sounding were scarce.

After 1978, satellite data (TIROS-NOAA) were added to climatic studies, improving observation quality and reliability, which make REANALYSIS a more trustable model. Camberlin *et al.* (2001), analyzing the accuracy of NCEP/NCAR to describe long-term climatic variations, sustain that after 1967-1968, a quality jump occurs as regards most used parameters, such as temperature, pressure, geopotential altitude, winds, etc., and for this reason recommend to not use data prior to 1968.

Each of REANALYSIS parameters is classified in 4 reliability classes, which show the influence of the observations over the physics of the model (Kalnay *et al.*, 1996; Kistler *et al.*, 2001). Those 4 classes are:

• class A: indicates that the analyzed parameter is strongly influenced by the observations. Altitude temperatures and winds fall among this category. Those parameters are generally well defined in the observations, and their assimilation allows for example a best estimation of atmosphere state than the observations. Class A is considered as the most reliable.

• class B: includes parameters which depend equally on observations and model, such as surface and 2m air temperature and humidity. Humidity rate in the atmosphere depends on the way convective processes are parameterized, thus is influenced by model climatology.

• class C: describes parameters which are not affected by the observations. This is due to the requisite of the model to assimilate values conform to atmosphere physics. Precipitation and surface fluxes fall among this category. However, if

those phenomenons are well parameterized, one can obtain a better estimation than those observed.

• class D: characterizes parameters which depend exclusively on the model, as for example geopotential surfaces.

This classification should not be used blindly, since it is only meant to help interpreting REANALYSIS data. The use of parameters classified as B or C do not mean that those values are far from reality.

For this work, only two parameters were used: air temperature at two meter height and precipitation, respectively corresponding to B and C classes.

Chapter 3

DATA PROCESSING

"A process cannot be understood by stopping it. Understanding must move with the flow of the process, must join it and flow with it."

Frank Herbert.

This chapter describes all the processing involved in this work. This processing has been carried out using IDL$^®$ (Interactive Data Language) software extensively. Data processing involves parameter estimation, cloud and snow masking, and orbital drift correction.

3.1.- Parameter estimation

Among the surface parameters that can be retrieved from AVHRR data (see Chapter 2), the ones better suited for vegetation monitoring have been selected for this work. Those are land surface temperature (LST), emissivity, normalized difference vegetation index (NDVI) and albedo. The first two parameters are retrieved following a method developed by Sobrino & Raissouni (2000), NDVI is retrieved as presented in Chapter 1, while albedo is estimated using Saunders (1990) method.

3.1.1.- Land surface temperature

Chapter 1 has showed how land surface temperature could be estimated from remote sensing using the split-window technique. The resulting equation is the following (Sobrino *et al.*, 1996):

$$LST = T_4 + A \cdot (T_4 - T_5) - B_0 + (1 - \varepsilon) \cdot B_1 - \Delta\varepsilon \cdot B_2 \qquad (3.1)$$

where T_4 and T_5 are brightness temperatures measured in AVHRR channels 4 and 5 respectively (see Chapter 2), $\varepsilon = (\varepsilon_4 + \varepsilon_5)/2$ and $\Delta\varepsilon = (\varepsilon_4 - \varepsilon_5)$ are, respectively, the average effective emissivity in both channels and the spectral variation of emissivity, and A, B_0, B_1 and B_2 are the split-window coefficients given by:

$$A = \frac{1 - \tau_4(\theta)}{\tau_4(\theta) - \tau_5(\theta)} \qquad (3.2)$$

$$B_0 = A \cdot \left[1 - \tau_5(\theta)\right] \cdot (T_{a4} - T_{a5}) \qquad (3.3)$$

$$B_1 = \frac{1 - \tau_4(\theta) \cdot \tau_4(53)}{\tau_4(\theta) - \tau_5(\theta)} \cdot (T_4 - T_5) + \tau_4(53) \cdot \frac{T_4}{4.667} \qquad (3.4)$$

$$B_2 = \tau_5(\theta) \cdot A \cdot B_1 \qquad (3.5)$$

T_{a4} and T_{a5} being the effective atmospheric temperatures in AVHRR channels 4 and 5 respectively, and $\tau_4(\theta)$, $\tau_5(\theta)$ and $\tau_4(53)$ the total atmospheric path transmittances in channels 4 and 5 respectively, at zenith angle θ and in the 53º view direction.

These split-window coefficients have been obtained through regression from *in situ* data in two regions of Australia (Prata, 1994), leading to an estimated error of the order of 1.3 K (Sobrino *et al.*, 1999).

Examples of LST estimates for the whole world at 6 month interval are shown in Figure 3.1. Those images have been calculated from PAL database (see Chapter 2).

3.1.2.- Emissivity

Following the method presented by Sobrino & Raissouni (2000), AVHRR NDVI images have been divided into three zones, according to each pixel value. Mean emissivities ε (average of the emissivities for channels 4 and 5 of the AVHRR) and spectral variations of emissivity Δε (emissivity difference between both channels) are estimated as presented below (all equations are taken from Sobrino & Raissouni, 2000). This method allows emissivity estimation with an error of 0.01 (Sobrino *et al.*, 1999).

3.1.2.1.- NDVI < 0.2:

The surface is then assumed to be bare soil, which emissivity is calculated from channel 1 reflectance (Ch1):

$$\varepsilon = 0.980 - 0.042 \cdot Ch1 \tag{3.6}$$

$$\Delta\varepsilon = -0.003 - 0.029 \cdot Ch1 \tag{3.7}$$

3.1.2.2.- 0.2 < NDVI < 0.5:

The surface is assumed to be a mix of bare soil and vegetation, which emissivity can be estimated from the proportion of vegetation Pv:

$$\varepsilon = 0.971 + 0.018 \cdot Pv \tag{3.8}$$

$$\Delta\varepsilon = 0.006 \cdot (1 - Pv) \tag{3.9}$$

where Pv is calculated from the NDVI itself (Carlson & Ripley, 1997):

$$Pv = \frac{(NDVI - 0.2)^2}{0.09} \tag{3.10}$$

3.1.2.3.- NDVI > 0.5:

The surface is assumed to be only vegetation, so the emissivity can be estimated as:

$$\varepsilon = 0.985 \qquad (3.11)$$

$$\Delta\varepsilon = 0 \qquad (3.12)$$

Examples of emissivity estimates for the whole world at 6 month interval are shown in Figure 3.2. Those images have been calculated from PAL database.

3.1.3.- NDVI

These data are provided directly in PAL database, since they are used to elaborate the 10-day composite images. NDVI is calculated using the reflectance at red (Ch1: 0.58 to 0.68 μm) and near-infrared (Ch2: 0.73 to 1.10 μm) wavelengths, as exposed in Chapter 1.

Examples of NDVI estimates for the whole world at 6 month interval are shown in Figure 3.3. Those images have been calculated from PAL database.

3.1.4.- Total atmospheric water vapor

To estimate the total amount of atmospheric water vapor, W, the split-window covariance-variance ratio (SWCVR) method has been used. This technique enables estimation of W from remotely sensed data only (Sobrino *et al.*, 1994). As regards NOAA-AVHRR data, W is estimated as follows:

$$W = 0.26 - 14.253 \cdot (\cos\theta \cdot \ln R_{54}) - 11.649 \cdot (\cos\theta \cdot \ln R_{54})^2 \qquad (3.13)$$

where θ is the satellite observation angle and R_{54} is the ratio of the spectral covariance and the variance of image brightness temperatures in the two AVHRR split-window channels 4 and 5 within boxes of N pixels. For our applications, N = 9 (3 x 3 pixels):

88

$$R_{54} = \frac{\sum\limits_{k=1}^{N}(T_{4k} - T_{4o}) \cdot (T_{5k} - T_{5o})}{\sum\limits_{k=1}^{N}(T_{4k} - T_{4o})^2} \qquad (3.14)$$

T_{4o} and T_{5o} are the mean brightness temperatures of the N pixels considered in each channel.

This method has been applied for validation to a large AVHRR dataset of the Iberian Peninsula with the corresponding radiosonde observations (Sobrino *et al.*, 1999). Its estimated error is 0.5 g·cm^{-2}. Examples of W estimates for the whole world at 6 month interval are shown in Figure 3.4. Those images have also been calculated from PAL database.
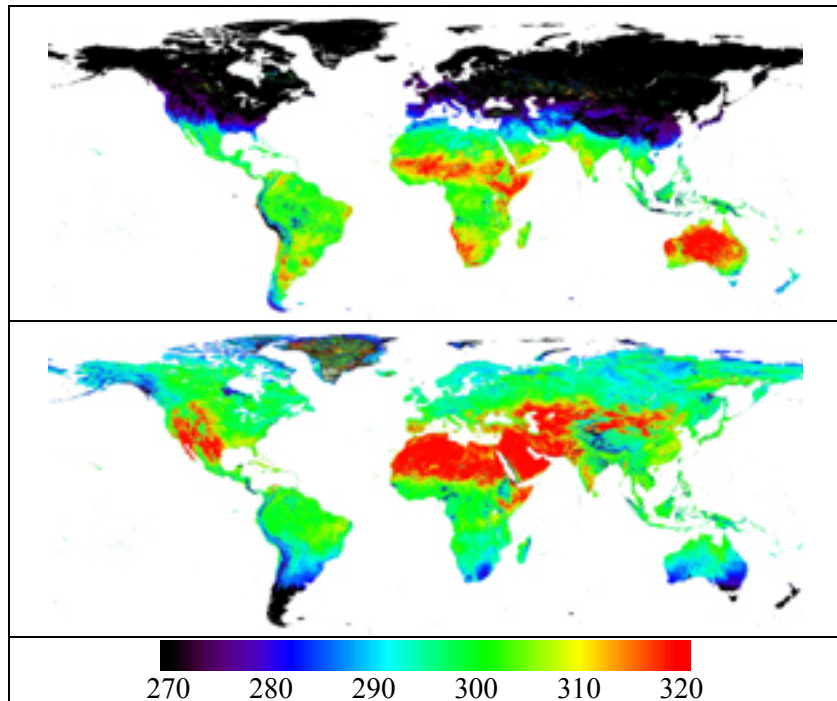
Figure 3.1.- LST images (in K) for January, 21st 2000 (up) and July, 21st 2000 (down). Black color corresponds to areas not retrieved by AVHRR since it was nighttime over those areas.

89
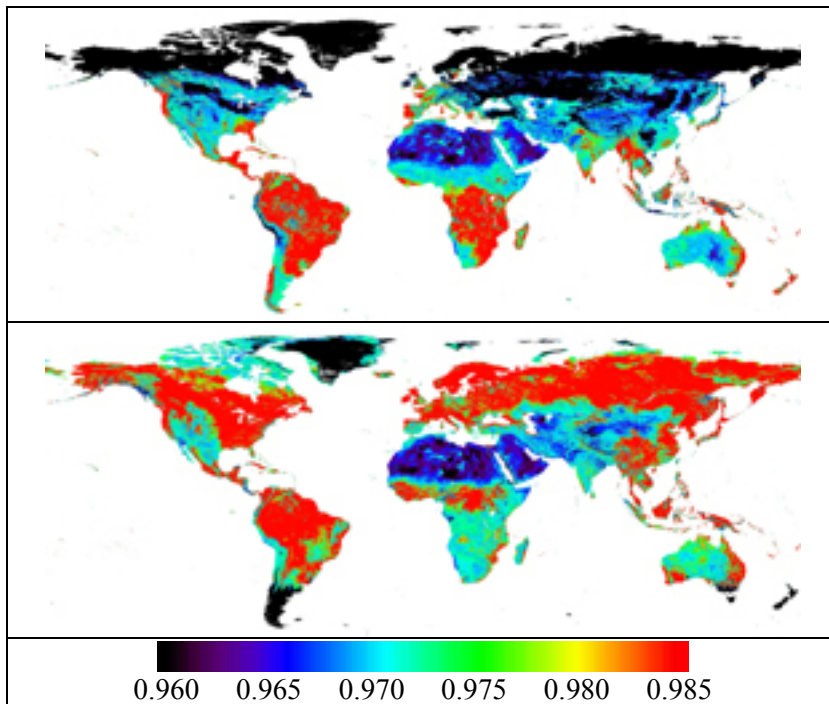
Figure 3.2.- Emissivity images for January, 21st 2000 (up) and July, 21st 2000 (down). Black color corresponds to areas not retrieved by AVHRR since it was nighttime over those areas.

3.1.5.- Albedo

Albedo (A) has been estimated using the formula developed by Saunders (1990), which is:

$$A = \omega_1 \cdot Ch1 + \omega_2 \cdot Ch2 \tag{3.15}$$

where ω_1 and ω_2 are factors which take into account the weight for each reflectance of the solar radiation quantity received by each channel. Those factors have been calculated by Saunders (1990) for channels 1 and 2 of NOAA obtaining a value of 0.5 for both factors. Examples of albedo estimates for the whole world at 6 month

interval are shown in Figure 3.5. Those images have also been calculated from PAL database.
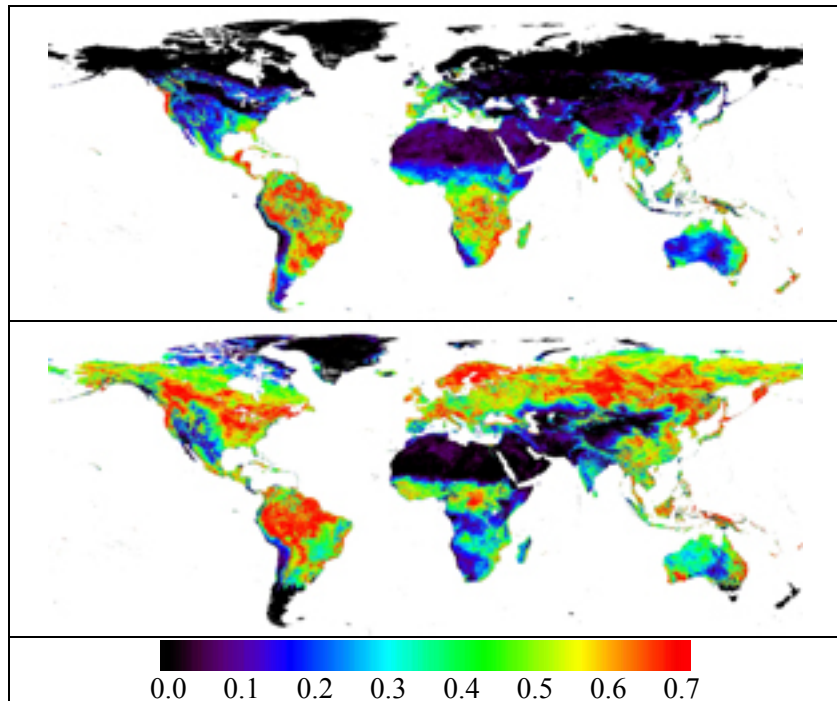
Figure 3.3.- NDVI images for January, 21st 2000 (up) and July, 21st 2000 (down). Black color corresponds to areas not retrieved by AVHRR since it was nighttime over those areas.

3.2.- Cloud and snow masks

Two approaches have been used in this work to deal with snow or cloud presence in the data, depending on the available parameters. The first method is an instantaneous pixel-by-pixel approach based on the method developed by Saunders & Kriebel (1988). The second method is based on a statistical analysis of temporal profile of the various parameters.
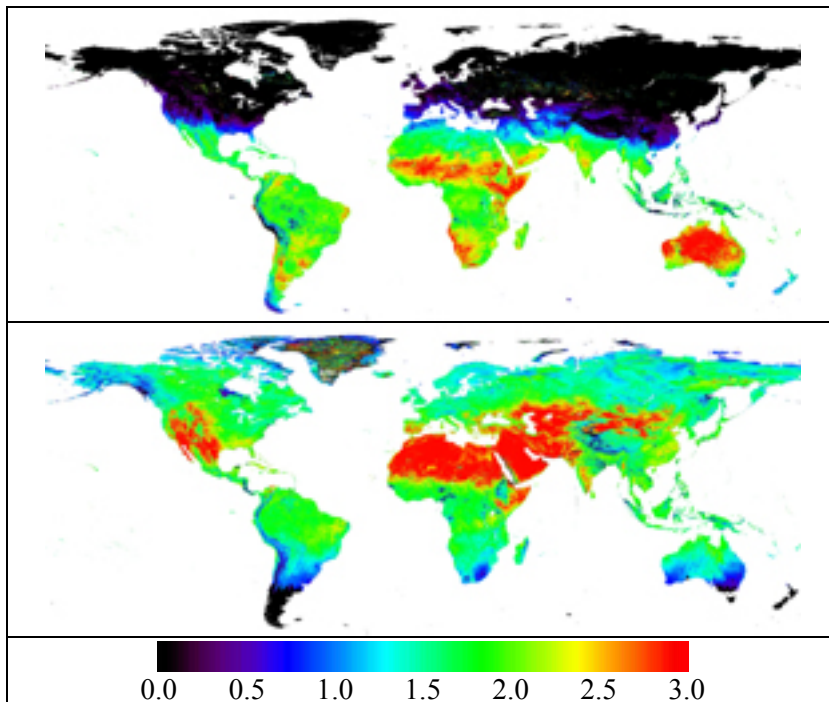
Figure 3.4.- Water vapor total amount images (in g·cm^{-2}) for January, 21st 2000 (up) and July, 21st 2000 (down). Black color corresponds to areas not retrieved by AVHRR since it was nighttime over those areas.

3.2.1.- Instantaneous approach

Saunders & Kriebel (1988) developed a series of 5 tests for cloud detection from AVHRR data. Those 5 tests require nighttime and daytime images of channels 1, 2, 3, 4 and 5. As detailed in Chapter 2, the data used in this work include neither nighttime images nor channel 3 data. Thus, from the 5 tests described by Saunders *et al.* (1988), only 3 tests are applicable.

3.2.1.1.- Dynamic reflectance threshold test

In a general manner, clouds have a higher reflectance than land or sea surface, as shows Figure 3.6a. This means that over land and sea, a cloud-free reflectance peak can be identified in the histogram of the image, allowing a threshold to be set at a slightly higher reflectance. Thus, all pixels with reflectances above this threshold are considered as cloud contaminated. Identifying a cloud-free

reflectance peak and then setting a threshold value removes uncertainties due to variation in calibration and changes in surface reflectance with solar zenith/azimuth angles. Over land, channel 1 reflectances are used since the reflectance in channel 1 is much less than in channel 2, which increases the contrast between land and cloud (Saunders, 1986).
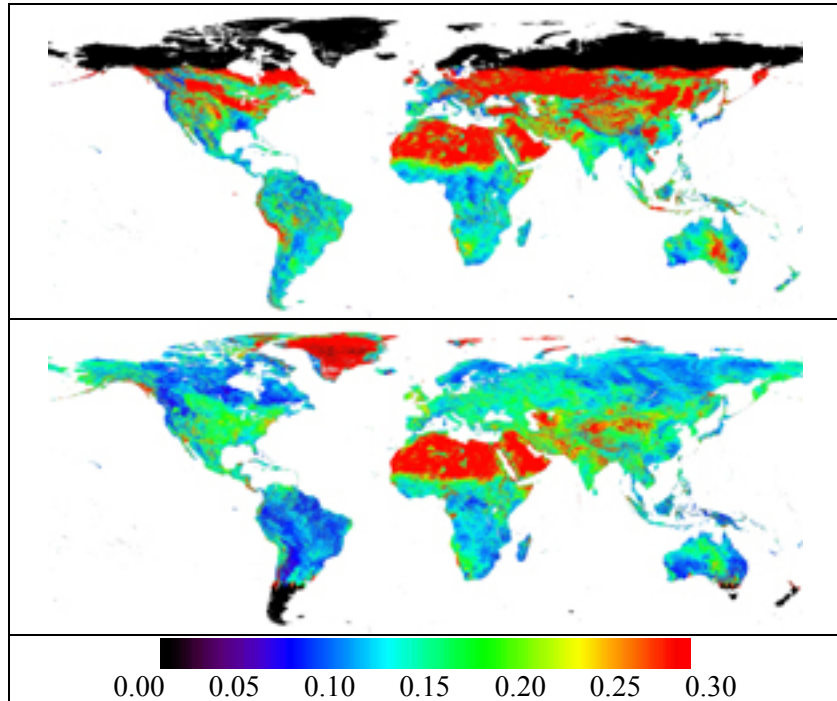
Figure 3.5.- Albedo images for January, 21st 2000 (up) and July, 21st 2000 (down). Black color corresponds to areas not retrieved by AVHRR since it was nighttime over those areas.

3.2.1.2.- Reflectance ratio test

This test makes use of the ratio of near-infrared bidirectional reflectances (AVHRR channel 2) to visible bi-directional reflectances (AVHRR channel 1). This ratio test can be simplified to the following expression (Saunders & Kriebel, 1988):

$$Q = \frac{Ch2}{Ch1} \qquad (3.16)$$

This ratio is close to unity over clouds (Figure 3.6b), while over water this ratio is close to 0.5. Over land, Q is greater than unity for all cases (vegetation, desert) except for snow and ice, even if there is often no well-defined peak due to the large variability of this ratio over land. Thus, a default threshold of 1.6 is set, while all pixels with a lower value of Q are assumed to be cloud-contaminated (Saunders & Kriebel, 1988).

3.2.1.3.- Radiometric temperature difference test

This final test examines the difference between the 11 μm (AVHRR channel 4) and 12 μm (AVHRR channel 5) brightness temperatures. This difference tends to increase in presence of clouds, due to differences in transmittance between those wavelengths. Thus, threshold values have been estimated for this difference, above which the pixels are considered as cloud-contaminated. Table 3.1 shows those threshold values for mid-latitudes (Saunders & Kriebel, 1988).

Table 3.1.- Temperature thresholds T_{diff} for the Ch4 – Ch5 cloud detection test at mid-latitudes (adapted from Saunders & Kriebel, 1988, table 1).

T_{11} (in K)	260	270	280	290	300	310
T_{diff} (in K)	0.55	0.58	1.30	3.06	5.77	9.41
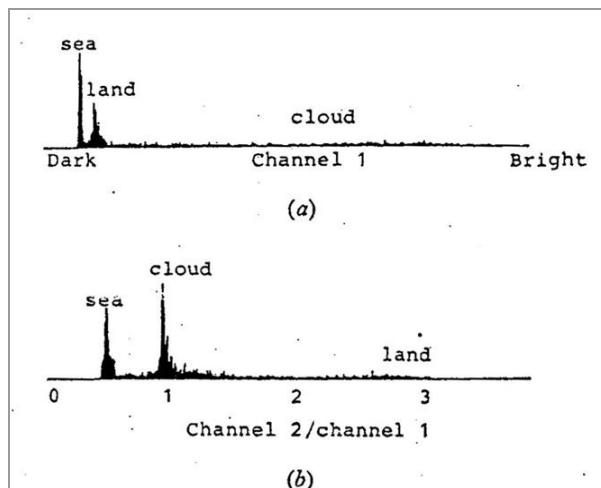
Figure 3.6.- Histograms of NOAA-9 AVHRR data for 15 April 1985 over the United Kingdom, containing clouds, cloud-free land and ocean. (a) Channel 1 reflectance; (b) channel 2 / channel 1 reflectance ratio histogram (adapted from Saunders & Kriebel, 1988, figure 1).

94

3.2.1.4.- Additional cloud test

Cloud tests 1 and 2 tend to overestimate cloud contamination, so we decided to condition those tests to an additional one, which only considers as possibly cloud-contaminated the pixels for which LST value is below 280 K. This allows the distinction between high reflectance areas (deserts) and clouds.

3.2.1.5.- Snow and ice mask

Snow is characterized by high reflectance values and low temperatures, so pixels with channel 1 values higher than 0.3 and LST values lower than 272 K are considered as snow. This approach is indeed quite similar to the dynamic reflectance threshold test, which means that snow covered pixel can be considered as clouds and reciprocally. Usually, channel 3 information is used to discriminate clouds from ice, but is unfortunately not available from PAL database (see Chapter 2). However, snow, ice and clouds are considered as noisy data for our study, which makes their discrimination pointless.

3.2.2.- Temporal profile analysis

As shown in Chapter 1, NDVI values tend to be diminished by cloud or snow presence, to reach negative values when the whole pixel is filled by cloud or snow. Thus, since NDVI values over land are positive, an easy way to screen out snow and cloud filled pixels is to set a positive threshold to NDVI values. Another approach is to monitor each pixel NDVI temporal profile, and consider the corresponding pixel as snow- or cloud-contaminated for dates showing punctual decreases in NDVI. This is the approach carried out by HANTS software for example, which is described in Chapter 4.

One can also consider the temporal series from a statistical point of view, in spite of analyzing its temporal coherence. This approach is quite simple, and relies on the estimation of average and standard deviation values. A histogram of the time series values is then computed, centered on the average value, and with bins of one standard deviation. If no outlier is present in the data, then all bins will be filled with a few values. If outliers are present, then they will be located at the far ends of the histogram, with empty intermediate bins. Then the time series can be cleaned by removing the dates corresponding to those outliers. This method relies on the assumption that the temporal series have been correctly georeferenced, in order to

be sure that each pixel describes the same scene through time. Another implicit assumption of this method is that the area is generally observed in cloud- and snow-free conditions. Thus, any cloud or snow contamination, as well as any abnormal value, would stand out of the usual range of values taken by a given parameter. Of course, this method will give good results only in cases of clear difference between contaminated and clear values. This is the case of radiometric temperatures for example.

3.3.- Orbital drift correction

As described in Chapter 1, LST retrieval from NOAA-AVHRR data is hindered by each platform's orbital drift. Only a few methods have been designed to correct this orbital drift. These methods are described quickly, to move on to the description of the method we implemented and its validation.

3.3.1.- Background

To our knowledge, only five methods have been developed for AVHRR orbital drift correction. Four of them (Gutman, 1999; Jin & Treadon, 2003; Pinheiro *et al.*, 2004; Pinzon *et al.*, 2005) rely on the knowledge of solar zenithal angle (SZA) data at the time of the acquisition, which are directly correlated to the orbital drift. The other method (Bacour *et al.*; 2006) is based on the estimation of the directional reflectances from POLDER data (POLarisation and Directionality of the Earth's Reflectance). Since this method has been applied to correct only AVHRR channels 1 (red) and 2 (infrared), and needs a considerable amount of additional data, it is not discussed here.

Gutman (1999) describes an orbital drift correction method based on solar zenithal angle (SZA) data. The methodology relies on the previous calculations of temperature and SZA time series anomalies. To this end, the time series are averaged over each compositing period, obtaining an average year of data corresponding to the shape of their yearly cycle. The anomalies are obtained by simple difference between the time series and its corresponding average year. Those anomalies are then averaged over homogeneous vegetation classes. A simple linear regression is then conducted between temperature and SZA cosine averaged

anomalies (Eq. 3.17), which coefficients allow to remove the part of temperature anomalies which can be explained by SZA anomalies:

$$\Delta T = a + b \cdot \cos(\Delta SZA) \qquad (3.17)$$

where ΔT and ΔSZA correspond respectively the temperature and SZA anomalies, and a, b are the regression coefficients.

Applying this method allows to decrease the variability within the temperature time series. Gutman (1999) designed this method for radiometric temperatures (AVHRR channel 4), but it can be equally applied to land surface temperature. However, this method relies on a previous classification of the study area in homogeneous vegetation types, which make its application useless in our case, since our goal is precisely to determine changes in land cover.

Jin & Treadon (2003) method relies on modeling land surface temperature daily cycle. To this end, land skin temperatures are retrieved from the National Center for Atmospheric Research (NCAR) Climate Community Model (CCM3), and coupled with the land surface model Biosphere-Atmosphere Transfer Scheme (BATS). Thus, a daily cycle is obtained, from which the difference of temperature between the nominal and actual overpass times can be estimated, and then added to the data for the corresponding date. Those daily cycles have been computed for 18 land covers (crop/mixed farming, short grass, evergreen needleleaf tree, deciduous needleleaf tree, deciduous broadleaf tree, evergreen broadleaf tree, tall grass, desert, tundra, irrigated crop, semi-desert, ice cap/glacier, bog or marsh, evergreen shrub, deciduous shrub, mixed woodland), for all 4 seasons (January-March, April-June, July-September and October-December), and for latitude bands of 5°. This means that this method also cannot be used in our case, due to the needed a priori information regarding land cover. We have nevertheless implemented this method to correct PAL's orbital drift (see Chapter 2), and obtained unsatisfactory results, due mainly to the 5° latitude band correction, which transforms temporal discontinuities in land surface temperatures into spatial discontinuities at latitude band transitions.

Pinheiro *et al.* (2004) have developed a model based on vegetation structural data and geometric optics, which allow the estimation of the fraction of sunlit and shaded endmembers observed by AVHRR for each pixel of each overpass. The

97

available endmembers are the following: sunlit tree crown, shaded crown, sunlit background and shaded background. In spite of the small number of available endmembers, this approach evidences the correlation between LST variability and sun/target/sensor geometry. This approach has been used to build a daily record of NOAA-14 AVHRR land surface temperature over Africa (Pinheiro *et al.*, 2006). However, due to the needed *a priori* knowledge of the land cover, to the model complexity and the computing time needed to process global data for more than 20 years, this approach was also discarded.

Pinzon *et al.* (2005) used an approach based on the Empirical Mode Decomposition (EMD) to correct NDVI data only. This decomposition is empirical, intuitive, direct, *a posteriori* and adaptive, with the basis functions based on, and derived from the data. The decomposition uses the simple assumption that any data consists of different simple intrinsic modes of oscillations. Each mode may or may not be linear, and will have the same number of extrema and zero-crossings. Furthermore, the oscillation will also be symmetric with respect to the "local mean". At any given time, the data X(t) may have many different coexisting modes of oscillation, each one superimposed on the others. The result of combining these modes is the final complicated data. In the EMD, each of these oscillatory modes is represented by an intrinsic mode function (IMF) with the following definitions: (a) in the whole data set, the number of extrema and the number of zero-crossings must either be equal or differ at most by one, and (b) at any point, the mean value defined by the envelopes of local maxima and local minima is zero.

With this definition, one can decompose any function or data as follows: derive the "local mean" m_1 by computing the mean between the upper envelope and lower envelope of the signal. The upper (lower) envelope is found by connecting all the local maxima (minima) by a cubic spline line. The difference, $h_1 = X(t) - m_1$, ideally should be an IMF, for the construction of h_1 described above should satisfy all the requirements of an IMF. However, even if the fitting is perfect, a gentle hump on a slope can be amplified to become a local extremum and a new iteration over h_1 will be needed.

While the first condition is absolutely necessary for separating the intrinsic modes and for defining a meaningful instantaneous frequency, the second condition is also necessary in case the neighboring wave amplitudes have too large a disparity. In this way, one can actually recover the proper modes lost in an initial

examination. Huang *et al.* (1998) named this process sifting. In fact, the sifting process can recover signals representing low amplitude riding waves by iteration. The sifting process serves two purposes: to eliminate riding waves, and to make the wave profiles more symmetric. Toward these ends, the sifting process has to be repeated as many times as is required to reduce the extracted signal to an IMF. In the subsequent sifting process, h_1 is treated as the data, then $h_1 - m_{11} = h_{11}$. After repeated sifting, up to k times, h_{1k} becomes an IMF, $h_{1(k-1)} - m_{1k} = h_{1k}$; then, the first IMF component from the data is designated as $c_1 = h_{1k}$.

Overall, c_1 should contain the finest scale or the shortest period component of the signal. We can separate c1 from the rest of the data by

$$X(t) - c_1 = r_1 \tag{3.18}$$

Since the residue r_1 may still contain longer period components, it is treated as the new data and subjected to the same sifting process as described above. This procedure can be repeated to all the subsequent r_j 's, and the result is

$$r_1 - c_2 = r_2,...,r_{n-1} - c_n = r_n \tag{3.19}$$

The sifting process can be stopped by any of the following predetermined criteria: either when the component c_n or the residue r_n becomes so small that it is less than the predetermined value of substantial consequence, or when the residue r_n becomes a monotonic function from which no more IMF can be extracted. Even for data with zero mean, the final residue still can be different from zero. If the data have a trend, the final residue should be that trend. By summing up Equations (3.18) and (3.19), we finally obtain

$$X(t) = \sum_{j=1}^{n} c_j + r_n \tag{Eq. 3.20}$$

Thus, we achieve a decomposition of the data into n-implicit modes, with a residue r_n, which can be either the mean trend or a constant. The trends are obtained from the last IMFs of the EMD approach. In this application of the EMD, the SZA and NDVI signals are overextended at the boundaries with seasonal profiles with no trends to reduce known boundary problems in the EMD decomposition that might also affect the correction. Then, cross-correlations of the

modes obtained from NDVI and SZA are estimated, and the NDVI modes showing significant correlation (>0.8) with SZA modes are removed from the NDVI time series.

This method has been proved efficient to remove SZA effect from NDVI. However, when we applied this method to LST retrieved from a subset of PAL data, the correlated modes between LST and SZA were multiple, and the removal of those LST modes from the time series led to aberrant time series, losing their seasonal coherence. Moreover, the correction of the whole database would have needed considerable computing time.

Taking all these aspects into account, we decided to implement our own correction to the data, which had to be simple, automated, and independent of *a priori* knowledge of land cover.

3.3.2.- Methodology

The method we have developed is based on the previous determination of solar zenithal angle (SZA) at solar time of nominal overpass (13:30), used as reference to calculate SZA anomaly, to which parameter temporal anomalies are fitted, and then removed from each time series to obtain orbital drift corrected parameter time series. This method has been elaborated in several steps, all presented in international congresses (Julien & Sobrino, 2006; Julien *et al.*, 2007), and has been submitted to IEEE Transactions on Geoscience and Remote Sensing for publication.

3.3.2.1.- Theoretical SZA determination

This first step is based on geometrical astronomy (Iqbal, 1983), and leads to the estimation of theoretical SZA at 13:30 (solar time) overpass at a given latitude for a given day. To this end, we first have to calculate the day angle (Γ, in radians) for a given day of the year (d_n, ranging from 1 on January, 1st to 365 on December, 31st), following Iqbal (1983):

$$\Gamma = 2 \cdot \pi \cdot \frac{(d_n - 1)}{365} \tag{3.21}$$

This day angle information corresponds to the position of the Earth on its orbit around the Sun. Then, we have to estimate solar declination δ (Iqbal, 1983):

$$\delta = (0.006918 - 0.399912 \cdot \cos\Gamma + 0.070257 \cdot \sin\Gamma$$
$$- 006758 \cdot \cos 2\Gamma + 0.000907 \cdot \sin 2\Gamma - 0.002697 \cdot \cos 3\Gamma \qquad (3.22)$$
$$+ 0.00148 \cdot \sin 3\Gamma) \cdot 180/\pi$$

Solar declination is the angular position of the Sun at solar noon with respect to the plane of equator, north positive. It has a value of 0 at vernal and autumnal equinoxes, about +23.5º at summer solstice, and about -23.5º at winter solstice (winter and summer refer here to northern hemisphere seasons). Next, we need to estimate the hour angle ω, which is the angle measured at the celestial pole between the observer's meridian and the solar meridian, noon zero and morning positive, changing 15º per hour (Iqbal, 1983). Thus, for our application, at 13:30, ω value is -22.5º. Finally, SZA (θ_z), defined as the angle between the local zenith and the line joining the observer and the Sun, can be estimated (Iqbal, 1983):

$$\theta_z = \cos^{-1}(\sin\delta \cdot \sin\Phi + \cos\delta \cdot \cos\Phi \cdot \cos\omega) \qquad (3.23)$$

where Φ is the geographic latitude, in degrees, north positive, all other angles having been introduced before, and are shown in Figure 3.7.

Equations 3.17 to 3.19 are used to determine nominal SZA (defined as SZA at 13:30 solar time overpass) for all pixels of the image for the whole time series. To this end, day of acquisition (DAY) and latitude information are necessary. Thus, the data described as additional GIMMS data in Chapter 2 have been used.

3.3.2.2.- Anomaly calculations

Anomalies are defined as the difference between temporal series and a reference time series. In the case of SZA, the reference time series refers to the time series obtained by the method described above. In the case of parameters (channels 1, 2, 4 or 5), the reference time series chosen is an average year of the given parameter. Average years are calculated for each parameter (Chi) as follows: we group each parameter data by compositing period (1-15 January; 16-31 January; 1-15 February; …), over which all available years are averaged. Thus, 24 average parameter images are obtained, describing the average behavior of this given

parameter over the available period, giving a reference as for parameter anomaly calculations. However, before anomaly calculation, parameter and actual SZA time series are screened out for outliers, using the method described in §3.2.2.
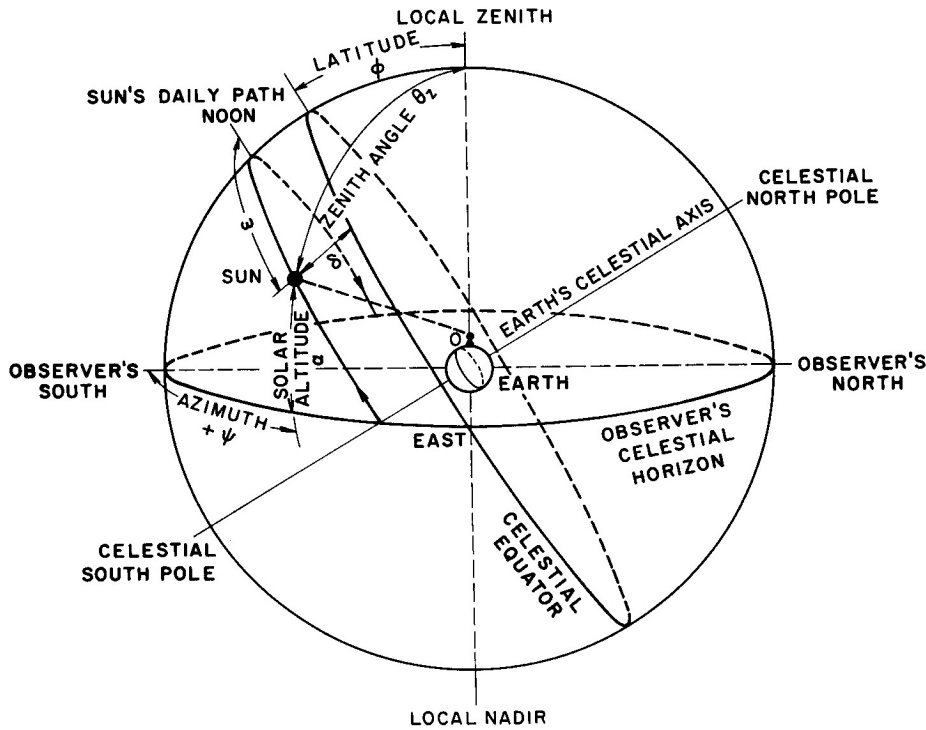
Figure 3.7.- Celestial sphere and Sun's coordinates relative to observer on Earth at point O (adapted from Iqbal, 1983).

3.3.2.3.- Fitting procedure

In order to remove SZA anomaly influence on parameter (Chi, i = 1, 2, 4 or 5) anomaly (Chi$_{an}$), an iterative procedure has been developed. This procedure consists first in a linear regression between parameter anomaly and SZA anomaly (SZA$_{an}$):

$$Chi_{an} = a + b \cdot SZA_{an} \qquad (3.24)$$

If this linear regression is statistically significant at 95% confidence level, then a new parameter time series (Chi^1) is calculated from the uncorrected one (Chi^0):

102

$$Chi^1 = Chi^0 - (a + b \cdot SZA_{an}) \qquad\qquad (3.25)$$

Then, new parameter anomalies are calculated from Chi^1, and a new linear regression is carried out from the same SZA anomalies. This iterative procedure finishes when the difference in the whole time series standard deviation between two iterations gets under a given threshold, fixed at 0.0001 for channel 1 and 2 reflectances, and 0.01K for channel 4 and 5 radiometric temperatures.

3.3.2.4.- Limitations

This method for NOAA orbital drift correction does not take into account the effects of other factors than SZA in image acquisition, meaning that the atmospheric absorption is still present in the data (see Chapter 2 for GIMMS additional data description). The approach presented here assumes that atmospheric absorption and SZA influence are decorrelated, which is only partially true. This means that for an adequate dataset correction, this approach should be applied to atmospherically corrected time series. Nevertheless, this does not affect the validity of the approach.

Another limitation of this method is the availability of various years of data from the same satellite platform, since the anomalies have to be estimated from a sufficiently long period of time to have statistical meaning.

3.3.3.- Results

NDVI and land surface temperature (LST) have been estimated following the method described in §3.1. An NDVI based classification has been calculated from corrected NDVI time series (Figure 3.8), following the methodology presented in Morales *et al.* (2004), Julien *et al.* (2005a; 2005b) and Sobrino *et al.* (2006a). This classification is based on annual average NDVI value (MN) and its variation coefficient (VC, defined as the standard deviation divided by MN), and includes 10 classes, defined as follow: 0 – Sea; 1 – (MN<0.2 & VC<0.33; 2 – MN<0.2 & 0.33≤VC<0.66; 3 – MN<0.2 & 0.66<VC; 4 – 0.2≤MN<0.5 & VC<0.33; 5 – 0.2≤MN<0.5 & 0.33≤VC<0.66; 6 – 0.2≤MN<0.5 & 0.66<VC; 7 – 0.5≤MN & 0.66<VC; 8 – 0.5≤MN & 0.33≤VC<0.66; and 9 – 0.5≤MN & VC<0.33.. This classification divides the arid areas in 3 classes (1, 2 and 3), and the vegetated areas in the remaining 6 classes. Classes 7 and 8 are absent of the image, due to the very

small amount of pixels attributed to these classes (respectively 0 and 76 pixels). The aim of the use of this classification is to average the corrected and uncorrected parameters over homogeneous classes, in order to observe the effects of the correction over extended areas.

Differences between corrected and uncorrected NDVI and LST have been averaged over classes containing a significant number of pixels (greater than 100 pixels) – all classes except classes 7 and 8. These differences are presented in Figure 3.9.
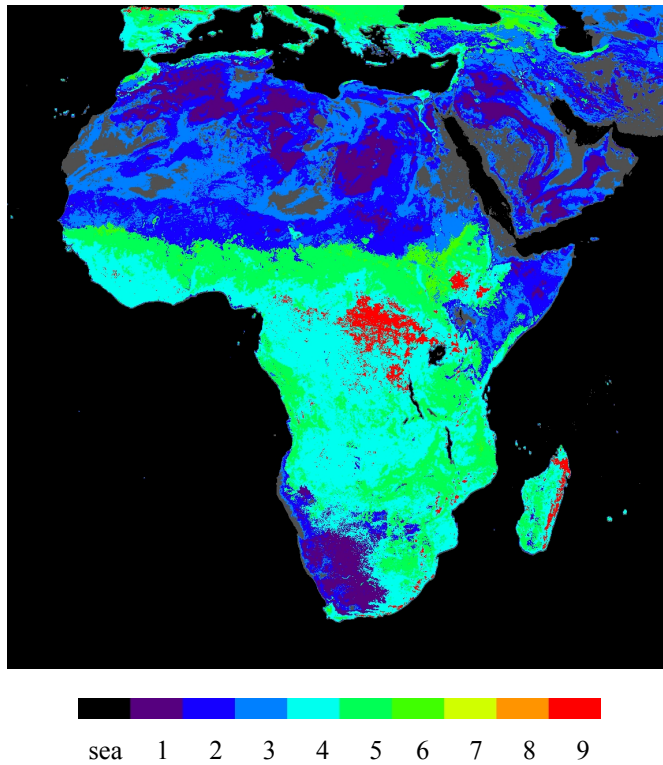
Figure 3.8.- Classification of the African continent vegetation. Dark grey areas correspond to areas with insufficient NDVI data.
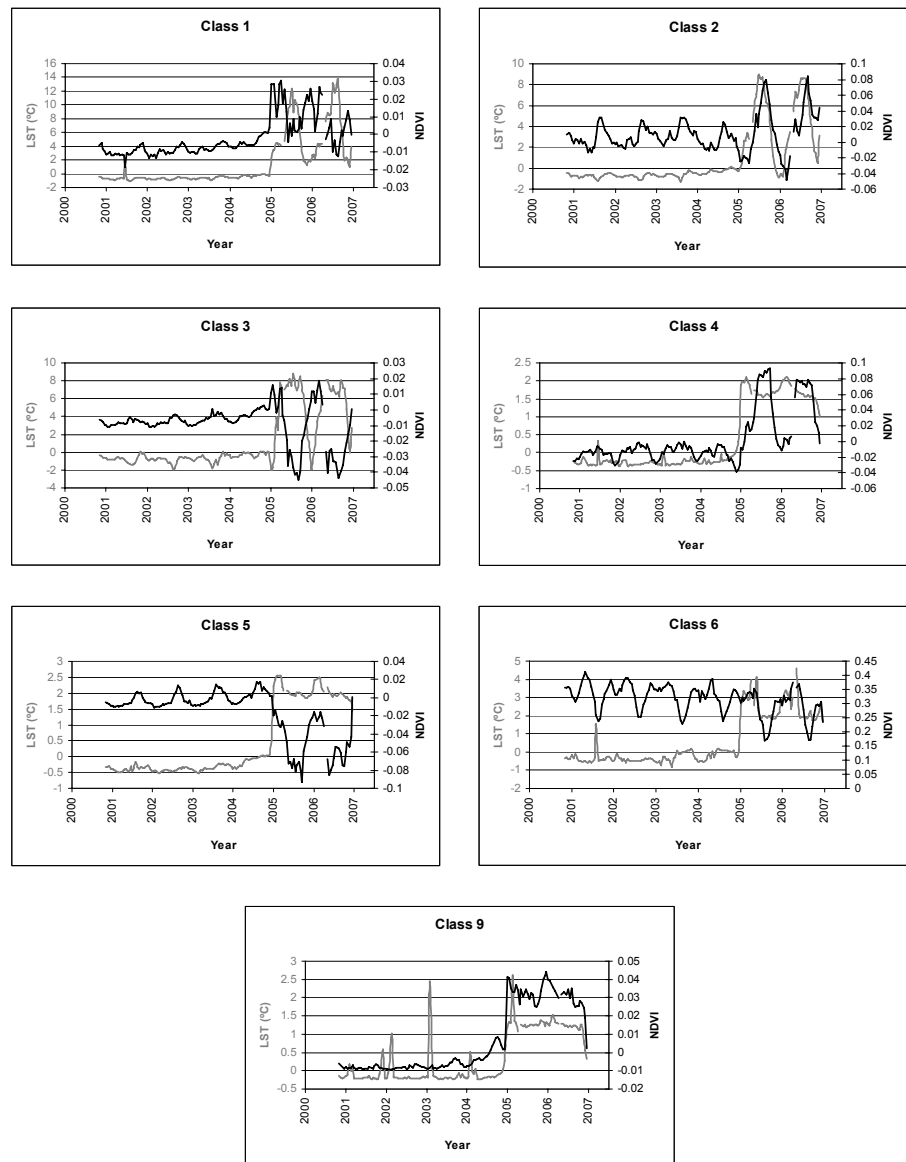
Figure 3.9.- Differences between corrected and uncorrected LST (left axis, grey) and NDVI (right axis, black) time series for all significant classes.

From a general point of view, the correction is more important at the end of the satellite life-period than at its beginning for all classes, corresponding to decreases

in both LST and NDVI uncorrected values, except in the case of NDVI for classes 2, 4 and 6. As one can easily observe in Fig. 3.9, correction amplitudes vary with class number, meaning that amplitudes are specific to vegetation types. Corrections are different for all classes, and present a common periodic pattern, with periods of one year and 6 months, due to variations in SZA, especially in NDVI time series, as well as LST in the case of arid areas (classes 1, 2 and 3). Correction also depends on the satellite platform, the correction being generally more important for NOAA-17 than for NOAA-16. This is due to the lack of intercalibration between both platforms (Molly E. Brown, personal communication).

NDVI corrections are more important for vegetated areas (classes 5, 6 and 9), corroborating Kaufmann *et al.* (2000) analysis that orbital drift affects little desert areas as regards NDVI values. Regarding LST correction, its amplitude is higher for arid areas (classes 1, 2 and 3), due to the high amplitude of the LST daily cycle over those areas.

3.3.4.- Validation

In order to validate the results presented above, we decided to use MSG (Meteosat Second Generation) SEVIRI (Spinning Enhanced Visible and Infrared Imager) data retrieved during the SPARC (SPectra bARrax Campaign) campaign of 2004 (10 to 17 July). The main objective of the Spectra Barrax Campaigns was to collect coincident in-situ data over the Barrax site, about 20 km west of Albacete, Spain, with CHRIS/PROBA multi-angular and multi-spectral in order to address the following critical issues in the Earth-Explorer SPECTRA Phase A study: validation of BRDF forward models, validation of SPECTRA geo-physical parameter retrieval algorithms, development and testing of atmospheric correction algorithms for multi-view images, and validation of multiple view image co-registration algorithms. Additional data from ROSIS, HYMAP and AHS airborne sensors, flying simultaneously with CHRIS overpasses, provided detailed images for validation of CHRIS data, particularly in the spectral domain. Moreover, multi-angular airborne HYMAP and AHS data were acquired, with high spectral and spatial resolution, so that both spectral and angular domains could be exploited with the combined dataset. Detailed soil/vegetation and atmospheric measurements complete the SPARC dataset, and data from other satellites (MERIS, SEVIRI, SPOT, Landsat) were collected as well, to address scaling issues.

The collected MSG data consist of a whole week of SEVIRI images, with all bands at 15 minute intervals. From these data, land surface temperatures have been estimated for images acquired at 13:30 (in concordance with AVHRR corrected images), using a split-window algorithm (Sobrino & Romaguera, 2004) similar to the one applied above.

Using DAY information from GIMMS data, two SEVIRI composites were created corresponding to GIMMS composites (July15a and July15b). Then, SEVIRI LSTs were resampled to fit GIMMS image projection (Albers). Finally, the corresponding GIMMS and SEVIRI LSTs were compared over the common days of the respective datasets. Since NOAA-AVHRR sensor thermal bands have a saturation value between 320 and 330 K, pixels with LST value higher than 320K were removed from the comparison, as well as pixels with LST value lower than 273K, in order to screen out residual clouds in the images.

The averaged difference between SEVIRI and GIMMS corrected LST over Africa is of -2.32 K. Since algorithm accuracies are respectively of 1.7K for NOAA-AVHRR and 2.4K for MSG-SEVIRI at high view angle, this result is satisfying, being lower than their quadratic sum ($\delta T = 2.9K$). The classification described previously has been used to average LST differences between SEVIRI and GIMMS over homogeneous vegetation classes. The results are presented in Table 3.1. Those results show that the vegetated classes (class number 4, 5, 8 and 9) exhibit generally lower LST differences. Since class 8 includes too few pixels to be statistically significant, those values will not be discussed. Classes 4, 5 and 9 correspond to stable vegetated areas, while the classes with higher averages correspond to arid and semi-arid areas. This means that algorithms for LST estimation from SEVIRI and GIMMS data agree better on vegetated areas (with accuracies better than δT) than on arid and semi-arid areas. This behavior could be due to angular effects. One can also observe that the differences are lower for the first composite (A) than for the second (B), probably due to the fact that only two days of SEVIRI data were available to create the second composite.

Since NOAA-16 had been launched on the 21st of September 2000, this satellite had already derived significantly from its nominal orbit by mid-July 2004. Thus, reaching such a good agreement between MSG SEVIRI and NOAA-16 AVHRR data after orbital drift correction shows the validity of the correction method described.

107

Table 3.1.- Differences between SEVIRI and GIMMS LST averaged over homogeneous vegetation classes (see Figure 3.1).

class	Pixel nb		SEVIRI – raw GIMMS		SEVIRI – corr GIMMS	
	A	B	A	B	A	B
1	12336	3982	-5.24	-12.26	-5.30	-12.31
2	36653	10041	-6.03	-10.17	-6.20	-10.23
3	30736	13506	-8.30	-12.24	-8.45	-12.13
4	24363	14560	-1.60	-1.75	-1.77	-1.84
5	19394	9433	-1.29	-2.52	-1.47	-2.61
6	1104	694	-3.15	-4.45	-3.35	-4.71
7	/	/	/	/	/	/
8	5	13	2.45	0.78	1.61	0.21
9	813	1629	-0.83	0.56	-0.98	0.45

3.3.5.- Correction of PAL database

This method has been applied to correct PAL database. As described in Chapter 2, no information is publicly available at global scale from this database for solar zenithal angle or day and hour of acquisition. Thus, this information has been extrapolated, using the method developed by Ignatov *et al.* (2004) to obtain acquisition time, and Iqbal (1983) to retrieve actual SZA at acquisition (see § 3.3.2.1), day of acquisition being fixed at half of the corresponding compositing period. The equator crossing time is estimated as follow (Ignatov *et al.*, 2004):

$$\eta = \eta_0 + \alpha_1 \cdot \sin(\omega_1 \cdot (JD - JD_0) + \Phi_1)$$
$$+ \alpha_2 \cdot \sin(\omega_2 \cdot (JD - JD_0) + \Phi_2)$$

(3.26)

where, for each satellite, η_0 is an average equator crossing time around which η oscillates, α_i, ω_i and Φ_i are the amplitude frequency and phase of the respective harmonics (i=1,2), JD is the Julian Day corresponding to image acquisition (estimated as the median day of the considered composite period), and JD_0 is the first Julian Day for which the satellite two-line-elements (describing orbital parameters) were available. These parameters values are given in Table 3.2 for each satellite contributing to PAL database.

Then, local time of observation for each pixel is given by:

$$\eta_\varphi = \eta + \frac{\sin^{-1}(\dfrac{\tan \varphi}{\tan i})}{15°} \qquad (3.27)$$

where i is the orbital inclination ($i \sim 99.0 \pm 0.4°$ for NOAA platforms), and φ is the latitude of the considered pixel.

Then, using the Iqbal (1983) method described before, we can estimate SZA values at overpass and at 13:30 solar time.

Table 3.2.- Parameters for Eq. 3.26 for all NOAA afternoon platforms contributing to PAL database.

	NOAA-07	**NOAA-09**	**NOAA-11**	**NOAA-14**	**NOAA-16**
JD_0	2444779	2446047	2447583	2449717	2451809
η_0 **(h)**	18.311	18.367	18.258	17.759	18.099
α_1 **(h)**	3.972	4.312	4.935	4.348	4.141
ω_1 **(JD^{-1})**	$5.419 \cdot 10^{-4}$	$5.160 \cdot 10^{-4}$	$4.989 \cdot 10^{-4}$	$5.728 \cdot 10^{-4}$	$4.955 \cdot 10^{-4}$
Φ_1 **(rad)**	5.008	5.064	5.036	4.809	4.531
α_2 **(h)**	0.140	0.207	0.164	0.224	0.212
ω_2 **(JD^{-1})**	$1.511 \cdot 10^{-3}$	$1.506 \cdot 10^{-3}$	$1.754 \cdot 10^{-3}$	$1.540 \cdot 10^{-3}$	$3.129 \cdot 10^{-4}$
Φ_2 **(rad)**	3.183	2.969	2.244	1.451	3.404

Of course, estimating these parameters does not replace their actual knowledge, and present several flaws. First, the error relative to day information is ± 5 days, which can lead to substantial errors in SZA. Then, all pixels are supposed to be observed at nadir, which is the case for only a few pixels in the image. However, since these parameters are not available, this method is the only way we could think of to apply this correction to the whole PAL database.

Then, AVHRR channel time series have been corrected from the orbital drift using the method described above (§ 3.3.2). LST and NDVI have been estimated, following the steps described in § 3.1. To validate the correction of the orbital drift of PAL database, stable control points over the whole globe have been chosen. These are described in Table 3.3. Finally, for each of these control points, corrected time series have been retrieved, and are presented Figure 3.10.

Corrected time series have not been screened out for cloud or snow presence, which show clearly for Amazonia, Sumatra and Norway. These "corrected" time

series show a clear orbital drift pattern, especially in desert areas for LST, showing that the correction is insufficient. Since this correction has been validated separately, this means that accurate day of acquisition and SZA information are crucial for adequate correction of the orbital drift.

Table 3.3.- Coordinates of the control points for PAL orbital drift correction validation.

Site	Land cover	Latitude	Longitude
Landes	Forest	43.9º N	1.0º W
Atacama	Desert	23.5º S	69.6º W
Libya	Desert	20.0º N	10.9º E
Gobi	Desert	38.8º N	83.8º E
Amazonia	Forest	7.5º S	59.6º W
Congo	Forest	1.2º S	24.6º E
Norway	Forest	65.7º N	14.8º E
Sumatra	Forest	1.0º S	102.2º E
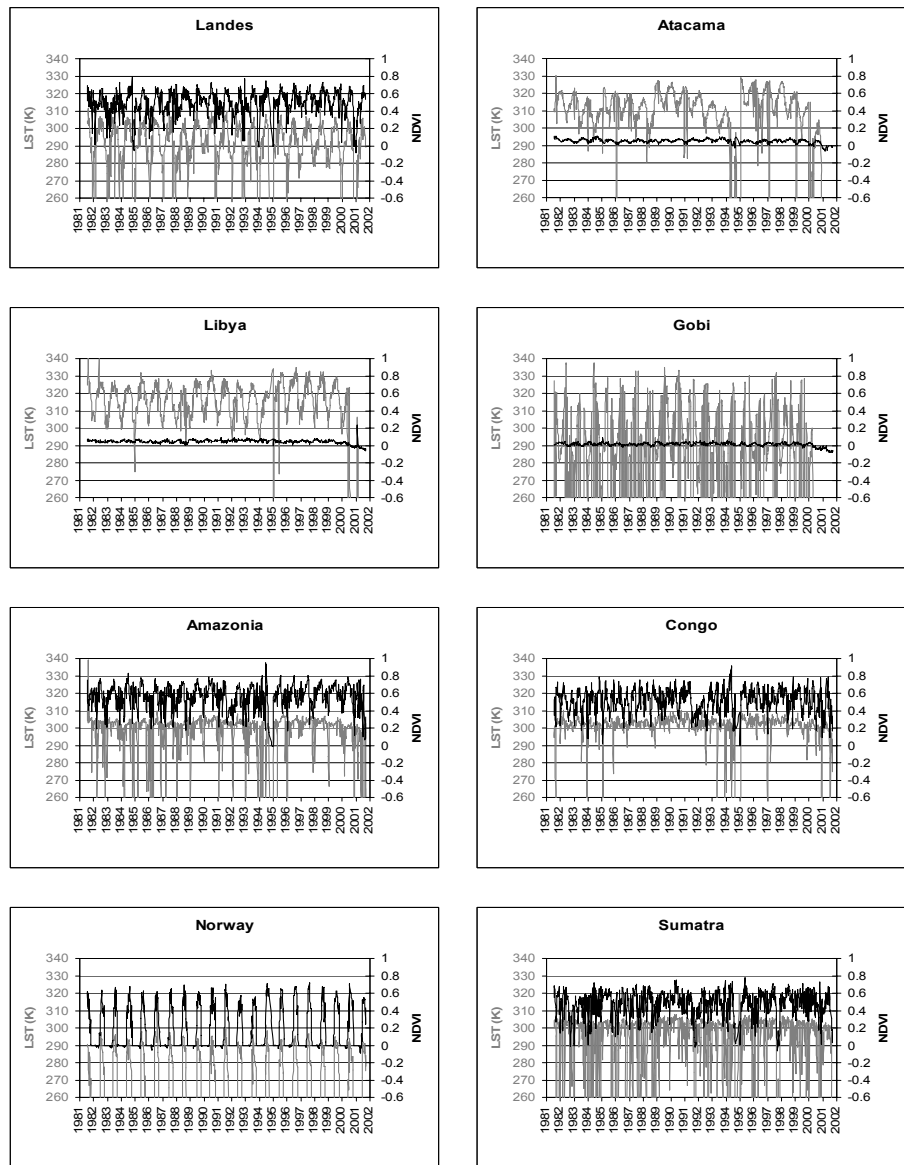
Figure 3.10.- Corrected time series of LST (left axis, grey) and NDVI (right axis, black) for 8 control points (see table 3.3).

Chapter 4

TIME SERIES ANALYSIS

"Ticking away the moments that make up a dull day
You fritter and waste the hours in an offhand way
Kicking around on a piece of ground in your home town
Waiting for someone or something to show you the way

Tired of lying in the sunshine / Staying home to watch the rain
And you are young and life is long / And there is time to kill today
And then one day you find / Ten years have got behind you
No one told you when to run / You missed the starting gun

And you run, and you run to catch up with the sun, but it's sinking
Racing around to come up behind you again
The sun is the same in a relative way, but you're older
Shorter of breath and one day closer to death

Every year is getting shorter / Never seem to find the time
Plans that either come to nought / Or half a page of scribbled lines
Hanging on in quiet desperation is the English way
The time is gone / The song is over
Thought I'd something more to say"

Pink Floyd (*Time*)

This chapter describes the analysis of the time series retrieved for various parameters from the databases described in Chapter 3. The methods we applied are described first, followed by NDVI time series analysis and their validation.

4.1.- Methods

The main difficulty with time series analysis is the determination of statistically significant trends from noisy data. This first paragraph describes how trends were retrieved in this work, followed by two methods to screen out noisy data from the retrieved time series parameters.

4.1.1.- Trend analysis

Ordinary least squares (OLS) regression is the most common method applied for trend analysis in long image time series. However, four basic assumptions affecting the validity of trends summarized by OLS regression are often violated: 1) all the Y-values should be independent of each other; the residuals should be 2) random with 3) zero mean; and 4) the variance of the residuals should be equal for

all values of X (De Beurs, 2005). Since time series of biophysical parameters are temporally correlated, OLS regression retrieved trends are not reliable.

The approach used in this work relies on Mann-Kendall monotonic trend tests, which have been applied in a few previous studies of time series of remotely sensed data (De Beurs & Henebry, 2004a; De Beurs & Henebry, 2004b; De Beurs & Henebry, 2005a; De Beurs & Henebry, 2005b). The basic principle of Mann-Kendall (MK) tests for trend is to examine the sign of all pairwise differences of observed values (Libiseller & Grimvall, 2002). A univariate form of such tests was first published by Mann (1945), and the theory of multivariate Mann-Kendall tests is due to Hoeffding (1948), Kendall (1975), and Dietz & Killeen (1981). During the past two decades, applications in the environmental sciences have given rise to several new MK tests. Hirsch & Slack (1984) published a test for detection of trends in serially dependent environmental data collected over several seasons.

The Mann-Kendall statistic for monotone trend in a time series $\{Z_k, k = 1, 2, ..., n\}$ of data is defined as:

$$T = \sum_{j<i} \text{sgn}(Z_i - Z_j) \tag{4.1}$$

where

$$\text{sgn}(x) = \begin{cases} 1, & if \quad x > 0 \\ 0, & if \quad x = 0 \\ -1, & if \quad x < 0 \end{cases} \tag{4.2}$$

If no ties are present and the values of $Z_1, Z_2, ..., Z_n$ are randomly ordered, this statistic test has expectation zero and variance:

$$Var(T) = \frac{n(n-1)(2n+5)}{18} \tag{4.3}$$

Furthermore, T is approximately normal, if n is large (n > 10 – Kendall, 1975).

116

Finally, the null trend hypothesis can be rejected at α% confidence level if T (in absolute value) is greater than a corresponding threshold, which value is $z \cdot \sqrt{Var(T)}$, retrieved from standard normal distribution tables. α and z values are presented in table 4.1.

Table 4.1.- Confidence levels and corresponding thresholds for Mann-Kendall trend tests.

α (%)	90	95	99
z	1.65	1.96	2.58

4.1.2.- Harmonic analysis

To carry out harmonic analysis, we have used the HANTS software developed by Wout Verhoef from the National Aerospace Laboratory (NLR) of Netherlands (for more information, see Menenti *et al.*, 1993, as well as Verhoef *et al.*, 1996, and Roerink *et al.*, 2000). This software can be downloaded freely from the NLR internet webpage:

http://remotesensing.nlr.nl/upload/verhoef@nlr.nl/Hants.zip

The HANTS algorithm was devised with the application to time series of NDVI images in mind. These images are usually composited by means of the so-called Maximum Value Compositing (MVC) algorithm in order to suppress cloud cover effects (Holben, 1986). Clouds always have a negative influence on the NDVI and therefore taking the maximum value of the NDVI over a limited period tends to remove most cloud contaminated observations. The HANTS algorithm also exploits this negative effect of clouds on the NDVI, but in a different way. In HANTS a curve fitting is applied iteratively, i.e. first a least squares curve is computed based on all data points, and next the observations are compared to the curve. Observations that are clearly below the curve are candidates for rejection due to cloud cover, and the points that have the greatest negative deviation from the curve therefore are removed first. Next a new curve is computed based on the remaining points and the process is repeated. Pronounced negative outliers are removed by assigning a weight of zero to them, and a new curve is computed. This iteration eventually leads to a smooth curve that approaches the upper envelope over the data points. In this way cloudy observations have been removed and the

117

amplitudes and phases computed are much more reliable than those based on a straightforward FFT (Fast Fourier Transform).

For display of phase information the IHS (Intensity, Hue, Saturation) transform is particularly useful, as phase can be connected to color hue, which is a much more natural choice that connecting it to a scale of grey levels from black to white. Besides the coupling of phase to color hue, it is possible to couple the amplitude of the same frequency to color saturation and the mean signal to the intensity. For this the following set of formulas is applied:

$$r = \frac{M-C}{S-C}\left[1 + \frac{A}{A_{max}}\cos(P-240)\right] \times 127$$

$$g = \frac{M-C}{S-C}\left[1 + \frac{A}{A_{max}}\cos(P-120)\right] \times 127 \qquad (4.4)$$

$$b = \frac{M-C}{S-C}\left[1 + \frac{A}{A_{max}}\cos P \right] \times 127$$

where r, g and b are the color signals in red, green and blue, P is the phase in degrees, A the amplitude and M is the mean signal. The mean is scaled by means of a cut-off (minimum) C and a saturation value (maximum) S. The amplitude is scaled between zero and a maximum value A_{max}. When the phase passes through the complete range from zero to 360 degrees, the colors go through the sequence blue-cyan-green-yellow-red-magenta-blue, similar to a rainbow. When the amplitude is small, the color components are almost equal, so the result will be a black and white image that is mainly controlled by the mean signal.

HANTS algorithm can be used on NDVI data as well as LST data, since disturbances like clouds, haze or large viewing angles have an effect in only one direction: they tend to decrease retrieved temperatures, as well as NDVI values. In that case, the algorithm filters out the disturbed observations, so that only good observations remain. HANTS can filter out positive as well as negative distortions, but the selection has to be made before processing. All details about HANTS parameters can be found in Roerink *et al.* (2000).

For easiest comprehension, the code color is shown in Figure 4.1, which establishes the correspondence between colors and maximum value occurrence in HANTS images. For example, blue/green colors correspond to a maximum during spring, while yellow/orange taints correspond to summer peak, and pink/violet to autumn maxima. Winter maxima would then appear in blue colors.
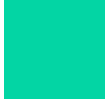
| January 15th | February 15th | March 15th | April 15th | May 15th | June 15th |
| July 15th | August 15th | September 15th | October 15th | November 15th | December 15th |

Figure 4.1.- Color code to identify phase values in HANTS images.

4.1.3.- Double logistic fitting procedure

A double logistic function has been used to describe NDVI yearly evolution only. The double logistic function can describe plateaus in NDVI evolution, corresponding to vegetation dormancy or extended photosynthesis peak period. These plateaus would require many harmonics to be described adequately through HANTS software for example, which would be too time-demanding for a global analysis on a pixel by pixel base.

To study yearly NDVI evolutions, retrieved data have been artificially divided in one year intervals, starting on January, 1st and ending on December, 31st for the Northern Hemisphere and starting on July, 1st and ending on June, 30th for the Southern Hemisphere. This distinction has been made in order to describe vegetation with the same function (see Eq. 4.5) for both hemispheres. These dates have been selected as boundaries for yearly evolution since they correspond to dormancy for most of the biomes. However, for biomes with peak chlorophyll activity at those boundary dates, another fitting function has been implemented (Eq. 4.6). Both fitting functions are shown in Figure 4.2. The choice between those two fitting functions is made after a first fit to the data, choosing the fitting

function for which the RMS (Root Mean Square) error is lower. NDVI yearly evolutions are thus fitted to the following double logistic function:

$$NDVI(t) = (mNDVI - wNDVI) \times \left(\frac{1}{1 + e^{-mS \times (t-S)}} + \frac{1}{1 + e^{mA \times (t-A)}} - 1 \right) + wNDVI \tag{4.5}$$

where NDVI(t) is the remotely sensed NDVI evolution for a given year (t=0 to 364), wNDVI is the winter NDVI value, mNDVI is the maximum NDVI value, S is the increasing inflection point (later referred to as spring date), A is the decreasing inflection point (autumn date), mS is related to the rate of increase at S inflection point, and mA is related to the rate of decrease at A inflection point.
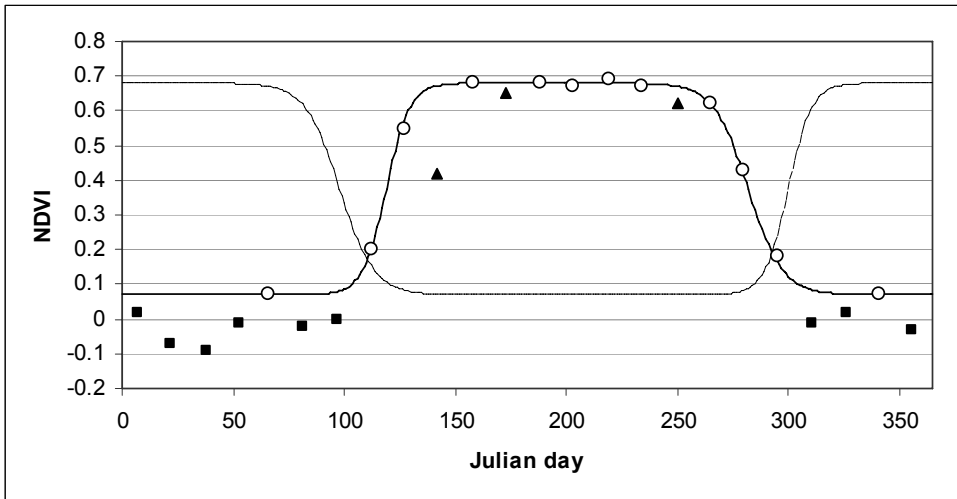
Figure 4.2.- Shape of the fitting functions. Original data have been divided in 3 categories: snow-contaminated (squares), correct (circles) and cloud-contaminated (triangles). The fitting function (solid line) used for these data is Eq. 4.5, with the following parameters: wNDVI=0.07, mNDVI=0.68, S=119, A=282, mS=0.19, and mA=0.13 (see text). For information, the same data have been fitted from day of year 181 to 365 and then 1 to 180 using Eq. 4.6 (dotted line).

120

Eq. 4.5 describes most of the world biomes accurately, since it includes a period of photosynthetic peak activity, with NDVI values close to mNDVI, and a period of lower photosynthetic activity, for which NDVI values are close to wNDVI. This lower photosynthetic activity period can correspond to vegetation dormancy (higher latitudes and deciduous species), to higher rate of leaf fall in evergreen forests (rainforests, see Huete *et al.*, 2006), to snow under or temporarily on the canopy of evergreen forests at higher latitudes (Beck *et al.*, 2006), or to vegetation under enduring cloud cover. Biomes with photosynthetic activity at boundary dates (usually in arid or semi-arid areas) are fitted to the following function:

$$NDVI(t) = mNDVI - (mNDVI - wNDVI) \times$$
$$\left(\frac{1}{1 + e^{-mS \times (t-S)}} + \frac{1}{1 + e^{mA \times (t-A)}} - 1 \right) \tag{4.6}$$

where all parameters are the same as for Eq. 4.5.

For those biomes with low NDVI amplitude variation throughout the year (lower than 0.1 NDVI unit), no fitting procedure is carried out, mNDVI and wNDVI being fixed to the mean value of NDVI over the considered year. These biomes correspond to arid or frozen areas, as well as evergreen vegetation. The fitting functions presented above (Eq. 4.5 and 4.6) do not describe correctly vegetation with more than one peak chlorophyllic activity (for example, two peaks, as can be seen in some tropical areas), one of the low NDVI period being considered as dormancy period while the other is considered as a plateau with cloud contaminated values. Nevertheless, the retrieved parameters are correct, even if half the information is missing. An additional consequence of this fact can be a high temporal variability of spring and autumn dates. However, this type of vegetation can be found in general in tropical areas, where enduring cloud cover is frequent, and thus undermining the fitting procedure. This is the reason why no third function has been added to the first two, the cost in terms of calculation time being too high.

The fitting procedure is carried out iteratively on a pixel by pixel basis for each of the 22 years available from GIMMS database (see Chapter 2), using the Levenberg-Marquardt technique (More, 1977). First, if yearly NDVI time series

are below zero or with an amplitude lower than 0.1, corresponding respectively to frozen and stable areas, the pixel is flagged as such, and no fitting procedure is carried out. Otherwise, as mentioned above, a preliminary fit is conducted in order to choose between Eq. 4.5 and Eq. 4.6. Then, from this preliminary fit, the dormancy period is estimated as the period before spring date and after autumn date. During this period, all eventual negative NDVI values are set to the highest positive value over the whole dormancy period. Then, a weighted fit is carried out iteratively to the selected function (Eq. 4.5 or Eq. 4.6), all NDVI values below the fitting function being considered as cloud-contaminated values, and thus a lower weight is attributed to them at each iteration. The procedure is stopped when the total difference between the weighted data and the fitting function is lower than 0.05 NDVI units. Finally, the fitting parameters are tested for consistency (wNDVI ≥ 0, mNDVI ≤ 1, wNDVI $\leq$ mNDVI, $0 \leq S$ and $A \leq 365$, $S \leq A$ for Eq. 4.5, and A $\leq S$ for Eq. 4.6). If these last tests are successful, the pixel is flagged as such, else it is flagged as unsuccessful. A schematic view of this fitting procedure can be seen in Figure 4.3. From the retrieved spring and autumn dates, growing season length is estimated as the difference between autumn and spring dates.

In the case of standard biomes (one chlorophyll peak activity per year), the main source of inaccuracy of this procedure is due to the composite nature of the data. In order to estimate the accuracy in determining spring and autumn dates, a simulation has been conducted, randomly attributing different dates for each 15-day period to a yearly time series of data. 100 000 simulations have been conducted, leading to standard deviations of ±5.5 days accuracy for spring and autumn dates, and ±7.8 days for growing season length.

The influence of the number of cloud-contaminated values on the determination of wNDVI, mNDVI, spring and autumn dates can lower parameter retrieval accuracy. To this end, 100 000 simulations have been conducted on a yearly time series of NDVI, attributing each time a different number of cloud-contaminated values to some randomly chosen dates. The results of this simulation are presented in Table 4.2.

Finally, our assumption that Eq. 4.5 describes correctly most of the biomes of our planet has been tested. To this end, the whole GIMMS database has been averaged over each compositing period, in order to obtain an average year of data.

122
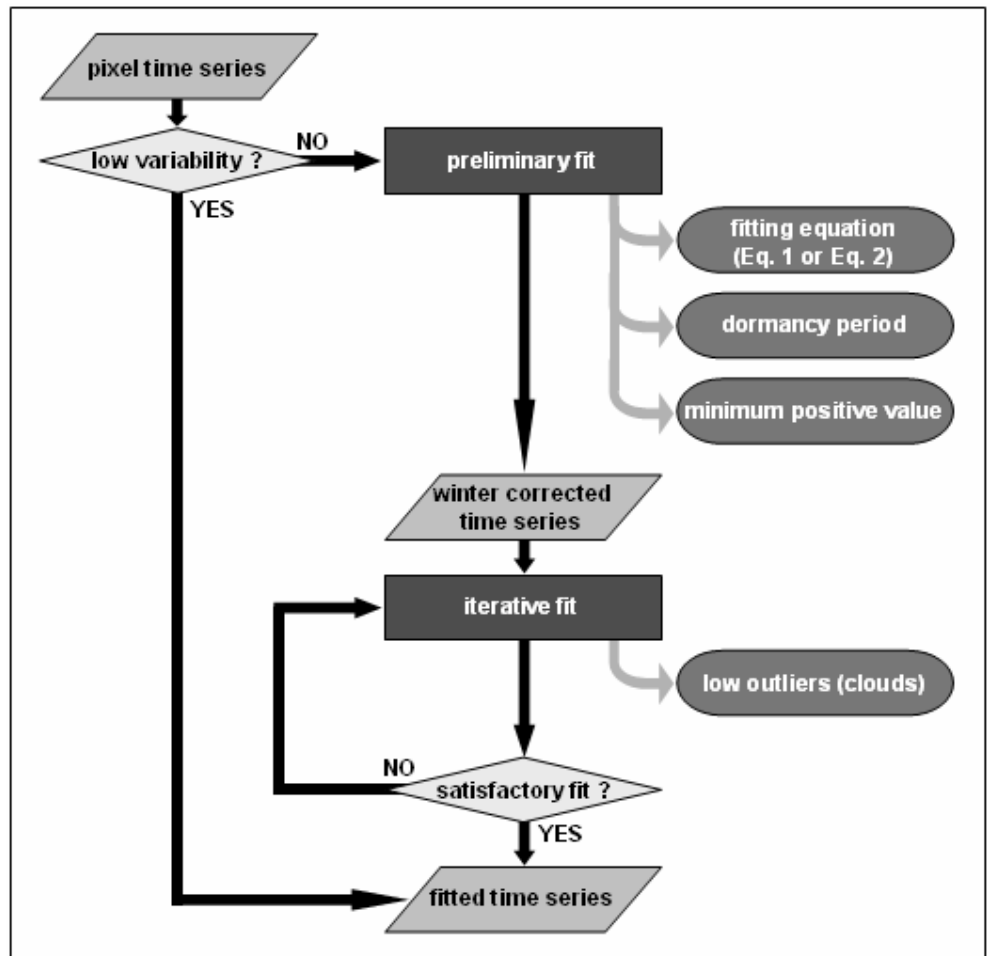
Figure 4.3.- Schematic view of the fitting procedure.

Yearly NDVI evolutions have then been analyzed pixel by pixel, creating a yearly evolution function library as the analysis progressed. For each pixel, its NDVI yearly evolution was tested for significant (at 95% confidence level) cross-correlation with each yearly evolution function of the library, and if no significant cross-correlation was evidenced, then the considered pixel yearly evolution function was added to the library. This procedure led to the retrieval of 38 different base functions. However, 97.5% of land pixels were described correctly by a single base function. This base function is displayed in Figure 4.4, along with its global representativity. This function is obviously described correctly by Eq. 4.5.

Table 4.2.- Accuracy of the yearly fitting procedure depending of cloud contaminated value number in the time series.

Cloud number	1	2	3	4	5
wNDVI ($\cdot 10^{-2}$)	2.5	3.6	4.5	5.3	6.1
mNDVI ($\cdot 10^{-2}$)	0.2	0.4	0.8	1.2	1.6
S (day)	3.4	4.8	6.4	7.8	9.3
A (day)	2.7	3.8	4.8	5.9	6.9
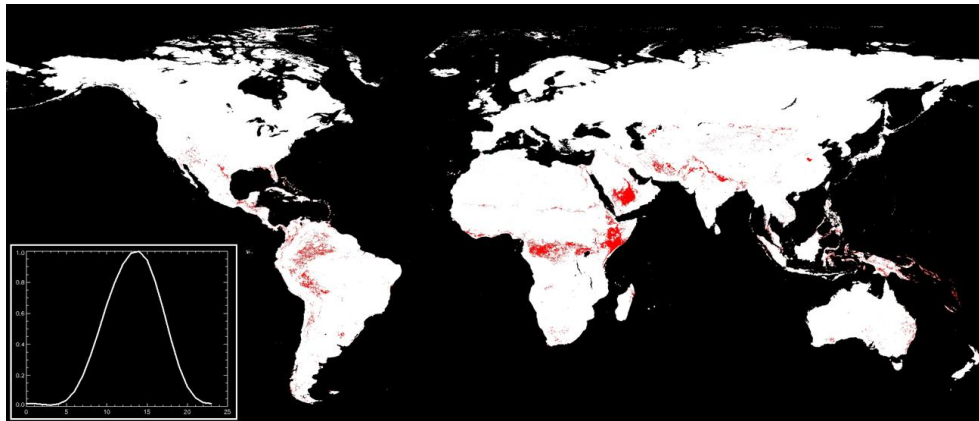
Figure 4.4.- Base function which describes accurately 97.5% of land cover vegetation. Areas not described correctly by this function are displayed in red.

4.2.- Analysis of NDVI time series

Harmonic analysis having been developed previously, this work is centered on the double logistic function fitting technique, which results regarding phenology and other NDVI metrics are then presented, followed by a comparison with the harmonic analysis techniques.

4.2.1.- Land surface phenology

This analysis has been submitted for publication to International Journal of Remote Sensing, and awaits acceptation at the time of redaction of this manuscript.

This work has also been presented at MULTITEMP 2007 congress (Julien & Sobrino, 2007a).

4.2.1.1.- Introduction

Vegetation phenology is the study of recurring vegetation cycles and their connection to climate. It has become of increasing interest to the scientific community with the focus on global change research, since an accurate detection of phenological phases allows estimating the spatiotemporal dynamics of carbon and water cycles. Numerous ground phenological studies have been conducted, but the difficulty of unifying data records over plant species and phenological events (Ahas *et al.*, 2002; Schwartz *et al.*, 2006) undermines the use of these data records for vegetation change detection at global scale. With the increasing length of the available satellite data record, NASA has evidenced land surface phenology as a supplementary tool for vegetation monitoring (Friedl *et al.*, 2006). Land surface phenology is defined as the seasonal pattern of variation in vegetated land surfaces observed from remote sensing, and presents the advantage of a global coverage, which dispenses from tedious field work, unachievable at global scale. However, remotely sensed data also present drawbacks, such as the influence of the atmosphere (cloud contamination, atmospheric absorption), spatial averaging over species due to pixel size, and temporal frequency of data acquisition (from 15 minutes to more than a week depending on the satellite orbits).

Land surface phenology is usually addressed through temporal monitoring of NDVI time series, available since the launch of the first earth observation satellites. Monitoring NDVI time series provides information on phenological phases, such as onset (green wave) or dormancy (brown wave) of vegetation, where these phases exist, evidenced respectively by increases and decreases of NDVI values (see Chapter 1).

4.2.1.2.- Results

The double logistic function fitting method has been applied to the whole GIMMS NDVI database. As stated above, this method allows the retrieval of yearly spring and autumn dates, which give an estimation of growing-season length for the 22 years of data. A principal component analysis has been carried out on the spring, autumn and growing-season length time series, in order to determine the stability of the approach. This principal component analysis (PCA) has been conducted on

both variance-covariance and correlation matrices, leading to similar results. Thus, only results of the PCA conducted on the correlation matrices are presented here. For this PCA analysis, only pixels with retrieved phenology have been considered, leaving out pixels corresponding to sea or stable areas. The first components are displayed in Figure 4.5 for these three growing season parameters. Regarding spring images (Fig. 4.5a), the first component explains 36% of the variance, the
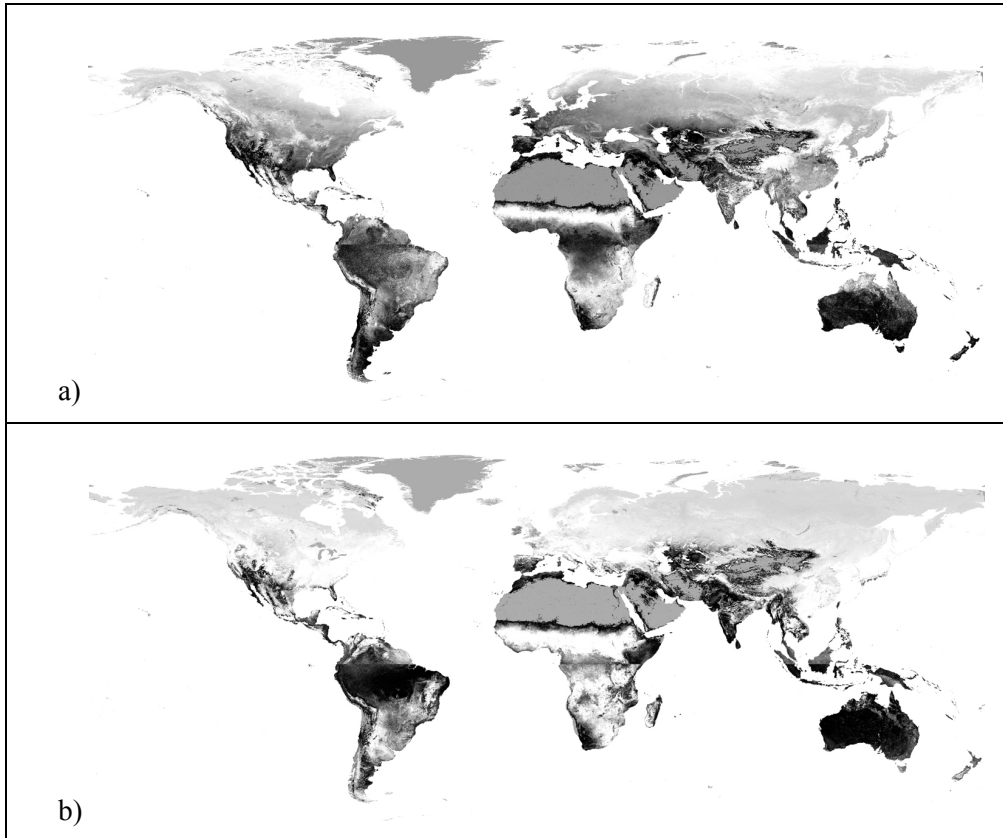
Figure 4.5.- Results of empirical orthogonal analysis on correlation matrices for time series of phenological parameters. First component are displayed for a) spring (1st component explains 36% of the total variance) and b) autumn (53%).
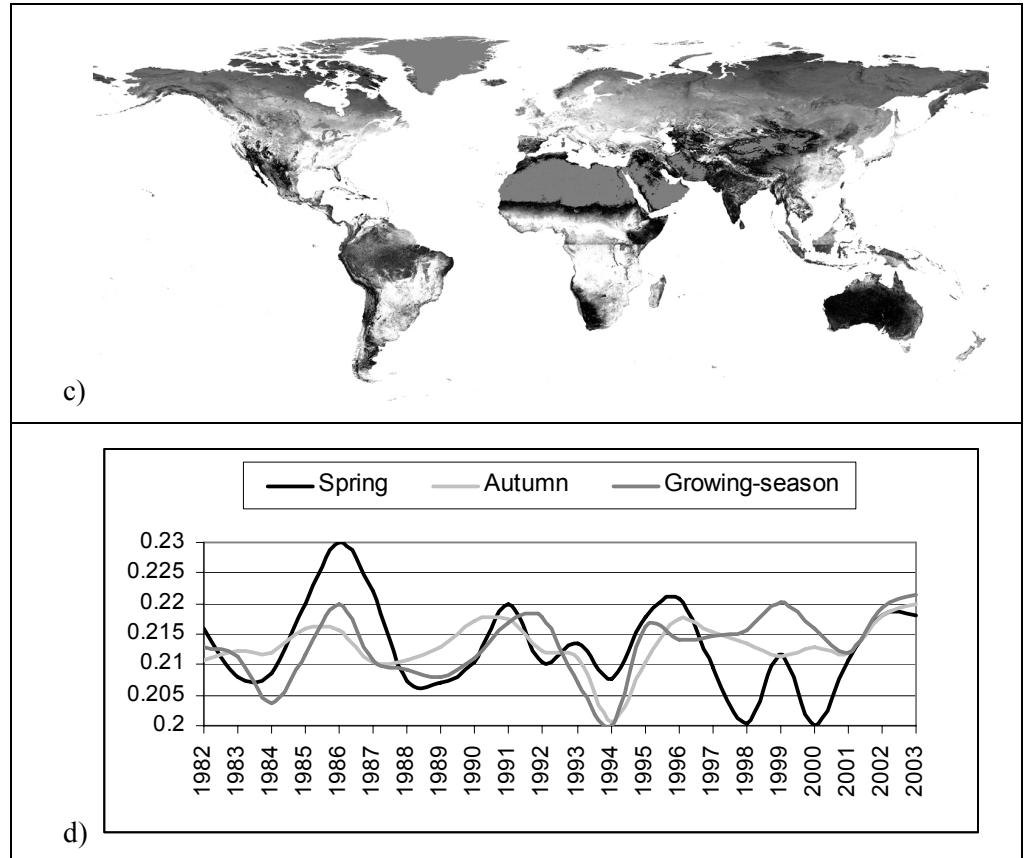
Figure 4.5.- (continued) Results of empirical orthogonal analysis on correlation matrices for time series of phenological parameters. First component is displayed for c) growing season (37%). Finally, the influence of each year in those first components is displayed (3d).

remaining variance being distributed homogeneously on the other components; regarding autumn images (Fig. 4.5b), the first component explains 53%, of the variance, the remaining variance being also distributed homogeneously on the other components. Finally, regarding growing-season images (Fig.4.5c), the first component explains 37% of the variance, the remaining variance being also distributed homogeneously on the other components. The variance explained by the first component is quite low. This is due to the yearly variability of phenological phases, as well as to local instability of the procedure (due to cloud or snow presence). In Figures 4.5a to 4.5c, spatial heterogeneity can be observed

locally around the Equator for example. This is due to the fact that along the Equator, similar ecosystems are fitted differently, on the Northern side using data from January, 1st to December, 31st, and on the Southern side using data from July, 1st to June, 30th (starting the previous year). This heterogeneity is reinforced by the enduring cloud cover during part of the year for the affected regions (Amazonia, Central Africa), but also in the Indian subcontinent. This is due to the fact that the fitting procedure interprets the enduring cloud cover as dormancy period (which is consistent with Huete *et al.*, 2006), which can be pixel dependent, leading to local spatial heterogeneity. This spatial variability is reinforced by the possible errors on wNDVI parameter due to the enduring cloud cover in these areas, which propagate on spring and autumn dates, as stated before. Figure 4.5d shows that the influence of each year in the first component for all three parameters is basically the same, indicating a good overall stability of the approach.

In order to estimate the validity of the spring and autumn time series, an analysis of the flag time series has to be conducted. Figure 4.6 shows the number of years for which each pixel has been flagged as frozen (a), stable (b), unsusccessful (c) or successful (d) during the 22 years of the study. Fig. 4.6a shows that the areas frozen throughout the year are located near the North Pole, consisting mainly of Greenland. In addition, a few areas are labeled as frozen, corresponding to inland water, which are not flagged as water within GIMMS database. Since these areas do not correspond to land vegetation, this has no influence on the study.Regarding stable pixels, Fig. 4.6b shows that arid areas are labeled as stable (Sahara, Atacama and Namib Deserts), as well as high mountains (Chilean Andes, Himalaya). On the other hand, many other areas are labeled only temporarily as stable, and correspond to rainforests (Central America, Amazonia, Equator, and Southern Asia) or to semi-arid areas (part of the Arabic peninsula, Central Australia, Southern Spain, South-Western USA). Temporary presence of clouds (for the first group of areas), or temporary presence of vegetation (for the second group) can explain these changes from year to year. Fig. 4.6c shows pixels with errors in the fitting procedure, corresponding to a fitting function inadequate with input time series (see above). Pixels with unsuccessful fitting are located around the Equator and in enduring cloud cover areas (Amazonia, South Asia, and Central Africa), corresponding to the areas with spatial heterogeneity in Fig. 4.5, but also semi-arid areas, like Australia, Sahel or Mexico. Finally, Fig. 4.6d shows the pixels

128

with successful fitting, which are logically complementary to the three previous images (Fig. 4.6a to 4.6c). The areas with the lowest successful fit are thus located around the Equator, in Amazonia, in Southern Asia and in Australia. Results for these areas are to be treated with caution.

Mann-Kendall tests have been carried out for each pixel time series, and trends have been determined by linear regression for those pixels for which the no-trend hypothesis could be rejected at 90% confidence level. The results are presented in Figure 4.7 for spring, autumn and growing-season time series. Retrieved spring

0 1 2 3 4 5 6 7 8 9 10 11 12 13 14 15 16 17 18 19 20 21 22
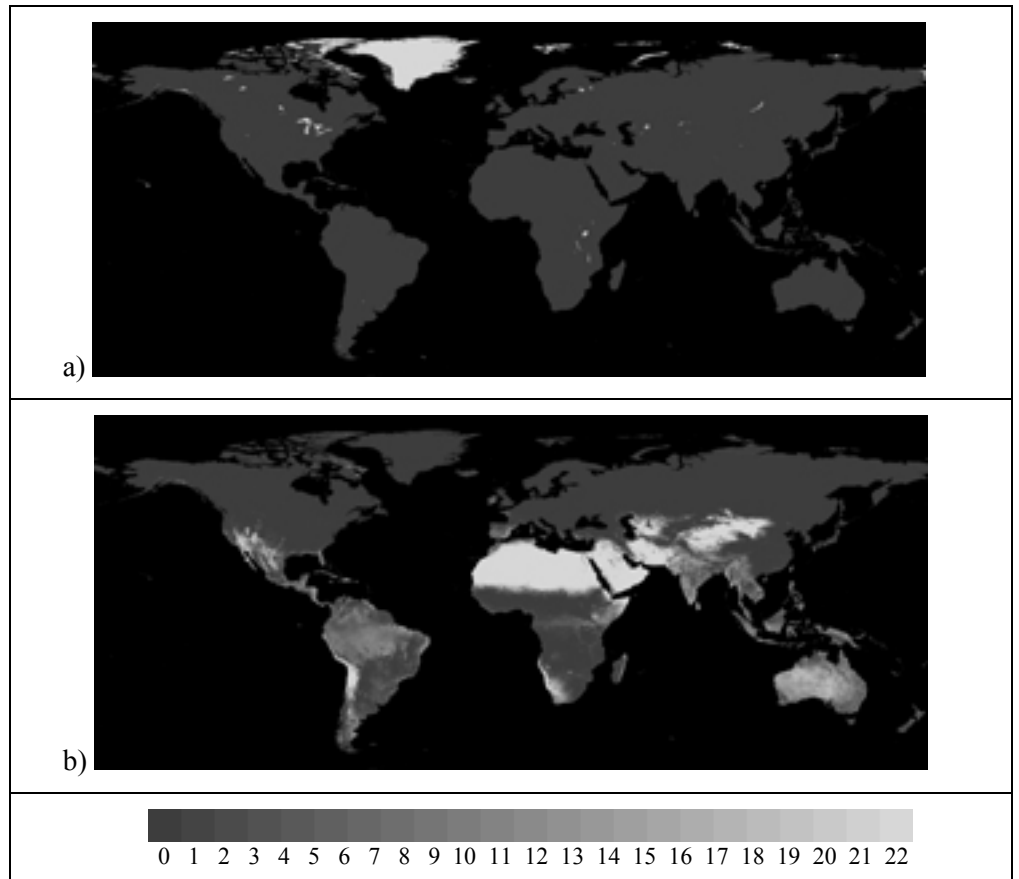
Figure 4.6.- Accumulated flags of the fitting procedure for the 22 years of the study: a) frozen; b) stable.
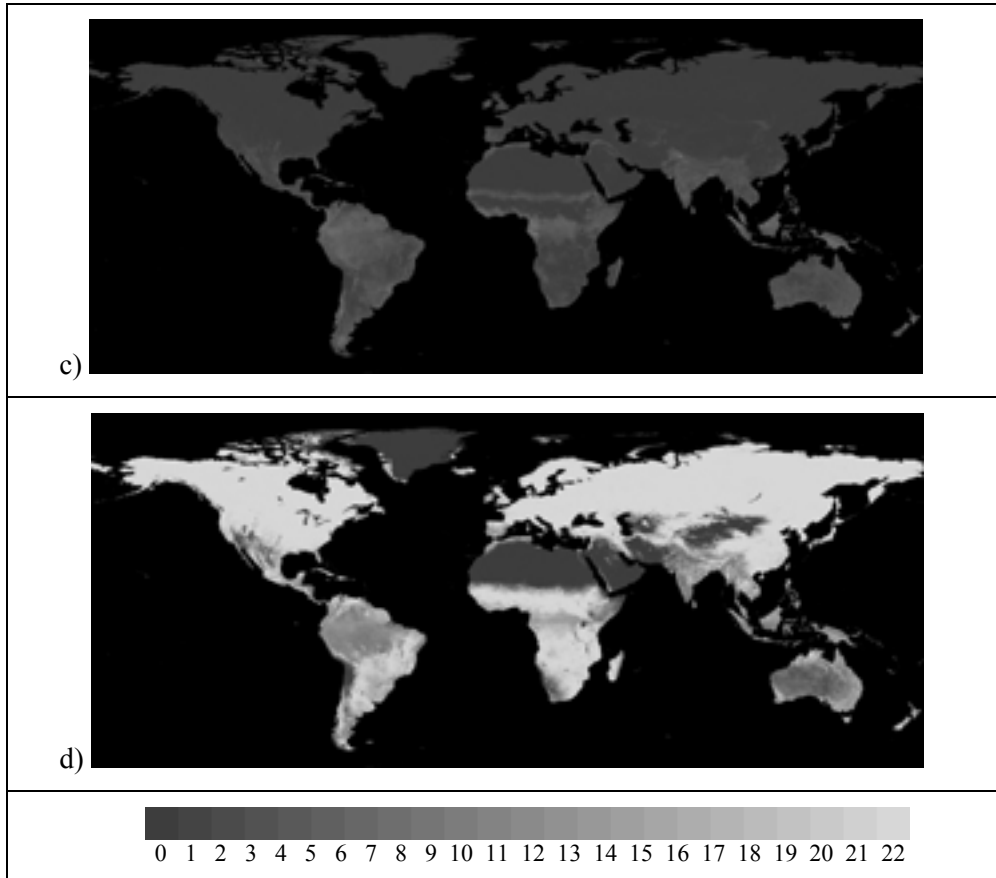
Figure 4.6.- (continued) Accumulated flags of the fitting procedure for the 22 years of the study: c) unsuccessful; and d) successful.

dates (Fig. 4.7a) have seen an advance in average of 0.38 days per year over the whole globe, the image being scaled between advances of 3.6 days per year and delays of 2.8 days per year. Areas seeing the highest advances in spring dates are located in Western Europe, Sahel, and patches of Eastern Asia, while areas seeing the highest delays are located in Central North America, South-Eastern South America, East Sub-equatorial Africa and patches of Eastern Asia. Regarding autumn dates (Fig. 4.7b), an average delay of 0.45 days per year can be evidenced, the image being scaled between advances of 4.8 days per year and delays of 5.7 days per year. Areas seeing the highest delays in autumn dates are located in Sub-
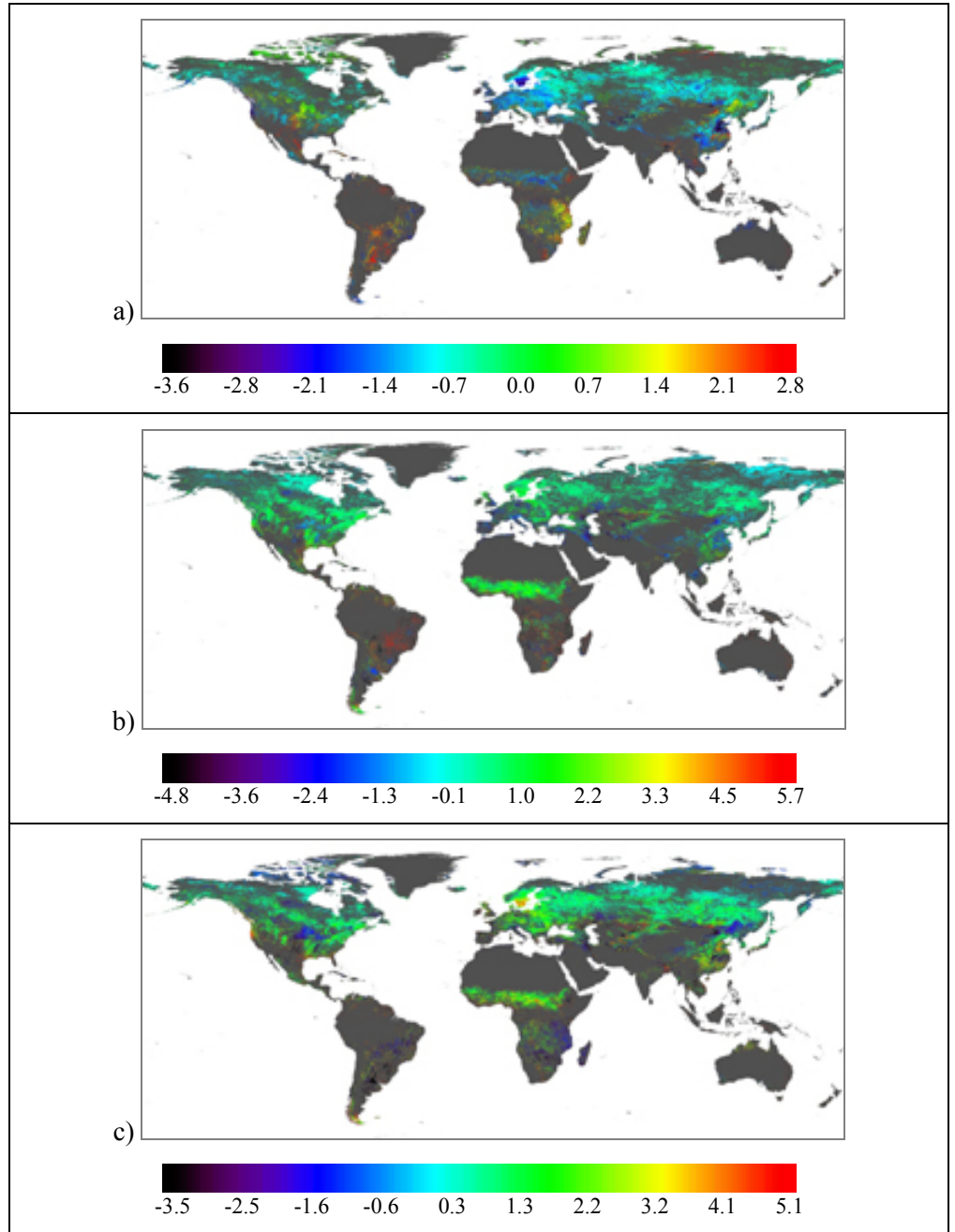
Figure 4.7.- Trends in a) spring; b) autumn; and c) growing-season time series for pixels exhibiting trends at 90% confidence level.

Saharan Africa and South-Eastern South America, while areas seeing the highest advances are located in patches of Western Europe, North America, Eastern Asia and around the Caspian Sea. Finally, regarding growing-season length (Fig. 4.7c), an average increase of 0.8 days per year can be evidenced at global scale, the image being scaled between decreases of 3.5 days per year and increases of 5.1 days per year. Areas seeing the highest increases are located in Southernmost South America, Southern Scandinavia, Westernmost USA and patches of Central Asia, while areas seeing the highest decreases are located at northernmost latitudes, in Central USA, Southern Amazonia, South Africa and patches of Eastern Asia.

One can observe than the areas mentioned in the previous paragraphs as unreliable due to unsuccessful fit or high spatial heterogeneity do not exhibit statistically significant trends, although those trends might exist. This lack of statistically significant trends is purely due to the fitting procedure. An other observation is that some of the trends present extreme values, which would correspond to changes in land surface phenology of 2 to 4 months during the 22 years of the study. These extreme values could be explained by abrupt changes in NDVI evolutions (due to deforestation or cloud cover), for example in Southern Amazonia.

4.2.1.3.- Validation

In order to compare the trends presented above with previous studies, averages have been calculated for comparable areas and time extent when possible, and are presented in Table 4.3. Geographic locations have been downscaled to country sizes, and study start years have been extended back to 1982 where previous years are indicated. Previous NDVI studies are easier to compare with the results presented above since land surface phenology phases were also retrieved from AVHRR data, while climate (C) and phenological (P) studies were carried out from totally different data. Nevertheless, those results serve as an estimation of the representativity of land surface phenology as to ground station based phenology. The results corresponding to this study presented in Table 4.3 have been obtained by spatial averaging over pixels within the concerned countries with successful fitting. This means that in spite of similar geographical coverage, the start, end and length of growing season can be estimated from smaller areas. Regarding NDVI studies, spring date trends are generally in agreement with previous ones (Tucker *et al.*, 2001; Zhou *et al.*, 2001; Stöckli & Vidale, 2004; Delbart *et al.*, 2006), while

132

Table 4.3.- Comparison of the results of the double logistic function fit (grey) with previous ones. "Type" indicates on which kind of records the previous studies were carried out: "NDVI" for satellite images, "P" for phenological ground stations and "C" for climate data. "Start", "End" and "Length" refer respectively to growing-season start, end and length in days per year. An "X" indicates that the corresponding parameter had not been estimated. Values in bold indicate statistically significant values at 95% confidence level.

Reference	Type	Period	Location	Previous studies Start	End	Length	This study Start	End	Length
Myneni et al. (1997)	NDVI	1981-1991	Global	-0.727	X	1.09	**-0.295**	0.053	0.554
Tucker et al. (2001)	NDVI	1982-1991	45N-75N	-0.6	X	0.4	**-0.648**	0.247	0.893
Tucker et al. (2001)	NDVI	1992-1999	45N-75N	-0.25	X	0.05	**-0.318**	0.512	0.816
Zhou et al. (2001)	NDVI	1981-1999	Eurasia	-0.368	X	0.947	**-0.293**	**0.156**	0.462
Zhou et al. (2001)	NDVI	1981-1999	N.America	-0.421	X	0.631	-0.121	**0.363**	0.461
Stöckli and Vidale (2004)	NDVI	1982-2000	Europe	-0.568	X	1.01	**-0.628**	0.193	0.883
Chen et al. (2005)	NDVI	1982-1993	China	X	X	1.083	**-0.653**	**-0.319**	0.359
Delbart et al. (2006)	NDVI	1982-1991	Boreal	-0.8	X	X	**-0.578**	**0.342**	0.92
Delbart et al. (2006)	NDVI	1993-2004	Boreal	0.3	X	X	**-0.354**	**0.169**	0.522
Piao et al. (2006)	NDVI	1982-1999	North China	-0.744	0.35	1.094	**-0.32**	0.075	0.367
Menzel and Fabian (1999)	P	1951-1996	Europe	-0.136	0.097	0.234	-0.466	0.235	0.787
Beaubien and Freeland (2000)	P	1987-1996	Canada	-0.8	X	X	**-0.572**	0.017	0.585
Chmielewski and Rötzer (2002)	P	1969-1998	Europe	-0.266	X	X	**-0.712**	0.305	1.092
Wolfe et al. (2005)	P	1965-2001	NE USA	-0.135	X	X	-0.025	0.358	0.395
Ahas et al. (2002)	P	1951-1998	C & W Europe	-0.583	X	X	**-0.702**	0.275	1.064
Ahas et al. (2002)	P	1951-1998	E Europe	0.218	X	X	**-0.223**	**0.198**	0.421
Schwartz et al. (2006)	P	1955-2002	NH	-0.125	X	X	**-0.189**	**0.143**	0.407
Keeling et al. (1996)	C	1964-1992	NH	X	X	0.241	-0.329	0.054	0.424
Carter (1998)	C	1890-1995	Fennoscandia	-0.075	0.047	0.132	-0.509	0.423	0.933
Schwartz and Chen (2002)	C	1959-1993	China	-0.171	0.114	0.285	**-0.653**	**-0.319**	0.359
Linderholm et al. (2006)	C	1951-2000	Baltic	-0.126	0.026	0.148	-0.263	0.189	0.456

133

regarding growing-season length only one estimation (Stöckli & Vidale, 2004) agrees. Regarding studies from phenological records, the results for spring date trends compare well with the ones obtained by the methodology described above in cases of global studies (Ahas *et al.*, 2002; Schwartz *et al.*, 2006), probably due to the high number of stations used for these studies. Trends in phenology retrieved from climate data compare badly with the results of this study. The differences observed with trends from previous studies are probably due to the fact that the pixels considered as stable or frozen in this study were not included in the trend estimations, since no phenology was retrieved from them, in opposition with previous studies. For example, past NDVI studies do include evergreen forests in their phenological trends, when those areas are excluded from this study, explaining why the retrieved trends are generally lower.

In order to validate the retrieved time series of start, end and length of growing-season, correlations have been calculated with time series of climate indices, such as SOI (Southern Oscillation Index), available at:

http://www.bom.gov.au/climate/current/soihtm1.shtml

NAO (North Atlantic Oscillation), available at:

http://www.cpc.noaa.gov/products/precip/CWlink/pna/nao.shtml

and PDO (Pacific Decadal Oscillation), available at:

http://jisao.washington.edu/pdo/PDO.latest

Those indices are monthly means, and have been averaged yearly, from January, 1st to December, 31st for the Northern Hemisphere, and from July, 1st to June, 30th for the Southern Hemisphere. Correlations were then calculated between these series of annual climate indices and time series of growing-season start, end and length for each pixel. Figure 4.8 shows the pixels for which correlations were significant at 95% confidence level, in black for negative correlations, and in white for positive correlations. SOI corresponds to the Tahiti minus Darwin normalized pressure index, which measures whether the climate system is in the El Niño or La Niña state. One can observe that SOI has a global influence on growing season parameters, and is not restricted to its geographical area. This occurs as teleconnections as the atmosphere transmits anomalous heating in the tropics to large-scale convection and thus to anomalous winds in the atmosphere. NAO index
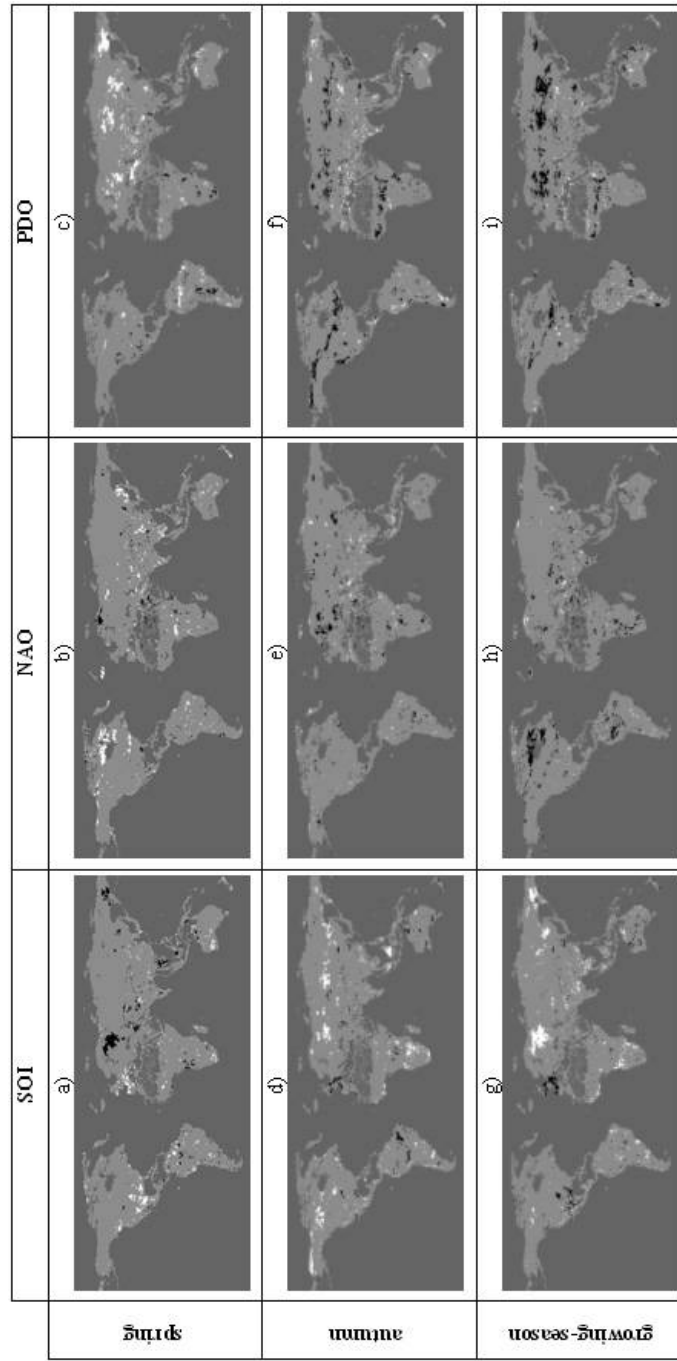
Figure 4.8.- Correlation between spring, autumn, growing-season and SOI, NAO, PDO indices. White indicates statistically significant positive correlation, black indicates statistically significant negative correlation, while grey indicates statistically insignificant correlation.

135

measures the large-scale alternation of atmospheric pressure between the North Atlantic regions of the sub-tropical high (near the Azores) and sub-polar low pressure (extending south and east of Greenland), which determines the strength and orientation of the poleward pressure gradient over the North Atlantic, and the mid-latitude westerlies in this area. PDO (also called Interdecadal Pacific Oscillation - IPO) index is derived as the leading principal component of monthly SST anomalies in the North Pacific Ocean, poleward of 20º N latitude. The monthly mean global average SST anomalies are removed to separate this pattern of variability from any "global warming" signal that may be present. This index has been shown to be a significant source of decadal climate variation throughout the South Pacific and Australia, and also the North Pacific (Salinger, 2005). Large spatial patterns of statistically significant correlations can be observed for spring over Western and Eastern Europe, Southern North America, and more locally over the rest of the globe (Fig. 4.8a). Regarding correlation with autumn time series (Fig. 4.8d), positive correlations are located at Northern- and Southernmost latitudes, while negative correlations are mainly located in Western Europe, and Amazonia. Regarding correlation with growing-season length time series (Fig. 4.8g), negative correlations are observable around the Northern Atlantic Ocean, while positive correlations are located in the rest of the globe, with greater spatial homogeneity over Eastern and Western Russia. Spring and NAO time series show significant positive correlations mainly in the Eastern North Atlantic Ocean (namely in Iceland and Great Lakes area), while negative correlations can be observed in Lapland (Fig. 4.8b). Regarding autumn time series (Fig. 4.8e), only Eastern Europe shows a clear pattern of negative significant correlation, while small patches of significant correlation can be observed locally all around the world. Regarding growing-season time series (Fig. 4.8h), significant negative correlations are located in the Great Lakes region, in Amazonia and in Southern Africa. Small patches of significant positive correlation are visible over the whole globe, with bigger extent in Lapland. Spring and PDO time series show significant positive correlation mainly over Asia, but also along the Equator (Fig. 4.8c). Small patterns of significant negative correlations can be observed in South America and South-East Africa. Regarding autumn time series (Fig. 4.8f), significant negative correlations can be observed North of 40º N, while significant positive correlations are distributed more locally over the rest of the globe. Regarding growing-season

136

time series (Fig. 4.8i), the distribution of significant correlation is similar to that of autumn time series.

These correlations between climate indices and growing-season parameters show in general a good spatial homogeneity: small patches of spatially contiguous pixels exhibit similar correlations, in opposition to the heterogeneity that can be observed in India or in the Sahara, where correlations do not show spatial coherence. This validates the approach developed above for most of the globe, in addition to providing insight of the drivers of the change.

4.2.2.- Extension to pre-satellite period (1948 -2006)

Since global estimations of phenological dates arose with satellite data, only few global results are available before the 1980s, and most of them resulting from ground measurements limited to the northern hemisphere (Schwartz *et al.*, 2006). Here, we used the results of the previous paragraphs to extrapolate spring dates to the period 1948-2006, using air temperature at 2m data from Reanalysis database (see Chapter 2). These results have been submitted for publication to the Remote Sensing of Environment.

4.2.2.1.- Methodology

We use the global spring dates retrieved from GIMMS data (see above), in comparison with degree-day values (see below) for the same period, to identify the thresholds necessary to calculate the amount of degree-days reached at spring date. With the help of these thresholds, we calculate the degree-day values for the second half of the 20th century, to finally estimate trends for phenological spring dates. Since this extrapolation is done only with air temperature data, the results obtained for areas where vegetation is not limited by temperature (tropical rainforests, for example) are not to be trusted.

Degree-days calculation

Réaumur (1735) introduced the degree-days as a descriptor of plant phenology. Each vegetal species has its own degree-day thresholds (Snyder *et al.*, 1999) corresponding to specific development events (such as bud sprouting, blooming, fruit maturation, senescence, etc.), and degree-days are calculated with different

thresholds depending on plant characteristics. The general formula for degree-day calculation is the following:

$$DG = \sum_{T>T_0}(T - T_0) \tag{4.7}$$

where DG is the degree-day total amount, T corresponds to the daily averaged air temperature at 2m (in Celsius degrees), and T_0 to a temperature threshold depending on the plant characteristics, the sum being calculated only for the days which daily averaged air temperature at 2m is higher than the given threshold (T_0), starting January, 1st for the northern hemisphere, and July, 1st for the southern hemisphere. Daily averaged air temperatures (T) are calculated as averages of the four 6-hourly air temperatures available from Reanalysis corresponding to the given day. Values of T_0 are plant dependent, and are the following (Chang, 1974):

- $T_0 = 5°C$ corresponds to cereals,

- $T_0 = 7°C$ corresponds to Mediterranean cultures,

- $T_0 = 10°C$ corresponds to tree bearing fruits.

Degree-day annual amounts are an indicator of the climate, and can be used for climatic area classification (Sobrino *et al.*, 2006a).

Thresholds retrieval

The two datasets used in this study have different spatial resolutions (see Chapter 2), thus GIMMS retrieved spring date images have been resampled at Reanalysis resolution, identifying for each Reanalysis pixel the GIMMS pixel closer to its geolocation (latitude and longitude). The spring date assigned to the resampled image is calculated from a 3 by 3 neighborhood around this GIMMS pixel, over which valid spring dates are averaged.

Then, two thresholds have to be determined for each pixel: T_0, associated with the characteristics of the vegetation present in the considered pixel, and DG, amount of degree-days corresponding to spring (or leaf outburst), related both to vegetation and climate (see Eq. 4.7). To this end, maps of the dates at which the DG threshold are reached for each of the three T_0 thresholds are calculated from 1981 to 2003, with DG thresholds fixed with steps of 10 degree-days, from 0 to 7000 degree-days. Pearson correlations between the time series of GIMMS and

Reanalysis retrieved spring dates are then calculated for all DG and T_0 values, and the DG and T_0 values corresponding to the highest Pearson correlations are selected as the adequate for degree-day calculations for this study. Correlation is expected to reach significant values for temperature-limited vegetation (in temperate and boreal areas), since degree-day amounts are a common tool for determining their phenological phases. Of course, for vegetation limited by soil nutrients or water availability, correlation values are expected to be low.

Finally, with the help of these two thresholds, spring date time series are calculated for the whole Reanalysis database, i.e. 1948 to 2006, and then tested for trends using Mann-Kendall trend tests (Hirsch & Slack, 1984).

4.2.2.2.- Results

Figure 4.9 shows the resampled spring date for 1990 in the northern hemisphere, and 1990-1991 for the southern hemisphere, in days of year. Those years have been chosen arbitrarily for display. In the northern hemisphere image, one can observe easily the latitudinal gradient in spring dates, the spring dates getting earlier as one gets closer to the equator, with the exception of the Indian subcontinent and the tropical areas, which can be easily explained by the special rain regimes that affect India and the tropical areas. Then, for the southern hemisphere, the same latitudinal gradient is visible, symmetric to the equator.

Figure 4.10 presents the Pearson correlation maximum values obtained between time series of GIMMS and Reanalysis retrieved spring dates for all DG and T_0 values for each pixel. These correlations are significant at 95% level for values higher than 0.42, and at 99% level for correlations higher than 0.54. From Figure 4.10, one can observe that the highest correlation values (above 0.5) for extended areas are located only in the Northern temperate areas. Polar, tropical and equatorial areas have lower values, down to 0.2 for a few given pixels, for which the estimated thresholds and trends must be considered cautiously.

Figure 4.11 shows the spatial repartition of T_0 and DG thresholds around the globe (see Eq. 4.7), only for pixels which significant correlation values at 95% confidence level. Pixels with insignificant correlation values are displayed in dark grey. T_0 threshold appears to be vegetation dependent, the polar areas tending to have a 5°C T_0 threshold with local exceptions, due mainly to land cover type. T_0 shows a great spatial variability, probably due to land occupation (Snyder *et al.*,

1999). DG thresholds show a latitudinal gradient, as expected, being lower near the poles and higher at low latitudes, with the exception of equatorial areas (see Figure 4.11b), where spatial consistency may be altered by enduring cloud cover, which degrades the precision of spring determination in GIMMS images.

Figure 4.12 shows an example of spring date images for 1990 in the northern hemisphere and 1990-1991 for the southern hemisphere, both calculated from degree-days amounts. Comparing this image with Figure 4.9, one can observe that the spring dates for Figure 4.12 occur globally sooner than for Figure 4.9,

Figure 4.9.- Spring dates (in days of year) for a) year 1990 (beginning on January, 1st) and b) year 1990-1991 (beginning on July, 1st) retrieved from GIMMS (Global Inventory Modeling and Mapping Studies) data.

Figure 4.10.- Correlation values in threshold determination for degree-day calculations.

140
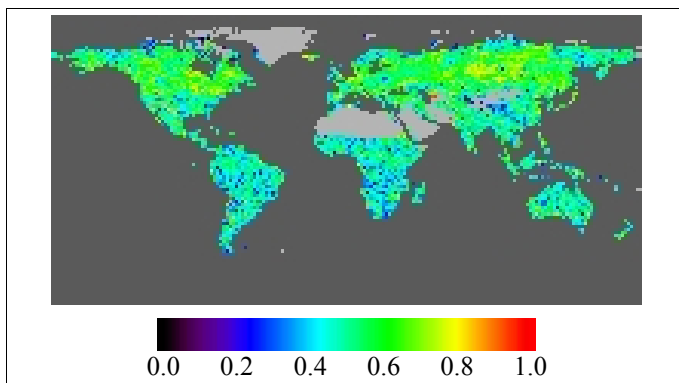
especially for the northern tropical area, corresponding to the noisy area mentioned in Figure 4.11b.

Figure 4.13a presents the global trends for the 1948-2006 period, showing only the trends (retrieved by ordinary least square method) for the pixels passing Mann-Kendall trend tests at 90% confidence level. The average trend for all the statistically significant values is around -0.0744 days per year, which correspond to a more than 4-day overall advance in spring dates at global scale over the past 59 years, with values ranging mainly from less than -0.8 days per year (advance) in Southern Africa and around the Himalayan mountains to more than +0.6 days per year (delay) along the Andes. Temperate areas see generally an advance in their Reanalysis retrieved spring dates, corresponding to the well documented increase in air temperatures (IPCC, 2001). Strong advances (greater than -0.5 days per year) are mainly located in mountains of the temperate areas, while strong delays (greater than +0.5 days per year) are mainly located in the Southern hemisphere.

4.2.2.3.- Discussion

The results presented in the above paragraph are in concordance with the well documented increase in air temperatures, which is part of the climatic change under way (IPCC, 2001). However, the results presented here are based on a fitting technique on yearly satellite images, which, in spite of the used compositing technique, can include cloud-contaminated images, especially in areas with high cloud coverage, such as equatorial areas. The repeated presence of clouds influences the accuracy of the determination of spring dates, which in return provokes artificial instability in temporal series of spring dates. This instability hinders in return the threshold estimations for degree-day calculations, since the correlation between dates for reached degree amounts and spring dates is then diminished.

Linderholm (2006) has compiled phenological changes from various previous studies based on phenological, satellite and climate data. Many of those studies are carried out at the local or regional scale, which can not be easily compared with our study since the resolution of the database we used is of 2.5º, leading to a small number of pixels for each considered country. The results presented above differ of the previous studies (Myneni *et al.*, 1997; Tucker *et al.*, 2001; Zhou *et al.*, 2001; Stöckli & Vidale, 2004) in the fact that some places see a delay of their spring

phenology, fact which does not appear in the mentioned studies. This can be due to the fact that the results are usually averaged on local to regional areas, when the approach described in this study is pixel by pixel based. Moreover, only pixels with a statistically significant trend are considered here, meaning that all pixels with trends statistically insignificant at 90% confidence level are rejected, when other studies usually average the estimated trends over a geographical area to, in a few cases, estimate the statistical significance of the results.

Trends for large areas (global, Northern hemisphere, 45N-75N latitude band) obtained from satellite data usually have an estimated spring trend around -0.2 to -0.3 days per year (Myneni *et al.*, 1997; Tucker *et al.*, 2001; Zhou *et al.*, 2001; Stöckli & Vidale, 2004), which is higher than the results presented here (-0.0744 days per year), but these global studies are carried out from satellite data only, which time extent never covers more than the last 25 years. When restricted to the period 1981-2006, the global average trend for this study decreases to -0.204 days per year, comparable to the values obtained in previous studies (see Figure 4.13b).

A few phenological studies have been conducted on large areas (Menzel & Fabian, 1999; Ahas *et al.*, 2002; Schwartz *et al.*, 2006). Retrieved trends in first leaf dates range from +0.4 days per year over Eastern Europe to -1.0 days per year over Central and Western Europe (Ahas *et al.*, 2002), while the average trend over Europe is of -0.2 days per year (Menzel & Fabian, 1999). Over the Northern hemisphere, phenological trend in first leaf date is of -0.12 days per year (Schwartz *et al.*, 2006). These trends are more scattered than the ones retrieved from satellite data, due to the low coverage of phenological stations, with areas excluded from the study (like boreal and tropical areas). Nevertheless, the results presented here are within the order of magnitude of those trends.

Of course, the model used here only takes into account air temperatures, without studying the influence of other parameters, like available water for example. Nemani *et al.* (2003) published a global map of climatic constraints to plant growth, which is presented in Figure 4.14. This map shows that plant growth is limited by temperature (at least partially) only in temperate and polar areas. Thus, those areas are susceptible to de described correctly with the use of degree-days, while the rest of the globe would need the inclusion of precipitation to complete the model. One can observe that those latter areas are the ones showing

142

Figure 4.11.- Retrieved thresholds for spring dates estimation from degree-days: a) T_0 - daily threshold (in ºC) and b) DG - total degree-day amount (cf. Eq. 4.7).
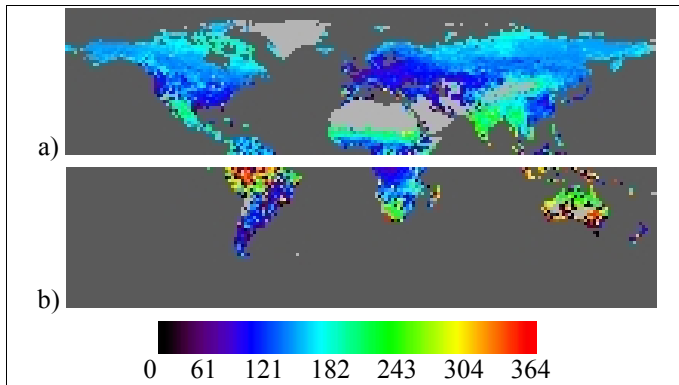

Figure 4.12.- Spring dates (in day of years) for a) year 1990 (beginning on January, 1st) and b) year 1990-1991 (beginning on July, 1st) estimated from degree-day amounts.

143
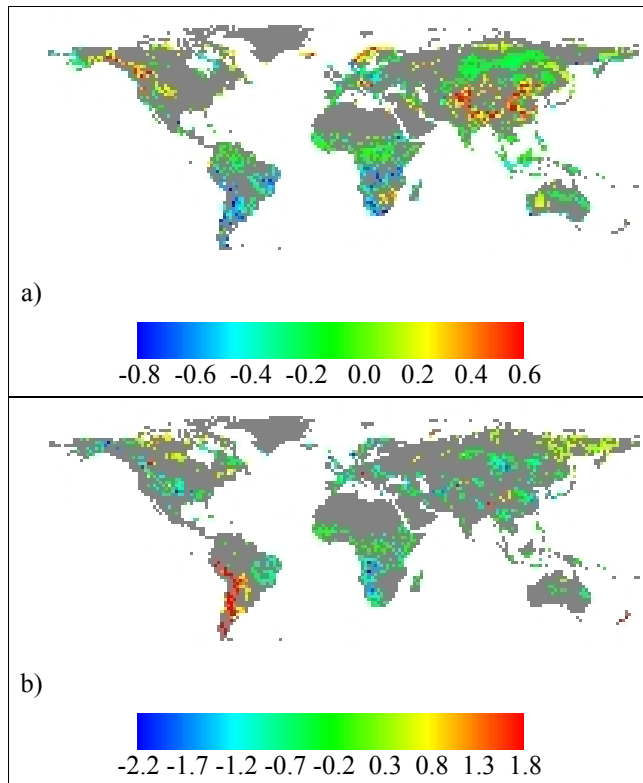
Figure 4.13.- Trends for spring dates (in days per year) estimated from degree-day amounts for the 1948-2006 period (a) and for the 1981-2006 period (b). Only statistically meaningful trends (Mann-Kendall trend tests) are shown.

Figure 4.14.- Geographic distribution of potential climatic constraints to plant growth (adapted from Nemani et al., 2003).

the higher concentration of small correlation values between satellite and degree-day estimates of spring date in Figure 4.10 (displayed in dark grey).

Moreover, Reanalysis model is known to behave badly around mountains, where high spatial variability can not be described correctly by its 2.5º grid. Mountainous areas are actually the ones showing the highest trend values (positive as well as negative) for both 1948-2006 and 1981-2006 periods (see Fig. 4.13). For 1981-2006 period, the highest delays (+1.8 days per year) in spring occurrence are obtained around the Andes mountains, while for 1948-2006 period, highest delays (+0.6 days per year) in spring occurrence are obtained around the Rocky and Himalaya mountains, while some pixels in the Andes mountains show the highest advances (-0.8 days per year). The inverse trend pattern around the Andes for 1948-2006 and 1981-2006 periods is highly suspicious, and would need some direct comparison with phenological ground data for validation. However, we could not find any regional or continental phenological record for direct validation.

4.2.3.- Other NDVI metrics

All the methods described above (section 4.1) can also allow retrieving other NDVI metrics, such as maximum and minimum values, or maximum and minimum slope values. Here, we will discuss the NDVI metrics retrieved by the double logistic fitting method, namely wNDVI, mNDVI, mS and mA, since spring and autumn dates have already been discussed above. To these metrics has been added the integrated NDVI (iNDVI), defined as the positive area below the double logistic function fitted to yearly NDVI evolution. At the time of redaction of this manuscript, this work is being submitted to an international journal for publication.

4.2.3.1.- Results

As proceeded above, to determine the stability of the approach and thus the validity of the retrieved trends, a principal component analysis has been carried out separately on wNDVI, mNDVI, mS, mA and iNDVI time series. Only the first components for all those parameters are displayed in Figure 4.15, since the rest of the components explain equally the rest of the variance. Regarding wNDVI images (Fig. 4.15a), the first component explains 67% of the variance; regarding mNDVI images (Fig. 4.15b), the first component explains 94% of the variance. Regarding mS images (Fig. 4.15c), the first component explains only 19% of the variance; regarding mA images (Fig. 4.15d), the first component explains 39% of the variance. Finally, regarding iNDVI images (Fig. 4.15e), the first component
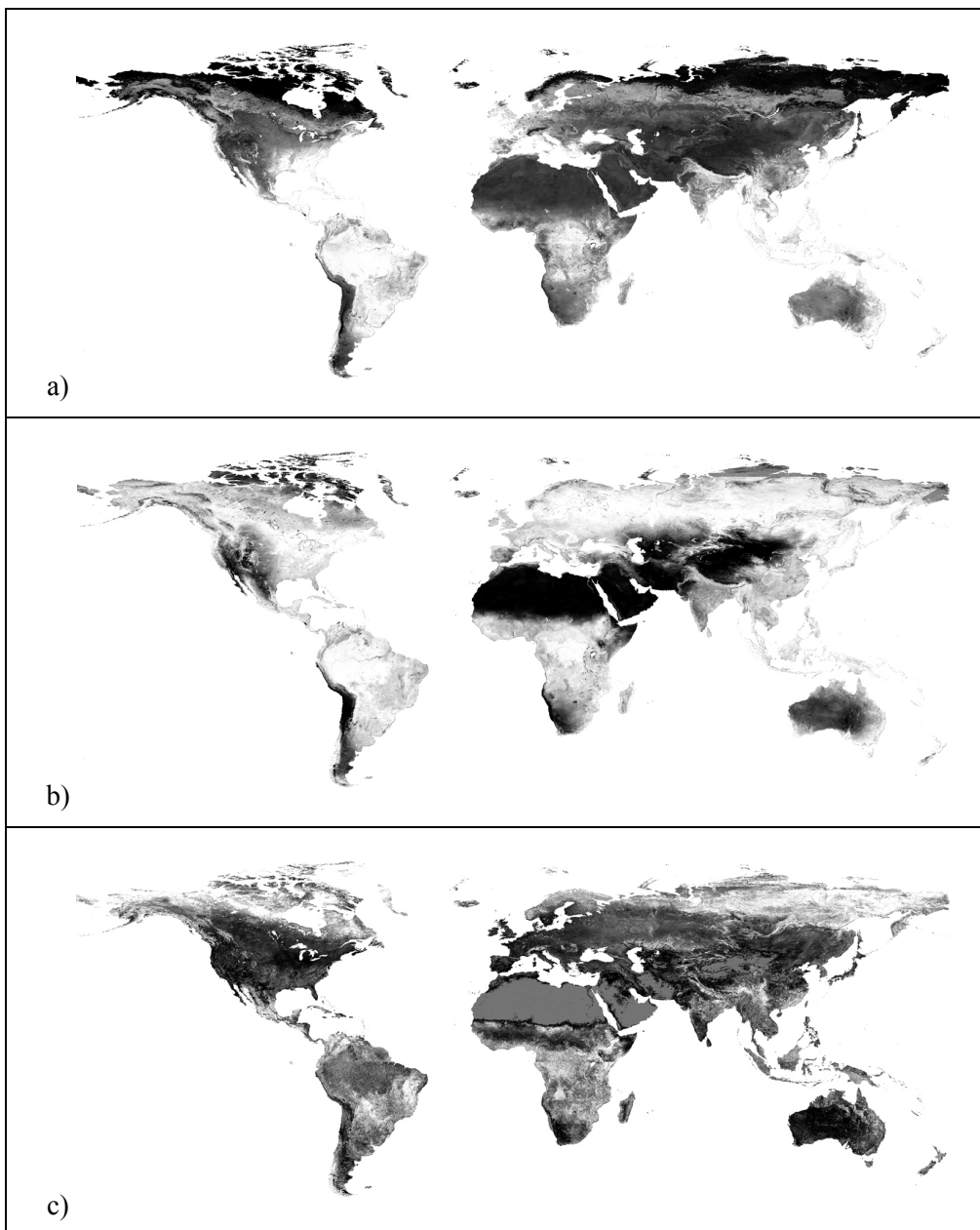
Figure 4.15.- Results of empirical orthogonal analysis on correlation matrices for time series of NDVI metrics. 1st components are displayed for a) wNDVI (1st component explains 67% of total variance); b) mNDVI (94%); and c) mS (19%).
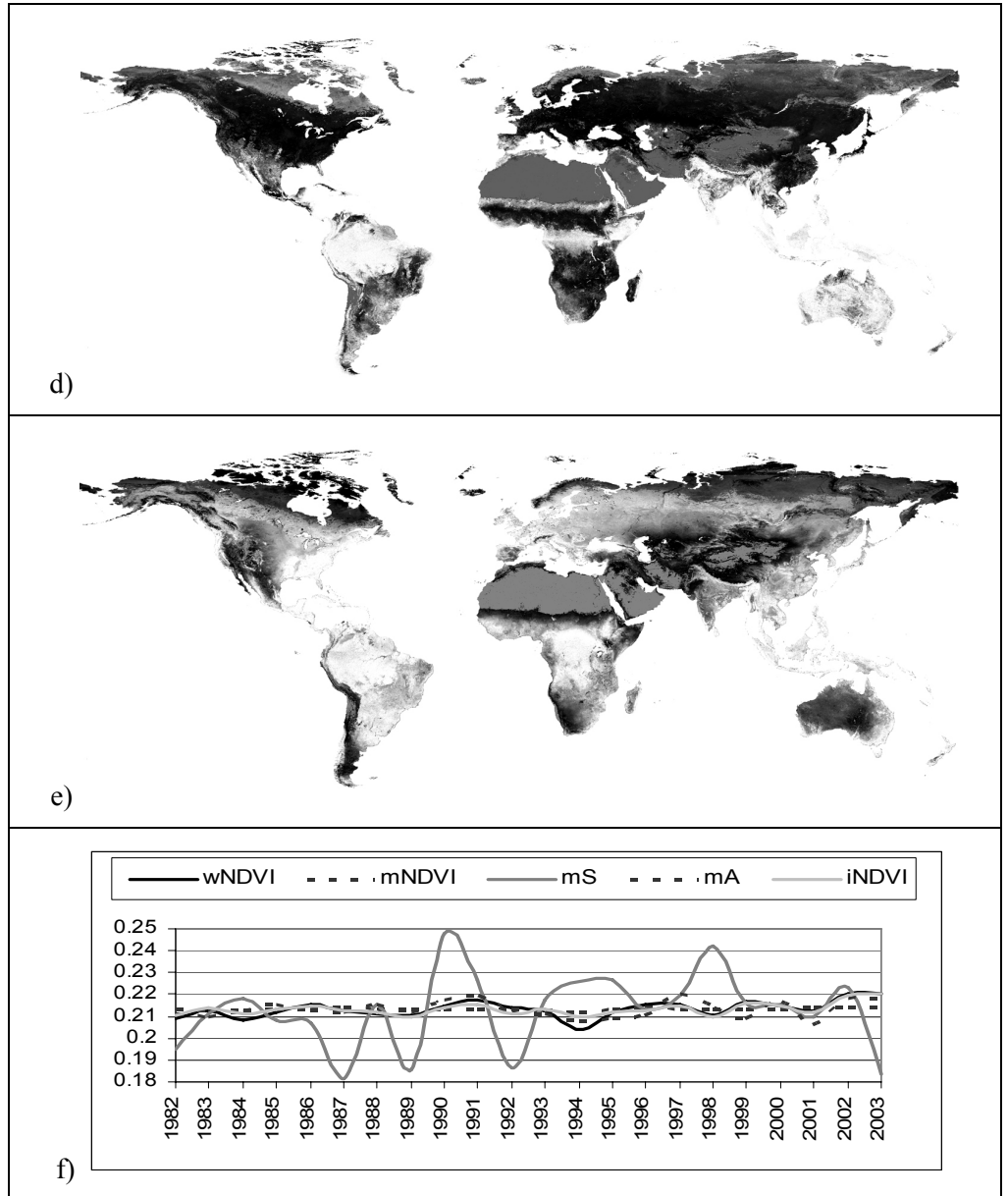
Figure 4.15.- (continued) Results of empirical orthogonal analysis on correlation matrices for time series of NDVI metrics. 1st components are displayed for d) mA (1st component explains 39% of total variance); and e) iNDVI (66%). Finally, the influence of each year in those first components is displayed (3f).

explains 66% of the variance. Figure 4.15f shows that the influence of each year in the first component for all five parameters is basically the same, indicating a good overall stability of the approach, except for mS parameter. This is logical since the percentage of the total variance explained by mS first component is quite low. As one can observe, the determination of mS parameter is quite unstable, which can also explain the relative instability of Spring and wNDVI parameters in comparison with Autumn and mNDVI parameters respectively. This is probably due to cloud or snow presence at the end of the dormancy period. However, visual inspection of Figure 4.15a to 4.15e allows the discrimination of vegetation types (for example arid versus vegetated areas) as well as more subtle variations such as mountains or riverbeds.

Figure 4.15 shows, in agreement with Figure 4.4, that fitting yearly evolution to double logistic function is highly stable spatially, except for areas along the Equator and South Eastern Asia, where special rain regimes occur, with enduring cloud cover. Obviously, wNDVI, mNDVI and iNDVI parameters are more stable, their 1st PCA component explaining at least two thirds of the total variance, while mS and mA 1st PCA components explain little of the total variance. This is due to the high sensitivity of the fitting method to cloud presence at transition dates (S and A), for which cloud correction is quite difficult to carry out. This explains the highest spatial variability of the results in areas with enduring cloud cover, especially regarding mS and mA parameters. These latter parameters show additional variability in polar areas, for which a similar phenomenon occurs, due mainly to snow melt in spring, and snow fall in autumn.

As with phenological parameters, Mann-Kendall tests have been carried out for each pixel time series, and trends have been determined by linear regression for those pixels for which the no-trend hypothesis could be rejected at 90% confidence level. The results are presented in Figure 4.16 for winter, maximum and integrated NDVI as well as mS and mA parameters time series. Retrieved wNDVI values (Fig. 4.16a) have seen an increase in average of $5.4 \cdot 10^{-4}$ year^{-1} over the whole globe, the image being scaled between decreases and increases of $9.0 \cdot 10^{-3}$ year^{-1}. Stronger increases are located mainly in Northern South-America, central Africa and Southern Asia, while stronger decreases are located mainly in semi-arid areas, as well as for a large latitude band between 45ºN and 60ºN. Regarding mNDVI values (Fig. 4.16b), the trend over the whole globe is towards a lower increase, of

148

$7.8 \cdot 10^{-5}$ year^{-1} in average, and the image has also been scaled between decreases and increases of $9.0 \cdot 10^{-3}$ year^{-1}. Areas seeing strongest increases in mNDVI are located in transition areas, around deserts (Sahel) or mountains (Northern India) as boreal areas. Strongest decreases are located in the areas singled out as highly variable (Amazonia, central Africa, South-East Asia) as well as in the 45-60ºN latitude band. One can also observe that desert areas (Sahara, Middle-East, Atacama) show a slight positive significant trend. This trend has a value lower than 0.001 year^{-1}, summing 0.02 NDVI units for the whole extent of the database, which is roughly the accuracy of NDVI estimation. Thus, the GIMMS database is quite stable throughout its 22 year extent. However, global average trend values for wNDVI and mNDVI are probably overestimated, due to this low trend in desert
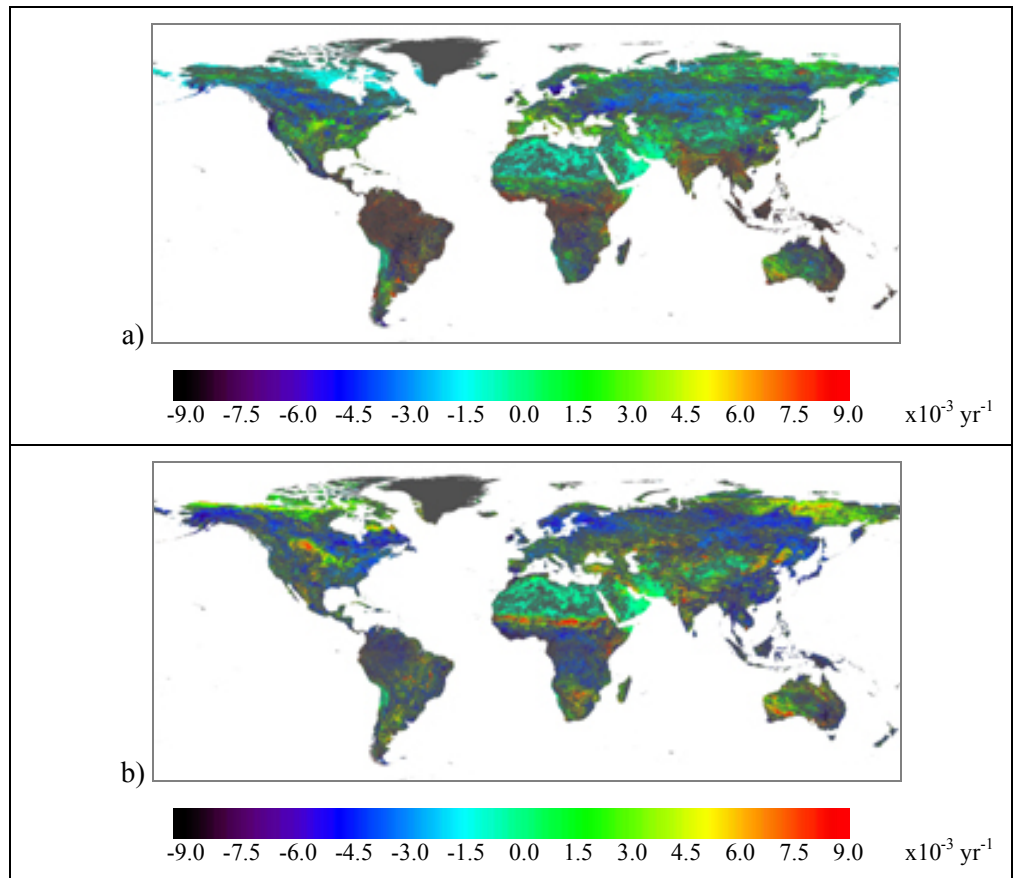
Figure 4.16.- Trends in a) wNDVI; b) mNDVI time series for pixels exhibiting trends at 90% confidence level.
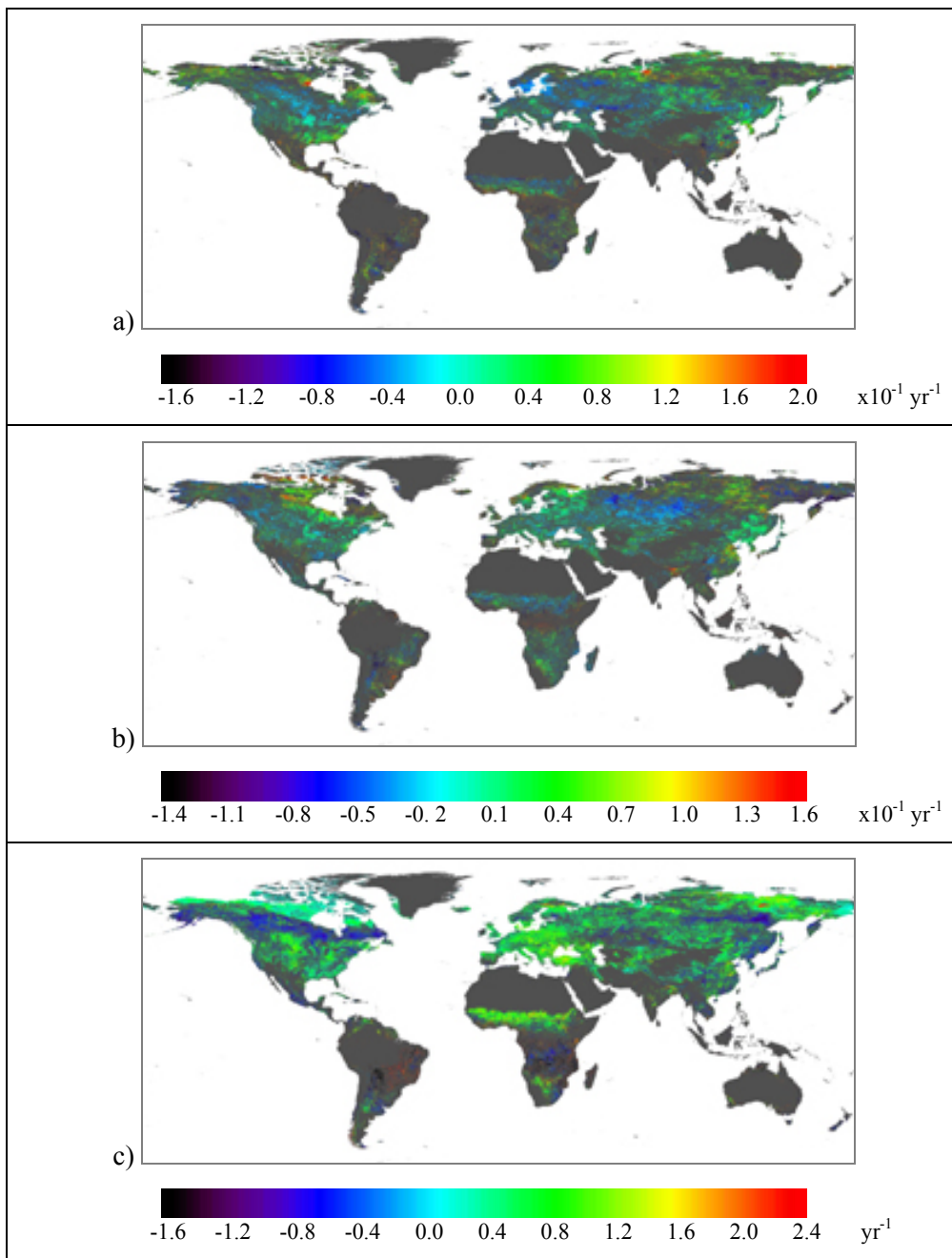
Figure 4.16.- (continued) Trends in c) mS; d) mA; and e) integrated NDVI (iNDVI) time series for pixels exhibiting trends at 90% confidence level.

areas (-5.0·10^{-4} yr^{-1} for wNDVI, and -1.0·10^{-3} yr^{-1} for mNDVI). Trends for mS and mA parameters are significant for a lesser number of pixels than the two previous parameters. This can be explained by their high dependence on cloud presence at spring and autumn dates. mS global trend (Fig. 4.16c) has an average of 0.2 yr^{-1}, the image being scaled between -1.6 and 2.0 yr^{-1}. Highest positive mS trends are located punctually in boreal areas, while strongest decreases are located in the Bolivian Andes. However, these trend patterns are very fragmented, especially south of 15ºN latitude. mA global trend (Fig. 4.16d) is of 0.01 yr^{-1}, the image being scaled between -1.4 and 1.6 yr^{-1}. Strongest decreases in mA parameter are located in Bolivia and in boreal regions, while strongest increases are located in Bangladesh and boreal regions. Trend patterns are also fragmented for this parameter. Finally, global trends for iNDVI (Fig. 4.16e) have an average trend value of 0.35 yr^{-1}, the image being scaled between -1.6 and 2.4 yr^{-1}. Extreme values are found in the already mentioned highly variable areas. The whole of central Europe has seen a significant positive trend in integrated NDVI values, while South Canada has seen a significant negative trend for this parameter.

4.2.3.2.- Validation

To validate those results at global scale, we decided to compare the retrieved trends with documented changes all around the world. To this end, we used the UNEP (United Nations Environment Programme) publication titled "One Planet Many People" (UNEP, 2005), which lists a series of locations (125) around the world for which changes have been documented, with satellite images of the area before the eighties and after 2000 (Landsat images). Those locations were geo-referenced to our GIMMS images, in order to monitor trends for various parameters corresponding to the documented areas. Changes have been classified in 14 categories, which are presented in Table 4.4.

The different control points are displayed in Figure 4.17. Some areas identified as changing in UNEP (2005) report have been attributed to different categories in function of the nature of the change occurring for specific locations included in the reported area.

For each control point of each change category, spring (S), autumn (A), growing-season (G-S), wNDVI (wVI), mNDVI (mVI), mS, mA and iNDVI (iVI) trends have been retrieved, considering the GIMMS pixel closest to control point

location (latitude and longitude, retrieved from UNEP Google™ Earth files). The results have been separated by change categories to make the validation easier. These results are presented in Tables 4.5 to 4.19. Those parameters which do not exhibit significant trends have been marked with an 'X', and control points for which significant change has been retrieved for at least one parameter are highlighted in grey.

Table 4.4.- Class change categories.

Category	Observation
0	No change
1	Deforestation
2	Desert to agriculture conversion
3	Water to land conversion
4	Land to water conversion
5	Volcanic eruption
6	Mine expansion
7	Urbanization
8	Glacier retreat
9	Pollution
10	Desertification
11	Mangrove t shrimp farm conversion
12	Land cover degradation
13	Land use change

A first observation regarding Tables 4.5 to 4.18 is that many control points do not show any significant trend (at 90% confidence level) for any parameter. This is due to various reasons: 1) 22 years of data are not such a long period to observe statistically significant trends, especially for areas with high variability; 2) some of the changes occurring at control points are very local and can not be resolved at GIMMS resolution (8 km by 8 km); 3) some changes occur in areas with enduring cloud cover, for which the procedure is unstable; 4) other changes are difficult to identify in terms of NDVI variations.

The first change category, no change, is quite difficult to evidence with the methodology presented here, since the absence of significant trend does not imply the absence of trend. Table 4.5 shows the retrieved trends for 2 control points

corresponding to no change category. One of these control points (Virunga National Park) does show a significant trend for mS parameter. It can be due to the fact that the no change area is quite small, and surrounded by areas where changes in the land cover have occurred (UNEP, 2005).

Figure 4.17.- Location of UNEP (2005) control points for validation.

Table 4.5.- Changes for all parameters for class 0 (no change) control points. S, A and G-S parameters are given in days per year; wVI and mVI are given in 10^{-3} NDVI units per year; iVI in NDVI units year per year; and mS and mA in days^{-1} per year. X indicates no significant trend (at 90% confidence level).

Control point	S	A	G-S	wVI	mVI	iVI	mS	mA
Sundarban	X	X	X	X	X	X	X	X
Virunga-National-Park-1	X	X	X	X	X	X	-0.122	X

Regarding deforestation category (Table 4.6), 19 out of 25 control points show significant trends for at least one parameter, the majority showing changes in at least one NDVI parameter (wNDVI, mNDVI or iNDVI), but not always in the same direction. However, for the few control points with significant trends in phenological parameters (spring and autumn dates, growing-season), change due to deforestation leads towards a later occurrence of spring, and an earlier occurrence of autumn, thus towards a shortening of growing-season. This is logical, since forests are usually cleared for agriculture purposes, for which phenological spring and autumn depends on sow and ripe dates, and usually occur after phenological spring and before phenological autumn. mS and mA parameters also show significant trends for a few control points, although without any clear pattern, since those parameters depend on the land cover replacing the forest. Of the 5 control points which do not exhibit significant trends, 2 correspond to pixels including also

153

no change category (Country Border, between Mexico and USA, and Paektu-San, in North Korea), the other 3 being located in areas with enduring cloud cover (Amazonia and central Africa).

Table 4.6.- Changes for all parameters for class 1 (deforestation) control points. S, A and G-S parameters are given in days per year; wVI and mVI are given in 10^{-3} NDVI units per year; iVI in NDVI units year per year; and mS and mA in days^{-1} per year. X indicates no significant trend (at 90% confidence level).

Control point	S	A	G-S	wVI	mVI	iVI	mS	mA
Adis-Abeba	X	X	X	-1.78	7.87	X	X	-0.180
Angangueo	X	X	X	-9.19	X	X	X	X
Arkhangelsk	X	X	X	X	X	0.598	X	X
British-Columbia	X	X	X	-3.97	3.67	X	X	-0.027
Country-Border	X	X	X	X	X	X	X	X
Gishwati	X	X	X	X	-10.82	X	X	X
Guinea-Refugee-Camps	X	X	X	7.37	X	X	X	-0.054
Iquazu	X	X	X	X	X	X	X	X
Itampolo	1.50	-1.02	-2.66	X	X	-0.761	0.064	X
Kisangani	X	-1.37	X	12.23	X	0.534	X	X
Lappi	X	X	X	X	-3.89	X	X	0.043
Mabira-Forest-Reserve	X	X	X	X	-3.67	X	X	X
Olympic-Peninsula	1.41	X	X	5.76	X	X	X	X
Oudomxay	X	X	X	8.85	X	X	X	X
Paektu-San	X	X	X	X	X	X	X	X
Rondonia	X	X	X	X	X	X	X	X
Sakhalin	X	X	-0.40	X	X	-0.420	X	0.123
Santa-Cruz	X	X	X	X	4.71	-4.318	-0.121	X
Shatt-Al-Arab	X	X	X	-5.42	-12.92	X	X	X
Shume-Magamba	X	X	X	X	X	X	X	X
Tai-National-Park	X	X	2.59	X	X	X	X	X
Tensas-River	X	X	X	X	X	-0.457	0.027	-0.033
Valdivian	4.37	-1.99	-2.23	X	X	X	X	X
Virunga-National-Park-2	X	X	X	X	X	X	X	X
Virunga-National-Park-3	X	X	6.97	-12.67	4.35	X	X	X

As regards desert to agriculture conversion, only four control points have been identified, which all show significant trends for at least one parameter. Two control points (Al Isawiyah, in Saudi Arabia, and Lake Djoudj, at the border of Mauritania and Senegal) have, as expected, significant positive trends in maximum NDVI value, while one control point (Lake Manantali, Mali), shows a surprising negative trend in this same parameter. This is due to the fact that this land conversion is originated by a dam construction, which created a lake of great extension (30 km by 10 km), partially included in the considered pixel. Finally the remaining control point exhibit positive trends in spring and autumn occurrence, which are difficult to link to the occurred change.

Regarding water to land conversion category (class 3), NDVI level parameters are supposed to increase, since water has negative NDVI values, while land has positive NDVI values. However, 5 out of 18 control points show no significant trend for any parameter. Those 5 control points can be divided in two groups: the first three control points (Aral Sea, in Kazakhstan, Huang He Delta, in China, and Kara Bogaz Gol, in Turkmenistan) correspond to areas identified in the GIMMS database as water or sea, while the last two (Lake Chad , at the borders of Niger, Nigeria, Chad and Cameroon, and Lake Tonga, at the border between Algeria and Tunisia) do have positive trends in NDVI levels (wNDVI and mNDVI) but do not pass Mann-Kendall trend tests. As expected, main significant trends are retrieved for NDVI level parameters, but not always in the expected direction. For example, Lake Hamoun (Iran), sees a decrease in both NDVI levels. This is due to the disappearance of surrounding marshes simultaneous to lake drying, converting the whole area to desert. As regards Lake Chapala (Mexico) water level drop, the newly emerged areas have not developed vegetation, which could explain the decrease in winter NDVI parameter. As for Mesopotamia marshlands (Iraq), the draining of these marshlands has resulted in the disappearing of forests, replaced by cultivated, desert, and urban land, which explains the negative trends observed in both NDVI level parameters.

Table 4.7.- Changes for all parameters for class 2 (desert to agriculture conversion) control points. S, A and G-S parameters are given in days per year; wVI and mVI are given in 10^{-3} NDVI units per year; iVI in NDVI units year per year; and mS and mA in days^{-1} per year. X indicates no significant trend (at 90% confidence level).

Control point	S	A	G-S	wVI	mVI	iVI	mS	mA
Al-Isawiyah	X	X	X	-1.43	8.05	X	X	X
Ataturk-Dam-2	4.60	9.27	X	X	X	X	X	X
Lake-Djoudj-2	X	X	X	4.40	5.46	X	X	X
Lake-Manantali	X	X	X	-3.76	-4.61	-1.48	X	-0.104

Regarding land to water conversion (class 4), this change has generally been conducted through dam construction, meaning that the change has occurred abruptly, and may not appear as a trend. This explains why 7 out 20 control points do not exhibit significant trends for any parameter. The remaining 13 control points do not show a clear pattern of change, which is probably due to the fact that water and irrigated land proportion have changed over the area averaged for each corresponding pixel. Since water appearance lowers NDVI values, while irrigated

land appearance increases them, their respective proportion over a former non-irrigated area explains this lack of pattern of change. For example, the Three Gorges Dam (China), has increased the water levels of the Yangtse river, but also triggered urbanization in the area, which both tend to decrease NDVI level parameters, as appears in table 4.9. Atatürk Dam (Turkey), on the contrary, has provided the surrounding lands with irrigation, which explain the large increase trend in maximum NDVI value.

Table 4.8.- Changes for all parameters for class 3 (water to land conversion) control points. S, A and G-S parameters are given in days per year; wVI and mVI are given in 10^{-3} NDVI units per year; iVI in NDVI units year per year; and mS and mA in days^{-1} per year. X indicates no significant trend (at 90% confidence level).

Control point	S	A	G-S	wVI	mVI	iVI	mS	mA
Aral-Sea	X	X	X	X	X	X	X	X
Huang-He-Delta	X	X	X	X	X	X	X	X
Ijsselmeer	X	1.89	2.70	-3.64	X	X	-0.045	X
Isahaya-Bay	3.44	4.98	X	X	X	X	X	-0.286
Kara-Bogaz-Gol-1	X	X	X	X	X	X	X	X
Lake-Balkhash	X	X	X	X	X	0.371	X	X
Lake-Chad	X	X	X	X	X	X	X	X
Lake-Chapala	X	3.44	X	-4.34	X	-0.510	X	-0.192
Lake-Faguibine-1	X	X	X	2.24	X	X	X	X
Lake-Faguibine-2	X	X	X	X	4.16	X	X	X
Lake-Faguibine-3	X	X	X	4.45	4.99	X	X	X
Lake-Faguibine-4	X	X	X	2.78	12.91	X	X	X
Lake-Hamoun-1	X	X	X	-1.49	-7.60	X	X	X
Lake-Ichkeul	X	X	X	X	5.65	X	X	X
Lake-Jipe	4.78	X	X	X	4.39	X	X	X
Lake-Tonga-3	X	X	X	X	X	X	X	X
Mesopotamia-Marshlands	X	X	X	-2.79	-6.12	X	X	X
Songor-Lagoon	X	X	X	2.51	X	X	X	X

Trends for the two control points which have suffered volcanic eruption are presented in Table 4.10. One of these points (Lake Kivu, Rwanda) does not show any significant trend, due to the date of neighboring Mt. Nyiragongo eruption (January 2002), which is too recent for trends to be retrieved. As for Mount St Helen, its eruption occurred before the start of GIMMS database, which allow monitoring vegetation regrowth. However, the pixel closest to Mount St-Helen coordinates has its center on the non-affected side of the volcano, which explains the negative trends observed for NDVI level parameters in table 4.10.

As regards mine expansion (class 6), trends for all parameters are summarized in Table 4.11. 5 out of 12 control points do not show any significant trend in any

parameter, including La Escondida (Chile), where changes in NDVI levels are one order of magnitude below the trend observed in deserts, and thus are not relevant. For most of these control points, this is due to the small area affected by the mines (Upper Green River, USA; Powder River Basin, USA; Ok Tedi Mine, Papua New Guinea), at kilometer scale when GIMMS resolution is of 8 km. Mine expansion is expected to lower NDVI level parameters, at least for those areas where the mines are surrounded by vegetation. Mines surrounded by bare soil are expected to show little change, as one can verify in the cases of La Escondida (Chile) and Ekati (Canada). Positive trends in NDVI level parameters are difficult to relate to mine expansion, as in the case of Prudhoe Bay (USA), where changes are relatively small compared to pixel size. On the other hand, Athabasca Oil Sands (Canada) show the expected decrease trends in NDVI level parameters, which is confirmed by the fact that mine expansion has been carried out clearing the surrounding vegetation.

Table 4.9.- Changes for all parameters for class 4 (land to water conversion) control points. S, A and G-S parameters are given in days per year; wVI and mVI are given in 10^{-3} NDVI units per year; iVI in NDVI units year per year; and mS and mA in days^{-1} per year. X indicates no significant trend (at 90% confidence level).

Control point	S	A	G-S	wVI	mVI	iVI	mS	mA
Ataturk-Dam-1	X	X	X	X	6.60	X	X	X
Challawa-Dam	X	0.61	X	X	X	X	0.093	X
Gabcikovo	X	X	X	-2.49	3.59	0.53	X	X
Kara-Bogaz-Gol-2	X	X	X	X	X	X	X	X
Lake-Al-Wahda	X	-2.66	-3.85	X	X	X	X	X
Lake-Alaotra	3.44	X	X	5.26	-5.04	1.30	0.258	X
Lake-Cahora-Basa	X	X	X	X	X	X	X	X
Lake-Chivero	X	X	X	X	X	X	X	X
Lake-Djoudj-1	X	X	X	X	1.57	X	X	X
Lake-Tonga-1	X	X	X	-3.28	X	X	X	X
Lake-Tonga-2	X	-2.88	-4.42	X	X	-0.95	X	X
Lake-Victoria	X	X	X	X	-5.33	X	X	X
Lesotho-Highlands	X	X	X	X	X	X	X	X
Phnom-Penh	X	X	X	X	X	X	X	0.220
Sudd-Swamp	X	1.13	X	X	X	X	-0.124	X
Three-Gorges-Dam	-0.85	2.20	3.05	-3.52	-3.18	-0.39	X	X
Toshka-Project-1	X	X	X	0.64	2.03	X	X	X
Toshka-Project-2	X	X	X	X	X	X	X	X
Toshka-Project-3	X	X	X	X	X	X	X	X
Walvis-Bay	X	X	X	X	X	X	X	X

Regarding class 7 (Urbanization), results are presented in Table 4.12. As for the previous class, changes due to urbanization are expected to lower NDVI level

parameters. 12 out of 22 control points do not exhibit any significant trend, although trends are generally negative, except for two control points (Dhaka, in Bangladesh, and Everglades, in USA) which corresponding pixels are considered as water or sea in GIMMS database. All the remaining control points show decreases in NDVI levels, except Santiago (Chile), which only sees a reduction in NDVI yearly amplitude (increase in wNDVI and decrease in mNDVI), and Brasilia (Brazil), where only integrated NDVI exhibits a positive trend. This trend subsists when results are averaged over a 3 by 3 neighborhood of the corresponding pixel, although significant negative trends in wNDVI and mNDVI appear (of respectively $1.04 \cdot 10^{-3}$ and $4.89 \cdot 10^{-3}$ NDVI unit per year), showing that this increase in integrated NDVI is due to phenological changes (in that 3 by 3 neighboring area, Autumn date shows a significant positive trend).

Table 4.10.- Changes for all parameters for class 5 (volcanic eruption) control points. S, A and G-S parameters are given in days per year; wVI and mVI are given in 10^{-3} NDVI units per year; iVI in NDVI units year per year; and mS and mA in $days^{-1}$ per year. X indicates no significant trend (at 90% confidence level).

Control point	S	A	G-S	wVI	mVI	iVI	mS	mA
Lake-Kivu	X	X	X	X	X	X	X	X
Mt-St-Helens	-3.32	1.24	4.56	-10.68	-2.34	X	-0.073	X

Table 4.11.- Changes for all parameters for class 6 (mine expansion) control points. S, A and G-S parameters are given in days per year; wVI and mVI are given in 10^{-3} NDVI units per year; iVI in NDVI units year per year; and mS and mA in $days^{-1}$ per year. X indicates no significant trend (at 90% confidence level).

Control point	S	A	G-S	wVI	mVI	iVI	mS	mA
Athabasca-Oil-Sands	X	0.29	0.56	-2.82	-5.47	-1.02	X	X
Ekati	X	0.11	X	0.32	X	0.16	0.090	X
Escondida	X	X	X	-0.08	0.18	X	X	X
Green-River	X	X	X	X	X	X	X	X
Jwaneng	X	X	X	X	X	X	X	X
Ok-Tedi-Mine	X	X	X	X	X	X	X	X
Powder-River-Basin-1	0.82	X	X	X	4.30	0.64	0.028	X
Powder-River-Basin-2	X	X	X	X	X	X	X	X
Prudhoe-Bay	X	-0.13	X	X	10.62	0.79	-0.084	X
The-Black-Triangle	-1.33	X	1.31	2.62	5.54	2.09	X	X
Weipa-Bauxite-Mine-1	7.06	X	X	X	X	X	X	X
Weipa-Bauxite-Mine-2	X	X	X	10.71	-4.44	X	X	X

Table 4.13 shows the trends retrieved for control points where glaciers have retreated (class 8). Only one out seven control points shows a significant trend, this

trend being positive for iNDVI, as expected, since ice has a negative NDVI, and thus a lesser proportion of ice in the pixel will tend to increase NDVI levels and integrated NDVI. The explanation for the lack of significant trends for the other control points is the small area affected by change (in comparison with AVHRR pixel size), except for Helheim Glacier (Greenland), for which the GIMMS database does not include any data.

Table 4.12.- Changes for all parameters for class 7 (urbanization) control points. S, A and G-S parameters are given in days per year; wVI and mVI are given in 10^{-3} NDVI units per year; iVI in NDVI units year per year; and mS and mA in days^{-1} per year. X indicates no significant trend (at 90% confidence level).

Control point	S	A	G-S	wVI	mVI	iVI	mS	mA
Banjul	X	X	X	X	X	X	X	X
Beijing	-2.45	2.38	4.82	-4.30	-9.15	-1.03	X	X
Brasilia	X	X	X	X	X	4.01	X	X
Cairo	X	X	X	X	X	X	X	X
Copperbelt	X	X	X	X	X	X	X	X
Damascus	X	X	X	X	X	X	X	X
Delhi	X	X	X	X	X	X	X	X
Dhaka	X	X	X	X	X	X	X	X
Everglades	X	X	X	X	X	X	X	X
Kuala-Lumpur	X	X	X	X	X	X	X	X
Las-Vegas	X	X	X	X	X	X	X	X
Manaus	X	X	X	X	X	X	X	X
Mexico-City	X	X	X	X	-2.44	X	X	X
Midrand	X	X	X	-5.36	X	X	X	-0.119
Moskva	-1.02	0.98	1.99	-1.80	-6.08	X	X	X
Paris	-2.16	2.27	4.43	-6.45	X	X	X	-0.069
San-Francisco	X	X	X	-1.57	X	X	X	X
Santiago	X	X	X	5.74	-8.33	X	X	X
Shenzhen	X	X	X	X	-10.11	X	X	X
Sydney	X	X	X	X	-3.99	X	X	X
Tripoli	X	X	X	X	X	X	X	X
Velingara	X	X	X	X	X	X	X	X

Changes due to pollution (class 9) are summarized in Table 4.14. This category includes only one control point (Copsa-Mica, in Romania), which shows a significant increasing trend in all parameters but spring and mS parameters. These increasing trends, especially in NDVI levels, can be explained by the fact that all polluting industries were closed in 1993. Thus, the retrieved trends correspond probably to vegetation regrowth after this date.

Control points regarding desertification (class 10) are presented in Table 4.15. This category includes 6 control points, out of which 2 do not show any significant

trend, due mainly to high variability in NDVI yearly cycle for these arid areas. In spite of an expected decrease in NDVI level parameters, the remaining control points all show at least one significant increase in those parameters. However, when averaging trends over a 3 by 3 pixel neighborhood, all control points show significant decreases in mNDVI parameters, combined with little changes in wNDVI, except in the case of Revane (Senegal). This may be due to the little extent of the monitored change (roughly 2 by 2 km), and the fact that the corresponding GIMMS pixel includes a portion of vegetation located North of the change area.

Table 4.13.- Changes for all parameters for class 8 (glacier retreat) control points. S, A and G-S parameters are given in days per year; wVI and mVI are given in 10^{-3} NDVI units per year; iVI in NDVI units year per year; and mS and mA in days^{-1} per year. X indicates no significant trend (at 90% confidence level).

Control point	S	A	G-S	wVI	mVI	iVI	mS	mA
Breidamerkurjokull	X	X	X	X	X	X	X	X
Helheim-Glacier	X	X	X	X	X	X	X	X
Hubbard-Glacier	X	X	X	X	X	0.56	X	X
Mt-Kilimandjaro	X	X	X	X	X	X	X	X
Rwenzori-Glacier-1	X	X	X	X	X	X	X	X
Rwenzori-Glacier-2	X	X	X	X	X	X	X	X
Rwenzori-Glacier-3	X	X	X	X	X	X	X	X

Table 4.14.- Changes for all parameters for class 9 (pollution) control points. S, A and G-S parameters are given in days per year; wVI and mVI are given in 10^{-3} NDVI units per year; iVI in NDVI units year per year; and mS and mA in days^{-1} per year. X indicates no significant trend (at 90% confidence level).

Control point	S	A	G-S	wVI	mVI	iVI	mS	mA
Copsa-Mica	X	0.49	0.89	2.77	2.71	1.52	X	0.012

Regarding mangrove to shrimp farm conversion (class 11), 2 (Gulf of Guayaquil, in Equator, and Myebon, in Myanmar) out of 5 control points (Table 4.16) are identified as water in GIMMS database, and thus exhibit no trend. Kantang (Thailand) control point does not exhibit significant trends either, probably due to the dotted pattern of shrimp farm spatial repartition. Mangrove clearing for shrimp farming is expected to lower NDVI level parameters, due to the disappearance of forests replace by water. However, this trend appears significantly only for wNDVI parameter in Thon-Buri (Thailand).

Table 4.15.- Changes for all parameters for class 10 (desertification) control points. S, A and G-S parameters are given in days per year; wVI and mVI are given in 10^{-3} NDVI units per year; iVI in NDVI units year per year; and mS and mA in days^{-1} per year. X indicates no significant trend (at 90% confidence level).

Control point	S	A	G-S	wVI	mVI	iVI	mS	mA
Dead-Sea	X	X	X	X	X	X	X	X
Knife-River-Delta	X	X	X	0.49	X	0.34	X	X
Lake-Hamoun-2	X	3.94	4.68	X	X	X	-0.065	-0.096
Revane	X	X	X	6.70	6.28	X	X	X
Torreon-1	X	X	X	X	X	X	X	X
Torreon-2	-3.01	X	X	2.93	-5.97	X	X	X

Table 4.16.- Changes for all parameters for class 11 (mangrove to shrimp farm conversion) control points. S, A and G-S parameters are given in days per year; wVI and mVI are given in 10^{-3} NDVI units per year; iVI in NDVI units year per year; and mS and mA in days^{-1} per year. X indicates no significant trend (at 90% confidence level).

Control point	S	A	G-S	wVI	mVI	iVI	mS	mA
Gulf-of-Fonseca	X	X	X	X	X	X	X	-0.022
Gulf-of-Guayaquil	X	X	X	X	X	X	X	X
Kantang	X	X	X	X	X	X	X	X
Myebon	X	X	X	X	X	X	X	X
Thon-Buri	X	X	X	-6.02	X	X	X	X

Results for land cover degradation control points (class 12) are summarized in Table 4.17. Two out of three control points do not exhibit any significant trend (Lake Nakuru, in Kenya, and Lake Sibaya, in South Africa), although their 3 by 3 pixel neighborhoods do exhibit significant decreasing trends in mNDVI parameter. As regards Wyperfield National Park (Australia) pronounced increasing trend in wNDVI parameter, this could be explained by the fact that the corresponding area is maintained both by intentional and natural fires, replacing bushes by low vegetation with a higher NDVI in winter (grassland), to be replaced gradually by bushes.

Finally, Table 4.18 summarizes retrieved trends for the remaining control points, which correspond to land use change category (class 13). 3 out of 7 control points do not exhibit significant trends (Kagera, at the border between Tanzania, Rwanda and Uganda, Almeria, in Spain, and Narok, in Kenya). The other control points do show various trend patterns, depending on the land use change. In Mashonaland (Zimbabwe), large productive commercial farms have been broken

into smaller farms, which effect on NDVI is difficult to predict. However, this region has seen its productivity decrease, leading to food shortages, which can be evidenced by integrated NDVI decreasing trend, integrated NDVI being a proxy for productivity (Field *et al.*, 1995; Prince & Goward, 1995). In Novovolynsk, at the border between Poland and Ukraine, field size has also diminished, but decreasing trends in wNDVI, mNDVI and iNDVI are difficult to relate to that particular change. In Papua (Indonesia), a large patch (15 by 10 km) of native forest has been logged for oil palm plantation, which can hardly be the cause of the observed strong decrease in winter NDVI. Since this area is often covered by clouds, this retrieved trend might be erroneous. Finally, in the Peanut Basin (Senegal), agricultural fields have been abandoned since the early eighties, and replaced with tree-dotted savannas, which can explain the strong retrieved trend in maximum NDVI.

Table 4.17.- Changes for all parameters for class 12 (land cover degradation) control points. S, A and G-S parameters are given in days per year; wVI and mVI are given in 10^{-3} NDVI units per year; iVI in NDVI units year per year; and mS and mA in days^{-1} per year. X indicates no significant trend (at 90% confidence level).

Control point	S	A	G-S	wVI	mVI	iVI	mS	mA
Lake-Nakuru	X	X	X	X	X	X	X	X
Lake-Sibaya	X	X	X	X	X	X	X	X
Wyperfield-National-Park	X	X	X	17.87	X	X	X	X

Table 4.18.- Changes for all parameters for class 13 (land use change) control points. S, A and G-S parameters are given in days per year; wVI and mVI are given in 10^{-3} NDVI units per year; iVI in NDVI units year per year; and mS and mA in days^{-1} per year. X indicates no significant trend (at 90% confidence level).

Control point	S	A	G-S	wVI	mVI	iVI	mS	mA
Kagera	X	X	X	X	X	X	X	X
Almeria	X	X	X	X	X	X	X	X
Mashonaland	0.94	-8.50	X	2.61	-2.43	-2.60	X	X
Narok	X	X	X	X	X	X	X	X
Novovolynsk	-0.96	0.80	1.76	-2.96	-7.66	-0.80	X	0.008
Papua	X	X	X	-24.96	X	X	X	X
Peanut-Basin	X	X	X	X	14.79	X	X	X

As a conclusion to this validation, the retrieved trends from our double logistic fitting procedure agree quite well with ground truth, for those areas large enough for change to be observable at 8 km scale. Thus, our results can help identify areas which have undergone changes in their land cover especially.

4.2.4.- Comparison between harmonic and double logistic techniques

Validation of the double logistic fitting approach has been presented previously, but based only on comparing phenology trends retrieved by this method with already published results. Here, we compare results obtained by this approach with results we retrieved using the harmonic approach presented above. At the time of redaction of this manuscript, this work is being submitted for publication to an international journal, and some of these images are published in Julien & Sobrino (2007b).

4.2.4.1.- Method

We have used all complete years of GIMMS database to carry out the harmonic analysis (1982 to 2003). The harmonic analysis was carried out with the following parameters of the HANTS software (see above):

- number of frequency: 3 (24 = yearly; 12 = half-yearly; 8 = 4-monthly)

- suppression flag: low,

- invalid data rejection threshold: low threshold: 0; high threshold: 1.0,

- fit error tolerance: 0.01,

- degree of over-determinedness: 5.

Then, yearly NDVI evolutions are reconstructed from yearly harmonic components, from which 4 parameters are retrieved: minimum and maximum NDVI values, and spring and autumn dates. Spring and autumn dates are simply retrieved as the dates for which NDVI evolution derivates are respectively maximum and minimum. Finally, averages and standard deviations of the whole times series are calculated for all pixels.

4.2.4.2.- Results

To summarize average and standard deviation information in the same image, the IHS (Intensity – Hue – Saturation) convention has been used:

- Standard deviation information is summarized in the intensity component of the image, the lowest intensities (darker colors) corresponding to higher standard deviations:

$$I = 1 - 4 \cdot \frac{\sigma_s}{V_{max}} \qquad (4.8)$$

where σ_s is the series standard deviation, and V_{max} is the series maximum value (365 for spring and autumn parameters, and 1 for minimum and maximum NDVI parameters).

- Average information is summarized in the hue component of the image, the lowest values being displayed in blue colors, while the highest values are displayed in red (hue scaled between 0 and 240º):

$$H = 240 - round(240 \cdot \frac{\overline{S}}{V_{max}}) \qquad (4.9)$$

where $\overline{S}$ is the series average, and V_{max} is the series maximum value (365 for spring and autumn parameters, and 1 for minimum and maximum NDVI parameters).

- The saturation component of the image is fixed to 1.

As a result, parameter averages are presented following the traditional rainbow color code, this information being completed by the variability of the time series (standard deviation), dark colors corresponding to high variability in parameter retrieval, while light colors correspond to low variability.

Figure 4.18 shows the resulting images for spring date stability analysis. Comparisons for NDVI stable areas are irrelevant since phenology is not retrieved when using the double logistic method. The first observation regarding Figure 4.18 is the difference in color spatial repartition. This illustrates the fact that different methods applied to the same data lead to different results, the difference being linked to the vegetation present at the considered pixel. For example, in boreal areas, spring date occurrence is estimated later when using the double logistic fitting method than when using harmonic analysis. This is due to the fact that snow effects on NDVI are removed from the data in the first case. A surprising fact is that regarding variability, both methods seem to be complementary, since where

164

one method shows great variability, the other one performs better. For example, over tropical rainforests (Amazonia, Indonesia), double logistic fitting method is showing great variability (darker colors), while harmonic analysis results are more stable. On the opposite, the rest of the Southern hemisphere (except South Australia) and part of the Northern hemisphere show more stable results using the double logistic fitting procedure.
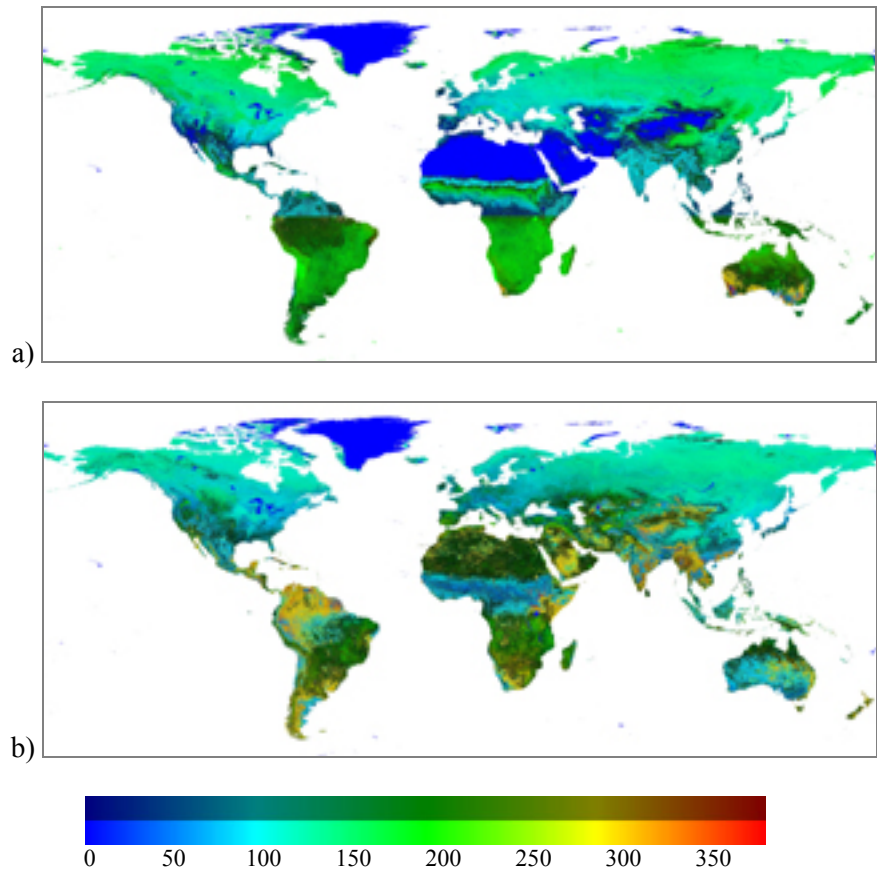
Figure 4.18.- Average spring date and its variability for a) double logistic fit and b) harmonic analysis. Lower color bar shows spring date for pixels with low interannual variability, while upper color bar shows spring date for pixels with high interannual variability.

Figure 4.19 shows results of both methods for autumn date retrieval. As for Figure 4.18, the Equator line is clearly visible for the double logistic fitting

procedure, due to the difference in data yearly separation between hemispheres. The same color differences and complementarities regarding variability than for spring dates can be observed between both methods, although in this case the harmonic analysis seems to perform better, especially in the Southern hemisphere.
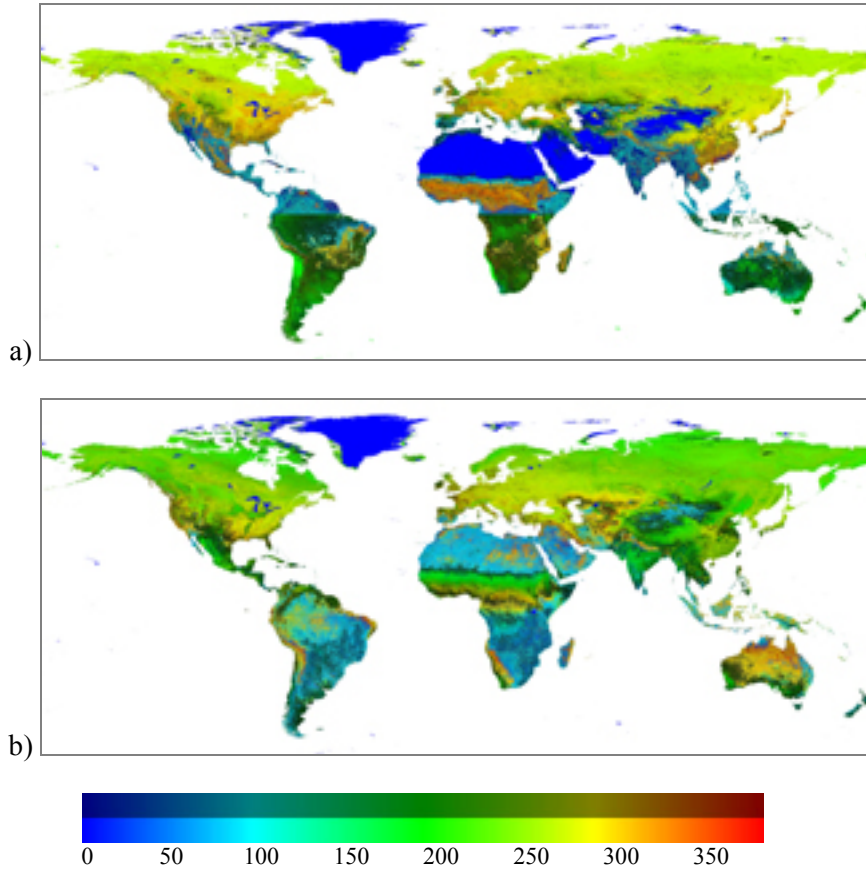
Figure 4.19.- Average autumn date and its variability for a) double logistic fit and b) harmonic analysis. Lower color bar shows spring date for pixels with low interannual variability, while upper color bar shows spring date for pixels with high interannual variability.

Results for NDVI minimum values are displayed Figure 4.20. Colors for both methods are quite identical, except in tropical rainforests, where double logistic fitting method gives abnormally low values. This is due to usual cloud persistency in these areas, which is considered by the algorithm as a dormancy period. Thus,

the retrieved minimum NDVI values for these areas correspond to cloud contaminated values. Regarding variability, minimum NDVI values retrieved using harmonic analysis are more stable over most of the globe, showing once more the influence of clouds during dormancy period in the double logistic fitting procedure.
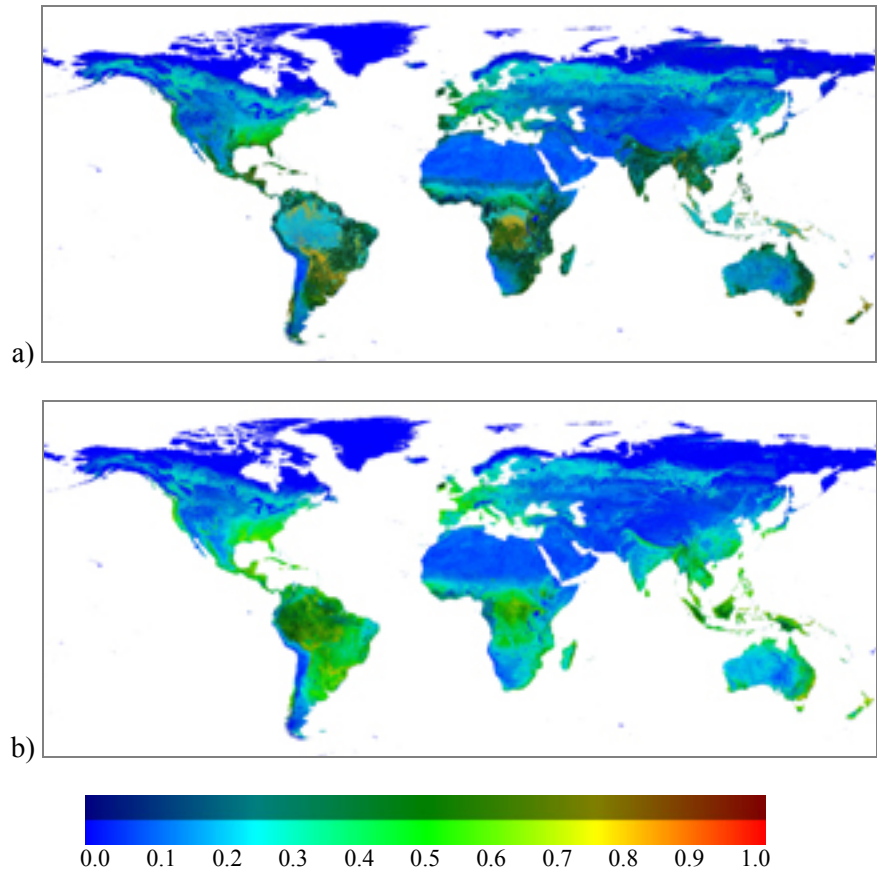
Figure 4.20.- Average minimum NDVI values and their variability for a) double logistic fit and b) harmonic analysis. Lower color bar shows spring date for pixels with low interannual variability, while upper color bar shows spring date for pixels with high interannual variability.

Finally, results regarding maximum NDVI values are presented Figure 4.21. In that case, the color spatial repartition is almost identical for both methods, showing good agreement between methods. However, values retrieved using harmonic

analysis tend to have a greater variability, showing the improvement brought by the inclusion of a plateau in the function to which is fitted the yearly NDVI evolution.
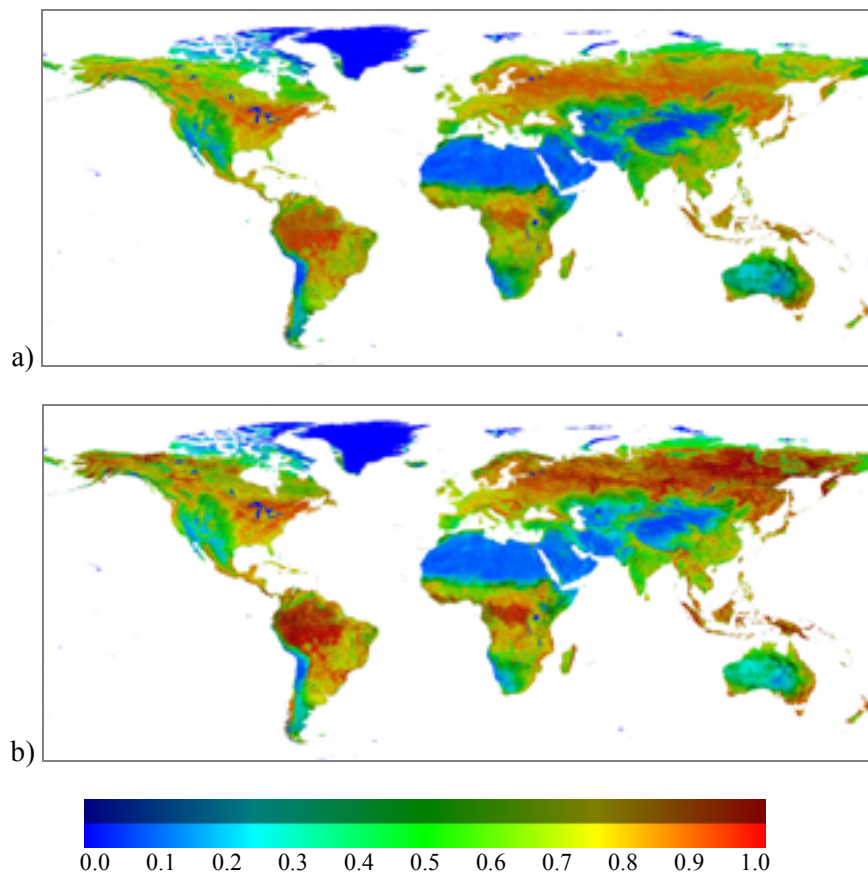
Figure 4.21.- Average maximum NDVI values and their variability for a) double logistic fit and b) harmonic analysis. Lower color bar shows spring date for pixels with low interannual variability, while upper color bar shows spring date for pixels with high interannual variability.

4.2.4.3.- Discussion

As commented above, harmonic analysis and double logistic fitting procedure show a good complementarity as regards yearly retrieval of spring and autumn dates, and minimum and maximum NDVI values. The inclusion of a plateau in the fitting function seems to provide a great improvement in maximum NDVI value

stability. We think that the inclusion of a plateau for vegetation dormancy period is also an improvement, but this hardly shows in these results due to the difficulty of a good retrieval of the dormancy NDVI value, usually masked within cloud and/or snow contaminated values.

An interesting point in this comparison between both methods is that harmonic analysis provides a good estimate of minimum NDVI values, which could be used to feed the double logistic fitting function with minimum NDVI (wNDVI) values, to increase the stability of this approach. This would of course not prevent all cloud contamination in minimum NDVI values, especially in tropical rainforests for example, nevertheless the gain in approach stability would be substantial. Additionally, this would help lowering the variability in phenological phases retrieval, since these depend greatly on NDVI winter levels. However, increased computer time would be needed to perform this improved procedure.

Finally, it is of interest to report that by combining both approaches, a low variability could be obtained over the whole globe, in spite of local flaws in NDVI data such as cloud contamination and snow presence.

4.2.4.4.- Combining both techniques

Taking advantage of the complementarities between the harmonic analysis and the double logistic function procedure, the whole GIMMS database has been reprocessed using the double logistic function after having fixed wNDVI value to the minimum value obtained by harmonic analysis. This sought to reduce the variability of wNDVI parameter in the double logistic function approach without changing the fitting method, which provides satisfying results as for the rest of the parameters.

However, the results of this second run of the whole procedure did not provide the expected improvements, since the time series of the retrieved parameters (wNDVI, mNDVI, S, A) showed a stability similar to the one of the parameter time series retrieved with the HANTS software. Table 4.19 presents the average and standard deviation for spring and autumn dates, as well as winter and maximum NDVI values retrieved with the harmonic analysis and the double logistic fitting procedure. Differences in average values between both methods are due to the

exclusion of stable areas from the double logistic fitting procedure while these areas are included in the harmonic analysis. As regards the standard deviation between both procedures, results are almost identical, showing that no additional stability is gained by using the double logistic fitting procedure based on the winter NDVI values estimated by the harmonic analysis.

Table 4.19.- Average (mean) and standard deviation (dev) over land for retrieved parameters with the harmonic analysis and the double logistic fitting procedure expressed in days for spring (S) and autumn (A), and in NDVI units for winter NDVI (wNDVI) and maximum NDVI (mNDVI) values.

	S (days)		A (days)		wNDVI		mNDVI	
	mean	dev	mean	dev	mean	dev	mean	dev
Hants	215	51	162	65	0.19	0.03	0.59	0.06
Logistic	189	49	129	65	0.16	0.04	0.52	0.06

Chapter 5

NDVI/LST FEATURE SPACE

"Well I think we've sorted all that out now. If you'd like to know, I can tell you that in your Universe you move freely in three dimensions that you call space. You move in a straight line in a fourth, which you call time, and stay rooted to one place in a fifth, which is the first fundamental of probability. After that it gets a bit complicated, and there's all sorts of stuff going on in dimensions 13 to 22 that you really wouldn't want to know about. All you really need to know for the moment is that the Universe is a lot more complicated than you might think."

Douglas Adams (*Mostly Harmless*)

This last chapter is dedicated to the simultaneous analysis of NDVI and LST parameters, in the so-called NDVI-LST feature space. To this end, theoretical aspects are first presented, followed by a simultaneous harmonic analysis of NDVI and LST.

5.1.- Theoretical aspects

The NDVI-LST feature space consists in plotting LST (ordinates) against NDVI (abscissas) in a graph. It has been studied mainly at local scale and on specific vegetation types. This section presents first the methods developed previously with their results, to end with a presentation of global results we have obtained with a new and simple approach of this NDVI-LST feature space.

5.1.1.- Previous results

Numerous methods have linked NDVI temporal variations to land surface temperature. Those methods have been used mainly to retrieve soil moisture (Goward *et al.*, 2002), soil water content (Gillies *et al.*, 1997), crop water stress

(Clarke, 1997) or evaporation parameters (Wang *et al.*, 2006; Nemani & Running, 1989). However, only few studies have used NDVI and LST to monitor land cover itself (Schultz & Halpert, 1995; Nemani & Running, 1997; Yue *et al.*, 2007). Nemani & Running (1997) used NDVI and LST relationships to classify land cover of continental United States. However, in all these studies, retrieved brightness temperatures were used as proxy for land surface temperatures, without any correction of orbital drift whatsoever.

We present here the approach chosen by Nemani & Running (1997) to characterize vegetation from NDVI & LST yearly trajectories. Their approach is summarized in Figure 5.1, adapted from their figure 2.
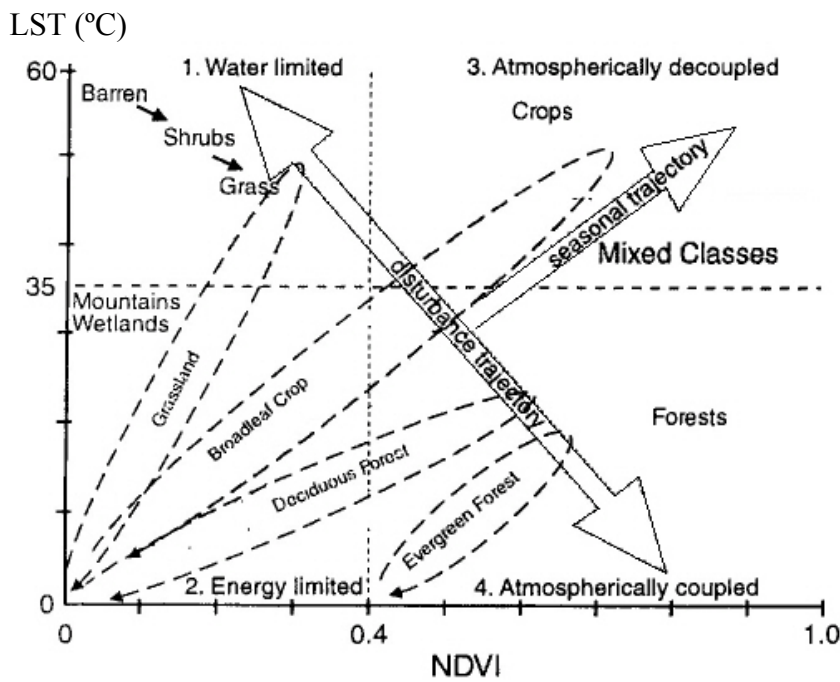

Figure 5.1.- Dynamics of LST-NDVI for various vegetation types (adapted from Nemani & Running, 1997).

Figure 5.1 shows yearly dynamics of different vegetation types in the NDVI-LST feature space, from which changes can be attributed to different causes. This

interpretation has been used to interpret changes in time series of NDVI and LST processed using the HANTS algorithm, which results are presented section 5.2.

5.1.2.- Global analysis

No global analysis of the NDVI-LST feature space has ever been carried out, due to the orbital drift present in NOAA/AVHRR data (see Chapter 2). However, we have developed a method for orbital drift correction that we have applied to GIMMS additional data (see Chapter 2), following the method presented in Chapter 3. This global analysis has been submitted for publication to Remote Sensing of Environment.

NDVI and LST time series have thus been retrieved for the period November 2000 to December 2006. In a first step, these data have been reprojected from continental Albers projection to global lat/lon projection. In a second step, average years of NDVI and LST have been calculated over the whole period, by averaging the data over each corresponding compositing period. Then, a few representative pixels have been selected for visualizing yearly trajectories in the NDVI-LST feature space. Those representative pixels are located in the following areas: Landes forest, in France; Atacama desert, in Chile; Sahara desert, in Lybia; Gobi desert, in China; a boreal forest, in Sweden; tropical rainforests, in Amazonia, central Africa, and Sumatra. Figure 5.2 present those trajectories.

Figure 5.2 shows that arid areas (Lybia, Gobi and Atacama deserts) tend to have a vertical trajectory in the NDVI-LST feature space, while tropical rainforests (Congo, Amazonia, Sumatra) tend to have a horizontal trajectory. Other areas (Landes, Sweden) show an oblique trajectory. As for yearly trajectory amplitude, Sweden shows by the far the longest, since snow presence in winter diminishes considerably NDVI and LST values. However, arid areas as well as tropical rainforests do exhibit significant yearly amplitude, limited to only one of the two parameters: NDVI for tropical rainforests, and LST for deserts.

From these trajectories, one can observe general patterns in NDVI-LST feature space, which can be summarized with 3 parameters, which can be obtained by simple linear regression between LST and NDVI:

- the angle of the regression line with the abscissas axis,

- the length of the yearly cycle,

- the accuracy of the regression.

To obtain the yearly cycle length, we decided to project orthogonally each NDVI-LST ensemble of points on its regression line. Since orthogonal projection only makes sense in an orthonormal basis, we decided to normalize LST data between 0 and 1 as follow:

$$L\hat{S}T = \frac{(LST - LST_{min})}{(LST_{max} - LST_{min})} \qquad \text{(Eq. 5.1)}$$

where $L\hat{S}T$ is the normalized LST, and LST_{min} and LST_{max} are respectively the chosen minimum and maximum LST values. We have fixed LST_{min} to 240 K, and LST_{max} to 340 K. This has also the advantage of setting the NDVI-LST regression line angle to the whole -90º to 90º range.

Finally, the 3 chosen parameters for description of the yearly trajectory in the NDVI-LST feature space are the following:

- θ, angle of the NDVI-$L\hat{S}T$ regression line with the abscissa axis,

- d, maximum distance of the projected NDVI-$L\hat{S}T$ on the regression line,

- R^2, describing the accuracy of the regression, as the rate between the variance of the regression values and the variance of the data.

These 3 parameters are presented Figure 5.3.

Once those 3 parameters identified, those have been retrieved for all pixels from the average year of NDVI and LST. Figure 5.4 shows the spatial repartition of those parameters at global scale. As one can observe from Figure 5.4a, θ gives a good description of vegetation type: arid areas tend to have vertical yearly trajectories in NDVI-LST feature space, translated in θ values of ±90º, due to a low NDVI variation throughout the year, while LST do have a yearly amplitude, result of seasonal differences in climate; semi-arid areas have negative θ values, showing that high NDVI values are reached at low LST values, easily explained by the fact that their vegetation is water limited and not temperature limited; tropical rainforests have θ values close to null, due to the fact that this vegetation type regulates its temperature (LST corresponding in this case to canopy temperature),

176

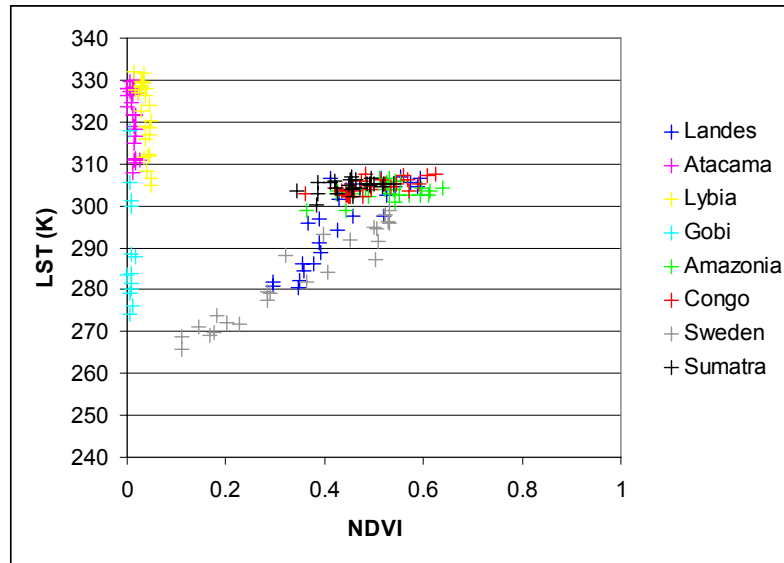*Figure 5.2.- Trajectories of LST-NDVI for 8 control points.*

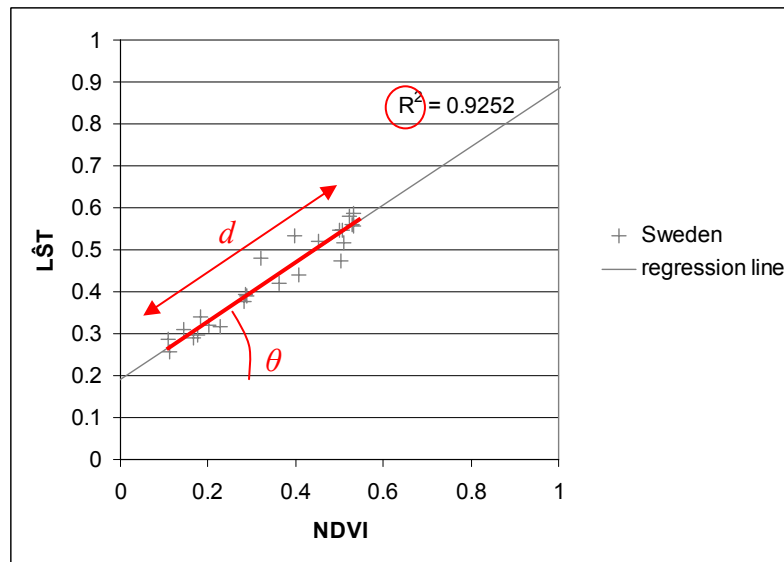

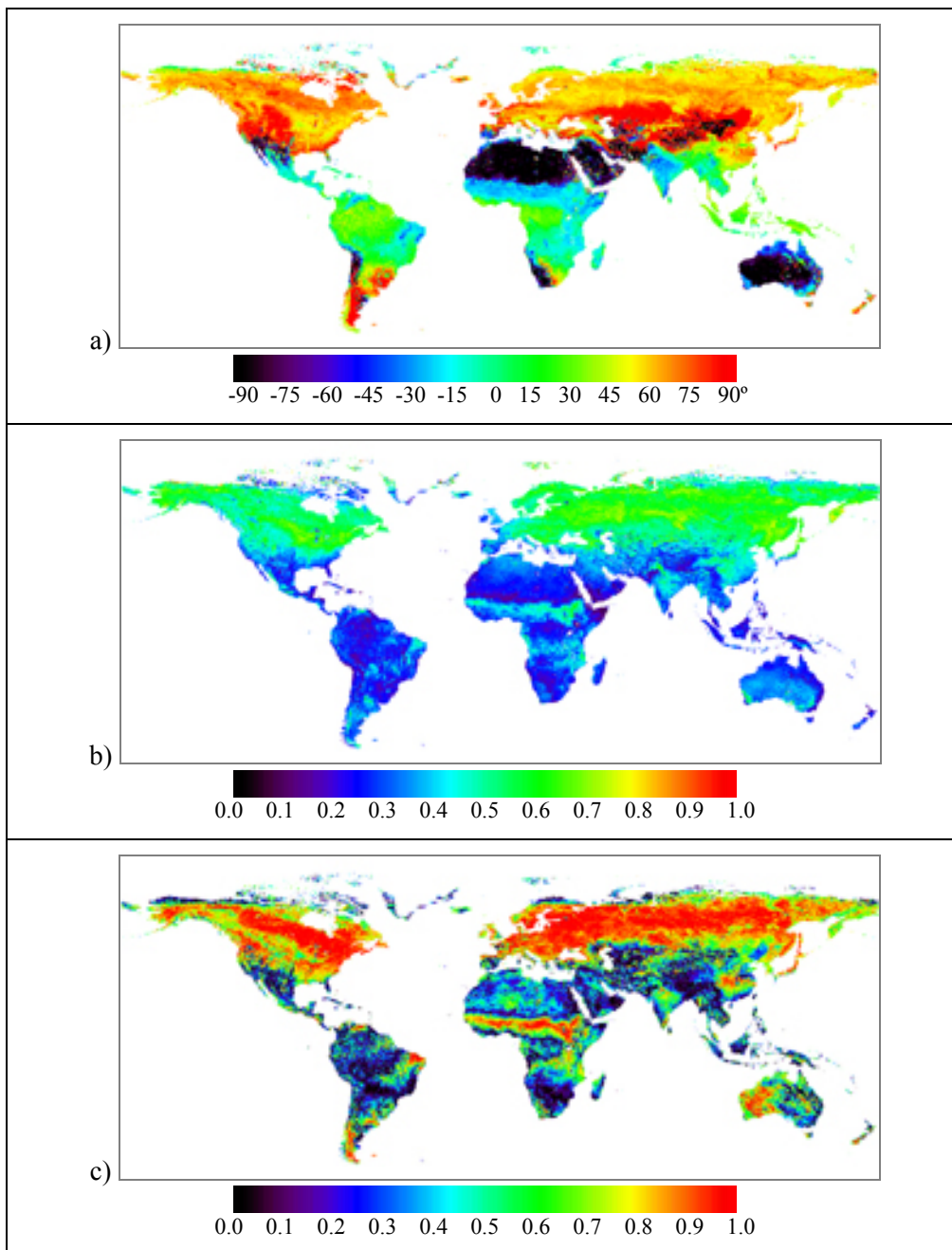*Figure 5.3.- Chosen parameters for vegetation description in the LŜT-NDVI feature space.*

Figure 5.4.- Spatial repartition of a) θ (from -90° to +90°), b) d (from 0 to 1), and c) R² (from 0 to 1) following the traditional rainbow color code.

maintaining it constant throughout the year, while NDVI values fluctuate depending on seasonal cloud cover (Huete *et al.*, 2006); finally, temperate and boreal areas show a positive θ value, corresponding to high NDVI values reached for high LST values, as temperature is usually the limiting parameter for plant growth in these areas.

As regards d parameter (Figure 5.4b), its repartition is simpler: areas with snow cover during winter show higher d values, since snow presence decreases both NDVI and LST values. Arid areas and tropical rainforests have little yearly amplitude in the NDVI-LST feature space, showing low d values. However, semi-arid areas have higher d values, due to the difference between NDVI values for bare soil and punctual vegetation growth, coupled with a LST yearly cycle comparable to arid areas.

As for the goodness of fit (figure 5.4c), R^2 values are close to 1 (perfect fit) for boreal and temperate areas, as well as for Sahel, North-East Brazil, Western Australia and Southern South America. R^2 values are low over deserts, due to noise in NDVI values, and over tropical rainforests, due to cloud presence. These low R^2 values over rainforests explain why some θ values in these areas are far from zero (up to 30º), evidencing residual cloud presence in the data.

Finally, Figure 5.5 shows all three parameters displayed using the IHS convention: θ is coded as hue, d as intensity, and R^2 as saturation. The reasons for this choice are the following:

-   θ is defined modulo 180º, meaning that angles of +90º and -90º represent the same regression line, and thus has to be coded in the same way (hue).

-   R^2 is relied to the confidence in the regression, which should be made clear at simple glance. To this end, saturation is a perfect tool, since low R^2 values will appear as gray, while high R^2 values appear in bright colors.

-   d describes the yearly amplitude of the considered pixel in the NDVI-LST feature space, which is coded in the remaining component, intensity, darker colors corresponding then to small yearly amplitudes, and light colors to more important yearly amplitudes.

Figure 5.5 shows that the NDVI-LST feature space is well-suited for vegetation monitoring, since it allows a good description of the vegetation, in term of

vegetation type as well as climate influence. However, one has to keep in mind that this analysis has been carried out on an average year of orbital drift corrected data, meaning that cloud contamination and orbital drift influence have been greatly diminished. Determining NDVI-LST feature-space parameters with cloud contaminated yearly time series may lead for example to an artificial lengthening of the yearly cycle amplitude, as well as a wrong value of NDVI-LŜT regression line angle.

5.2.- Harmonic analysis

For this analysis, an approach similar to the one presented in Chapter 4 has been used. This approach is presented briefly with its results, the whole procedure being described thoroughly in Julien *et al.* (2006).

5.2.1.- Analysis of NDVI and LST time series

This analysis has been carried out once again using the HANTS software. In spite of being designed originally for NDVI analysis, this software is perfectly suited for LST time series analysis, since outliers in LST, as well as for NDVI, have an effect in only one direction: cloud and snow contaminated pixels tend to have a lower LST than cloud or snow free pixels.

For this study, the analysis has been conducted on a yearly basis, for series of 36 10-day composite images. Only the years of the PAL database (see Chapter 2) with complete data were selected for analysis, which led to the exclusion of years 1981, 1994 and 2001, due to the absence of data for several months.

5.2.1.1.- NDVI

HANTS settings for NDVI harmonic analysis were the following:

- number of frequency: 2 (36 = yearly; 18 = half-yearly),

- suppression flag: low,

- invalid data rejection threshold: low threshold: 0; high threshold: 0.7,

- fit error tolerance: 0.05,

- degree of overdeterminedness: 13.

180

The evolution of NDVI is shown in Figure 5.6. Because all images were very similar, only NDVI HANTS image for year 1982 is displayed following the color code presented in Chapter 4. Then, difference between each following year and year 1982 are displayed as follow: mean value difference is coded as intensity, 1st harmonic amplitude difference is coded as saturation, and 1st harmonic phase difference as hue. For these figures, colors have been limited from blue to red to avoid confusion between extreme phase increases and decreases. This color code is shown in Figure 5.7. The parameters in Equation (4.4) for image display are the following:

- $S = 0.2$,

- $C = -0.45$,

- $Amin = -0.05$,

- $Amax = 0.05$,

- $Pmin = -40°$,

- $Pmax = 40°$,

The dissymmetry in mean threshold values (S and C) allows clearer images. Because of the eruption of El Chichón occurring at the beginning of the time span of the database (1982), its influence on NDVI values can not be evidenced. On the opposite, Mount Pinatubo's eruptions of June 1991 caused a temporal decrease in NDVI mean values, which can be observed in the image of NDVI difference for 1992, which appears with lower intensity value than both 1991 and 1993. As for long term tendencies, one can see that NDVI difference images are progressively more saturated from 1983 to 1999, with an interruption in 1992, confirming the influence of Mount Pinatubo's eruption on NDVI (see Tucker *et al.*, 2001).

In NDVI image for year 1982, the difference in vegetation peak can be appreciated, appearing as variation in color (hue). Following the color code presented before (see Figure 4.1), semi-arid vegetation appear in turquoise (corresponding to a peak in early spring), while Western Europe vegetation has a peak in early autumn (forest areas) and summer (cultivated areas). In a general manner, northern and higher altitude areas see their vegetation peak later than other areas at similar latitudes.

181

Changes can be observed from the variation in the coloration of the NDVI difference images, corresponding to variation in NDVI peak occurrence. These changes can be observed when amplitude also changes; otherwise the pixel appears as grey. The biggest variations are seen over arid and semi-arid areas, where NDVI values are very low, thus these variations are due to noise. European continent appears mainly as green, which means that phase values are globally stable: peak NDVI occurs globally at the same period of the year. Only the image difference for year 2000 appears different from the other ones, due to the slowly decrease in NDVI values for all pixels beginning in 2000 until September 2001 (end of the database). This is due to sensor defects rather than vegetation change, as the decrease is similar for all land covers.

Amplitude changes are globally small, with absolute values inferior to 0.05 in comparison with 1982. Decreases in central Europe are particularly obvious for years 1989, 1990, 1995 and 1998. Increases are evidenced for northern and eastern Europe.

5.2.1.2.- LST

As regards HANTS settings for LST harmonic analysis, those are:

- number of frequency: 2 (36 = yearly; 18 = half-yearly),

- suppression flag: low,

- invalid data rejection threshold: low threshold: 220 K; high threshold: 339.9 K,

- fit error tolerance: 5 K,

- degree of overdeterminedness: 7.

These parameters were chosen after probing various combinations of fit error tolerance and degree of overdeterminedness, the invalid data rejection thresholds being chosen from valid range of values (160 to 340 K) of the sensor and setting the lowest threshold to the smallest temperature physically meaningful. The evolution of land surface temperature is shown in Figure 5.8. The code color is the same than above. The parameters in equation (4.4) for image display are the following:
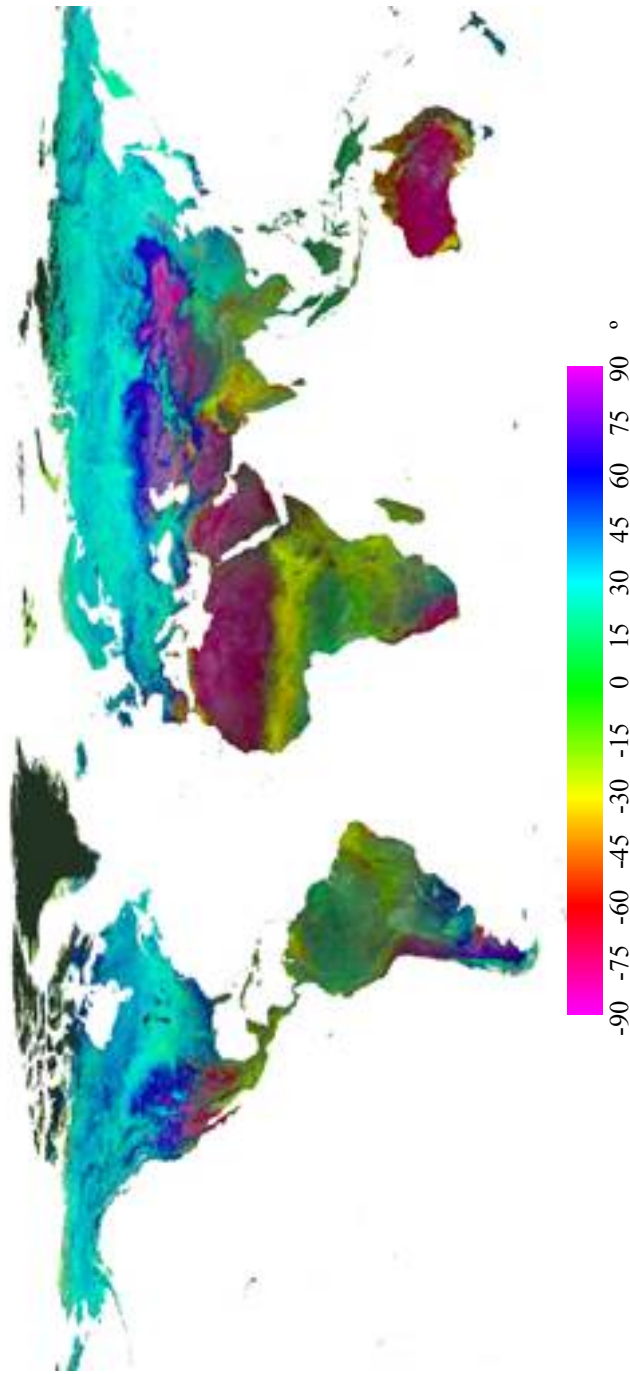
Figure 5.5.- IHS image of NDVI-LST feature space parameter at global scale.
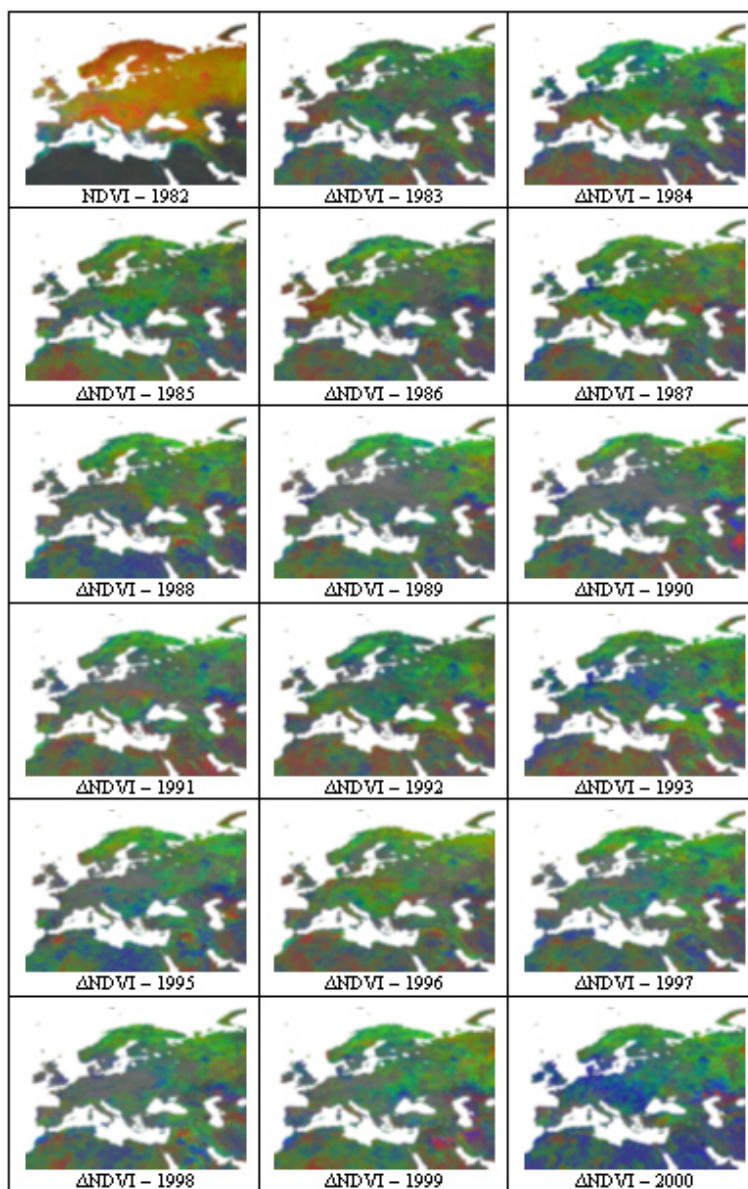
Figure 5.6.- HANTS image of NDVI for 1982 and IHS difference images between NDVI for 1983 to 2000 and NDVI for 1982. The following thresholds have been applied to NDVI difference images: -0.45 < Δaverage < 0.2 ; -0. 05 < Δamplitude < 0.05 ; -40º < Δphase < 40º.

184

- S = 7 K,

- C = -20 K,

- Amin = -3 K,

- Amax = 3 K,

- Pmin = -10º,

- Pmax = 10º,

The first observation on these figures is that satellite orbital drift is obvious, resulting in a progressive lesser intensity value in the difference images during each satellite activity period: 1985 appears with higher intensity than 1984 because of the transition from NOAA-7 to NOAA-9 at the beginning of 1985; the same occurs between 1988 and 1989 (transition from NOAA-9 to NOAA-11 at the end of 1988), and between 1993 and 1995 (transition from NOAA-11 to NOAA-14 at the very end of 1994, not displayed because of the absence of data from September to December inclusive). This permanent change in intensity value makes it difficult to interpret changes in saturation values.

| $-p_{max}$ | $-3p_{max}/4$ | $-p_{max}/2$ | $-p_{max}/4$ | 0 | $+p_{max}/4$ | $+p_{max}/2$ | $+3p_{max}/4$ | $+p_{max}$ |
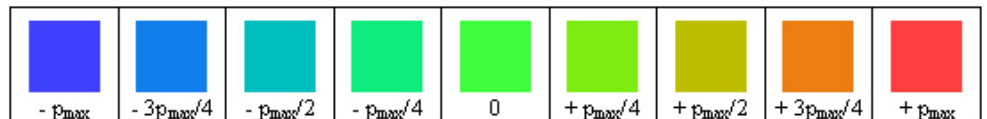
Figure 5.7.- Color code to identify phase values in IHS difference images.

5.2.2.- Application of NDVI-LST feature space to 1982-1999 period

5.2.2.1.- Averages

For an easier study of the evolution, average values of NDVI and LST for the periods 1982/1986 and 1995/1999 have been calculated. 5 year averages have been chosen to limit inter-annual variability for both parameters, as well as to limit the influence of orbital drift in LST mean value changes. Difference images (between the two above-mentioned periods) for average value, 1st harmonic amplitude and phase are displayed in Figure 5.9 for NDVI, and in Figure 5.10 for LST. First, regarding the average NDVI value, it is obvious that arid and semi-arid areas (Northern Africa, Middle East and Southern Spain) NDVI values are stable, while

Figure 5.8.- HANTS image of LST for 1982 and IHS difference images between LST for 1983 to 2000 and LST for 1982. The following thresholds have been applied to LST difference images: -20 K < Δaverage < 7 K ; -3 K < Δamplitude < 3 K ; -10º < Δphase < 10º.

186

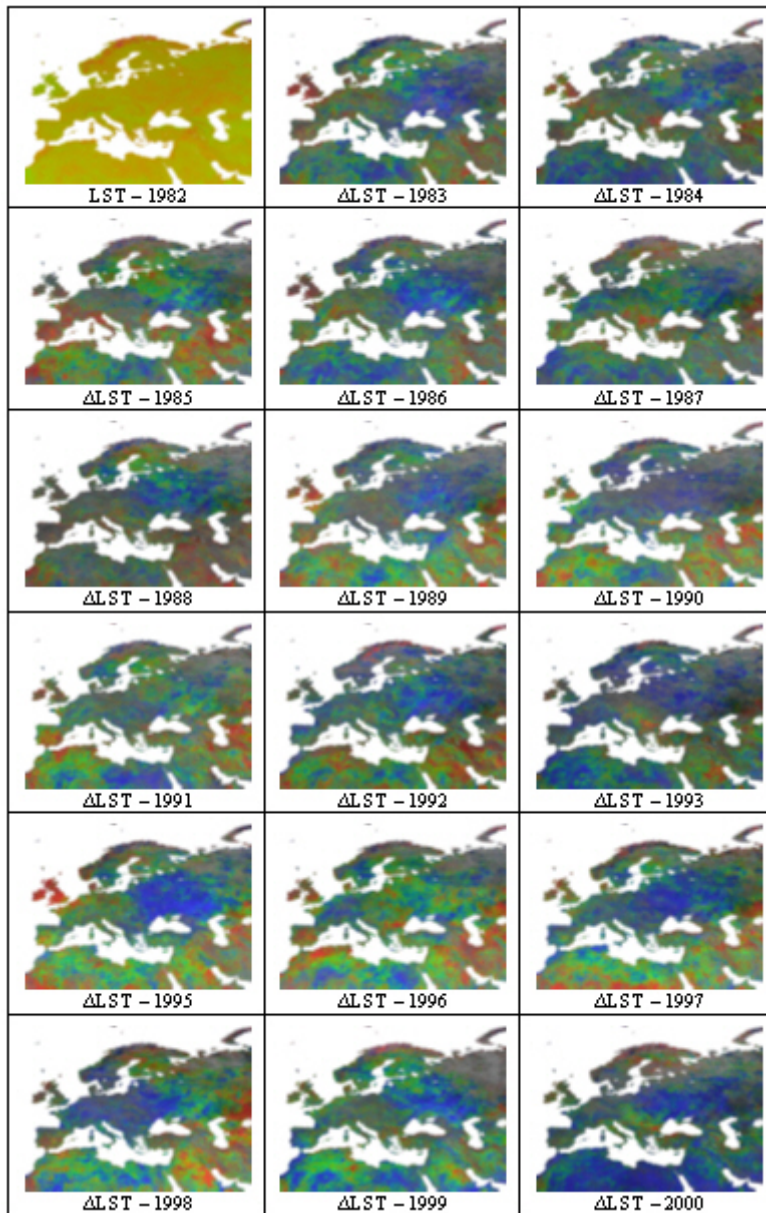forests (from Northern Spain to East Russia) have increased their NDVI average, with increases in 1st harmonic amplitudes reduced from Ireland to Poland, while arid areas have seen great changes in 1st harmonic phase values (due to noise in low values), along with northern France and southern England. Northern Scandinavia and Eastern Europe have seen a slight increase in 1st harmonic phase (around 10º). From the image of average land surface temperature difference, it seems that southern Europe has globally seen an increase of its average LST, while it decreased in Scandinavia. Regarding 1st harmonic amplitude difference, mild mountainous areas have suffered a decrease of temperature amplitudes, while central Europe has seen an increase of its 1st harmonic amplitude, as well as Scandinavia. Finally, regarding phase difference, the Alps and most of Western Europe have suffered an advance in phase, respectively of 9 and 3 days approximately. Russia, Scandinavia and Northern Africa have seen an increase in phase values of 5 to 10 days.

5.2.2.2.- Changes in NDVI and LST

Changes in both NDVI and LST mean, 1st harmonic amplitude and phase values between periods 1982/1986 and 1995/1999 are presented respectively in Figure 5.11. From the difference between mean values for the two periods, conclusions are clear: arid and semi-arid areas (northern Africa, Southern Spain and Middle East) have seen their LST and NDVI mean values decrease; temperate areas (western and central Europe) have suffered a slight decrease in LST and an increase in NDVI mean values, especially in Germany, Czech Republic, Poland and Belarus, where NDVI values have increased by more than 0.07; continental and northern Europe have seen a slight increase or decrease in NDVI while LST values have decreased.

Changes in 1st harmonic amplitudes between 1982/1986 and 1995/1999 are more fractionated. From a global perspective, NDVI 1st harmonic amplitude values have decreased by 0.03, Western Europe seeing a decrease in LST 1st harmonic amplitude, while Eastern Europe saw an increase, especially in Ukraine and western Russia. Along with northern areas of Scandinavia and Russia, these regions are the one which saw maximum increase in NDVI amplitude.

Finally, changes in 1st harmonic phase values between 1982/1986 and 1995/1999 are a bit easier to evidence: arid areas phase values are very noisy, due

to the low values of NDVI, with little variation during the year; Western Europe (from Portugal to Germany), along with southern Scandinavia and central Europe (Ukraine and Belarus) have seen an advance in phase (related to a sooner peak occurrence) for both NDVI (-10º or more) and LST (-5º). Central Europe (from Greece and Italia to Poland) has seen its peak occurrence for NDVI postponed (up to 20º), while it occurs sooner for LST (up to -10º). Eastern and northern Europe has suffered a delay in both LST (10º) and NDVI (20º) peak occurrence.

From a more general perspective, southern arid areas have become more arid (higher temperature and lower vegetation), while the rest of Europe has globally seen vegetation increase, confirming previous works (Myneni *et al.*, 1997; Tucker *et al.*, 2001; Zhou *et al.*, 2001; Bogaert *et al.*, 2002; Zhou *et al.*, 2003), except for northern Europe, which tends to become more arid (lower vegetation and lower temperatures). Seasonal variations have increased in Eastern Europe, and peak occurrence delayed for both parameters. Since peak occurrence is a bad phenological indicator, further comparisons with phenological tendencies like onset of spring or length of growing season can not be carried out.

Following Nemani & Running (1997) interpretation of simultaneous changes in LST and NDVI (in their Figure 2), the observation of Figure 5.11-a) allows drawing several conclusions. First, northern Europe has seen a change in its seasonal trajectory towards lower amplitude, which could be explained by a shorter temporal extent of the snow cover (see Dye, 2002). The rest of Europe has suffered a change in land cover (disturbance trajectory), the already arid areas tending to become more arid (desertification), while several areas in Europe (with vegetation already), especially in central Europe, have seen their wooden land proportion increase, as pointed out in FAO (2005).

5.3.- Long-term analysis

The approach presented in section 5.1.2. has been applied to the whole PAL database (see Chapter 2) without any correction of the orbital drift (see Chapter 3). The results of the application of this new global method for combined monitoring of NDVI and LST are shown in the first part, followed by an analysis of the influence of NOAA's orbital drift on the results, to end with a discussion of these results.
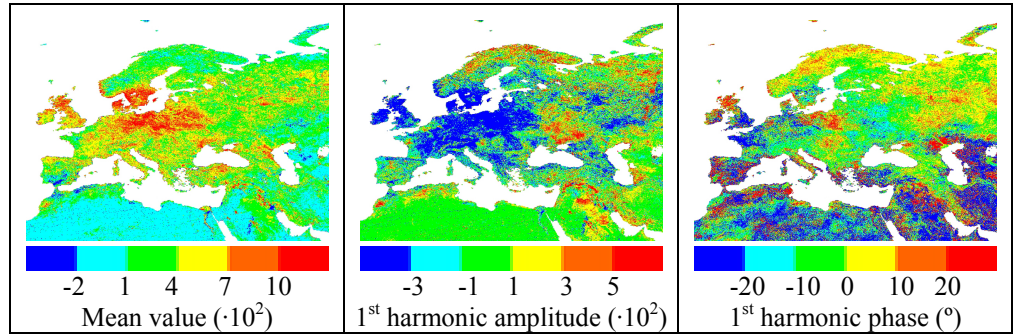
Figure 5.9.- Differences in NDVI between periods 1982/1986 and 1995/1999.
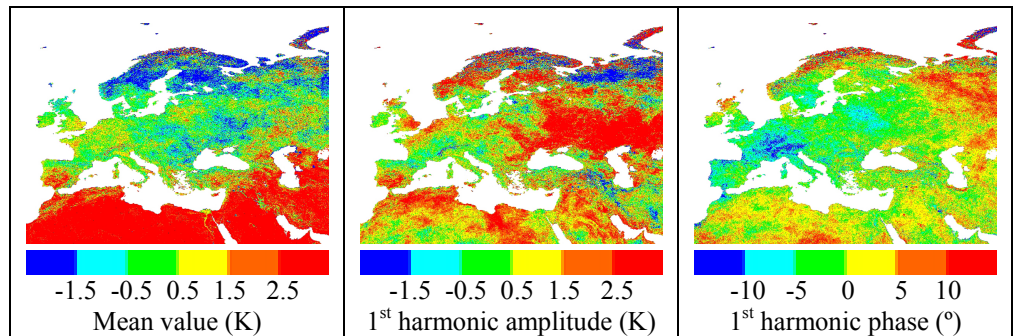
Figure 5.10.- Differences in LST between periods 1982/1986 and 1995/1999.

5.3.1.- Results

The aforementioned method has been applied to the whole PAL database, incomplete years inclusive, which means that results for years 1981, 1994 and 2001 must be analyzed with caution, since at least 3 months of data are missing. An average year of PAL data has been calculated as the average over the 22 years of data over each corresponding compositing period. Figure 5.12 shows an IHS image of the retrieved parameters from these results, accompanied by a legend explaining its color in terms of θ values. This image is similar to Figure 5.5, showing that the results described in section 5.1.2 are not specific to the GIMMS database, but can be generalized.

Since the whole PAL database has been processed to obtain yearly θ, d and R^2 parameters, trends can be retrieved for the 22 years of data. These trends have been retrieved following the procedure described in Chapter 4, by carrying out non-

189

Figure 5.11.- Difference images for NDVI and LST between periods 1982/1986 and 1995/1999 for a) mean value, b) 1st harmonic amplitude and c) 1st harmonic phase.

parametric Mann-Kendall trend tests for the times series for each pixel, and trend values have been retrieved by linear regression. Only trend values for pixels passing the Mann-Kendall trend tests at 90% confidence level are displaye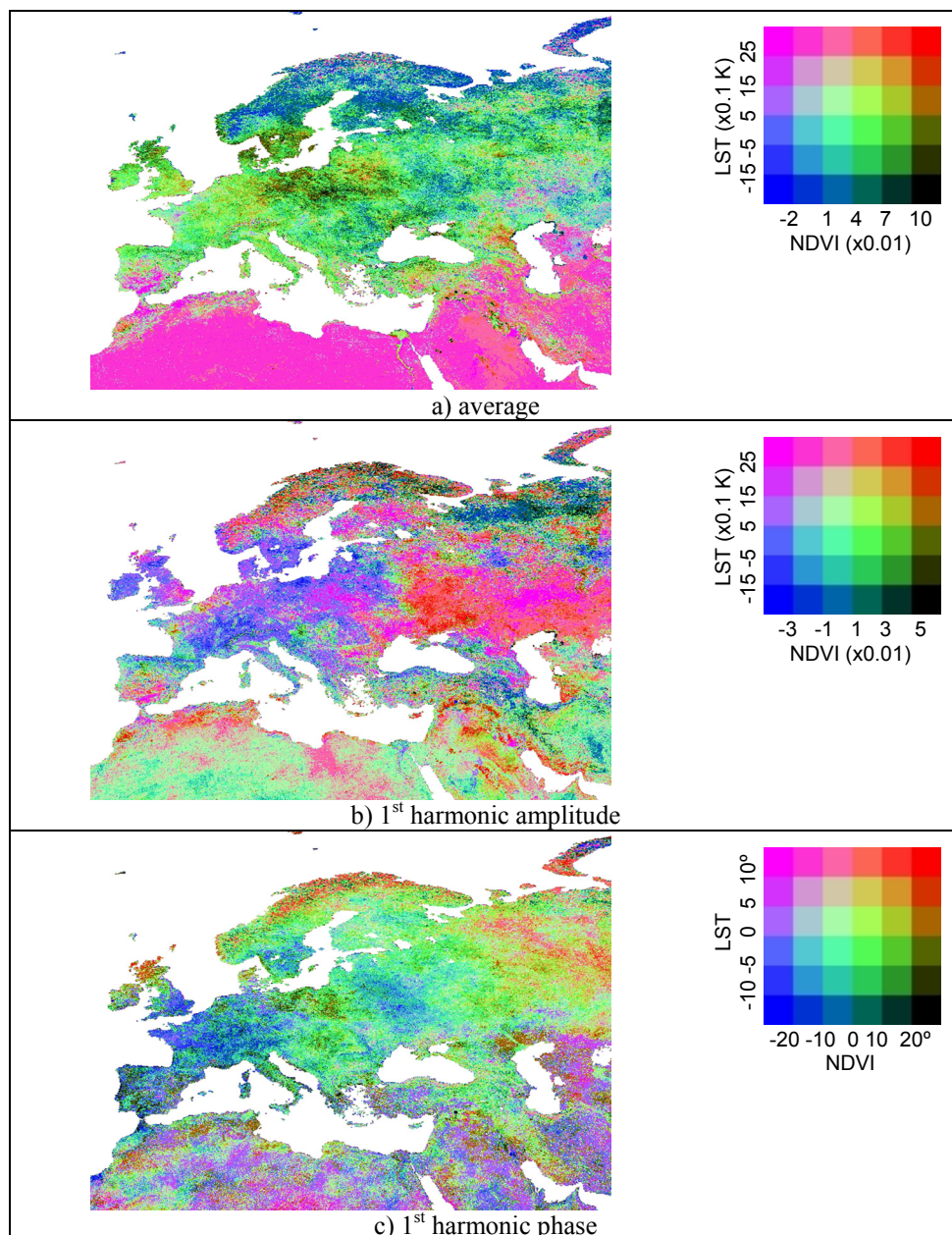d in Figure 5.13 for all three parameters. Once more, one has to keep in mind that the absence of trend in the images does not mean that there is no change for the considered pixel, but only that there is no significance in the retrieved trend for the 22 years of data available. A discussion of these retrieved trends is developed in section 5.3.3, after an analysis of the influence of the orbital drift on the retrieved time series for the θ, d and R^2 parameters.

5.3.2.- Orbital drift influence

In order to interpret changes correctly in the θ, d and R^2 parameters for the whole PAL time series, one has to take into consideration the effect of the orbital drift on the data, since this database is known to suffer from the orbital drift affecting AVHRR channel data. To this end, a statistical test has been chosen to assess the independence of each retrieved parameter. However, to test for statistical independence, each parameter time series has to be compared to a time series related to orbital drift. Since no data are available for the PAL database other than channel information, a time series of yearly averaged overpass times has been simulated. The simulation consists in calculating an estimated overpass time for each pixel and for each composite period of the PAL database, and then in averaging yearly these estimated overpass time to obtain a time series of 22 overpass times to be analyzed. The overpass times have been estimated by the method developed in Ignatov et al. (2004) which has been presented in Chapter 3. This method suffers from two flaws: since the acquisition date is not provided in the PAL database, acquisition date is estimated as the median date of the corresponding composite period; and the acquisition is supposed to be done at nadir angle for the same reason. Since the obtained 10-day images of overpass time are averaged over each year, these flaws are averaged over 36 composites, thus considerably decreasing their influence on the time series.

Once the yearly time series of overpass times have been obtained, statistical tests have to be carried out to address the independence between these time series and θ, d and R^2 parameter time series. The Kendall rank correlation test has been chosen as the most suitable for this task since it is non-parametric, and allows one

to check if two time series are independent of one another. The following explanation of this statistical test has been adapted from Hipel & McLeod (1994).

Suppose that the data consist of a bivariate random sample of size n, (x_i, y_i), for $i = 1, 2, \ldots, n$. Two observations are concordant if both members of one bivariate observation are larger than their respective members of the other observation. For example, the two bivariate observations (3.2,9.6) and (4.7,11.2) are concordant. Out of the $(n^2 - n)$ possible pairs, let N_c denote the number of concordant pairs of observations. A pair of bivariate observations, such as (5.2,8.6) and (4.3,12.4), is considered discordant since it is not concordant. Let N_d be the total number of discordant pairs. Under the independence hypothesis, the test statistic for the Kendall rank correlation test is:

$$\tau = \frac{N_c - N_d}{\frac{1}{2} n(n-1)} \qquad \text{(Eq. 5.2)}$$

If all pairs are concordant, the two series are perfectly correlated and $\tau = 1$. For the case of total discordance, $\tau = -1$. Consequently, τ varies between -1 and +1. Because τ is asymptotically normally distributed ($n > 10$) and its distribution can be tabulated exactly for small n, one can determine the significance level for a computed value of τ. If the calculated τ is greater than or less than a given threshold, one can respectively accept or reject the independence hypothesis at the corresponding significance level. Theoretical results regarding this test can be found in Valz *et al.* (1995).

Therefore, independence between time series of θ, d and R^2 parameters on one hand, and estimated overpasses on the other hand, have been tested with the help of this test, and the corresponding significance levels have been retrieved for all three parameters. These significance levels are shown in Figure 5.14. A first observation is that all parameters can be considered independent from overpass time, and therefore from the orbital drift, at 50% confidence level, and most of the world at 80% confidence level. Pixels for which the independence hypothesis is rejected at 80% confidence level are located around the Equator, where the orbital drift effect on NDVI is stronger (Privette *et al.*, 1995), and in arid and semi-arid areas, for which the orbital drift effect on temperatures is easier to identify (Gleason *et al.*,
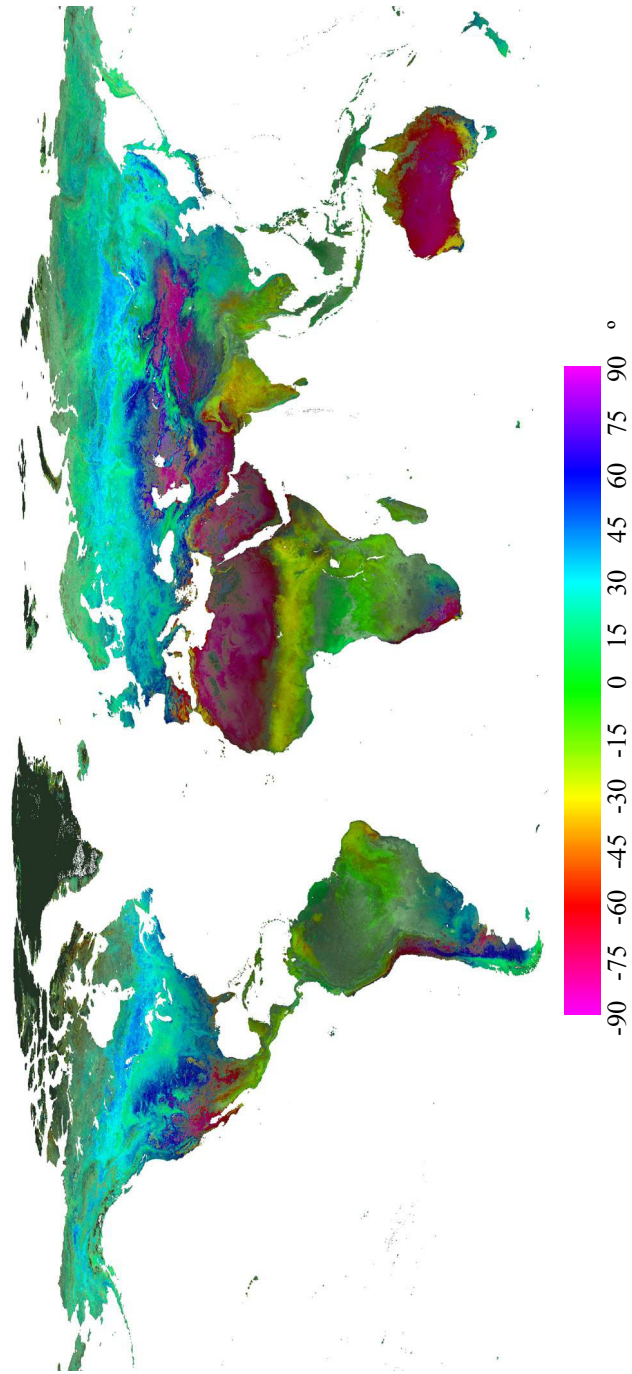
192

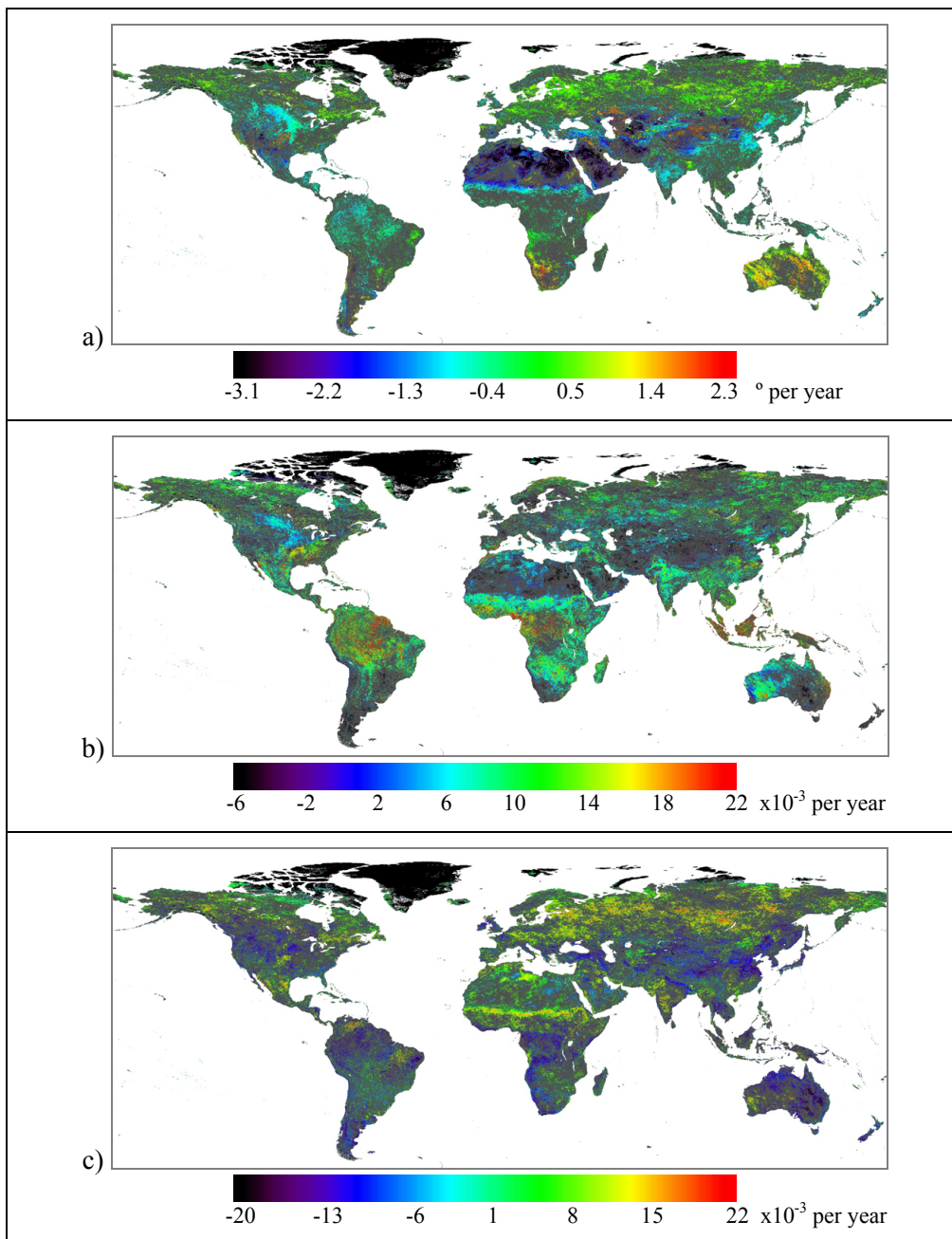*Figure 5.12.- IHS image of PAL NDVI-LST feature space parameter at global scale.*

193

Figure 5.13.-Trends over the whole PAL database for a) θ, b) d, and c) R^2 parameters following the traditional rainbow color code.

2002; Sobrino *et al.*, 2006a). Worldwide averages of the significance level reached by the Kendall rank correlation test are 0.87 for θ, 0.89 for d and R^2 parameters, showing a good overall independence of the proposed method from the orbital drift. The fact that θ parameter is more affected than the other two parameters is due to the direct dependence of the angle determination to changes in LST and NDVI.

5.3.3.- Discussion

Since most of the globe is not affected by NOAA's orbital drift as regards θ, d and R^2 parameters, the trends retrieved in these three parameters can be analyzed. To this end, the pixels showing the most extreme changes have been analyzed. This has been carried out by selecting in each of the parameter trend image the pixels showing a trend at 90% significance level (which are the ones appearing in color in Figure 5.13), and then by identifying the pixels corresponding to the highest trends in absolute values. The trends corresponding to the highest values have been identified as the pixels with a higher trend in absolute values than twice the standard deviation around the mean trend value for pixels exhibiting a trend at 90% significance level. Finally, a histogram has been built to relate these high trends to θ values, and therefore to land cover types. Two histograms have been built, to show the difference between downward extreme trends and upward extreme trends for all three parameters. These two histograms have then been normalized by the histogram of θ over the pixels exhibiting a trend at 90% significance level, which are presented in Figure 5.15.

A first observation regarding Figure 5.15 is that extreme trends in R^2 parameter do not show any particular behavior with θ parameter. However, extreme trends in θ and d do show a clear pattern depending on θ values. First, one has to keep in mind that trends in θ are not to be trusted over arid areas due to the orbital drift effect, which means that extreme trends in θ located around mean θ values of ±90º could be due only to orbital drift. Extreme decreasing trends in θ values are located between mean θ values of -80º and -30º, which correspond to arid and semi-arid land covers, which therefore tend to be more arid, since decreasing trends in θ values makes their θ values closer to arid θ values (-90º). This is in agreement with previous studies over Europe (Julien *et al.*, 2006) as well as in the Arab Region (Abahussein *et al*., 2002). Extreme decreasing trends can also be evidenced for

mean θ values between 50º and 80º. These θ values correspond to land covers with a short NDVI cycle and a larger LŜT cycle, which describe vegetation with low capacity to control their temperature, such as tundra, pasture or cereal fields for example, mainly located in the Northern Hemisphere (see Figure 5.12). The decreasing trends for this land cover correspond to an increase in the plant capacity to control its temperature (shorter LST cycle and/or longer NDVI cycle), which has been documented previously as a greening trend across the Northern Hemisphere by Bogaert *et al.* (2002), Myneni *et al.* (1997) and Zhou *et al.* (2001). Extreme increasing trends in θ values can also be found for the same vegetation types (5.15b), but the number of pixels concerned is much lower in this case.

Changes in *d* parameter are easier to interpret, since they correspond to variations in NDVI-LST yearly cycle. Extreme decreases for *d* parameter correspond to the same areas as the ones for θ parameter. Semi-arid areas (-80º < θ < -30º) tend to become more arid (shorter vegetation cycle), thus confirming the conclusions of the previous paragraph. Vegetation with low capacity to control their temperature also saw a decrease in their seasonal cycle, which is probably due to milder winters, with shorter snow cover over the Northern Hemisphere (Dye, 2002) and therefore a more extended vegetation growth cycle. Finally, extreme increases for *d* parameter are concentrated around θ values of 0º, which correspond to forest areas. The corresponding pixels are shown in Figure 5.13b) in red and are located mainly in tropical rainforests. Therefore, this shows that parts of tropical rainforests have seen an increase in their seasonal cycle, which can be interpreted as a change in land occupation such as deforestation, which replaces natural rainforests by crops with a higher seasonality due mainly to sowing and harvesting cycles. Visual comparison of the affected area in Central Africa with Laporte *et al.* (2007) findings on industrial logging in this region shows that this explanation is correct.
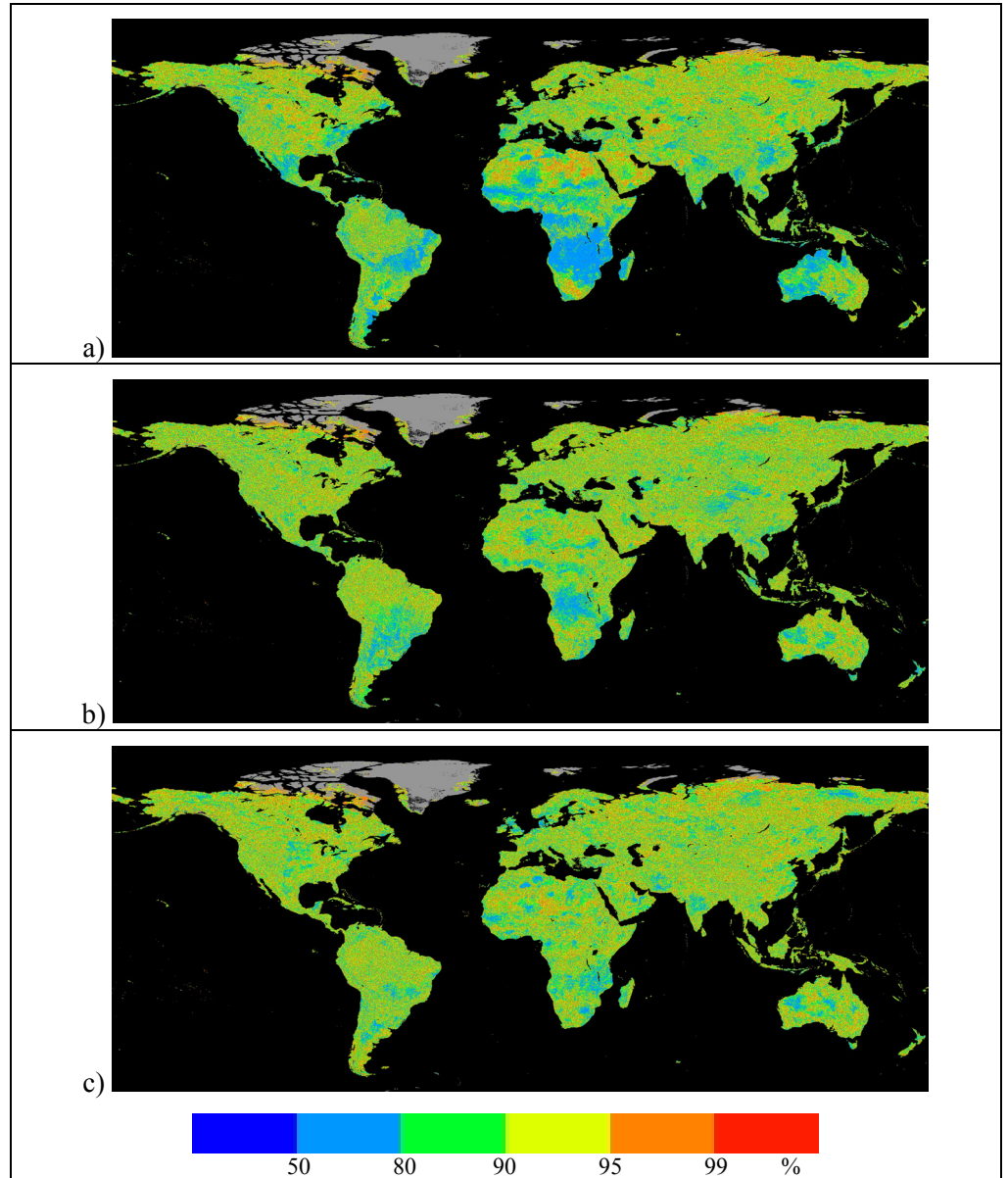
196

Figure 5.14.- Significance levels obtained with Kendall rank correlation test used to assess the independence between estimated satellite overpass times and a) θ, b) d, and c) R^2 parameters.
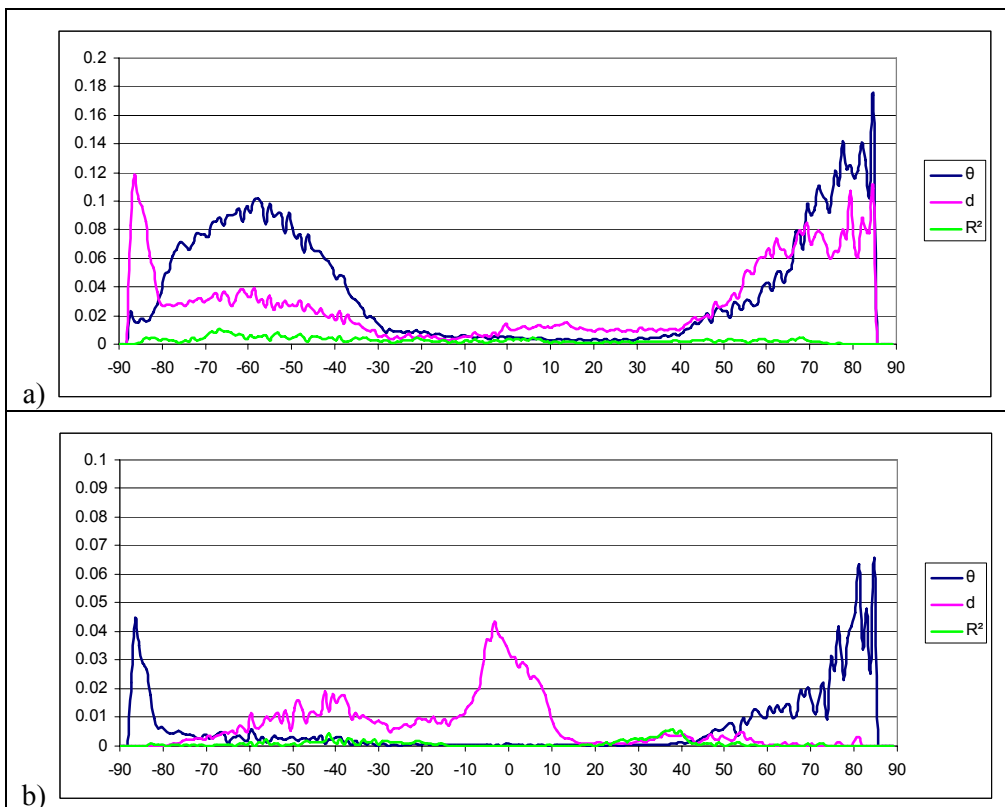
Figure 5.15.- Normalized histograms for a) extreme downward trends and b) extreme upward trends in θ (blue), d (pink), and R² (green) parameters in function of θ mean values, in degrees.

CONCLUSION

As a conclusion, we would like to emphasize the achievements of this work, through a quick revision of the results presented in the previous chapters, completed by some implicit achievements not detailed in the dissertation. Finally, some possible extensions for future work are outlined.

ACHIEVEMENTS

The first achievement of this work is the development of a method for orbital drift correction. The correction of this effect is required for land surface temperature (LST) time series analysis. The correction presented here presents two advantages on the already published methods: this method is pixel based, and does not need any *a priori* information on land use or land cover. This means that this correction is perfectly well-suited for change analysis. Moreover, this correction provides corrected LST comparable to the ones retrieved by a geostationary sensor, making the corrected time series totally reliable, while previous corrections of the orbital drift effect failed to show more than an improvement in the statistical behavior of the data. However, this correction needs previous knowledge of solar zenithal angle (SZA) at the time of image acquisition, information that is not

usually provided in the public databases. This means that we have not been able, despite all our efforts, to correct the entire Pathfinder AVHRR Land (PAL) database from this effect. Of course, the availability of these SZA data would allow the correction of the orbital drift effect for the whole PAL database, from which the entire scientific community would benefit.

This work also led to the development of a fitting procedure which describes most of the world vegetation correctly, through the estimation of vegetation parameters from NDVI yearly data. This fitting procedure provides six meaningful parameters, which can easily be related to vegetation photosynthetic activity. Thus changes in vegetation can be studied directly from those few parameters, instead of having to deal with the whole time series, which represent a considerable amount of data.

The third achievement of this work resides in the phenological phases retrieved from the before mentioned fit parameters, from which trends have been evidenced through Mann-Kendall tests, and then retrieved. Those trends compare well with the ones obtained from previous studies, whether from satellite data or ground phenological records. Moreover, those trends are obtained for each pixel, allowing direct comparison with ground stations, instead of comparing averages over large areas as has been done to this day.

This work has also validated the trends retrieved from the fitting procedure with numerous already documented change hotspots. This validation shows the potential of low resolution data for change detection at finer scale, though the inversion of the procedure might be extremely complicated, due to the amount of possible change patterns, combined to the large volume of data. However, we believe that such a task is worth the effort, and we will try and identify changing areas from low resolution data in a close future.

Moreover, this work has helped characterizing the changes in European vegetation through the use of harmonic analysis. The observed changes (desertification of the most arid areas, vegetation re-growth in Northern Central Europe and changes in vegetation cycle) respond to documented changes climate (air temperature increase, precipitation pattern, etc.). The extension of this analysis to a global dataset with LST corrected from orbital drift effect would help understand the changes affecting our planet.

Another achievement of this work is the development of a method for combined analysis of LST and NDVI at global scale, through the characterization of their temporal interdependence. This dependence being clearly related to vegetation type and local climate, this analysis led to the creation of a color composition of the Earth in which climate and vegetation links are obvious and easily identified. This method represents a great improvement in vegetation monitoring, since only 3 parameters describe the annual vegetation cycle, leaving to a side phenological phases which can be highly variable. The monitoring of those 3 parameters allows the description of the patterns of vegetation change, as well as a first explanation of the reasons behind those changes. The results obtained with this method show good agreement with previous findings, though using only low resolution satellite data. These results validate the approach developed in this PhD dissertation by showing the usefulness of historical low resolution databases.

An implicit achievement of this work lies in the computational aspects of this work. All this data processing has been carried out on a standard computer, proving that such global analyses can be handled easily by little structures. Additionally, we have developed methods for managing high quantities of information, focusing on automated methods for data processing and analysis.

Finally, this work has provided additional knowledge of our planet health by means of the retrieved trends in vegetation between 1981 and 2003, which give us insight both in land cover inter-annual variability and human impact, allowing us a better assessment of the changes.

FUTURE DEVELOPMENTS

With the implantation of various antennas at the Global Change Unit, daily data from several sensors are now available to us. Therefore, we plan to adapt the methodologies developed here to these other sensors, with better spatial and temporal coverage at local to continental scale. Thus, application of combined LST and NDVI time series analysis to MODIS (MODerate resolution Imaging Spectroradiometer) and SEVIRI (Spinning Enhanced Visible and InfraRed Imager) data could lead to additional information on the vegetation of our planet, as regards day to day temporal evolution as well as daily cycles.

Additionally, temporal analyses of historical databases in terms of local homogeneous entities, such as ecoregions or ecosystems, could help characterize our environment and the imprint we have on it, especially at local scale, but from a global perspective.

REFERENCES

A

Abahussain, A. A., Abdu, A. S., Al-Zubari, W. K., El-Deen, N. A. & Abdul-Raheem, M. (2002). Desertification in the Arab Region: analysis of current status and trends, *Journal of Arid Environments*, 51 (2002) 521-545.

Abreu, L. W., & Anderson, G. P. (1996). *The MODTRAN 2/3 report and LOWTRAN 7 model*, Modtran Rep., Contract F19628-91-C-0132, Phillips Lab., Hanscom Air Force Base, Massachusetts, 1996 (Eds.).

Achard, F., Malingreau, J. P., Phulpin, T., Saint, G., Saugier, B., Seguin, B. & Vidal-Madjar, V. (1994). A Mission for Global Monitoring of the Continental

Biosphere, *VEGETATION International Users Committee Secretariat*, Joint Research Centre, Ispra, Italy.

Adams, J. B., Sabol, D. E., Kapos, V., Almeida Filho, R., Robers, D. A., Smith, M. O. & Gillespie, A. R. (1995). Classification of multi-spectral images based on fractions of end members: applications to land-cover change in the Brazilian Amazon, *Remote Sensing of Environment*, 12, 137–154.

Ahas, R., Aasa, A., Menzel, A., Fedotova, V. G., & Scheifinger, H. (2002). Changes in European spring phenology, *International Journal of Climatology*, 22(14), 1727−1738.

Alwashe, M. A. & Bokhari, A. Y. (1993). Monitoring vegetation changes in Al Madinah, Saudi Arabia, using Thematic Mapper data, *International Journal of Remote Sensing*, 14, 191–197.

Aminou, D. M. A., Luhmann, H. J., Hanson, C., Pili, P., Jacquet, B., Bianchi, S., Coste, P., Pasternak, F. & Faure, F. (2003). Meteosat Second Generation. A comparison of on-ground and on-flight Imaging and Radiometricerformances of SEVIRI on MSG-1, *Proceedings of The 2003 EUMETSAT Meteorological Satellite Conference*, Weimar, Germany, 19 September – 3 October. Eumetsat, Darmstadt (Germany).

Andres, L., Salas, W. A. & Skole, D. (1994). Fourier analysis of multitemporal AVHRR data applied to a land cover classification, *International Journal of Remote Sensing*, 15, 1115–1121.

Asner, G. P., Townsend, A. R. & Braswell, B. H. (2000). Satellite observation of EI Niño effects on Amazon forest phenology and productivity, *Geophysical Research Letters*, 27 (7), 981–984.

Atitar, M., Sobrino, J. A., Soria, G., **Julien**, Y. & Raissouni, N. (2007). A Comparison of SEVIRI, AVHRR and MODIS LST products, *ICTIS'07, Information Communication Technologies Intenational Symposium*, pp. 478-481, Fès, Marocco, 3-5 Abril 2007.

B

Bacour, C., Bréon, F.-M., & Maignan, F. (2006). Normalization of the directional effects in NOAA-AVHRR reflectance measurements for an improved monitoring of vegetation cycles, *Remote Sensing of Environment*, 102 (2006) 402-413.

Badhwar, G. D. (1984). Automatic corn-soybean classification using Landsat MSS data, I, Near-harvest crop proportion estimation, *Remote Sensing of Environment*, 14, 15-29.

Baldwin, D. & Emery, W. J. (1993). Systematized approach to AVHRR navigation, *Annals of Glaciology*, 17: 414-420.

Baldwin, D. & Emery, W. J. (1995). Spacecraft altitude variations in NOAA-11 infrared from AVHRR imagery, *International Journal of Remote Sensing*, 16: 531-548.

Banner, A. & Lynham, T. (1981). Multi-temporal analysis of Landsat data for forest cutover mapping – a trial of two procedures, *Proceedings of the 7th Canadian Symposium on Remote Sensing*, Winnipeg, Canada, pp. 233-240.

Barbosa, H. A., Huete, A. R. & Baethgen, W. E. (2006). A 20-year study of NDVI variability over the Northeast Region of Brazil, *Journal of Arid Environments*, 67 (2006) 288-307.

Baret, F. & Guyot, G. (1991). Potentials and limits of vegetation indices for LAI and APAR assessment, *Remote Sensing of Environment*, 35: 161-173.

Bayarjargal, Y., Karnieli, A., Bayasgalan, M., Khudulmur, S., Gandush, C. & Tucker, C. J. (2006). A comparative study of NOAA-AVHRR derived drought indices using change vector analysis, *Remote Sensing of Environment*, 105 (2006) 9-22.

Beaubien, E. G. & Freeland, H. J. (2000). Spring phenology trends in Alberta, Canada: links to ocean temperature, *International Journal of Biometeorology*, 44, 53–59.

Beck, P., Atzberger, C., Høgda, K. A., Johansen, B. & Skidmore A. (2006). Improved monitoring of vegetation dynamics at very high latitudes: A new method using MODIS NDVI, *Remote Sensing of Environment*, 100 (2006) 321-334.

Becker, F. & Li, Z.-L. (1990). Temperature-independent spectral indices in thermal infrared bands, *Remote Sensing of Environment*, 32: 17-33.

Bengtsson, L., & Shukla, J. (1988). Integration of space and in situ observations to study global climate change, *Bulletin of American Meteorological Society*, 69, 1130–1143.

Bogaert, J., Zhou, L., Tucker, C. J., Myneni, R. B. & Ceulemans, R. (2002). Evidence for a persistent and extensive greening trend in Eurasia inferred from satellite vegetation index data, *Journal of Geophysical Research*, Vol. 107 (D11), 10.1029/2001JD001075.

Boisvenue, C. & Running, S. W. (2006). Impacts of climate change on natural forest productivity - evidence since the middle of the 20th century, *Global Change Biology*, (2006) 12, 862-882.

Borak, J. S., Lambin, E. F. & Strahler, A. H. (2000). The use of temporal metrics for land cover change detection at coarse spatial scales, *International Journal of Remote Sensing*, 2000, Vol. 21, No. 6 & 7, 1415-1432.

Bradley, B. A., Jacob, R. W., Hermance, J. F. & Mustard, J. F. (2007). A curve fitting procedure to derive inter-annual phenologies from time series of noisy satellite NDVI data, *Remote Sensing of Environment*, 106 (2007) 137-145.

Braswell, B. H., Schimel, D. S., Linder, E. & Moore III, B. (1997). The Response of Global Terrestrial Ecosystems to Interannual Temperature Variability, *Science*, 278, 870-872.

Brown, O. B., Brown, J. W. & Evans, R. H. (1985). Calibration of advanced very high resolution radiometer infrared observations, *Journal of Geophysical Research*, 90, 11667–11677.

Burns, G. S. & Joyce, A. T. (1981). Evaluation of land cover change detection techniques using Landsat MSS data, *Proceedings of the 7th PECORA Symposium*, Sioux Falls, SD, USA (Bethesda, MD: ASPRS), pp. 252–260.

C

Camberlin, P., Janicot, S. & Poccard, I. (2001). Seasonality and atmospheric dynamics of the teleconnection between African rainfall and tropical sea-surface temperature, Atlantic vs. ENSO, *International Journal of Climatology*, v. 21, p. 973-1005.

Carlson, T., & Ripley, D. (1997). On the relation between NDVI, fractional vegetation cover, and leaf area index, *Remote Sensing of Environment*, 62: 241-252.

Carter, T. R. (1998). Changes in the thermal growing season in Nordic countries during the past century and prospects for the future, *Agricultural and Food Science Finland*, 7, 161–179.

Chang, J.-H. (1974). *Climate and Agriculture*, Aldine Publishing Company, Chicago, USA, 304 p.

Chen, P. Y., Srinivasan, R., Fedosejevs, G. & Kiniry, J. R. (2003). Evaluating different NDVI composite techniques using NOAA-14 AVHRR data, *International Journal of Remote Sensing*, 2003, Vol. 24, No. 17, 3403-3412.

Chen, X. & Pan, W. (2002). Relationships among phenological growing season, time-integrated normalized vegetation index and climate forcing in the temperate region of eastern China, *International Journal of Climatology*, 22: 1781-1792 (2002).

Chen, X., Hu, B. & Yu, R. (2005). Spatial and temporal variation of phenological growing season and climate change impacts in temperate eastern China, *Global Change Biology*, 11, 1118–1130.

Chmielewski, F.-M. & Rötzer, T. (2002). Annual and spatial variability of the beginning of growing season in Europe in relation to air temperature changes, *Climate Research*, 19, 257–264.

Clarke, T. R. (1997). An empirical approach for detecting crop water stress using multispectral airborne sensors, *HortTech*, Vol. 7 (1), January-March 1997.

Colwell, J. E., Davis, G. & Thomson, F. (1980). *Detection and measurement of changes in the production and quality of renewable resources*, USDA Forest Service Final Report No. 145300-4-F, ERIM, Ann Arbor, Michigan.

Coppin, P., Jonckheere, I., Nackaerts, K., Muys, B. & Lambin, E. (2004). Digital change detection methods in ecosystem monitoring: a review, *International Journal of Remote Sensing*, 2004, Vol. 25, No. 9, 1565-1596.

D

D'Arrigo, R. D., Malmstrom, C. M., Jacoby, G. C., Los, S. O. & Bunker, D. E. (2000). Correlation between maximum latewood density of annual tree rings

and NDVI based estimates of forest productivity, *International Journal of Remote Sensing*, 21 (11): 2329-2336.

Dash, P., Göttsche, F.-M., Olesen, F.-S. & Fischer, H. (2002). Land surface temperature and emissivity estimation from passive sensor data: theory and practice - current trends, *International Journal of Remote Sensing*, 23 (13), 2563-2594.

Davenport, M. L. & Nicholson, S. E. (1993). On the Relation between Rainfall and the Normalized Difference Vegetation Index for Diverse Vegetation Types in East Africa, *International Journal of Remote Sensing*, 14 (12): 2369-2389.

De Beurs, K. M. (2005). *A statistical framework for the analysis of long image time series: the effect of anthropogenic change on land surface phenology*, PhD dissertation, Faculty of The Graduate College, University of Nebraska, 2005.

De Beurs, K. M. & Henebry, G. M. (2004a). Land surface phenology, climatic variation, and institutional change: Analyzing agricultural land cover change in Kazakhstan, *Remote Sensing of Environment*, 89 (2004) 497-509.

De Beurs, K. M. & Henebry, G. M. (2004b). Trend Analysis of the Pathfinder AVHRR Land (PAL) NDVI Data for the deserts of Central Asia, *IEEE Geoscience and Remote Sensing Letters*, Vol. 1, No. 4, October 2004.

De Beurs, K. M. & Henebry, G. M. (2005a). A statistical framework for the analysis of long image time series, *International Journal of Remote Sensing*, 2005, Vol. 26, No. 8, 1551-1573.

De Beurs, K. M. & Henebry, G. M. (2005b). Land surface phenology and temperature variation in the International Geosphere-Biosphere Program high-latitude transects, *Global Change Biology*, (2005) 11, 779-790.

Delbart, N., Kergoat, L., Le Toan, T., Lhermitte, J. & Picard, G. (2005). Determination of phenological dates in boreal regions using normalized difference water index, *Remote Sensing of Environment*, 97, 26−38.

Delbart, N., Le Toan, T., Kergoat, L., & Fedotova, V. (2006). Remote sensing of spring phenology in boreal regions: A free of snow-effect method using NOAA-AVHRR and SPOT-VGT data (1982-2004), *Remote Sensing of Environment*, 101 (2006) 52-62.

Desclée, B., Bogaert, P. & Defourny, P. (2006). Forest change detection by statistical object-based method, *Remote Sensing of Environment*, 102 (2006) 1-11.

Dietz, E. J. & Killeen, T. J. (1981). A nonparametric multivariate test for monotone trend with pharmaceutical applications, *Journal of American Statistical Association*, 76, 169-174.

Duchemin, B., Guyon, D. & Lagouarde, J. P. (1999). Potential and limits of NOAA-AVHRR temporal composite data for phenology and water stress monitoring of temperate forest ecosystems, *International Journal of Remote Sensing*, 1999, Vol. 20, No. 5, 895-917.

Dutton, E. (1994). Aerosol optical depth measurements from four NOAA/CMDL monitoring sites, *Oak Ridge, Tennessee, Carbon Dioxide Information Analysis Center, Oak Ridge National Laboratory*: 484-494.

Dye, D. G. (2002). Variability and trends in the annual snow-cover cycle in Northern Hemisphere land areas, 1972-2000, *Hydrological Processes*, 16, 3065-3077 (2002).

Eastman, J. R. & Fulk, M. (1993). Long sequence time series evaluation using standardized principal components, *Photogrammetric Engineering and Remote Sensing*, 59, 991–996.

Ehrlich, D. & Lambin, E. F. (1996). Broad scale land-cover classification and interannual climatic variability, *International Journal of Remote Sensing*, 17 (5), 845-862.

El Saleous, N. Z., Vermote, E. F., Justice, C. O., Townshend, J. R., Tucker, C. J., & Goward, S. N. (2000). Improvements in the global biospheric record from the Advanced Very High Resolution Radiometer (AVHRR), *International Journal of Remote Sensing*, 21 (6-7), 1251-1277.

Etter, A., McAlpine, C., Phinn, S., Pullar, D. & Possingham, H. (2006). Characterizing a tropical deforestation wave: a dynamic spatial analysis of a

deforestation hotspot in the Colombian Amazon, *Global Change Biology*, (2006) 12, 1409-1420.

Evans, J. P. & Geerken, R. (2006). Classifying rangeland vegetation type and coverage using a Fourier component based similarity measure, *Remote Sensing of Environment*, 105 (2006) 1-8.

F

FAO (2005). *Global Forest Resources Assessment*, Report available from FAO website:
http://www.fao.org/forestry/foris/webview/forestry2/index.jsp?sitetreeId=24690&langId=1&geoId=0.

Field, C. B., Randerson, J. T. & Malmström, C. M. (1995). Global net primary production: Combining ecology and remote sensing, *Remote Sensing of Environment*, 51 (1995) 74-88.

Fischer, A. (1994). A model for the seasonal variations of vegetation indices in coarse resolution data and its inversion to extract crop parameters, *Remote Sensing of Environment*, 48, 220-230.

Friedl, M., Henebry, G., Reed, B., Huete, A., White, M., Morisette, J., Nemani, R., Zhang, X. & Myneni, R. (2006). *Land Surface Phenology*, A Community White Paper requested by NASA, Apr 2006:
ftp://zeus.geog.umd.edu/Land_ESDR/Phenology_Friedl_whitepaper.pdf

Fung, T. & LeDrew, E. (1987). Application of principal components analysis to change detection, *Photogrammetric Engineering and Remote Sensing*, 53: 1649-1658.

G

Gates, D. M. (1980). *Biophysical Ecology*, Springer-Verlag, New York, 611 p.

Gibson, J. K., Kållberg, P., Uppala, S., Nomura, A., Hernandez, A. & Serrano, E. (1997). ERA Description, *ECMWF Re-Analysis Final Report Series*, 1, 71 pp.

Gieske, A. (2007). *ShellMSG, A user interface to extraction of SEVIRI HRIT/LRIT images* (in preparation).

Gilabert, M. A., González-Piqueras, J., García-Haro, F. J. & Meliá, J. (2002). A generalized soil-adjusted vegetation index, *Remote Sensing of Environment*, 82, 303−310.

Gillies, R. R., Carlson, T. N., Cui, J., Kustas, W. P. & Humes, K. S. (1997). A verification of the 'triangle' method for obtaining surface soil water content and energy fluxes from remote measurements of the Normalized Difference Vegetation Index (NDVI) and surface radiant temperature, *International Journal of Remote Sensing*, 1997, Vol. 18, No. 15, 3145-3166.

Giri, C., Defourny, P., & Shrestha, S. (2003). Land cover characterization and mapping of continental Southeast Asia using multi-resolution satellite sensor data, *International Journal of Remote Sensing*, 2003, Vol. 24, No. 21, 4181-4196.

Gitelson, A. A. (2004). Wide dynamic range vegetation index for remote quantification of biophysical characteristics of vegetation, *Journal of Plant Physiology*, 161, 165−173.

Gitelson, A. A., Kaufman, Y. J. & Merzlyak, M. N. (1996). Use of a green channel in remote sensing of global vegetation from EOS-MODIS, *Remote Sensing of Environment*, 58, 289−298.

Gitelson, A. A., Kaufman, Y. J., Stark, R. & Rundquist, D. (2002). Novel algorithms for remote estimation of vegetation fraction, *Remote Sensing of Environment*, 80, 76−87.

Gleason, A. C. R., Prince, S. D., Goetz, S. J. & Small, J. (2002). Effects of orbital drift on land surface temperature measured by AVHRR thermal sensors, *Remote Sensing of Environment*, 79 (2002) 147-165.

Goetz, S. J. (1997). Multi-sensor analysis of NDVI, surface temperature and biophysical variables at a mixed grassland site, *International Journal of Remote Sensing*, 1997, Vol. 18, No. 1, 71-94.

Goetz, S. J., Fiske, G. J. & Bunn, A. G. (2006). Using satellite time-series data sets to analyze fire disturbance and forest recovery across Canada, *Remote Sensing of Environment*, 101 (2006) 352-365.

Gong, P., Pu, R., Biging, G. S. & Larrieu, M. R. (2003). Estimation of forest leaf area index using vegetation indices derived from hyperion hyperspectral data, *IEEE Transactions on Geoscience and Remote Sensing*, 40, 1355−1362.

Gordon, H. R., Brown, J. W. & Evans, R. H. (1988). Exact Rayleigh scattering calculations for use with the Nimbus-7 coastal zone colour scanner, *Applied Optics*, 27: 2111-2122.

Goward, S. N., Markhan, B., Dye, D. G., Dulaney, W., & Yang, J. (1991). Normalized difference vegetation index measurements from the Advanced Very High Resolution Radiometer, *Remote Sensing of Environment*, 35: 257-277.

Goward, S. N., Xue, Y. & Czajkowski, K. P. (2002). Evaluating land surface moisture conditions from the remotely sensed temperature/vegetation index measurements – An exploration with the simplified simple biosphere model, *Remote Sensing of Environment*, 79 (2002) 225-242.

Gusso, A., Fontana, D. C. & Goncalves, G. A. (2007). Mapping land surface temperature using AVHRR/NOAA sensor, *Pesquisa Agropecuária Brasileira*, 2007, Vol. 42, No. 2, pp. 231-237.

Gutman, G. G. (1999). On the monitoring of land surface temperature with the NOAA/AVHRR: removing the effect of satellite orbit drift, *International Journal of Remote Sensing*, 1999, Vol. 20, No. 17, 3407-3413.

Gutman, G., Tarpley, D., Ignatov, A. & Olson, S. (1995). The enhanced NOAA Global Land datasets from the Advanced Very High Resolution Radiometer, *Bulletin of American Meteorological Society*, 76: 1141-1156.

Hall, R. J., Crown, P. H. & Titus, S. J. (1984). Change detection methodology for aspen defoliation with Landsat MSS digital data, *Canadian Journal of Remote Sensing*, 10: 135-142.

Hall, F. G., Botkin, D. B., Strebel, D. E., Woods, K. D. & Goetz, S. J. (1991). Large-scale patterns of forest succession as determined by remote sensing, *Ecology*, 72: 628-640.

Hall-Beyer, M. (2003). Comparison of Single Year and Multiyear NDVI Time Series Principal Components In Cold Temperate Biomes, *IEEE Transactions on Geoscience and Remote Sensing*, Vol. 41, No. 11, part 1, pp. 2568-2574.

Han, K.-S., Viau, A. A. & Anctil, F. (2004). An analysis of GOES and NOAA derived land surface temperatures estimated over a boreal forest, *International Journal of Remote Sensing*, 2004, Vol. 25, No. 21, 4761-4780.

Heumann, B. W., Seaquist, J. W., Eklundh, L. & Jönsson, P. (2007). AVHRR derived phenological change in the Sahel and Soudan, Africa, 1982-2005, *Remote Sensing of Environment*, 108 (2007) 385-392.

Higgins, R. W., Mo, K. C. & Schubert, S. D. (1996). The moisture budget of the Central United States in Spring as evaluated in the NCEP/NCAR and the NASA/DAO Reanalysis, *Monthly Weather Review*, 124, 939-963.

Hipel, K. W. & McLeod, A. I. (1994). *Time Series Modelling of Water Resources and Environmental Systems*, Elsevier Scientific Publishing Company, Amsterdam, 1013 pp.

Hirsch, R. M. & Slack, J. R. (1984). A nonparametric trend test for seasonal data with serial dependence, *Water Resources Research*, 20, 727-732.

Hoeffding, W. (1948). A class of statistics with asymptotically normal distribution, *Annals of Mathematical Statistics*, 19, 293-325.

Høgda, K. A., Karlsen, S. R., Solheim, I., Tømmervik, H. & Ramfjord, H. (2002). The start dates of birch pollen seasons in Fennoscandia studied by NOAA AVHRR NDVI data, *Proceedings of IGARSS 2002*, ISBN 0-7803-7536-X, Toronto, Ontario, Canada, June 2002, Vol. 6, pp. 3299-3301.

Høgda, K. A., Karlsen, S. R. & Tømmervik, H. (2005). Changes in growing season in Fennoscandia 1982-1999 Part. 2, pp. 71-84, In: Springer Berlin Heidelberg (Ed.), *Arctic Alpine Ecosystems and People in a Changing Environment*, 2007. ISBN 978-3-540-48512-4.

Holben, B. N. (1986). Characteristics of maximum-value composite image from temporal AVHRR data, *International Journal of Remote Sensing*, 7: 1417-1434.

Hope, A., Engstrom, R. & Stow, D. (2005). Relation between AVHRR surface temperature and NDVI in Arctic tundra ecosystems, *International Journal of Remote Sensing*, 2005, Vol. 26, No. 8, 1771-1776.

Howarth, P. J. & Wickware, G. M. (1981). Procedures for change detection using Landsat, *International Journal of Remote Sensing*, 2, 277–291.

Huang, N. E., Shen, Z., Long, S. R., Wu, M. C., Shih, H. H., Zheng, Q., Yen, N. C., Tung, C. C. & Liu, H. H. (1998). The empirical mode decomposition and the Hilbert spectrum for nonlinear and non-stationary time series analysis, *Proceedings of the Royal Society London*, A 454(1971), 903-995.

Huang, N. E., Shen, Z. & Long, S.R. (1999). A new view of nonlinear water waves: the Hilbert spectrum, *Annual Review of Fluid Mechanics*, 31, 417-457.

Huete, A. R. (1988). A soil-adjusted vegetation index (SAVI), *Remote Sensing of Environment*, 25, 53-70.

Huete, A. R., Justice, C. O. & Liu, H. Q. (1994). Development of vegetation and soil indices for MODIS-EOS, *Remote Sensing of Environment*, 49 (3), 224-234.

Huete, A. R., Liu, H. Q., Batchily, K. & van Leeuwen, W. (1997). A Comparison of Vegetation Indices over a Global Set of TM Images for EOS-MODIS, *Remote Sensing of Environment*, Vol. 59, No. 3, pp. 440-451.

Huete, A. R., Didan K., Shimabukuro, Y. E., Ratana, P., Saleska, S. R., Hutyra, L. R., Yang, W., Nemani, R. R. & Myneni, R. (2006). Amazon rainforests green-up with sunlight in dry season, *Geophysical Research Letters*, Vol. 33, L06405, doi:10.1029/2005GL025583, 2006.

Ignatov, A., Laszlo, I., Harrod, E. D., Kidwell, K. B. & Goodrum, G. P. (2004). Equator crossing times for NOAA, ERS and EOS sun-synchronous satellites, *International Journal of Remote Sensing*, 2004, Vol. 25, No. 23, 5255-5266.

IPCC (2001). *Climate Change 2001: Impacts, Adaptation, and Vulnerability*, Contribution of Working Group II to the Third Assessment Report of the Intergovernmental Panel on Climate Change [McCarthy, James J., Canziani, Osvaldo F., Leary, Neil A., Dokken, David J., and White, Kasey S. (eds.)], Cambridge University Press, Cambridge, United Kingdom and New York, NY, USA, 1032 p.

Iqbal, M. (1983). *An Introduction to Solar Radiation*, Academic Press, Toronto. Kasten F. A., 1966.

J

Jarlan, L., Tourre, Y. M., Mougin, E., Philippon, N. & Mazzega, P. (2005). Dominant patterns of AVHRR NDVI interannual variability over the Sahel and linkages with key climate signals (1982-2003), *Geophysical Research Letters*, Vol. 32, L04701, doi: 10.1029/2004GL021841, 2005.

Ji, L. & Peters, A. J. (2007). Performance evaluation of spectral vegetation indices using a statistical sensitivity function, *Remote Sensing of Environment*, 106 (2007) 59-65.

Jia, G. S. J., Epstein, H. E., & Walker, D. A. (2003). Greening of arctic Alaska, 1981-2001, *Geophysical Research Letters*, 30, doi:10.1029/2003GL018268.

Jiang, Z., Huete, A. R., Chen, J., Chen, Y., Li, J., Yan, G. & Zhang, X. (2006). Analysis of NDVI and scaled difference vegetation index retrievals of vegetation fraction, *Remote Sensing of Environment*, 101 (2006) 366-378.

Jin, M. & Treadon, R. E. (2003). Correcting the orbit drift effect on AVHRR land surface skin temperature measurements, *International Journal of Remote Sensing*, 2003, Vol. 24, No. 22, 4543-4558.

Johnson, R. D., & Kasischke, E. S. (1998). Change vector analysis: a technique for the multi-spectral monitoring of land cover and condition, *International Journal of Remote Sensing*, 19, 411–426.

Jönsson, P. & Eklundh, L. (2002). Seasonality extraction by function fitting to time-series of satellite sensor data, *IEEE Transactions on Geoscience and Remote Sensing*, 40, 1824-1832.

Julien, Y. & Sobrino, J. A. (2006). A new method for NOAA-AVHRR land surface temperature correction of orbital drift effect, *2nd International Symposium on Recent Advances in Quantitative Remote Sensing*, pp. 866-871, Torrent, España, 25-29 Septiembre, 2006.

Julien, Y. & Sobrino, J. A. (2007a). Changes in the global vegetal cover through a phenological analysis of GIMMS data, MULTITEMP 2007, Fourth International Workshop on the Analysis of Multi-Temporal Remote Sensing Images, *MULTITEMP 2007 Proceedings CD-ROM*, Leuven, Belgium, 18-20 Julio 2007.

Julien, Y. & Sobrino, J. A. (2007b). NDVI seasonal amplitude and its variability, *International Journal of Remote Sensing*, in press.

Julien, Y., Sobrino, J. A., Zaragoza, M., Cuenca, J., Gómez, M., Jiménez-Muñoz, J.-C., Romaguera, M., Shen, Q. & Sòria, G. (2005a). Global vegetation monitoring through multitemporal analysis of pathfinder AVHRR land database, *Proceedings of SPIE*, Vol. 5976, 59761F, (2005), 0277-786X/05/$15, doi: 10.1117/12.626809, Brugge, Belgium, 19-22 September 2005.

Julien, Y., Sobrino, J. A., Zaragoza, M., Cuenca, J., Gómez, M., Jiménez-Muñoz, J.-C., Romaguera, M., Shen, Q. & Sòria, G. (2005b). Global Monitoring of Land Cover through PAL and Reanalysis Data, 9th International Symposium on Physical Measurements and Signatures in Remote Sensing (ISPMSRS), *ISPMSRS 2005 Conference Proceedings (Part One)*, pp. 423-425, Beijing, China, 17-19 October 2005.

Julien, Y., Sobrino, J. A. & Verhoef, W. (2006). Changes in land surface temperatures and NDVI values over Europe between 1982 and 1999, *Remote Sensing of Environment*, 103 (2006) 43–55.

Julien, Y., Sobrino, J. A. & Nerry, F. (2007). Correcting NOAA-AVHRR orbital drift: a simple and automatic methodology, MULTITEMP 2007, Fourth International Workshop on the Analysis of Multi-Temporal Remote Sensing Images, *MULTITEMP 2007 Proceedings CD-ROM*, Leuven, Belgium, 18-20 Julio, 2007.

Justice, C. O., Markham, B. L., Townshend, J. R. G. & Kennard, R. L. (1989). Spatial degradation of satellite data, *International Journal of Remote Sensing*, 10: 1539-1561.

K

Kalnay, E. & Jenne, R. (1991). Summary of the NMC/NCAR Reanalysis Workshop of April 1991, *Bulletin of the American Meteorological Society*, 72, 1897-1904.

Kalnay, E., Kanamitsu, M., Kistler, R., Collins, W., Gandin, L., Iredell, M., Saha, S., White, G., Woollen, J., Zhu, Y., Chelliah, M., Ebisuzaki, W., Higgins, W., Janowiak, J., Mo, K. C., Ropelewski, C., Wang, J., Leetmaa, A., Reynolds, R., Jenne, R. & Joseph, D. (1996). The NCEP/NCAR 40-Year Reanalysis Project, *Bulletin of the American Meteorology Society*, 1996, Vol. 77, No. 3427-471.

Kanamitsu, M. (1989). Description of the NMC global data assimilation and forecast system, *Weather and Forecasting*, 4, 334-342.

Kanamitsu, M., Alpert, J. C., Campana, K. A., Caplan, P. M., Deaven, D. G., Iredell, M., Katz, B., Pan, H.-L., Sela, J. & White, G. H. (1991). Recent changes implemented into the global forecast system at NMC, *Weather and Forecasting*, 6, 425-435.

Kaufman, Y. J. & Tanré, D. (1992). Atmospherically resistant vegetation index (ARVI) for EOS-MODIS, in: *Proceedings of IEEE International Geoscience and Remote Sensing Symposium '92*, IEEE, New York, 261-270.

Kaufmann, R. K., Zhou, L., Knyazikhin, Y., Shabanov, N. V., Myneni, R. B. & Tucker, C. J. (2000). Effect of orbital drift and sensor changes on the time series of AVHRR vegetation index data, *IEEE Transactions on Geoscience and Remote Sensing*, 2000, Vol. 38, No. 6, 2584-2597.

Kaufmann, R. K., Zhou, L., Myneni, R. B., Tucker, C. J., Slayback, D., Shabanov, N. V. & Pinzon, J. (2003). The effect of vegetation on surface temperature: A statistical analysis of NDVI and climate data, *Geophysical Research Letters*, Vol. 30, No. 22, 2147, doi: 10.1029/2003GL018251, 2003.

Keeling, C. D., Chin, J. F. S. & Whorf, T. P. (1996). Increased activity of northern vegetation inferred from atmospheric CO2 measurements, *Nature*, 382, 146–149.

Kendall, M. G. (1975). *Rank Correlation Methods*, Charles Griffin, London.

Kidwell, K. B. (1991). *NOAA polar orbiter data (TIROS-N, NOAA-6, NOAA-7, NOAA-8, NOAA-9, NOAA-10, NOAA-11, and NOAA-12) users guide*. NOAA/NESDIS, Washington D.C., USA.

Kidwell, K. B. (1998). *NOAA Polar Orbiter Data User's Guide*, US Department of Commerce, NESDIS, NOAA, National Climatic Data Centre, Satellite Data Services Division, Washington, D.C., USA.

Kistler, R., Kalnay, E., Collins, W., Saha, S., White, G., Woollen, J., Chelliah, M., Ebisuzaki, W., Kanamitsu, M., Kousky, V., van den Dool, H., Jenne, R. & Fiorino, M. (2001). The NCEP-NCAR 50-Year Reanalysis: monthly means CD-ROM and documentation, *Bulletin of the American Meteorology Society*, 2001, Vol. 82, No. 2, 247-267.

Kogan, F. N. & Zhu, X. (2001). Evolution of long-term errors in NDVI time series: 1985-1999, *Advances in Space Research*, Vol. 28, No. 1, pp. 149-153, 2001.

Lambin, E. F. & Strahler, A. H. (1994). Change-vector analysis in multitemporal space: a tool to detect and categorize land-cover change processes using high temporal-resolution satellite data, *Remote Sensing of Environment*, 48: 231-244.

Lambin, E. F. & Ehrlich, D. (1996). The surface temperature-vegetation index space for land cover and land-cover change analysis, *International Journal of Remote Sensing*, 1996, Vol. 17, No. 3, 163-487.

Lambin, E. F. & Ehrlich, D. (1997). Land-cover changes in sub-Saharan Africa (1982–1991): application of a change index based on remotely sensed surface temperature and vegetation indices at a continental scale, *Remote Sensing of Environment*, 61, 181–200.

Laporte, N. T., Stabach, J. A., Grosch, R., Lin, T. S. & Goetz, S. J. (2007). Expansion of industrial logging in Central Africa, *Science*, Vol. 316, 8 June 2007, 145.

Libiseller, C. & Grimvall, A. (2002). Performance of partial Mann-Kendall test for trend detection in the presence of covariates, *Environmetrics*, 13: 71-84.

Linderholm, H. W. (2006). Growing season changes in the last century, *Agricultural and Forest Meteorology*, 137 (2006) 1-14.

Linderholm, H. W., Walther, A., Chen, D. & Moberg, A. (2006). Twentieth-century trends in the thermal growing-season in the Greater Baltic Area, *Climatic Change*, DOI 10.1007/s10584-007-9327-3.

Liu, H. Q. & Huete, A. R. (1995). A feedback based modification of the NDVI to minimize canopy background and atmosphere noise, *IEEE Transactions on Geoscience and Remote Sensing*, Vol. 33, No. 2, pp. 457-465.

Liu, A. X., Wang, J., Liu, Z. J. & Wang, J. (2005). Monitoring desertification in arid and semi-arid areas of China with NOAA-AVHRR and MODIS data, IGARSS 2005: *IEEE International Geoscience and Remote Sensing Symposium, Vols 1-8, Proceedings*, 2362-2364, 2005.

Lloyd, D. (1990). A phenological classification of terrestrial vegetation cover using shortwave vegetation index imagery, *International Journal of Remote Sensing*, 11, 2269-2279.

Los, S. O. (1998). *Linkages between global vegetation and climate: an analysis based on NOAA-Advanced Very High Resolution Radiometer Data*. PhD Dissertation, Vrije Universiteit, Amsterdam.

Los, S. O., Collatz, G. J., Bounoua, L., Sellers, P. J. & Tucker, C. J. (2001). Global Interannual Variations in Sea Surface Temperature and Land Surface Vegetation, Air Temperature, and Precipitation, *Journal of Climate*, 14, 1535–1549.

Los, S. O., North, P. R. J., Grey, W. M. F. & Barnsley, M. J. (2005). A method to convert AVHRR Normalized Difference Vegetation Index time series to a standard viewing and illumination geometry, *Remote Sensing of Environment*, 99 (2005) 400-411.

Lotsch, A., Friedl, M. A., Anderson, B. T. & C. J. Tucker (2003a). Coupled vegetation-precipitation variability observed from satellite and climate records, *Geophysical Research Letters*, 30 (14), 1774, doi:10.1029/2003GL017506.

Lotsch, A., Friedl, M. A. & Pinzon, J. E. (2003b). Spatio-Temporal Deconvolution of NDVI Image Sequences Using Independent Component Analysis, *IEEE Transactions on Geoscience and Remote Sensing*, 41 (12): 2938-2942.

Loveland, T. R., Reed, B. C., Brown, J. F., Ohlen, D. O., Zhu, Z., Yang, L. & Merchant, J. W. (2000). Development of a global land cover characteristics database and IGBP DISCover from 1 km AVHRR data, *International Journal of Remote Sensing*, 2000, Vol. 21, No. 6 & 7, 1303-1330.

Lovell, J. L. & Graetz, R. D. (2001). Filtering Pathfinder AVHRR land NDVI data for Australia, *International Journal of Remote Sensing*, 2001, Vol. 22, No. 13, 2649-2654.

Lupo, F., Linderman, M., Vanacker, V., Bartholome, E. & Lambin, E. F. (2007). Categorization of land-cover change processes based on phenological indicators extracted from time series of vegetation index data, *International Journal of Remote Sensing*, 28 (11): 2469-2483.

Lyon, G. J., Yuan, D., Lunetta, R. S. & Elvidge, C. D. (1998). A change detection experiment using vegetation indices, *Photogrammetric Engineering and Remote Sensing*, 64 (1998), pp. 143–150.

M

Malmström, C. M., Thompson, M. V., Juday, G. P., Los, S. O., Randerson, J. T. & Field, C. B. (1997). Interannual variation in global-scale net primary production: Testing model estimates, *Global Biogeochemical Cycles*, 11 (3), 367–392.

Mann, H. B. (1945). Non-parametric tests against trend, *Econometrica*, 13, 245-259.

Manzo-Delgado, L., Aguirre-Gómez, R. & Álvarez, R. (2004). Multitemporal analysis of land surface temperature using NOAA-AVHRR: preliminary relationships between climatic anomalies and forest fires, *International Journal of Remote Sensing*, 2004, Vol. 25, No. 20, 4417-4423.

Maselli, F. (2004). Monitoring forest conditions in a protected Mediterranean coastal area by the analysis of multiyear NDVI data, *Remote Sensing of Environment*, 89 (2004) 423-433.

Maselli, F. & Chiesi, M. (2005). Integration of multi-source NDVI data for the estimation of Mediterranean forest productivity, *International Journal of Remote Sensing*, 2005, Vol. 27, No. 1, 55-72.

Maselli, F., Barbati, A., Chiesi, M., Chirici, G. & Corona, P. (2006). Use of remotely sensed and ancillary data for estimating forest gross primary productivity in Italy, *Remote Sensing of Environment*, 100 (2006) 563-575.

May, D. A., Stowe, L. L., Hawkins, J. D. & McClain E. P. (1992). A correction for Saharan dust effects on satellite sea surface temperature measurements, *Journal of Geophysical Research*, 97 (C3), 3611–3619.

McPeters, R. D., Krueger, A. J., Bhartia, P. K., Herman, J. R., Oaks, A., Ahmad, Z., Cebula, R. P., Schlesinger, B. M., Swissler, T., Taylor, S. L., Torres, O. & Wellemeyer, C. G. (1993). Nimbus-7 Total Ozone Mapping Spectrometer (TOMS) Data Products User's Guide, *NASA Reference Publication 1323*.

Menenti, M., Azzali, S., Verhoef W. & van Swol, R. (1993). Mapping agro-ecological zones and time lag in vegetation growth by means of Fourier analysis of time series of NDVI images, *Advances in Space Research*, 13, 233-237.

Menzel, A. & Fabian, P. (1999). Growing season extended in Europe, *Nature*, 397, 659.

Mito, C. O., Laneve, G. & Castronuovo, M. M. (2002). A general split window algorithm for land surface temperature estimation, Conference on Remote Sensing for Agriculture, Ecosystems, and Hydrology III, *Proceedings of SPIE 2002*, Toulouse, France, September 17-19, 2001, pp. 170-177.

Mo, K. C., Wang, X. L., Kistler, R., Kanamitsu, M. & Kalnay, E. (1995). Impact of satellite data on the CDAS-reanalysis system, *Monthly Weather Review*, 123, 124-139.

Moody, A. & Johnson, D. M. (2001). Land-surface phenologies from AVHRR using the discrete Fourier transform, *Remote Sensing of Environment*, 75, 305-323.

Morales, L., Castellaro, G., Sobrino, J. A. & El Kharraz, J. (2004). *Land cover dynamic monitoring in the region of Coquimbo (Chile) by the analysis of multitemporal NOAA-AVHRR NDVI images*, ISPRS Conference, Commission VI, 12-23 July 2004, Istanbul, Turquia.

More, J. J. (1977). The Levenberg-Marquardt Algorithm: Implementation and Theory. In: *Numerical Analysis*, ed. Watson, G. A., Lecture Notes in Mathematics 630, Springer-Verlag, 1977.

Moulin, S., Kergoat, L., Viovy, N. & Dedieu, G. (1997). Global-scale assessment of vegetation phenology using NOAA/AVHRR satellite measurements, *Journal of Climate*, 10, 1154-1170.

Muzylev E. L., Startseva Z. P., Uspensky A. B. & Volkova E. V. (2001). Utilization of AVHRR/NOAA based land surface temperature in modelling the hydrological cycle of river basins, IRS 2000. In: *Current problems in Atmospheric Radiation*, pp. 40-43, ed. Smith, W. L. & Timofeyev, Y. M., St. Petersburg, 2001.

Myneni, R. B., Hall, F. G., Sellers, P. J. & Marshak, A. L. (1995). The interpretation of spectral vegetation indexes, *IEEE Transactions on Geoscience and Remote Sensing*, 33, 481-486.

Myneni, R. B., Keeling, C. D., Tucker, C. J., Asrar, G., & Nemani, R. R. (1997). Increased plant growth in the northern high latitudes from 1981 to 1991. *Nature*, 386 (17 april 1997).

Myneni, R. B., Yang, W., Nemani, R. R., Huete, A. r., Dickinson, R. E., Knyazikhin, Y., Didan, K., Fu, R., Negrón Juárez, R. I., Saatchi, S. S., Hashimoto, H., Ichii, K., Shabanov, N. V., Tan, B., Ratana, P., Privette, J. L., Morisette, J. T., Vermote, E. F., Roy, D. P.,Wolfe, R. E.,Friedl, M. A., Running, S. W., Votava, P., El-Saleous, N., Devadiga, S., Su, Y. & Salomonson, V. V. (2007). Large seasonal swings in leaf area of Amazon rainforests, *Proceedings of the National Academy of Sciences of the United States of America*, 104, 4820-4823, Mar 13, 2007, doi:10.1073/pnas.0611338104.

N

Nackaerts, K., Vaesen, K., Muys, B. & Coppin, P. (2005). Comparative performance of a modified change vector analysis in forest change detection, *International Journal of Remote Sensing*, 2005, Vol. 26, No. 5, 839-852.

Neigh, C. S. R., Tucker, C. J. & Townshend, J. R. G. (2007). Synchronous NDVI and surface air temperature trends in Newfoundland: 1982 to 2003, *International Journal of Remote Sensing*, Vol. 28, No. 11, 10 June 2007, 2581-2598.

Nelson, R. F. (1983). Detecting forest canopy change due to insect activity using Landsat MSS, *Photogrammetric Engineering and Remote Sensing*, 49, 1303–1314.

Nemani, R. R. & Running, S. W. (1989). Estimation of regional surface resistance to evapotranspiration from NDVI and thermal-IR AVHRR data, *Journal of Applied Meteorology*, Vol. 28, pp. 276-284.

Nemani, R. R. & Running, S. W. (1997). Land cover characterization using multitemporal red, near-IR, and thermal-IR data from NOAA/AVHRR, *Ecological Applications*, 7 (1), 1997, pp. 79-90.

Nemani, R., Pierce, L., Running, S. & Goward, S. (1993). Developing Satellite-derived Estimetes of Surface Moisture Status, *Journal of Applied Meteorology*, 1993, Vol. 32, pp 548-557.

Nemani, R., White, M., Thornton, P., Nishida, K., Reddy, S., Jenkins, J. & Running, S. (2002). Recent trends in hydrologic balance have enhanced the terrestrial carbon sink in the United States, *Geophysical Research Letters*, 29 (10), 1468, doi:10.1029/2002GL014867.

Nemani, R. R., Keeling, C. D., Hashimoto, H., Jolly, W. M., Piper, S. C., Tucker, C. J., Myneni, R. B. & Running, S. W. (2003). Climate-driven increases in global terrestrial net primary production from 1982 to 1999, *Science*, Vol. 300, 1560-1563.

NGDC (1993). ETOPO5 5-minute gridded elevations/bathymetry for the world, National Geophysical Data Center, *Global Relief Data CD-ROM*, USA, 1993.

Osborne, C. P., Chuine, I., Viner, D. & Woodward, F. I. (2000). Olive phenology as a sensitive indicator of future climatic warming in the Mediterranean, *Plant, Cell and Environment*, (2000) 23, 701-710.

P

Parrish, D. F. & Derber, J. C. (1992). The National Meteorological Center's spectral statistical interpolation analysis system, *Monthly Weather Review*, 120, 1747-1763.

Paruelo, J. M., Garbulsky, M. F., Guerschman, J. P. & Jobbágy, E. G. (2004). Two decades of Normalized Difference Vegetation Index changes in South America: identifying the imprit of global change, *International Journal of Remote Sensing*, 2004, Vol. 25, No. 14, 2793-2806.

Patt, F. & Gregg, W. (1994). Exact closed-form geolocation algorithm for Earth survey sensors, *International Journal of Remote Sensing*, 15, 3719-3734.

Pearson, R. C. & Miller, L. D. (1972). Remote mapping of standing crop biomass for estimation of the productivity of the shortgrass Prairie Pawnee National Grasslands, Colorado, *Proceedings of the 8th International Symposium on Remote Sensing of the Environment*, 2, 1355-1379.

Piao, S., Fang, J., Zhou, L., Ciais, P. & Zhu, B. (2006). Variations in satellite-derived phenology in China's temperate vegetation, *Global Change Biology*, (2006) 12, 672-685.

Pinheiro, A. C. T., Privette, J. L., Mahoney, R. & Tucker C. J. (2004). Directional Effects in a Daily AVHRR land surface temperature dataset over Africa, *IEEE Transactions on Geoscience and Remote Sensing*, 2004, Vol. 42, No. 9, 1941-1954.

Pinheiro, A. C. T., Mahoney, R., Privette, J. L. & Tucker C. J. (2006). Development of a daily long term record of NOAA-14 AVHRR land surface temperature over Africa, *Remote Sensing of Environment*, 103 (2006) 153-164.

Pinty, B. & Verstraete, M. M. (1992). GEMI: A non-linear index to monitor global vegetation from satellites, *Vegetation*, 101, 15-20.

Pinzon, J. (2002). Using HHT to successfully uncouple seasonal and interannual components in remotely sensed data, *SCI 2002 Conference Proceedings*, July 14-18. Orlando, Florida.

Pinzón, J. E., Pierce, J. F. & Tucker, C. J. (2001). Analysis of remote sensing data using Hilbert-Huang transform, *SCI 2001 Proceedings*, July 22 - 25, Orlando, FL.

Pinzon, J., Brown, M. E. & Tucker, C. J. (2005). Satellite time series correction of orbital drift artifacts using empirical mode decomposition, Huang N. E., Shen SSP, eds. *EMD and Its Applications*, Singapore: World Scientific 10: 285–295.

Plisnier, P.-D., Serneels, S. & Lambin, E. F. (2000). Impact of ENSO on East African ecosystems: multivariate analysis based on climatologic and remote sensing data, *Global Ecology and Biogeography Letters*, 9, 481–497.

Poveda, G. & Salazar, L. F. (2004). Annual and Interannual (ENSO) Variability of Spatial Scaling Properties of a Vegetation Index (NDVI) in Amazonia, *Remote Sensing of Environment*, 93:33, 391-401.

Prata, A. J. (1994). Land surface temperatures derived from the advanced very high resolution radiometer and the along-track scanning radiometer, *Journal of Geophysical Research*, 99: 13025-13058.

Prata, A. J. & Platt, C. (1991). Land surface temperature measurements from the AVHRR, *Proceedings of the 5th AVHRR Data Users Meeting*, June 25-28, Tromso, Norway, pp. 433-438.

Price, J. C. (1984). Land surface temperature measurements from the split-window channels of the NOAA- 7/AVHRR, *Journal of Geophysical Research*, 89, 7231–7237.

Price, J. C. (1991). Using spatial context in satellite data to infer regional scale evapotranspiration, *IEEE Transactions in Geoscience and Remote Sensing*, 28, 940-948.

Prince, S. D. & Goward, S. N. (1995). Global primary production: a remote sensing approach, *Journal of Biogeography*, Vol. 22, No. 4, pp. 815-835.

Privette, J. L., Fowler, C., Baldwin, D., Wick, G. A. & Emery, W. J. (1995). Effects of orbital drift on advanced very high resolution radiometer (AVHRR) products: normalized difference vegetation index (NDVI) and sea surface temperature (SST), *Remote Sensing of Environment*, 53, 164-171.

Q

Qin, Z., Olmo, G. D. & Karnieli, A. (2001). Derivation of split window algorithm and its sensitivity analysis for retrieving land surface temperature from NOAA-advanced very high resolution radiometer data, *Journal of Geophysical Research*, 106 (2001) (D19), pp. 22655–22670.

Qin, Z., Xu, B., Zhang, W., Li, W. & Zhang, H. (2004). Comparison of split window algorithms for land surface temperature retrieval from NOAA-AVHRR data, *IEEE 2004 International Geosciences and Remote Sensing Symposium*, VI, 3740-3743, September 20-24, 2004, Anchorage, Alaska, USA.

Qui, J., Chehbouni, A. L., Huete, A. R., Kerr, Y. H. & Sorooshian, S. (1994). A modified soil adjusted vegetation index (MSAVI), *Remote Sensing of Environment*, 48: 119-126.

R

Rao, C. R. N. (1993a). Non-linearity corrections for the thermal infrared channels of the Advanced Very High Resolution Radiometer: assessment and recommendations, *NOAA Technical Report NESDIS-69*, NOAA/NESDIS, Washington D.C, USA.

Rao, C. R. N. (1993b). Degradation of the visible and near-infrared channels of the Advanced Very High Resolution Radiometer on the NOAA-9 spacecraft: Assessment and recommendations for corrections, *NOAA Technical Reoprt NESDIS-70*, NOAA/NESDIS, Washington D.C, USA.

Réaumur, R. A. F. De (1735). *Observations du thermomètre*, Acadadémie Royale des sciences des Pays-Bas Mem., pp. 737-754.

Reed, B. C., White, M. & Brown, J. F. (2003). Remote Sensing Phenology, in *Phenology: An Integrative Environmental Science*, edited by M. D. Schwartz, pp. 365-381, Kluwer Academic Publishers, Dordrecht, the Netherlands.

Richardson, A. J. & Wiegand, C. L. (1977). Distinguishing vegetation from soil background information, *Photogrammetric Engineering and Remote Sensing*, 43, 1541-1552.

Ridd, M. K. & Liu, J. (1998). A comparison of four algorithms for change detection in an urban environment, *Remote Sensing of Environment*, 63, 95–100.

Roberts, D. A., Batista, G. T., Pereira, J., Waller, E. K. & Nelson, B. W. (1998). Change identification using multitemporal spectral mixture analysis: applications in eastern Amazonia. In: *Remote Sensing Change Detection: Environmental Monitoring Applications and Methods*, edited by C. Elvidge and R. Lunetta (Ann Arbor: Ann Arbor Press), pp. 137–161.

Roerink, G. J., Menenti, M. & Verhoef, W. (2000). Reconstructing cloudfree NDVI composites using Fourier analysis of time series, *International Journal of Remote Sensing*, 2000, Vol. 21, No. 9, 1911-1917.

Rondeaux, G., Steven, M. & Baret, F. (1996). Optimization of soil-adjusted vegetation indices, *Remote Sensing of Environment*, 55, 95−107.

Rosen, J. M., Kjome, N. T., McKenzie, R. L. & Liley, J. B. (1994). Decay of Mount Pinatubo aerosol at midlatitudes in the northern and southern hemispheres, *Journal of Geophysical Research*, 99, 25 733–25 739.

Rouse, J. W., Haas, R. H., Schell, J. A. & Deering, D. W. (1973). Monitoring vegetation systems in the Great Plains with ERTS, *Third ERTS Symposium*, NASA SP-351 I, 309-317.

Running, S. W., Nemani, R. R., Heinsch, F. A., Zhao, M., Reeves, M. & Hashimoto, H. (2004). A continuous satellite-derived measure of global terrestrial primary production, *BioScience*, June 2004 / Vol. 54, No. 6, 547-560.

Russell, P. B., Livingston, J. M., Dutton, E. G., Pueschel, R. F., Reagan, J. A., DeFoor, T. E., Box, M. A., Pilewskie, P., Herman, B. M., Kinne, S. A. & Hofmann, D. J. (1993). Pinatubo and pre-Pinatubo optical-depth spectra: Mauna Loa measurements, comparisons, inferred particle size distributions, radiative effects, and relationship to lidar data, *Journal of Geophysical Research*, 98 (D12): doi: 10.1029/93JD02308. issn: 0148-0227.

Sader, S. A. (1988). Remote sensing investigations of forest biomass and change detection in tropical regions. In: *Satellite Imageries for Forest Inventory and Monitoring; Experiences, Methods, Perspectives*, Research Notes No. 21, Department of Forest Mensuration and Management, University of Helsinki, Helsinki, Finland, pp. 31-42.

Sakamoto, T., Yokosawa, M., Toritani, H., Shibayama, M., Ishitsuka, N. & Ohno, H. (2005). A crop phenology detection method using time-series MODIS data, *Remote Sensing of Environment*, 96 (2005) 366-374.

Salinger, M. J. (2005). Climate variability and change: past, present and future - an overview, *Climatic Change*, (2005) 70: 9-29.

Sandholt, I., Rasmussen, K. & Andersen, J. (2002). A simple interpretation of the surface temperature/vegetation index space for assessment of surface moisture status, *Remote Sensing of Environment*, 79 (2002) 213-224.

Sato, M., Hansen, J. E., McCormick, M. P. & Pollack, J. B. (1993). Stratospheric aerosol optical depth, 1850-1990, *Journal of Geophysical Research*, 98, 22987-22994.

Saunders, R. W. (1986). An automated scheme for the removal of cloud contamination from AVHRR radiances over western Europe, *International Journal of Remote Sensing*, 7, 867.

Saunders, R. W. (1990). The determination of broad band surface albedo from. AVHRR visible and near-infrared radiances, *International Journal of Remote Sensing*, 11, 1, 49-67.

Saunders, R. W. & Kriebel, K. T. (1988). An improved method for detecting clear sky and cloudy radiances from AVHRR data, *International Journal of Remote Sensing*, 1988, Vol. 9, No. 1, 123-150.

Schubert, S. D., Pfaendtner, J. & Rood, R. (1993). An assimilated data set for Earth Science applications, *Bulletin of American Meteorological Society*, 74, 2331-2342.

228

Schultz, P. A. & Halpert, M. S. (1995). Global analysis of the relationships among a vegetation index, precipitation and land surface temperature, *International Journal of Remote Sensing*, 1995, Vol. 16, No. 15, 2755-2777.

Schwartz, M. D. & Chen, X. (2002). Examining the onset of spring in China, *Climate Research*, 21, 157–164.

Schwartz, M. D., Ahas, R. & Aasa, A. (2006). Onset of spring starting earlier across the Northern Hemisphere, *Global Change Biology*, (2006) 12, 343-351.

Sellers, P. J. (1985). Canopy reflectance, photosynthesis, and transpiration, *International Journal of Remote Sensing*, 6, 1335-1372.

Sellers, P. J. (1987). Relations between canopy reflectance, photosynthesis and transpiration: Links between optics, biophysics and canopy architecture, *Advances in Space Research*, Vol. 7, No. 11, pp. 27-44.

Sellers, P., Los, S. O., Tucker, C. J., Justice, C. O., Dazlich, D. A., Collatz, G. J. & Randall, D. A. (1994). A global 1*1 degree NDVI data set for climate studies. Part 2: The generation of global fields of terrestrial biophysical parameters from the NDVI, *International Journal of Remote Sensing*, 15 (17): 3519-3545.

Shabanov, N. V., Zhou, L. M., Knyazikhin, Y., Myneni, R. B. & Tucker, C. J. (2002). Analysis of Interannual changes in northern vegetation activity observed in AVHRR data from 1981 to 1994, *IEEE Transactions on Geoscience and Remote Sensing*, 40, 115-130.

Singh, A. (1989). Digital change detection techniques using remotely-sensed data, *International Journal of Remote Sensing*, 10, 989–1003.

Singh, A. & Harrison, A. (1985). Standardized principal components, *International Journal of Remote Sensing*, 6: 883-896.

Singh, D., Meirelles, M. S. P., Costa, G. A., Herlin, I., Berroir, J. P. & Silva, E. F., (2004). Environmental degradation analysis using NOAA/AVHRR data, *Advances in Space Research*, doi: 10.1016/j.asr.2004.12.052.

Slayback, D. A., Pinzon, J. E., Los, S. O. & Tucker, C. J. (2003). Northern hemisphere photosynthetic trends 1982-99, *Global Change Biology*, (2003) 9, 1-15.

Snyder, R. L., Spano, D., Cesaraccio, C. & Duce, P. (1999). Determining degree-day thresholds from field observations, *International Journal of Biometeorology*, Volume 42, Issue 4, pp. 177-182.

Sobrino, J. A. & Raissouni, N. (2000). Toward remote sensing methods for land cover dynamic monitoring: application to Morocco, *International Journal of Remote Sensing*, 2000, Vol. 21, No. 2, 353-366.

Sobrino, J. A. & Romaguera, M. (2004). Land surface retrieval from MSG1-SEVIRI data, *Remote Sensing of Environment*, 92 (2004) 247-254.

Sobrino, J., Coll, C. & Caselles, V. (1991). Atmospheric correction for land surface temperature using NOAA-11 AVHRR channels 4 and 5, *Remote Sensing of Environment*, 38: 19-34.

Sobrino J., Caselles, V. & Coll, C. (1993). Theoretical split window algorithms for determining the actual surface temperature, *II Nuovo Cimento*, 16: 219-236.

Sobrino, J. A., Li, Z.-J., Stoll, M. P. & Becker, F. (1994). Improvement in the Split-Window Technique for Land Surface Temperature Determination, *IEEE Transactions on Geoscience and Remote Sensing*, 44, 343-253.

Sobrino, J. A., Li, Z.-L., Stoll, M. P. & Becker, F. (1996). Multi-channel and multi-angle algorithms for estimating sea and land surface temperature with ATSR data, *International Journal of Remote Sensing*, 1996, Vol. 17, No. 11, 2089-2114.

Sobrino, J. A., Raissouni, N., Simarro, J., Nerry, F. & Petitcolin, F. (1999). Atmospheric Water Vapor Content over Land Surfaces Derived from the AVHRR Data: Application to the Iberian Peninsula, *IEEE Transactions on Geoscience and Remote Sensing*, 1999, Vol. 37, No. 3, 1425-1434.

Sobrino, J. A., Jiménez-Muñoz, J. C., Labed-Nachbrand, J. & Nerry, F. (2002). Surface emissivity retrieval from Digital Airborne Imaging Spectrometer data, *Journal of Geophysical Research*, 107, D23, doi:10.1029/2002JD002197.

Sobrino, J. A., **Julien**, Y. & Morales, L. (2006a). Multitemporal analysis of PAL images for the study of land cover dynamics in South America, *Global and Planetary Change*, 51 (2006) 172-180.

Sobrino, J. A., Cuenca, J., Sòria, G., Jiménez-Muñoz, J.-C., Gómez, M., Zaragoza-Ivorra, M. M., Romaguera, M., **Julien**, Y., Shen, Q., Sepulcre, G., Morales, L., Gillespie, A., Balick, L., Peres, L., Libonati, R., Nerry, F. & Portier, M. (2006b). Thermal remote sensing in the framework of the SEN2FLEX Project: Field measurements, airborne data and applications, *2nd International Symposium on Recent Advances in Quantitative Remote Sensing*, pp. 142-146, Torrent, Spain, 25-29 September 2006.

Sobrino, J. A., Jiménez-Muñoz, J.-C., Sòria, G., Gómez, M., Barella-Ortiz, A., Zaragoza-Ivorra, M. M., **Julien**, Y. & Cuenca, J. (2007). Thermal Remote Sensing in the Framework of the SEN2FLEX Project: Field Measurements, Airborne Data and Applications, *International Journal of Remote Sensing*, in press.

Sperber, K. R., Sling, J. M., Inness, P. M. & Lau, W. K.-M. (1997). On the maintenance and initiation of the intraseasonal oscillation in the NCEP/NCAR reanalysis and in the GLA and UKMO AMIP simulations, *Climate Dynamics*, 13: 769-795.

Stehman, S. V., Sohl, T. L., & Loveland, T. R. (2005). An evaluation of sampling strategies to improve precision of estimates of gross change in land use and land cover, *International Journal of Remote Sensing*, 2005, Vol. 26, No. 22, 4941-4957.

Steinwand, D. R. (1994). Mapping raster imagery to the Interrupted Goode Homolosine projection, *International Journal of Remote Sensing*, 15, 3463-3472.

Stöckli, R. & Vidale, P. L. (2004). European plant phenology and climate as seen in a 20-year AVHRR land-surface parameter dataset, *International Journal of Remote Sensing*, 25, 3303–3330.

Stowe, L. L., Davis, P. & McClain, E. P. (1995). Evaluating the CLAVR (CLouds from AVhrR) phase I-cloud cover experimental product, *Advances in Space Research*, Vol. 16, No. 10, 1995, pp. 21-24.

Sun, D., & Pinker, R. T. (2003). Estimation of land surface temperature from a Geostationary Operational Environmental Satellite (GOES-8), *Journal of Geophysical Research*, 108 (11), 4326, doi:10.1029/2002JD002422.

231

Suzuki, R., Masuda, K & Dye, D. G. (2007). Interannual covariability between actual evapotranspiration and PAL and GIMMS NDVIs of northern Asia, *Remote Sensing of Environment*, 106 (2007) 387-398.

Tao, F., Yokozawa, M., Xu, Y., Hayashi, Y. & Zhang, Z. (2006). Climate changes and trends in phenology and yields of field crops in China, 1981-2000, *Agricultural and Forest Meteorology*, 138 (2006) 82-92.

Tateishi, R. & Ebata, M. (2004). Analysis of phenological change patterns using 1982-2000 Advanced Very High Resolution Radiometer (AVHRR) data, *International Journal of Remote Sensing*, 25 (12), 2287-2300.

Tømmervik, H., Høgda, K. A. & Solheim, I. (2003). Monitoring vegetation changes in Pasvik (Norway) and Pechenga in Kola peninsula (Russia) using multitemporal Landsat MSS/TM data, *Remote Sensing of Environment*, 85 (2003) 370-388.

Townshend, J. R. G. (1994). Global data sets for land applications from the Advanced Very High Resolution Radiometer, *International Journal of Remote Sensing*, 15, 3319-3332.

Trefethen, L. N. & Bau, D. (1997). *Numerical Linear Algebra*, Philadelphia, Society for Industrial and Applied Mathematics.

Tucker, C. J. (1979). Red and Photographic Infrared Linear Combinations for Monitoring Vegetation, *Remote Sensing of Environment*, 8 (2), 127-150.

Tucker, C. J. (1980). Remote Sensing of Leaf Water Content in the Near Infrared, *Remote Sensing of Environment*, 10: 23-32.

Tucker, C. J., Gatlin, J. A. &Schneider, S. R. (1984). Monitoring Vegetation in the Nile Delta with NOAA-6 and NOAA-7 AVHRR Data, *Photogrammetric Engineering and Remote Sensing*, 50: 53-61.

Tucker, C. J., Townshend, J. R. G. & Goff, T. E. (1985). African Land-Cover Classification Using Satellite Data, *Science*, 25 January 1985, Vol. 227, No. 4685, pp. 369-375.

Tucker, C. J., Dregne, H. E. & Newcomb, W. W. (1991). Expansion and contraction of the Sahara Desert between 1980 and 1990, *Science*, 253: 299-301.

Tucker, C. J., Slayback, D. A., Pinzon, J. E., Los, S. O., Myneni, R. B. & Taylor, M. G. (2001). Higher northern latitude NDVI and growing season trends from 1982 to 1999, *International Journal of Biometeorology*, 45, 184−190.

Tucker, C. J., Pinzon, J. E., Brown, M. E., Slayback, D. A. Pak, E. W., Mahoney, R., Vermote, E. F. & El Saleous, N. (2005). An extended AVHRR 8-km NDVI dataset compatible with MODIS and SPOT vegetation NDVI data, *International Journal of Remote Sensing*, Vol. 26, No. 20, 4485-4498.

Ulivieri, C., Castronouvo, M. M., Francioni, R. & Cardillo, A. (1992). *A Split Window Algorithm for Estimating Land Surface from Satellites*. COSPAR, 27 Aug.-5 Sept., Washington DC.

Ulivieri, C., Castronuovo, M., Francioni, R. & Cardillo, A. (1994). A split window algorithm for estimating land surface temperature from satellites, *Advances in Space Research*, 14 (3): 59-65.

UNEP (2005). *One Planet Many People: Atlas of Our Changing Environment*, Division of Early Warning and Assessment (DEWA), United Nations Environment Programme (UNEP), P.O. Box 30552, Nairobi, Kenya, http://na.unep.net/OnePlanetManyPeople/index.php

Ünsalan, C. & Boyer, K. L. (2004). Linearized vegetation indices based on a formal statistical framework, *IEEE Transactions on Geoscience and Remote Sensing*, 42, 1575−1585.

Valz, P. D., McLeod, A. I. & Thompson, M. E. (1995). Cumulant generating function and tail probability approximations for Kendall's score with tied rankings, *Annuals of Statistics*, Vol. 23, No. 1, 144-160.

Veith, W. (2000). The MSG Satellite and its subsystems, *Proceedings of The 2000 EUMETSAT Meteorological Satellite Data User's Conference*, Bologna, Italia, 29 May – 2 June.

Verhoef, W., Menenti, M. & Azzali, S. (1996). A colour composite of NOAA-AVHRR-NDVI based on time series analysis (1981-1992), *International Journal of Remote Sensing*, Vol. 17, No. 2, 231-235.

Verhoef, W., van der Kamp, A. & Koelemeijer, R. (2005). *Climate indicators from time series of NDVI images (CITISEN)*, Final report.

Vermote, E. F. & Kaufman, Y. J. (1995). Absolute calibration of AVHRR visible and near infrared channels using ocean and cloud views, *International Journal of Remote Sensing*, 16 (1995) (13), pp. 2317–2340.

Vermote, E., El Saleous, N., Kaufman, Y. J. & Dutton, E. (1997). Data Pre-Processing: stratospheric aerosol perturbing effect on the remote sensing of vegetation: Correction method for the composite NDVI after the Pinatubo Eruption, *Remote Sensing Reviews*, 15, 7-21.

Viña, A., Henebry, G. M. & Gitelson, A. A. (2004). Satellite monitoring of vegetation dynamics: Sensitivity enhancement by the wide dynamic range vegetation index, *Geophysical Research Letters*, 31, L04503.

Wan, Z., & Li, Z.-L. (1997). A Physics-Based Algorithm for Retrieving Land-Surface Emissivity and Temperature from EOS/MODIS Data, *IEEE Transactions on Geoscience and Remote Sensing*, 35 (4), 980-996.

Wang, K., Li, Z. & Cribb, M. (2006). Estimation of evaporative fraction from a combination of day and night land surface temperatures and NDVI: A new method to determine the Priestley-Taylor parameter, *Remote Sensing of Environment*, 102 (2006) 293-305.

Wang, Q. & Tenhunen, J. D. (2004). Vegetation mapping with multitemporal NDVI in North Eastern China Transect (NECT), *International Journal of Applied Earth Observation and Geoinformation*, 6 (2004) 17-31.

Wang, Q., Adiku, S., Tenhunen, J. & Granier, A. (2005). On the relationship of NDVI with leaf area index in a deciduous forest site, *Remote Sensing of Environment*, 94 (2005) 244-255.

Weinreb, M. P., Hamilton, G., Brown, S. & Koczor, R. J. (1990). Nonlinearity corrections in calibration of Advanced Very High Resolution Radiometer infrared channels, *Journal of Geophysical Research*, 95: 7381-7388.

White, M. A. & Nemani, R. R. (2006). Real-time monitoring and short-term forecasting of land surface phenology, *Remote Sensing of Environment*, 104 (2006) 43-49.

White, M. A., Thornton, P. E. & Running, S. W. (1997). A continental phenology model for monitoring vegetation responses to interannual climatic variability, *Global Biogeochemical Cycles*, 11, 217-234.

Wilks, D. S. (1995). *Statistical Methods in the Atmospheric Sciences, an Introduction*, San Diego, Academic Press.

Wilson, E. H. & Sader, S. A. (2002). Detection of forest harvest type using multiple dates of Landsat TM imagery, *Remote Sensing of Environment*, 80, 385–396.

Wolfe, D. W., Schwartz, M. D., Lakso, A. N., Otsuki, Y., Pool, R. M. & Shaulis, N. J. (2005). Climate change and shifts in phenology of three horticultural woody perennials in northeastern USA, *International Journal of Biometeorology*, 49, 303–309.

X

Xiao, X., Hagen, S., Zhang, Q., Keller, M. & Moore III, B. (2006). Detecting leaf phenology of seasonally moist tropical forests in South America with multi-temporal MODIS images, *Remote Sensing of Environment*, 103 (2006) 465-473.

Xu, H. & Young, J. A. T. (1990). Monitoring changes in land use through integration of remote sensing and GIS, In: *Proceedings of the 1990 International Geoscience and Remote Sensing Symposium*, pp. 957-960.

Y

Yang, H. & Yang, Z. (2006). A modified land surface temperature split window retrieval algorithm and its applications over China, *Global and Planetary Change*, Vol. 52, No. 1-4, July 2006, pp. 207-215.

Yokota, T. & Matsumoto, Y. (1988). Detection of seasonal and long-term changes in land cover from multitemporal Landsat MSS data, *Proceedings of IGARSS'88 Symposium*, ESA SP-284, Edinburgh, Scotland, pp. 215-218.

Young, S. S. & Wang, C. Y. (2001). Land-cover change analysis of China using globalscale Pathfinder AVHRR Landover (PAL) data, 1982–92, *International Journal of Remote Sensing*, 22, 1457–1477.

Yue, W., Xu, J., Tan, W. & Xu, L. (2007). The relationship between land surface temperature and NDVI with remote sensing: application to Shanghai Landsat 7 ETM+ data, *International Journal of Remote Sensing*, Vol. 28, No. 15, 3205-3226.

Z

Zhang, X. Y., Friedl, M. A., Schaaf, C. B., Strahler, A. H., Hodges, J. C. F., Gao, F., Reed, B. C. & Huete, A. (2003). Monitoring vegetation phenology using MODIS, *Remote Sensing of Environment*, 84 (3), 471-475.

Zhang, X., Friedl, M. A., Schaaf, C. B. & Strahler, A. H. (2004). Climate controls on vegetation phenological patterns in northern mid- and high latitudes inferred from MODIS data, *Global Change Biology*, (2004) 10, 1133-1145.

Zhou, L., Tucker, C. J., Kaufmann, R. K., Slayback, D., Shabanov, N. V. & Myneni, R. B. (2001). Variations in northern vegetation activity inferred from satellite data of vegetation index during 1981 to 1999, *Journal of Geophysical Research*, 106 (D17), 20069−20083.

Zhou, L., Kaufmann, R. K., Tian, Y., Myneni, R. B. & Tucker, C. J. (2003). Relation between interannual variations in satellite measures of vegetation greenness and climate between 1982 and 1999, *Journal of Geophysical Research*, 108 (D1), doi: 10.1029/2002JD002510.

Apendix

PUBLICATIONS

This section presents the articles published and to be published within the year 2008 in relation with this PhD dissertation. These articles are the following:

Julien, Y., Sobrino, J. A. & Verhoef, W. (2006). Changes in land surface temperatures and NDVI values over Europe between 1982 and 1999, *Remote Sensing of Environment*, 103 (2006) 43–55.

Julien, Y. & Sobrino, J. A. (accepted). Global land surface phenology trends from GIMMS database, *International Journal of Remote Sensing*.

Sobrino, J. A., Julien, Y. & Morales, L. (2006). Multitemporal analysis of PAL images for the study of land cover dynamics in South America, Global and Planetary Change, 51 (2006) 172-180.

Sobrino, J. A., Julien, Y., Atitar, M. & Nerry, F. (accepted). NOAA-AVHRR Orbital Drift Correction from Solar Zenithal Angle Data, *IEEE Transactions on Geoscience and Remote Sensing*.

Changes in land surface temperatures and NDVI values over Europe between 1982 and 1999

Yves JULIEN, José A. SOBRINO, & Wout VERHOEF

Remote sensing of environment, 2006, Vol. 103, Pages 43–55

Global land surface phenology trends from GIMMS database

Y. JULIEN. & José A. SOBRINO

International journal of remote sensing, 2008, Vol. 29

Multitemporal analysis of PAL images for the study of land cover dynamics in South America

J.A. SOBRINO, Y. JULIEN and L. MORALES

Pages 274-282 :

La publication présentée ici dans la thèse est soumise à des droits détenus par un éditeur commercial.

Les utilisateurs de l'ULP peuvent consulter cette publication sur le site de l'éditeur :

http://dx.doi.org/10.1016/j.gloplacha.2006.01.006

La version imprimée de cette thèse peut être consultée à la bibliothèque ou dans un autre établissement via une demande de prêt entre bibliothèques (PEB) auprès de nos services :

http://www-sicd.u-strasbg.fr/services/peb/

NOAA-AVHRR orbital drift correction from solar zenithal angle data (accepted)

José A. SOBRINO, Yves JULIEN, M. ATITAR & F. NERRY

IEEE transactions on geoscience and remote sensing, 2008